

DOCTORAL THESIS

Development of Low Gain Avalanche Detectors (LGAD) for high- and low-penetrating particles in silicon

Author:

Jairo Antonio Villegas Domínguez

Supervisors:

Salvador Hidalgo Villena
Giulio Pellegrini

Academic Tutor:

Pilar Casado Lechuga

*A thesis submitted in fulfillment of the requirements
for the degree of Doctor in Physics*

Physics Department
Universitat Autònoma de Barcelona

November 28, 2024

CERN-THESIS-2024-327
28/11/2024



CSIC
CONSEJO SUPERIOR DE INVESTIGACIONES CIENTÍFICAS



Centro Nacional de Microelectrónica



IMB



Radiation
Detectors
Group

Declaration of Authorship

This document certifies that the thesis “Development of Low Gain Avalanche Detectors (LGAD) for high- and low-penetrating particles in silicon” has been written by Jairo Antonio Villegas Dominguez under the supervision of Dr. Salvador Hidalgo Villena and Dr. Giulio Pellegrini, to fulfill the requirements to obtain the degree of Doctor in Physics.

Author:

Jairo Antonio Villegas
Domínguez

Supervisor:

Salvador Hidalgo Villena

Supervisor:

Giulio Pellegrini

Academic Tutor:

Pilar Casado Lechuga

Barcelona, November 28, 2024

Acknowledgements

First of all, let us thank the scientific community, whose members work hard for critical thinking to continue prevailing over mundane quackery. Without their efforts to elevate reason above fervor, the Earth would have been declared officially flat a few decades ago. Let us continue by thanking myself for contributing a tiny grain of sand to such a monumental task, as a scientist hardly abandons their work when getting out of research facilities, especially in these times when everything is dystopically questioned without a shred of evidence - whether at a family dinner, a friends' reunion at the bar, or even under the sheets.

This tiny grain of sand, which I hope will grow larger in the times to come, would not have been possible without the mentoring I have received over the last few years from Salvador Hidalgo and Giulio Pellegrini, the directors of my thesis, and Albert Doblas and Neil Moffat, my "unofficial mentors". Without them, not only the work presented in this thesis wouldn't have been materialized at all, but my experience in Science would now be ridiculously valueless. An extra hype for Pablo Fernandez, who wrote the first thesis about LGAD detectors, and which help during the last months of my PhD were fundamental.

However, my mentoring in Science has a longer tail in time. A mandatory expression of gratitude has to be made to MariCarmen Jimenez and Javier López, which helped me embark on my career while directing my Master's thesis.

Apart from mentoring, I would like to emphasize my gratitude to Salvador Hidalgo, MariCarmen Jimenez and Javier López, which thought me in a very clear way that climbing positions in a professional career does not necessarily require one to be a vulture, something I used to take for granted before starting to work in Science.

Before entering the personal part, I want to thank all the engineers that work in the clean-room, that literally and physically take all the flamboyant ideas that IMB-CNM physicist may have and turn them into a being. Thanks to Nuria, Elena, Andrea, David, Alberto, María, Ricard, Javier, Leyre and Sara, among others. Notice to navigators who think they are the smartest: without them, the LGAD wouldn't have gone further than a draft in a napkin.

I'd like to thank Vishal, Oliver and Kawal, staff of the B16 beamline of Diamond Light Source, for offering essential support and maintenance throughout the experiments (Grant Number OM33419). Also, I'd like to thank Roger and Dani for their reverse engineering and SRP measurements.

Next in line, I would like to thank my family. I would be lying if I said they have been my rock during these years of my thesis, as it was complicated for them to be so given the circumstances. The circumstances made me have to be such rock, something I neither pity nor regret. My greatest gratitude is that all the members of my family will be able to see me graduate, something I did not take for granted not long ago. Moreover, this only strengthens my determination to raise my voice in favor of Science, as a cure for cancer, not as harmless as the existing ones, lies within it.

Regarding rocks, I must emphasize my gratitude to many of my friends. They not only supported me during difficult times but also reminded me of something so necessary that we sometimes forget: the louder the laugh, the cheekier the soul. Thanks to Gloria, Cristian, Amanda, Emilio, Marina, Cecilia, Carlota, Alicia, Luis, Judit, Alejandro and Zoraida, among many others. You are *shrimpy* the best.

I would also like to thank Gianmarco not only for accompanying me throughout most of the journey of writing this thesis, but also for teaching me that love is not always for ever, and that parting ways with people is a natural part of life.

An additional thank you to Ezequiel, Jose, Nacho, Vasilis, William, Rodolfo, and Asier, for those things that are not elegant enough to say out loud but should be, given the way they lift your spirits and brighten your day.

During my stay in Glasgow, I want to thank Dima, Richard, Lojius and Rory for being such a great mentors and jobmates (both personally and professionally).

I would also like to thank the restaurants 'Jardín de Chen' and 'Pizzeria Capri' for feeding me during the last weeks of writing this thesis, especially when I had no time to cook my grandma's amazing recipes.

This work has been funded by the Spanish Ministry of Science, Innovation and Universities (MICIU/AEI/10.13039/501100011033/) and by the European Union's ERDF program "A way of making Europe". Grant references: PID2020-113705RB-C32, PID2021-124660OB-C22, PDC2021-121718-C32 and PDC2023-145925-C32. Also, it was supported by European Union's Horizon 2020 Research and Innovation funding program, under Grant Agreement No. 101004761 (AIDAInnova).

Contents

Abstract	viii
List of Figures	xviii
List of Tables	xix
List of Abbreviations	xx
Introduction	1
1 Semiconductors as radiation detectors	3
1.1 Brief history of radiation detectors	3
1.2 Band theory of solids	4
1.3 The PN junction	6
1.4 Interaction of ionizing radiation with semiconductors	9
1.5 Signal formation	10
1.6 Leakage current in silicon detectors	12
1.6.1 Temperature dependence	12
1.6.2 Impurity concentration dependence	13
1.6.3 Geometrical effects	14
1.6.4 Radiation damage dependence	14
1.7 The choice of Silicon	15
2 The Low Gain Avalanche Detector (LGAD)	17
2.1 Introduction	17
2.2 The PiN diode	17
2.3 Silicon detectors with intrinsic multiplication: LGAD concept	23
2.3.1 Gain and shot noise	26
2.3.2 Time resolution in LGADs	28
2.3.3 Breakdown and depletion voltages: finding the best trade	29
2.3.4 Avalanche mechanism for electrons and holes	30
2.4 Applications	32
2.4.1 Tracking and timing in High Energy Physics experiments	32
2.4.2 Detection of low-penetrating particles in silicon	33
3 Design and fabrication of LGADs	34
3.1 Introduction	34
3.2 Engineering fabrication techniques for planar technology	34
3.2.1 From crust to silicon wafer: an overview	34
3.2.2 Outline of engineering techniques for silicon detector fabrication at the IMB-CNM	37
Photolithography	37
Deposition/oxidation and selective etching	39
Dopant implantation	40

	Annealing and activation/diffusion of dopants	42
	Wafer cleaning	43
	Other techniques for quality control during fabrication	43
3.3	Fabrication process of single-pad LGADs at the IMB-CNM	44
3.3.1	The field oxide	45
3.3.2	The Channel Stopper and the P-stop	46
3.3.3	The Junction Termination Extension (JTE) and the guard ring	47
3.3.4	The multiplication layer	48
3.3.5	The electrodes	49
3.3.6	Metallization: the ohmic contacts	50
3.3.7	Passivation	52
3.3.8	Overview of the etching techniques at the IMB-CNM	53
3.4	Fabrication process of pixelated LGAD detectors	54
4	Optimization of LGAD core using TCAD Sentaurus	57
4.1	Introduction	57
4.2	TCAD Sentaurus simulation of dopant activation and diffusion in silicon	57
4.3	Optimization of the LGAD core design	59
4.4	The importance of quality control during the fabrication process	66
4.5	Future work on TCAD Sentaurus simulation	68
5	LGADs for High Energy Physics experiments	70
5.1	Introduction	70
5.2	Radiation damage in LGAD and PiN detectors	71
5.2.1	Leakage current increase	72
5.2.2	Conductivity type inversion	73
5.2.3	Acceptor removal effect	73
5.2.4	The role of carbon	74
5.3	The ATLAS and CMS experiments phase-II upgrade	75
5.4	Review of previous IMB-CNM LGAD runs	80
5.4.1	Non-carbonated IMB-CNM LGADs	80
5.4.2	Carbonated IMB-CNM LGADs	82
5.5	ATLAS HGTD LGAD 6LG2-v1 run and its comparison to the ATLAS-CMS Engineering 6LG3-v2 run	85
5.5.1	TCAD Sentaurus simulation of carbonated LGADs	86
5.5.2	Basic electrical characterization: IV and CV measurements	89
5.5.3	Stabilization of the LGAD technology at the IMB-CNM	92
5.5.4	Gain response to 15 keV x-rays	95
5.5.5	Radiation tolerance of 6LG2-v1 detectors	98
5.5.6	Fulfilment of ATLAS HGTD and CMS ETL phase-II upgrade specifications	100
5.5.7	IV measurements of ATLAS 6LG2-v1 pixelated detectors	102
5.5.8	Overview of 6LG2-v1 run results	107
5.6	CMS LGAD 6LG2-v2 run	107
5.6.1	Growing oxide in doped-silicon: an brief overview	109
5.6.2	Basic electrical characterization: IV and CV measurements at 20°C	111
5.6.3	Comparative analysis of CMS 6LG2-v2 run with ATLAS-CMS engineering 6LG3-v2 run and ATLAS 6LG2-v1 run	113
5.6.4	SRP of 6LG2-v1 and 6LG2-v2 samples	116

5.6.5	TCAD Sentaurus simulation of CMS 6LG2-v2 detectors	121
5.6.6	IV measurements of CMS 6LG2-v2 pixelated detectors	122
5.7	IMB-CNM 6DLG technology: Deep Profile LGADs	125
5.7.1	Design and fabrication of the first dLGAD prototypes: CMS 6DLG2-v1 run	128
5.7.2	Optimization of the periphery elements in a dLGAD	130
5.7.3	Basic electrical characterization: IV and CV measurements of 6DLG2-v1 detectors	133
5.7.4	The choice of dopant for the N^{++}	136
5.7.5	CMS 6DLG2-v2 run	138
5.7.6	CMS 6DLG3-v1 run	140
5.8	Conclusions and future work	141
6	nLGAD for low-penetrating particles detection	143
6.1	Introduction	143
6.2	LGAD limitations for low-penetrating particles detection	143
6.3	Potential nLGAD applications	145
6.3.1	Detection of low-penetrating photons	145
6.3.2	Detection of low-penetrating charged particles	146
6.4	IMB-CNM 4NLG1-v1 fabrication run	147
6.4.1	nLGAD response to TCT visible light of 660 nm wavelength	148
6.4.2	nLGAD response to synchrotron 15 keV x-rays	150
6.4.3	Review of the gain response measurements for 4NLG1-v1 detectors	152
6.5	IMB-CNM Fabrication run 4NLG1-v2	154
6.5.1	Evaluation of the entrance window thickness: SRP measurements	156
6.5.2	Basic electrical characterization: IV and CV measurements at 20°C	157
6.5.3	Gain response to UV, visible and IR light	158
6.5.4	Gain response to 404 nm wavelength visible light as a function of the beam flux	161
6.5.5	Gain response to low-energy protons	164
6.6	Conclusions and future work	168
7	Trench iLGADs for fill factor optimization	170
7.1	Introduction	170
7.2	LGAD designs for fill factor optimization	170
7.3	Design and fabrication of TiLGAD devices at the IMB-CNM	175
7.3.1	TiLGAD core optimization via TCAD Sentaurus simulation	177
7.3.2	TiLGAD fabrication process at the IMB-CNM	180
7.4	4TiLG3-v1 run: TiLGAD on epitaxial wafers	185
7.4.1	IV and CV measurements of single-pad TiLGAD sensors	185
7.4.2	Reverse engineering measurements: SRP and cross-section	187
7.4.3	TCT Gain response to 1064 nm wavelength photons	191
7.5	4TiLG2-v1: TiLGAD on Si-Si wafers	192
7.6	4TiLG2-v2 and 4TiLG3-v2 runs	194
7.6.1	Preliminary IV measurements	196
7.6.2	Preliminary TCAD Simulation of the TiLGAD periphery	197
7.7	Conclusions and future work	199

Conclusions and future lines of work	201
Scientific Contributions	205
Appendix A: Acronyms for IMB-CNM Runs	207
Bibliography	208

UNIVERSITAT AUTÒNOMA DE BARCELONA

Abstract

Physics Department
Universitat Autònoma de Barcelona

Doctor in Physics

Development of Low Gain Avalanche Detectors (LGAD) for high- and low-penetrating particles in silicon

by Jairo Antonio Villegas Domínguez

This thesis presents the development of Low Gain Avalanche Detectors (LGAD) at the Institute of Microelectronics of Barcelona (IMB-CNM). The work is primarily focused on the design, optimization and fabrication of LGAD sensors for High Energy Physics (HEP) experiments and, specifically, for High-Luminosity Large Hadron Collider (HL-LHC) experiments at CERN. The HL-LHC aims to upgrade in the next few years, increasing its luminosity to enable the collection of more data in shorter time frames which, in turns, will increase the likelihood of new particle discoveries. Consequently, the silicon detectors used in HL-LHC experiments must demonstrate exceptional radiation tolerance as well as tracking and timing performance to prevent pile-up effects, being the LGAD a great candidate to fulfil such zealous task.

While the primary focus of LGAD development has been HEP experiments, these detectors also offer potential applications beyond this field. Specifically, LGADs hold promise for detecting low-penetrating particles in silicon. To accommodate these applications, a redesign of the LGAD was necessary, as it was originally optimized exclusively for HEP experiments. As a result, the nLGAD was first developed at IMB-CNM, which retains the excellent performance of traditional LGAD devices while being specifically optimized to detect low-penetrating particles. The design, optimization and fabrication of IMB-CNM nLGAD sensors represent a significant aspect of this thesis.

Additionally, an LGAD or nLGAD can be technologically tailored to achieve a fill factor of 100 %, which is crucial for applications requiring enhanced silicon detector sensitivity. This thesis will specifically address the potential of the Trench iLGAD (TiLGAD) in achieving this goal.

Overall, this work will cover the design, simulation, optimization, fabrication and characterization of IMB-CNM LGAD sensors across various technological configurations, each tailored to address specific key issues in the realm of particle detection.

List of Figures

1.1	schematic of the electron bonding arrangement in an intrinsic, n-type and p-type silicon crystal lattice.	5
1.2	Band diagram and E_F level for intrinsic, n-type silicon and p-type silicon.	6
1.3	a) n and p-type silicon pieces. b) joint of n- and p-type silicon, where a built-in potential creates a small depletion region. c) widening of the depletion region by reverse bias application.	8
1.4	Absolute minimum of the function $F(\beta\gamma) = \frac{1}{\beta^2} [0.5 \ln(\beta^2\gamma^2) - \beta^2] \propto -dE/dx$	10
1.5	schematic of the drift of electrons and holes generated by a mip in the space-charge region of a fully depleted PN junction.	11
1.6	Representation of the pileup phenomenon.	12
1.7	Illustration of mid-gap energy states (E_{mg}) within the bandgap.	13
2.1	2D TCAD Sentaurus simulation of the net active doping concentration of a n-type PiN diode of $1.3 \times 1.3 \text{ mm}^2$ of active area and $50 \text{ }\mu\text{m}$ thickness.	18
2.2	2D TCAD Sentaurus simulation of the optical generation for light pulses of 404 nm (A) and 1064 nm (B) wavelength in an n-type PiN diode of $1.3 \times 1.3 \text{ mm}^2$ of active area and $50 \text{ }\mu\text{m}$ thickness	19
2.3	TCAD Sentaurus simulation of the electric field (at 450 V reverse bias and 20°C) and leakage current dependence on active thickness for an n-type PiN diode.	20
2.4	TCAD Sentaurus simulation of the output generated signal, at 450 V reverse bias and 20°C , dependence on active thickness for an n-type PiN diode when illuminated with light pulses of 404 and 1064 nm wavelength.	20
2.5	Generated output signals displayed along with different noise levels $N \gg 1$. If N exceeds certain limit, some of the signals cannot be processed.	21
2.6	SNR dependence on the background noise level $N \approx N_{i_L}$	22
2.7	TCAD Sentaurus simulation of the signal dependence on IR beam intensity, at 450 V and 20°C . I_0 corresponds to the intensity used in the simulations shown in Figures 2.5 and 2.6.	23
2.9	TCAD Sentaurus simulation of the CC and SNR dependence on reverse bias for an p-type PiN diode illuminated with a low intensity 1064 nm IR pulse-beam.	24
2.8	TCAD Sentaurus simulation of the generated signal and electric field dependence on reverse bias for an p-type PiN diode illuminated with a 1064 nm IR pulse-beam and at 20°C	24
2.10	TCAD Sentaurus simulation of the doping profile of an p-type detector with intrinsic amplification and its electric field.	25

2.11	TCAD Sentaurus simulated gain and SNR for a p-type silicon detector with intrinsic amplification.	26
2.12	Gain measurements on a 50 μm thick LGAD when irradiated with a high-flux 15 keV X-rays beam at Diamond Lightsource [23].	28
2.13	Gain, SNR, risetime and σ_{jitter} for an LGAD while being illuminated with a 1064 nm beam pulse of high intensity ($Q \gg 1$).	29
2.14	Leakage current and capacitance vs reverse bias measurements, at 20°C, for three IMB-CNM manufactured LGADs, each one corresponding to a different fabrication batch.	30
2.15	2D TCAD Sentaurus simulation of the active doping concentration profiles of an n a p-type LGAD. The optical generations for a 404 nm and 1064 nm beam-pulse are also displayed.	31
3.1	schematic of how a CZ ingot is created, to thereafter go through a FZ process and obtain a high-purity silicon ingot.	35
3.2	schematic of how Si-Si and epitaxial wafers are processed.	36
3.3	Illustration of the beginning and end of a silicon detector wafer fabrication process.	38
3.4	Outline of a photolithography process to create a pattern on the surface of a silicon wafer.	38
3.5	Outline of a photolithography process to create a pattern on a deposited/ <i>growth</i> SiO_2 layer tailored onto the surface of a silicon wafer.	40
3.6	Outline of the dopant implantation and activation/diffusion onto the surface of a silicon wafer.	41
3.7	schematic of a boron ion implantation on a $\langle 100 \rangle$ silicon wafer, with a growth screen oxide and a tilt of 7° and without.	41
3.8	Cross section of a single-pad LGAD of active volume $1.3 \times 1.3 \text{ mm}^2 \times 50 \mu\text{m}$ fabricated on a high resistivity p-type wafer on a low-resistivity handle wafer of 350 μm . The device elements are not scaled in order to better distinguished each part.	45
3.9	Front view and cross section of a single-pad LGAD where a channel stopper and a p-stop have been constructed.	46
3.10	Front view and cross section of a single-pad LGAD where a JTE and a guard ring have been constructed.	48
3.11	Front view and cross section of a single-pad LGAD where a multiplication layer has been constructed.	49
3.12	Front view and cross section of a single-pad LGAD where an N^{++} electrode has been constructed.	50
3.13	Front view and cross section of a single-pad LGAD where contacts have been opened on the electrodes and the guard ring.	50
3.14	Front view and cross section of a single-pad LGAD where the metalization process has been done.	52
3.15	Front view and cross section of a single-pad LGAD where the passivation process has been done.	53
3.16	schematic of how the lateral etch changes from wet to plasma etching.	54
3.17	Cross section of a detector of 2 x 2 LGAD pixels.	55
3.18	schematic of the photolithographic steps for the manufacturing of a detector of 2 x 2 LGAD pixels.	56
4.1	TCAD simulation of the net active doping concentration of an LGAD core.	58

4.2	TCAD Sentaurus simulation prediction, for different Advanced Calibration version and at 20°C, of the IV and CV curves for LGADs of the 6LG2-v2 fabrication run.	59
4.3	Color code mapping of the D_B , D_P sets that better fit the measured V_{gl} for IMB-CNM LGADs of the 6LG2-v2 fabrication batch.	61
4.4	TCAD Sentaurus simulation prediction, for different diffusivity sets (listed in Table 4.2) and at 20°C, of the IV and CV curves for LGADs of the 6LG2-v2 fabrication run.	61
4.5	(A): Simulated doping profiles for the different $[D_B, D_P]$ sets listed in Table 4.2. (B): peak of active boron and width of the multiplication layer as a function of the $[D_B, D_P]$ set.	62
4.6	(A): Simulated boron concentration in the multiplication layer for the different $[D_B, D_P]$ sets listed in Table 4.2.(B): Charge integral of the multiplication layer as a function of the $[D_B, D_P]$ set.	63
4.7	CV extracted boron profiles (via Equation 4.2) for LGADs of the 6LG2-v2 fabrication batch, shown along with the simulated profiles obtained via TCAD Sentaurus with the $[D_B, D_P]$ value sets listed in Table 4.2.	64
4.8	CV extracted boron profiles for LGADs of the 6LG2-v2 fabrication batch, shown along with the TCAD Sentaurus simulation obtained with the calibrated set $[D_B, D_P]=[0.82, 0.26]cm^2/s$	64
4.9	IV and CV measurements, at 20°C, for LGADs of the 6LG2-v2 fabrication batch, shown along with the TCAD Sentaurus simulation obtained with the calibrated set $[D_B, D_P]=[0.82, 0.26]cm^2/s$ and the Van Overstraeten - De Man avalanche model.	65
4.10	TCAD Sentaurus simulation of the doping profile, breakdown voltage at 20°C and V_{gl} for IMB-CNM LGADs of the 6LG2-v2 fabrication batch, as a function of the screen oxide growth prior to the multiplication layer implantation.	66
4.11	TCAD Sentaurus simulation of the doping profile, breakdown voltage at 20°C and V_{gl} for IMB-CNM LGADs of the 6LG2-v2 fabrication batch, as a function of the screen oxide growth prior to N^{++} layer implantation.	67
4.12	TCAD Sentaurus simulation of the breakdown voltage at 20°C and V_{gl} for IMB-CNM LGADs of the 6LG2-v2 fabrication batch, as a function of the high-resistivity layer thickness.	67
4.13	TCAD Sentaurus simulation of the doping profile, breakdown voltage at 20°C and V_{gl} for IMB-CNM LGADs of the 6LG2-v2 fabrication batch, as a function of time ramp to reach 1100°C in the multiplication layer annealing of 3h.	68
5.1	(A) TCAD Sentaurus simulation of the boron and phosphorus doping profiles around the PN junction, in a IMB-CNM fabricated LGAD, with and without the presence of a carbon layer. (B): Same as (A) but showing the net active doping profiles.	75
5.2	schematic of the HGDT within the ATLAS detector [72]	77
5.3	schematic of the ETL within the CMS detector [4]	77
5.4	V_{op} (CMS ETL specifications) dependence on n_{eq} irradiation fluence for 6LG2-v2 detectors. Data extracted from [75], [78].	84
5.5	Photograph of a manufactured wafer from the 6LG2-v1 run. The single-pad LGADs for testing are located within the yellow boxes.	85

5.6	schematic of the front view and cross section of a carbonated single-pad LGAD from the 6LG2-v1 run.	85
5.7	TCAD Sentaurus simulation of LGAD doping profiles dependence on the carbon implantation dose. (A): profiles in logarithmic scale to distinguish the carbon layers. (B): profiles in linear scale and narrowed around the PN junction.	87
5.8	TCAD Sentaurus simulation of an LGAD doping profile (as fabricated in the 6LG3-v2 run) dependence diffusivity pre-factors choice (Table 5.6).	88
5.9	TCAD Sentaurus simulation of V_{gl} and V_{BD} at -30°C dependence on the carbon implantation dose and diffusivity pre-factors choice.	88
5.10	TCAD Sentaurus simulation of IV at -30°C and CV curves of 6LG3-v2 detectors, shown along with actual data. The diffusivity pre-factors is the one labelled as "tuned" in Table 5.6.	89
5.11	(A): Average IV measurements, at -30°C , of 6LG2-v1 detectors. (B): Method to infer the V_{BD} per device.	90
5.12	Average CV measurements, at 20°C , of 6LG2-v1 detectors.	90
5.13	Methodology to infer V_{gl}	90
5.14	V_{gl} and V_{BD} (at -30°C) dependence on carbon implantation dose for 6LG2-v1 detectors.	91
5.15	CV-extracted boron doping profiles for 6LG2-v1 detectors, along with the average boron concentration peak dependence on carbon implantation dose.	92
5.16	Average V_{gl} and V_{BD} data from 6LG3-v2 and 6LG2-v1 detectors, along with their Sentaurus predicted values using the tuned diffusivity parameters shown in Table 5.6.	92
5.17	Optical view of a cross section of 6LG3-v2 and 6LG2-v1 LGAD samples.	93
5.18	V_{BD} data from 6LG3-v2 and 6LG2-v1 detectors, along with their Sentaurus predicted values using the tuned diffusivity parameters shown in Table 5.6 and thicknesses of 49 and 55 μm	93
5.19	CV-extracted doping profiles for 6LG3-v2 (dashed line) and 6LG2-v1 (solid line) devices.	94
5.20	Example of photocurrent derivation for the non carbonated 6LG2-v1 LGAD and reference PiN.	96
5.21	(A): Gain response vs bias, at 20°C , of 6LG2-v1 detectors to 15 keV x-rays. (B) Gain vs carbon implantation dose at different bias points.	96
5.22	(A): Gain response vs relative intensity of the 15 keV x-ray beam, at 20°C and 100 V. (B) Gain vs carbon implantation dose, at 20°C and 100V, at different relative beam intensities.	97
5.23	Gain response vs bias and relative intensity of the 15 keV x-ray beam, at 20°C , for the 6LG2-v1 device carbonated with a dose of $3 \cdot 10^{14} \text{ at/cm}^2$	98
5.24	Acceptor removal constant c for 6LG3-v2 [25] and 6LG2-v1 detectors [51], [86].	99
5.25	IV curves dependence on irradiation fluence for 6LG2-v1 detectors carbonated with implantation doses 0, 1, 3 and $6 \cdot 10^{14} \text{ at/cm}^2$	99
5.26	(A): Leakage current, at 300 V and -30°C dependence on irradiation fluence. (B): Same as (A), but analysing the dependence on carbon implantation dose.	100
5.27	Mask design for the temporary metal in the 6LG2-v1 LGAD run.	102

5.28	Leakage current of a 6LG2-v1 segmented LGAD of 2x2 pixels with and without the temporary metal.	103
5.29	Leakage current of 6LG2-v1 segmented detectors of 15x15 pixels, measured with temporary metal at -30°C.	103
5.30	On wafer location of tested devices.	104
5.31	Leakage current of 6LG2-v1 segmented detectors of 15x15 pixels, measured with temporary metal at -30°C (IMB-CNM) and with a probe card at 20°C (USTC).	104
5.32	Average leakage current per pixel of 6LG2-v1 segmented detectors of 15x15 pixels, measured with a probe card at 20°C (USTC) [87].	105
5.33	Color code mapping of the reverse bias at which every pixel reaches 200 nA of leakage current, for 6LG2-v1 segmented detectors IV measured with a probe card at 20°C.	106
5.34	Photograph of a manufactured wafer from the 6LG2-v2 run. The single-pad LGADs for testing are located within the yellow boxes.	108
5.35	schematic of the front view and cross section of a carbonated single-pad LGAD from the 6LG2-v2 run.	108
5.36	TCAD Sentaurus simulation of the doping profile, breakdown voltage at 20°C and V_{gl} for IMB-CNM LGADs of the 6LG2-v2 fabrication batch, as a function of the screen oxide growth prior to N^{++} layer implantation.	111
5.37	Averaged IV curves, at 20°C, of 6LG2-v2 detectors.	112
5.38	Averaged CV curves, at 20°C, of 6LG2-v2 detectors.	112
5.39	V_{gl} and V_{BD} dependence (at 20°C) on carbon implantation dose for 6LG2-v2 detectors.	112
5.40	CV-extracted boron doping profiles for 6LG2-v2 detectors.	113
5.41	Average V_{gl} and V_{BD} data from 6LG3-v2, 6LG2-v1 and 6LG2-v2 detectors.	114
5.42	CV-extracted doping profiles for ATLAS-CMS 6LG3-v1, ATLAS 6LG2-v1 and CMS 6LG2-v2 IMB-CNM runs.	114
5.43	CV-extracted doping profiles for 6LG2-v2 detectors with a carbon dose of $4 \cdot 10^{14} \text{ at/cm}^2$	115
5.44	schematic of the SRP technique. Figure extracted from [92].	116
5.45	Example of a p-type calibration curve for SRP measurements. Such curve was used when studying the doping profiles of 6LG2-v1 detectors.	117
5.46	Example of doping profile extraction from raw spreading resistance data. The shown profile corresponds to a non-carbonated 6LG2-v1 LGAD.	117
5.47	Doping profile around the PN junction for a non-carbonated 6LG2-v1 LGAD, obtained via SRP and with different junction field correction models.	118
5.48	SRP doping profiles of ATLAS 6LG2-v1 LGAD samples.	118
5.49	SRP doping profiles of CMS 6LG2-v2 LGAD samples.	119
5.50	PN junction depth vs carbon implantation dose, extracted from SRP measurements.	119
5.51	SRP extracted multiplication layer boron peak and charge integral for 6LG2-v1 and 6LG2-v2 detectors.	120
5.52	SRP-simulated V_{gl} and V_{BD} for 6LG2-v1 and 6LG2-v2 detectors, at 20°C.	120
5.53	TCAD Sentaurus predicted V_{gl} (A) and V_{BD} , at 20°C, of 6LG2-v2 detectors after diffusivity model calibration.	121
5.54	On wafer location of tested devices.	122

5.55	Total Leakage current (A) and average leakage current per pixel (B) of 6LG2-v2 segmented detectors of 16x16 pixels, measured with a probe card at 20°C in USTC.	122
5.56	Average leakage current per pixel of 6LG2-v2 segmented detectors of 16x16 pixels, measured with a probe card at 20°C (USTC) [87].	123
5.57	Color code mapping of the reverse bias at which every pixel reaches 200 nA of leakage current, for 6LG2-v2 segmented detectors IV measured with a probe card at 20°C.	124
5.58	Histogram showing the number of ATLAS 6LG2-v1 and CMS 6LG2-v2 pixels that reach 200 nA of leakage current, at 20°C, and its dependence on reverse bias.	125
5.59	Schematically representation of the differences in the PN junction of an LGAD and a dLGAD.	126
5.60	TCAD Sentaurus simulation of the typical doping profile of an LGAD and a dLGAD	126
5.61	TCAD Sentaurus simulation of the electric field (at 20°C and 200 V) of an LGAD and a dLGAD	127
5.62	TCAD Sentaurus prediction of the PN junction and carbon layers of 6DLG2-v1 run. (A): PN and carbon layers in logarithmic scale. (B): Multiplication layer in linear scale.	129
5.63	TCAD Sentaurus prediction of V_{gl} and V_{BD} for 6DLG2-v1 devices.	130
5.64	TCAD Sentaurus simulation of the JTE (at different thermal loads) and multiplication layer for 6DLG2-v1 detectors.	131
5.65	TCAD Sentaurus simulation of the p-stop and channel stopper profiles for 6LG2-v2 and 6DLG2-v1 devices. (A): logarithmic scale. (B): linear scale.	131
5.66	480 keV carbon and boron ions distribution as they pass through a 1.5 μm of oxide, obtained via Stopping and Range of Ions in Matter (SRIM) simulation [104].	132
5.67	30 keV phosphorus ions distribution as they pass through a 0.1 μm of oxide grown onto the cutlines, obtained via SRIM simulation [104].	133
5.68	Average IV and CV measurements of 6DLG2-v1 dLGAD and PiN devices.	133
5.69	(A): CV-extracted boron profiles for 6DLG2-v1 dLGADs. (B): Comparison of the profiles in (A) with TCAD Sentaurus simulations.	134
5.70	(A): CV-extracted boron profiles for 6DLG2-v1 devices. (B): Comparison of the profiles in (A) with TCAD Sentaurus simulations.	135
5.71	TCAD Sentaurus simulations of the V_{gl} and V_{BD} dependence on screen oxide grown prior to the N^{++} and multiplication layer implantations for 6DLG2-v1 dLGADs.	135
5.72	TCAD Sentaurus simulations of a dLGAD doping profile when using arsenic and phosphorus for the N^{++} layer fabrication. (A): logarithmic scale. (B): linear scale around the PN junction.	136
5.73	TCAD Sentaurus simulations of a dLGAD electric field at 20°C and 100 V for dLGAD devices constructed with the doping profiles shown in Figure 5.72.	137
5.74	TCAD Sentaurus simulations of V_{BD} (at 20°C) of dLGAD devices as a function of the N^{++} dopant species, t_{ox} prior to the N^{++} and multiplication layer implantations, and boron implantation dose.	137

5.75	TCAD Sentaurus simulations of V_{gl} of dLGAD devices as a function of the N^{++} dopant species, t_{ox} prior to the N^{++} and multiplication layer implantations, and boron implantation dose.	138
5.76	SEM pictures of the core and guard ring opening contacts of a PiN detector from 6DLG2-v2 run, where spikes can be spotted.	139
5.77	Average bulk and surface current measurements, at 20°C, of dLGAD and PiN detectors from 6DLG2-v2 run.	140
6.1	LGAD gain response, at 20°C, to 404 and 1064 nm wavelength photons inferred via TCT.	144
6.2	Penetration depth of different photon species that interact mainly via photo-effect with silicon [17], [22], [107].	145
6.3	Range in silicon for protons and alpha particles of relative low energy [113].	146
6.4	schematic of the front view and cross section of an nLGAD from the IMB-CNM 4NLG1-v1 fabrication run.	148
6.5	TCT output signal, at 20°C, for the studied nLGAD and reference nPiN under illumination with 660 nm visible light.	149
6.6	CC vs reverse bias, at 20°C, of an nLGAD and a reference nPiN from the 4NLG1-v1 run when illuminated with TCT 660 nm wavelength light.	150
6.7	Leakage current and Beam On current for the studied nLGAD and reference nPiN diode, while illuminated with synchrotron 15 keV x-rays.	151
6.8	Photocurrent (difference between leakage and Beam On) for the studied nLGAD and reference nPiN diode, while illuminated with synchrotron 15 keV x-rays.	152
6.9	Gain response of 4NLG1-v1 detectors to 660 nm wavelength visible light and 15 keV x-rays, by using the techniques and methodologies described in sections 6.4.1 and 6.4.2.	152
6.10	Gain response of 4NLG1-v1 and 6LG3-v1 detectors, at 50 V below their breakdown voltage value and 20°C, for different photon species.	153
6.11	schematic of the cross section of an nLGAD from the 4NLG1-v2 run.	154
6.12	(A): schematic of the front view of nLGAD from the 4NLG1-v2 run. (B): Actual photograph of a single-pad nLGAD.	155
6.13	Photograph of a manufactured wafer from the 4NLG1-v2 run. The single-pad LGADs for testing are located within the red boxes.	155
6.14	Doping concentration around the PN junction of the studied nLGAD samples, extracted via SRP technique [91]	156
6.15	Average curves (with standard deviation errors) of the capacitance and leakage current measurements at 20°C.	157
6.16	TCT output signals for illumination of an nLGAD and an nPiN with light of 369, 404 and 1064 nm wavelength. The Y axis is adjusted for every wavelength to better distinguished the differences between the nLGAD and the nPiN signals.	159
6.17	(1): Gain response to TCT light pulses of 369, 404 and 1064 nm wavelength for the three studied nLGAD detectors. (2): Average gain (with standard deviation error bars) at 100, 150 and 200 V of reverse bias as a function of the penetration depth [17] of the photon species.	160
6.18	Gain response to TCT light pulses of 369 nm wavelength for the nLGAD labelled as LG13.	161

6.19	CC of the laser-generated nPiN signals (CC) dependence on V_{th} within a linear range, at 100 V and 20°C. The projected area $A \approx (\pi/4)155 \cdot 136 \mu\text{m}^2$ was unchanged during the measurements.	162
6.20	CC of the laser-generated nLGAD and nPiN signals dependence on the projected area A , at 100 V and 20°C. The DAC threshold $V_{th} = 1056\text{mV}$ was unchanged during the measurements. The CC is normalized, for every device, with respect to its maximum value across A , in order to better distinguish the trend for the nLGAD and the reference nPiN.	163
6.21	nLGAD gain response, at 100 V and 20°C, as a function of the 404 nm wavelength laser beam flux (as defined in Equation 6.1). The intensity is scaled to its maximum value, which corresponds to the minimum value of V_{th} and A in Table 6.1.	163
6.22	Energy spectrum, at normal incidence, 50 V and room temperature, for 600 keV impinging on the nLGAD under test. The left picture shows the spectrum in logarithmic scale, where counts in the nLGAD periphery elements can be grasped. The right picture shows, in linear scale, only the channel range around the multiplication area, along with its Gaussian centroid.	164
6.23	(1): Spectra of the nPiN and nLGAD, at normal incidence, 50 V and room temperature. (2): Image reconstruction of the nLGAD spectrum in (1), where both the active area and the periphery elements (Figures 6.11 and 6.12) can be distinguished. The channel number has been scaled, in both pictures, to the CC of the reference nPiN, so a gain spectrum and map are obtained.	165
6.24	nLGAD gain response to 600 keV protons (with the beam incident to the device front and backside) and 1064 nm IR TCT beam pulses. . . .	166
6.25	(1): Bragg peak depth dependence on rotation angle, inferred via SRIM simulations, for 600 keV protons impinging on the studied nLGAD. (2): nLGAD gain response, at 50 V and room temperature, to 600 keV protons as a function of the Bragg peak depth.	167
6.26	CC vs rotation angle for the studied nLGAD and nPiN irradiated with 600 keV protons.	168
7.1	Cross-section schematic of a pixelated TI-LGAD with a matrix of 2 x 2 pixels.	171
7.2	Cross-section schematic of a pixelated AC-LGAD with a matrix of 2 x 2 pixels.	172
7.3	Cross-section schematic of a pixelated 4ILG1-v1 detector with a matrix of 2 x 2 pixels.	173
7.4	Cross-section schematic of a 4ILG1-v2 single-pad detector.	174
7.5	Cross-section schematic of a pixelated TiLGAD with a matrix of 2 x 2 pixels.	174
7.6	Photograph of the first TiLGAD wafer fabricated with the CNM1086 mask.	175
7.7	schematic of a Si-Si or epitaxial wafer used for 4TiLG2 and 4TiLG3 fabrication runs.	176
7.8	TCAD Sentaurus predicted V_{gl} and V_{BD} for TiLG2-v1 (A) and TiLG3-v1 (B) devices.	178
7.9	TCAD Sentaurus simulation of the doping profiles for TiLGAD fabricated on Si-Si (W3 in Table 7.1) and epitaxial wafers.	179

7.10	TCAD Sentaurus simulation of a single-pad TiLGAD gain response, at 20°C, to 404 nm (blue light) and 1064 (IR light) wavelength.	179
7.11	TCAD Sentaurus simulation of a single-pad n-type and p-type TiLGAD gain responses, at 20°C, to 404 nm (blue light) and 1064 (IR light) wavelength.	180
7.12	Cross section of a detector of 2 x 2 TiLGAD pixels after the P^{++} , guard ring and Channel stopper fabrication.	181
7.13	Cross section of a detector of 2 x 2 TiLGAD pixels after the DRIE process to create the trenches.	181
7.14	Cross section of a detector of 2 x 2 TiLGAD pixels after trench filling process.	182
7.15	Top view of a filled trench, obtained via SEM.	182
7.16	Optical view of the TiLGAD wafer around the trenches after the oxide and poly-silicon filling process.	183
7.17	Cross section of a detector of 2 x 2 TiLGAD pixels after metallization and passivation processes.	184
7.18	Front view and cross section schematic of a single-pad TiLGAD.	184
7.19	Average leakage current, at 20°C, of 4TiLG3-v1 devices.	185
7.20	Average CV curve (A) and CV-extracted boron profile (B) of 4TiLG3-v1 devices.	186
7.21	Leakage current dependence on temperature for a TiLG3-v1 device.	186
7.22	Structure used to simulate the breakdown voltage nature of TPiNs.	187
7.23	TCAD Sentaurus simulation of the leakage current dependence on temperature for a TPiN.	187
7.24	Averaged SRP doping profiles of TiLG3-v1 devices dependence on the junction field correction model.	188
7.25	TCAD Sentaurus simulation of TiLG3-v1 devices using the averaged SRP PN junction profiles.	188
7.26	SRP doping profiles of raw epitaxial wafers (before fabrication) dependence on the junction field correction model.	189
7.27	Optical view of the cross-section of a TiLGAD sample around a trench, before chemical development.	190
7.28	Optical view of the cross-section of a TiLGAD sample around a trench, after chemical development.	190
7.29	Signal (A) and gain (B) responses to TCT IR light of 1064 nm wavelength for a TiLG3-v1 device and a reference PiN.	191
7.30	2D map of the average TCT signal amplitude for the TiLGAD at 20.5 and 22 V.	192
7.31	Leakage current, before (solid lines) and after (dashed lines) the passivation process, of 4TiLG2-v1 devices at 20°C.	193
7.32	TiLG-v2 wafer, fabricated with the mask CNM1202.	195
7.33	TCAD Sentaurus prediction of the IV and CV curves of 4TiLG3 devices when annealed for 180 minutes at 1250°C, based on the raw wafer SRP profiles for every junction field correction model.	196
7.34	IV measurements, at 20°C, for TiLGAD on Epitaxial and Si-Si wafers (implanted with a boron dose of $3.7 \cdot 10^{14} \text{ at/cm}^2$).	196
7.35	TCAD Sentaurus simulation of the TiLGAD periphery termination (left) and its IV curve, at 20°C, for a core composed of a PiN detector (right).	197

7.36	TCAD Sentaurus simulation of the electric field, at 350 V and 20°C, of a TiLGAD termination with a core composed of a PiN detector (left) and cutlines of such electric field at the Si-Trench interface and core (right).	198
7.37	TCAD Sentaurus simulation of the TiLGAD periphery with the termination removed (left) and its IV curve, at 20°C, for a core composed of a PiN detector (right).	198
7.38	TCAD Sentaurus simulation of the electric field, at 350 V and 20°C, of a TiLGAD, with a core composed of a PiN detector, with its termination removed (left) and cutlines of such electric field at the Si-Trench interface and core (right).	199

List of Tables

4.1	Diffusivity pre-factor and activation energy of boron and phosphorus for different Sentaurus Advanced Calibration versions.	60
4.2	Diffusivity pre-factor and activation energy of boron and phosphorus that predict the V_{gl} of CNM-6LG2-v2 LGADs.	62
5.1	Technical and geometrical specifications for the CMS ETL and ATLAS HGTD LGAD sensors	79
5.2	Technical and geometrical specifications for the CMS ETL (2021) and ATLAS HGTD (2023) sensors, along with the characterization of 4LG1-v2 and 6LG3-v1 detectors [25], [77].	81
5.3	Fabrication features for the 6LG3-v1 and 6LG3-v2 LGAD runs.	82
5.4	Technical and geometrical specifications for the CMS ETL (2021) and ATLAS HGTD (2023) sensors, along with the characterization of 6LG3-v2 detectors [25], [75], [77], [78].	83
5.5	Fabrication features for 6LG2-v1 LGAD run.	86
5.6	Diffusivity pre-factor of boron and phosphorus through interstitials.	87
5.7	Technical and geometrical specifications for the CMS ETL (2021) sensors, along with the characterization of 6LG2-v1 detectors [51].	101
5.8	Technical and geometrical specifications for the ATLAS HGTD (2023) sensors, along with the characterization of 6LG2-v1 detectors [67], [78].	101
5.9	Percentage of pixels in segmented 6LG2-v1 detectors (measured at 20°C with a probe-card at USTC) that do not exceed 200 nA of leakage current up to V_{opCMS} and $V_{opATLAS}$	105
5.10	Fabrication features for 6LG2-v2 LGAD run.	109
5.11	Percentage of pixels in segmented ATLAS 6LG2-v1 and CMS 6LG2-v2 detectors (measured at 20°C with a probe-card at USTC) that do not exceed 200 nA of leakage current up to 100 V.	123
5.12	Overview of the differences in implantation and annealing processes for LGAD and dLGAD fabrication.	127
5.13	Fabrication features for 6DLG2-v1 run.	129
5.14	V_{BD} (at 20°C) and V_{gl} average variation per 100 Å of screen oxide thickness (for the N^{++} and multiplication layer implantations) and its dependence on the N^{++} dopant species for LGAD and dLGAD devices.	138
5.15	Fabrication features for 6DLG2-v2 LGAD run.	139
5.16	Fabrication features for 6DLG3-v1 run.	141
5.17	Overview of the performance of 6LG detectors.	142
6.1	DAC, CC(nPiN) at 20°C and 100 V, axes length in X and Y for the beam projection, estimated A and relative flux.	162
7.1	Fabrication features of the 4TILG2-v1 and 4TILG3-v2 runs.	177
7.2	Fabrication features of the 4TILG2-v2 and 4TILG3-v2 runs.	194

List of Abbreviations

4iLG2	inverse LGAD on Si-Si(2) wafers of 4 inches (100 mm) diameter
4LG2	LGAD on Si-Si(2) wafers of 4 inches (100 mm) diameter
4NLG1	nLGAD on FZ(1) wafers of 4 inches (100 mm) diameter
4TiLG2	Trench inverse LGAD on Si-Si(2) wafers of 4 inches (100 mm) diameter
4TiLG3	Trench inverse LGAD on Epitaxial(3) wafers of 4 inches (100 mm) diameter
6DLG2	Deep profile LGAD on Si-Si(2) wafers of 6 inches (150 mm) diameter
6DLG3	Deep profile LGAD on Epitaxial(3) wafers of 6 inches (150 mm) diameter
6LG2	LGAD on Si-Si(2) wafers of 6 inches (150 mm) diameter
6LG3	LGAD on Epitaxial(3) wafers of 6 inches (150 mm) diameter
AC-LGAD	Alternating Current Capacitively Coupled Low Gain Avalanche Detector
AIDA	Advancement and Innovation for Detectors and Accelerators
APD	Avalanche PhotoDetector
ATLAS	A Toroidal LHC ApparatuS
CB	Conduction Band
CC	Collected Charge
CCE	Charge Collection Efficiency
CERN	Conseil Européen pour la Recherche Nucléaire
CMS	Compact Muon Sollenoid
CRL	Compound Refractive Lens
CSIC	Consejo Superior de Investigaciones Científicas
CVD	Chemical Vapor Deposition
CV	Capacitance vs reverse bias Voltage
CZ	CZochralski
dLGAD	Deep profile Low Gain Avalanche Detector
DRIE	Deep Reactive Ion Etching
ETL	Endcap Timing Layer
FWHM	Full Width at Half Maximum
FZ	Flat Zone
HEP	High Energy Physics
HGTD	High Granularity Timing Detector
HL-LHC	High Luminosity Large Hadron Collider
IFAE	Institut de Física d'Altes Energies
IFCA	Instituto de Física de Cantabria
iLGAD	inverse Low Gain Avalanche Detector
IMB-CNM	Institute of Microelectronics of Barcelona - National Center of Microelectronics
IP	Inter Pad
IR	InfraRed
IV	Current Intensity vs reverse bias Voltage
JSI	Jozef Stefan Institute
JTE	Junction Termination Extension
LGAD	Low Gain Avalanche Detector

LHC	Large Hadron Collider
mip	minimum ionizing particle
MNC	Metales Nobles y Contaminante (Noble Metals or Contaminant)
nLGAD	n-type Low Gain Avalanche Detector
PE	Plasma Etching
PECVD	Plasma Enhanced Chemical Vapor Deposition
PiN	P-type – intrinsic silicon – N-type detector
R&D	Research and Development
RD50	Radiation Hard Semiconductor Detectors For very High Luminosity Colliders
RTA	Rapid Thermal Annealing
SEM	Scanning to Electron Microscopy
SIMS	Secondary Ion Mass Spectroscopy
SNR	Signal to Noise Ratio
SRP	Spreading Resistance Profiling
TCAD	Technology Computer Aided Design
TI-iLGAD	Trench Isolated inverse Low Gain Avalanche Detector
TiLGAD	Trench inverse Low Gain Avalanche Detector
USTC	University of Science and Technology of China
UV	Ultra Violet
VB	Valence Band

Introduction

The drive to unveil the origins of mass, the nature of dark matter, and the fundamental forces shaping the universe led to the establishment of CERN (Conseil Européen pour la Recherche Nucléaire) in Geneva, Switzerland, and the development of the Large Hadron Collider (LHC), the most powerful particle accelerator on Earth [1]. Operational since 2008, the LHC is able to accelerate protons to nearly the speed of light and make them collide in high-energy events. These collisions simulate the conditions that existed just after the Big Bang, enabling scientists to investigate the fundamental building blocks of matter. The construction of the LHC and its experiments involved extensive international collaboration with thousands of scientists, engineers, and technicians from around the world. One key project within this context is the RD50 collaboration [2], which focused on overcoming the limitations of standard silicon detectors in the extreme radiation environments inherent to the LHC experiments. Specifically, part of the RD50 collaboration worked on designing, fabricating, and testing silicon detectors for the ATLAS (A Toroidal LHC Apparatus) and CMS (Compact Muon Solenoid) phase-II upgrades, which is intended to prepare these detectors for the High-Luminosity LHC (HL-LHC) [3], [4]. The HL-LHC will increase the rate of proton-proton collisions by ~ 10 , allowing for the collection of more data in shorter periods and enhancing the potential for new particle discoveries. This upgrade inevitably requires that the silicon detectors used in HL-LHC experiments exhibit unprecedented radiation tolerance and timing performance to avoid pile-up phenomena.

This technological challenge in the realm of High Energy Physics (HEP) experiments led to the development of Low Gain Avalanche Detectors (LGADs), which use the principle of avalanche multiplication to enhance the signal generated by incident radiation. Initially designed and fabricated at the Institute of Microelectronics of Barcelona (IMB-CNM) [5], LGADs swiftly demonstrated their potential to overcome the limitations of standard silicon detectors to be functional at the HL-LHC environments. The optimization of LGAD design and fabrication at the IMB-CNM for HEP experiments is a central focus of this thesis.

In addition to HEP experiments, LGADs have potential applications in physics experiments that require the detection of low-penetrating particles in silicon, such as low-energy protons, alpha particles, and soft x-rays. Traditional IMB-CNM LGADs are not suitable for detecting these particles because their performance is limited by their design, which is optimized for HEP experiments. To address this limitation, the nLGAD was developed at the IMB-CNM [6] as a redesign LGAD optimized for the detection of low-penetrating particles in silicon, which introduces another central topic of this thesis. Conversely, nLGADs are not suitable for HEP experiments, as their performance degrades when detecting high-penetrating particles in silicon. The main difference between an LGAD and an nLGAD is the substrate used for their fabrication. LGADs are built on p-type substrates, while nLGADs are manufactured on n-type substrates.

Beyond the nature and energy of the particle to be detected, enhancing the sensitivity of LGADs through improved fill factor has been a significant focus within the

RD50 collaboration. Typical segmented LGADs inherently have regions where the aforementioned avalanche mechanism is not triggered by design. These regions are intended to isolate the pixels and preserve spatial resolution during the detection. Thus, addressing the fill factor challenge involves designing and fabricating LGADs with uniform performance regardless of the particle interaction point. To achieve this, Trench iLGADs (TiLGADs) were first designed and manufactured at the IMB-CNM, which constitutes the last central focus of this thesis. In TiLGADs, the pixels are fabricated on the opposite side of the detector compared to traditional pixelated LGADs, and includes a trench termination to guarantee proper device functionality. This design ensures that no part of the detector area is excluded from avalanche multiplication, achieving a 100% fill factor. Additionally, the TiLGAD design has the potential to overcome the limitations of LGADs and nLGADs, making it suitable for detecting both high- and low-penetrating particles in silicon.

This thesis is organized in nine chapters, each focusing on a different topic, as hereunder detailed:

- Chapter 1 offers a didactic approach to the theory of solids for semiconductors, a crucial topic for understanding the importance of silicon sensors in particle detection experiments.
- Chapter 2 digs deeper into the detection of radiation with silicon sensors, highlighting the differences between a standard PiN detector and an LGAD.
- Chapter 3 focuses on the design and fabrication of LGADs at the IMB-CNM. It offers a detailed outline of the manufacturing techniques used at the IMB-CNM to transform a design into a tangible detector.
- Chapter 4 provides a comprehensive overview of using TCAD Sentaurus simulations for LGAD optimization.
- Chapter 5 provides a chronological overview of LGAD development at the IMB-CNM for the ATLAS and CMS experiments phase-II upgrade, highlighting the latest findings that are central to this thesis.
- Chapter 6 introduces the LGAD fabrication on n-type substrates (nLGAD), an innovative LGAD design extending beyond HEP experiments. Specifically, it is designed to address the limitations of traditional LGADs for applications requiring the detection of low-penetrating particles in silicon.
- Chapter 7 presents another novel LGAD design, the TiLGAD, which not only aims to overcome the limitations of traditional LGADs for low-penetrating particles detection but also achieves a fill factor of 100%.
- Finally, the main findings, conclusions and potential future lines of work on LGAD design, fabrication, and applications will be addressed.

Chapter 1

Semiconductors as radiation detectors

1.1 Brief history of radiation detectors

The development of quantum mechanics during the 20th century led to a deeper understanding of the underlying physics, along with many other fields of science, of solid-state materials. In turn, it gave rise to a long period of technological upgrade and development of electronic devices. Particularly, the design and performance of radiation detectors was highly enhanced during these times onwards, being it still an open field of research.

The most rudimentary radiation detector ever used by science researchers were, oddly, their own bodies. Unaware of the (nowadays known) fatal health risks that radiation exposure may lead to, Walkoff and Giesel (1900), among others, would spread radium salt over their bare skin to estimate the level of radiation: the higher it was, the redder the burn [7]. By then, the first scintillator able to detect individual radiation-matter interactions was being fashioned by Crookes (1903) [7]. Along with skin reddening, scintillation counting with the naked eye was one of the oldest radiation detection techniques [8]. No wonder that, deprived from the sophisticated techniques that were about to start up developing, human senses were the primary means to carry out experiments of this sort.

Little after that, the primitive version of the Geiger-Müller counter (Rutherford and Geiger, 1908) was being built [7]. Both gaseous ionization chambers and scintillators were tested and developed during the following decades, giving rise to few challenges to deal with. It was already known that a solid medium was more efficient than a gaseous one in absorbing the incident radiation due to its larger density. Despite scintillation crystals seemed to overcome this drawback, they brought another in. In a scintillator, the energy of an incident particle is converted into light, that in turn generates an electrical signal to be read out. Having a middle step between the particle incidence and the output signal, along with the crude amplifiers of those times, made scintillators quite unefficient. With the development of photomultipliers from 1935 onwards [7] it was possible to turn a scintillation photon into many charge carriers (electrons) rather than only a few, so counting particles became much more efficient.

Even with the addition of upgraded photomultipliers, the number of photoelectrons that generate the pulse in a scintillator is not large enough to deal with the statistical fluctuations inherent to spectrometry, resulting in a poor resolution when measuring the particle energy. The only means to improve energy resolution is the boost of available charged carriers to create the output signal, fact that pushed the development of semiconductor detectors (available from 1960 [7]). In a semiconductor detector, the incident particle generates a large number of charged carriers that

are collected under the application of an external electric field without the need of a middle step as it's the case of scintillators. Among all materials, silicon is one of the best semiconductors for charged particles detection and spectroscopy, as we will be discussing within this chapter.

1.2 Band theory of solids

A solid-state piece of material can be described as an arrangement of atoms forming a crystalline lattice. Applying the Pauli exclusion principle to this lattice, electrons on it cannot occupy energy levels with the same quantum numbers, resulting in a set of allowed atomic orbitals for each one of them. In a macroscopic solid, the number of orbitals is so large (of the order of the Avogadro's number) and their difference in energy so slight that it's acceptable to mathematically treat the energy spectrum as continuous: an energy band.

In solids, the electronic levels split up into two bands: the valence (VB) and the conduction (CB) ones. The VB has the lower energy levels and is firstly filled by electrons, while the CB can be partially filled or empty depending on the solid. In between there's a forbidden energy bandgap. The energy width of such bandgap, defined as the difference between the highest energy level in the VB and the lowest energy level in the CB: $E_g = E_C - E_V$, gives rise to the familiar classification of solids according to their conductivity: conductors, semiconductors and insulators. In a conductor E_g is so small (or even null) that the CB is partially filled at room temperature, so the electrons on it can move freely throughout the crystal. On the other hand, in an insulator E_g is large enough so the CB is empty at room temperature and electrons have a negligible probability of being promoted to such band by thermal excitation.

In the middle ground we classify semiconductors, which E_g is moderate enough so few electrons can be thermally excited from the VB to the CB and migrate throughout the semiconductor causing conduction. Likewise, the empty bond in the crystal lattice left behind by the electron can be seen as a positive charge (a so-called hole) that can also contribute to conduction. In silicon $E_g = 1.12 \text{ eV}$. It can be shown that the concentration of electrons (n) and holes (p) for any semiconductor can be approximately given as [9].

$$\begin{cases} n = n_i e^{(E_F - E_i)/kT} \\ p = n_i e^{(E_i - E_F)/kT} \end{cases} \quad (1.1)$$

where n_i a function of temperature and $E_g (n_i \propto e^{-E_g/2kT})$, k is the Boltzmann constant, T is the temperature and E_F is the Fermi level, defined as the energy level of the atomic orbital at which the occupation probability is 0.5 (an extensive derivation of Equation 1.1 can be found in [9], [10]). In turn, E_i is defined as the Fermi level for an intrinsic semiconductor, i.e. without impurities or a negligible amount of them, and lies close to the middle of the bandgap $E_i \approx (E_C + E_V) / 2$. It's clear from Equation 1.1 that for a pure semiconductor the concentration of the different charge carriers are equal: $n = p = n_i$. The latter identity only tells us that the semiconductor must be electrically neutral in equilibrium. Thus, n_i is defined as the concentration of free charge carriers (p) in an ideal intrinsic semiconductor. In the case of silicon, $n_i \sim 10^{10} p/cm^3$ at room temperature.

As we will discuss later in this section, having the same concentration of electrons and holes in a semiconductor is not useful for practical applications. Instead,

intrinsic semiconductors are doped with a certain amount of impurities to break the balance. For silicon, with four valence electrons, we have two scenarios. In one hand, let's replace a silicon atom of the lattice by a dopant atom with five valence electrons, such as phosphorus (Figure 1.1). Four of these electrons will bond to the neighboring silicon atoms, but the fifth does not fit into the bonding arrangement of the crystal structure and is weakly bound to the lattice site. Thus, at room temperature this electron can easily be excited to the CB, becoming a charge carrier available for conduction and leaving behind a positive ion fixed in the lattice. On the other hand, let us think about the same procedure but with an atom with three valence electrons, such as boron (Figure 1.1). In this case the dopant atom is missing one electron to complete the 4-bond lattice structure. However, dopants are chosen such that it's energetically more favorable to have the dopant-silicon bonds completed than the silicon-silicon ones. Thus the latter bonds tend to break to give away an electron to create the first ones, creating a hole available for conduction and leaving behind a fixed negative silicon ion. Dopants that increase the electron concentration are called donors, and the silicon obtained after doping is called n-type. Analogously, if the hole concentration is increased, the dopant is called acceptor and the silicon obtained is called p-type.

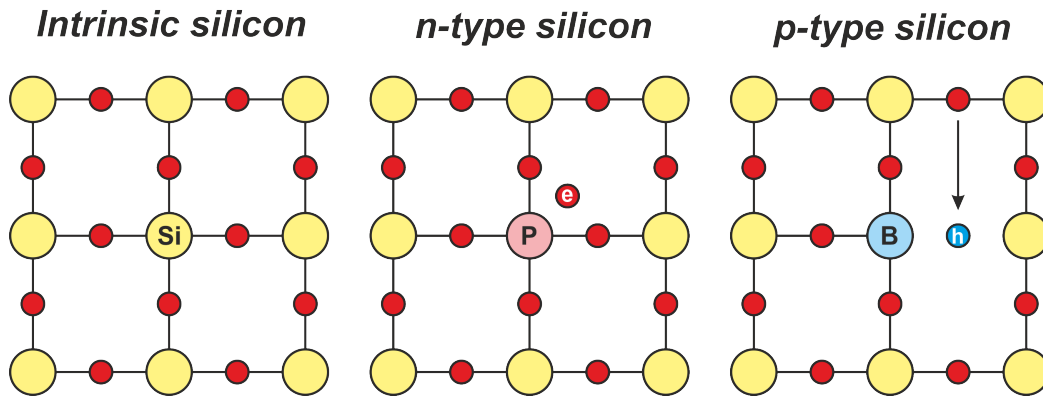


FIGURE 1.1: schematic of the electron bonding arrangement in an intrinsic, n-type and p-type silicon crystal lattice.

The main effect in the band structure of semiconductors after doping is the displacement of the Fermi level E_F from its intrinsic value E_i . Donors tend to shift E_F closer to the CB, while acceptors displace it towards the VB, as Figure 1.2 shows. This is a direct consequence of the creation of energy levels within the bandgap when impurities are introduced in a pure semiconductor. Donors create levels that lay very close to E_C , so electrons in these states are easily promoted to the CB at room temperature. Similarly, acceptors create levels laying quite close to E_V , so they are easily occupied by electrons from the VB via thermal excitation. From Equation 1.1 we can see that

$$E_F - E_i = kT \ln \left(\frac{n}{n_i} \right) = -kT \ln \left(\frac{p}{n_i} \right) \quad (1.2)$$

which is just 0 for intrinsic silicon ($n = p = n_i$). For doped silicon the latter identity no longer holds but still the semiconductor as a whole is electrically neutral. Then

$$n + N_A = p + N_D \quad (1.3)$$

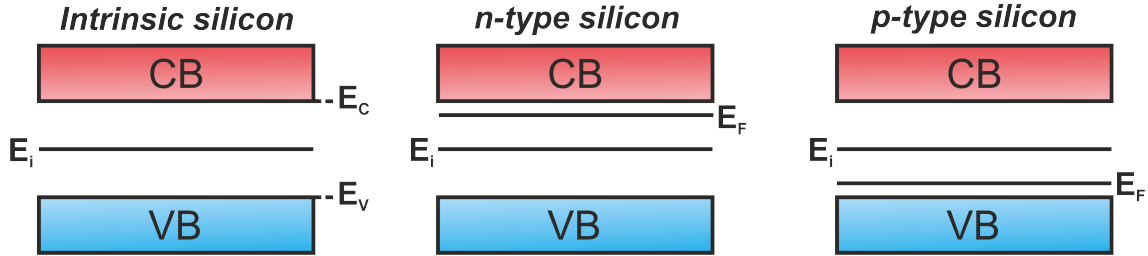


FIGURE 1.2: Band diagram and E_F level for intrinsic, n-type silicon and p-type silicon.

where N_D (N_A) is the donor (acceptor) concentration, equal to the concentration of fixed positive (negative) ions within the crystal if all dopant atoms are ionized, which is the usual case at room temperature. For n-type silicon $N_A = 0$ and $p \ll n$, hence $n \simeq N_D$. Likewise, for p-type silicon $N_D = 0$ and $p \gg n$, so $p \simeq N_A$. Thus

$$E_F = \begin{cases} E_i & \text{intrinsic silicon} \\ E_i + kT \ln \left(\frac{N_D}{n_i} \right) & \text{n-silicon} \\ E_i - kT \ln \left(\frac{N_A}{n_i} \right) & \text{p-silicon} \end{cases} \quad (1.4)$$

1.3 The PN junction

As we've discussed, for doped silicon we obtain a semiconductor with an excess of charge carriers available for conduction (electrons for n-type and holes for p-type). In the general case the doping concentration largely exceeds the intrinsic concentration n_i , hence the concentration of majority charge carriers is nearly equal to the doping one: $n \simeq N_D$ and $p \simeq N_A$ (Equation 1.3). When a p-type and a n-type semiconductor are brought into contact, the system acquires a set of physical properties that makes it optimal for radiation detection, as well as for nearly every application in electronics. This system is called the PN junction, and its main features are discussed below.

When the two pieces of semiconductor are joined, the concentration gradient that appears at the vicinity of the junction makes charge carriers diffuse throughout it (electrons from the n to the p-side, and holes the other way around). Most of the diffused electrons and holes will recombine with their analogous of opposite charge, leaving a region of fixed nuclear positive charge in the n-side and a region of fixed nuclear negative charge in the p-one. These regions are called, as a whole, the space charge region, and as it grows larger, an electric field \vec{E} is generated within it that grows more intense until it counteracts completely the diffusion process. At this point the semiconductor has reached equilibrium and the space charge region has been completely depleted of mobile charge carriers, hence it's also called the depletion region. The potential difference thus created between the edges of the depletion

region is proportional to the difference of the Fermi levels between the n and p semi-conductors before their joint [11]. Using equations 1.4 this built-in potential can be obtained as

$$V_{bi} = \frac{E_F(n) - E_F(p)}{e} = \frac{kT}{e} \ln \left(\frac{N_D N_A}{n_i^2} \right) \quad (1.5)$$

The natural emergence of V_{bi} across the PN junction ensures that the Fermi level is constant throughout the system, required condition for reaching equilibrium.

For the seek of simplicity, we will assume that the fixed nuclear charge is homogeneously distributed at both the p and n-sides (despite this approach is quite approximate, it gives a clear insight of the PN junction functionality). Thus, the charge density can be expressed as

$$\rho(x) = \begin{cases} eN_D & -x_n < x \leq 0 \\ -eN_A & 0 \leq x < x_p \end{cases} \quad (1.6)$$

where x_n and x_p are the widths of the depletion region at the n and the p-side, respectively. Applying the Poisson's equation to this charge distribution: $\nabla^2 \varphi = -\nabla \varepsilon = -\rho/\epsilon$ one obtains [8]

$$\varepsilon(x) = \begin{cases} \frac{eN_D}{\epsilon} (x + x_n) & -x_n < x \leq 0 \\ -\frac{eN_A}{\epsilon} (x - x_p) & 0 \leq x < x_p \end{cases} \quad (1.7)$$

$$\varphi(x) = \begin{cases} -\frac{eN_D}{2\epsilon} (x + x_n)^2 + V_{bi} & -x_n < x \leq 0 \\ \frac{eN_A}{2\epsilon} (x - x_p)^2 & 0 \leq x < x_p \end{cases} \quad (1.8)$$

where the boundary conditions $\varepsilon(x_p) = \varepsilon(-x_n) = 0$ (that is, that the electric field is limited within the depletion region) and $\varphi(-x_n) - \varphi(x_p) = V_{bi}$ (definition of built-in potential) have been taken. The values of the widths x_n and x_p can also be estimated by taking into account that, in equilibrium, both the electric field and the potential must be continuous at the junction ($x=0$). This condition leads to an equation system for x_n and x_p which solution is [11]

$$\begin{cases} x_n = \sqrt{\frac{2\epsilon V_{bi}}{e} \frac{N_A}{N_D(N_A + N_D)}} \\ x_p = \sqrt{\frac{2\epsilon V_{bi}}{e} \frac{N_D}{N_A(N_A + N_D)}} \\ w = x_n + x_p = \sqrt{\frac{2\epsilon V_{bi}}{e} \frac{N_A + N_D}{N_D N_A}} \end{cases} \quad (1.9)$$

As we will explain in detail in Chapter 2, silicon detectors are designed such that one side of the junction is much more doped and is way thinner than the other, so the depletion region extends almost entirely on the less-doped and larger side (the so-called bulk). This way the width of the depletion region can be easily expressed as

$$w = \sqrt{\frac{2\epsilon V_{bi}}{eN}} \quad (1.10)$$

where N corresponds to the dopant concentration of the bulk.

Since the depletion region has been stripped from charge carriers, it forms a capacitor limited by the conductive n and p-sides. Assuming valid the parallel plate model, the capacitance per unit area of the depletion region can be calculated as

$$C_D = \frac{\epsilon}{w} = \sqrt{\frac{e\epsilon N}{2V_{bi}}} \quad (1.11)$$

Generally, the built-in potential is not high enough to deplete the bulk from carriers. However, one can achieve that by applying a reverse bias at both the far edges of the p and n-sides, as Figure 1.3 illustrates. Thus, electrons will diffuse further to the p-side and holes to the n-one, increasing both the electric field and the depletion region width until a new equilibrium has been reached.

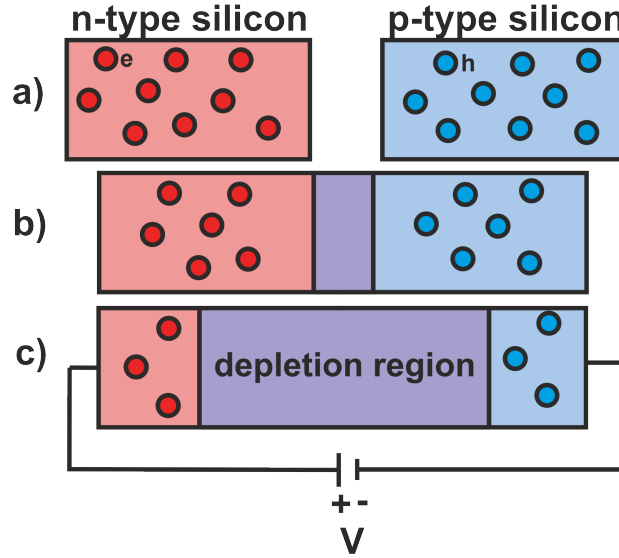


FIGURE 1.3: a) n and p-type silicon pieces. b) joint of n- and p-type silicon, where a built-in potential creates a small depletion region. c) widening of the depletion region by reverse bias application.

The same mathematical treatment that for $V = 0$ can be carried out but replacing V_{bi} for $V_{bi} + V$, obtaining [11]

$$w = \sqrt{\frac{2\epsilon (V_{bi} + V)}{eN}} \quad (1.12)$$

$$C_D = \frac{\epsilon A}{w} = \sqrt{\frac{e\epsilon N}{2(V_{bi} + V)}} \quad (1.13)$$

V can be increased until the depletion region has covered the entire bulk ($w = d$, being d the thickness of the bulk) and the detector capacitance has reached a saturation minimum value. The bias voltage at which this happens is called the full depletion voltage V_{FD} and is one of the most important parameters in silicon detectors design.

Equation 1.6 is a good first approximation to understand the main electrical features of the PN junction in a qualitative way. However, in the real case, the doping concentration of both the p- and n-sides is not constant throughout the PN junction system but a function of the three spatial coordinates ($N = N(x, y, z)$). Hence, solutions of the Poisson's equation are not as straightforward as Equations 1.7 and 1.8 and numerical methods are needed to get the mathematical problem solved. TCAD

(Technological Computing Aided Simulation) Sentaurus is a powerful tool to do so, as we will discuss in Chapter 4.

1.4 Interaction of ionizing radiation with semiconductors

When ionizing radiation traverses the depletion region of a PN junction, a certain number of electron-hole pairs is created within it along the particle track. Due to the electric field present in the region, these charge carriers are quickly drifted away from it. If we are able to collect these charges, the resulting signal will inform us that a particle has just went through the system. This is the key to semiconductors as radiation detectors.

Ionization in the semiconductor can occur in a different way for charged particles or photons. In the case of charged particles, they directly ionize the atoms of the material by losing part of the energy along their track, which is approximately linear. Apart from ionization, which results from interaction of the charged particle with the electronic atoms of the material, nuclear reactions may also occur. Interactions with the nuclei of the material cause a damage in the semiconductor structure that needs to be taken into account for an optimal detector design and performance. This will be briefly discussed in Chapter 1 and comprehensively addressed in Chapter 5.

The mean energy loss by unit length (the so-called stopping power) for a relativistic heavy charged particle ($\beta > 0.1$) of charge z and relative velocity $\beta = v/c$ impinging in a material of density ρ , atomic number Z and mass number A is given by the Bethe-Bloch formula [12]:

$$-\frac{dE}{dx} \propto \rho \frac{Z}{A} \frac{z^2}{\beta^2} \left[\frac{1}{2} \ln \left(\frac{2m_e c^2 T_{max}}{I^2} (\beta\gamma)^2 \right) - \beta^2 + f(\beta\gamma) \right] \quad (1.14)$$

where m_e is the electron rest mass, T_{max} is the maximum kinetic energy that can be transferred in a collision, I is the mean excitation energy of the material, $\gamma = [1 - \beta^2]^{-1/2}$ and $f(\beta\gamma)$ is a correction factor for high energies. A heavy charged particle with a energy such that the stopping power is minimum is called a minimum ionizing particle (mip).

Regardless of the material, the Bethe-Bloch formula has a minimum at $\beta\gamma \sim 3$, which corresponds to $v \sim 0.95c$. After this minimum is reached, the stopping power barely changes over a wide range of relativistic velocities, as Figure 1.4 shows. Thus, any relativistic particle in the range $3 \lesssim \beta\gamma \lesssim 1000$ ($0.95c \lesssim v \lesssim 0.9995c$) can be treated as a mip, as the difference in energy lost as ionization of the material by the former and the latter differ little. In silicon, a mip has an average stopping power of $\sim 400 \text{ eV}/\mu\text{m}$ [12]. Since the energy required to create an electron-hole pair in silicon is $E_{eh} \approx 3.6 \text{ eV}$ [8], a mip crossing a detector with a typical thickness of $\sim 100 \mu\text{m}$ is able to generate $\sim 10^4$ electron-hole pairs.

In the case of photons, they are not able to cause direct ionization as there's no Coulomb interaction between them and the atomic electrons. Instead, they can interact with the material in three different ways [7]. For low energy photons such as x-rays or visible light, the main interaction is the photoelectric effect: the photon is absorbed by an atom, that in turn releases an electron. For gamma rays up to $\sim 10 \text{ MeV}$ the main interaction is the scattering of the photon with an electron, losing the former a fraction of its energy and leaving the latter with a certain recoil energy (Compton scattering). Also, for gamma rays over $2m_e c^2 = 1.022 \text{ MeV}$, the photon can be absorbed to produce a electron-positron pair. In any of these interactions, electrons (and positrons in the latter case) are released within the semiconductor

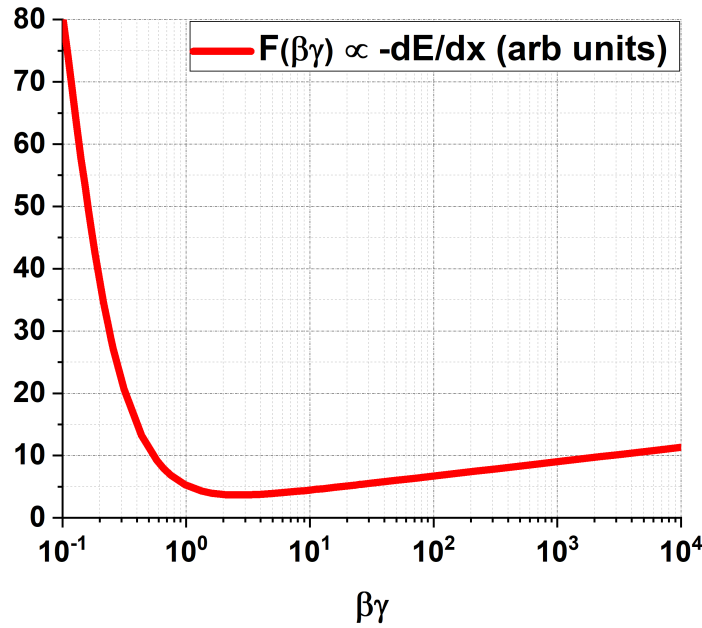


FIGURE 1.4: Absolute minimum of the function $F(\beta\gamma) = \frac{1}{\beta^2} [0.5 \ln(\beta^2 \gamma^2) - \beta^2] \propto -dE/dx$

that cause the actual ionization, producing the electron-holes pairs composing the detectable signal.

1.5 Signal formation

As discussed in section 1.3, the concentration gradient inherent to a PN junction is translated into a movement of the charge carriers by means of diffusion. However, the detectable signal that allows us to determine whether a particle has crossed the depletion region of a silicon detector is caused by another sort of charge carrier transport phenomena: the so-called drift [7].

In the absence of an external field, most of the PN junction is non-depleted and its existing charge carriers can only undergo a thermal motion governed by fortuitous collisions with scattering centers, such as pure silicon or dopant atoms. This randomness leads to a net zero displacement of the free charge carriers. Moreover, any electron-hole pair that is generated by an external particle crossing an unbiased and non-depleted junction is quickly recombined before it can form a detectable signal. When an external reverse bias (electric field) is applied, the situation is quite different.

For the seek of pragmatism, we will assume that the applied voltage exceeds V_{FD} (Equation 1.13), so the space-charge region of the PN junction is at its maximum width. In the absence of akin carriers to recombine with, electrons and holes generated by impinging ionizing particles are accelerated along the direction of the field. Despite random collisions still occur, the superimposed drift motion that adds the application of the external voltage combines to give a net displacement of the charges. Electrons and holes drift in opposite directions until they reach, respectively, the N and the P electrodes (e.g. the edges of the depletion region) as Figure

1.5 illustrates. With the appropriate electronics, the readout of this signal will inform us that a particle has just crossed our PN junction.

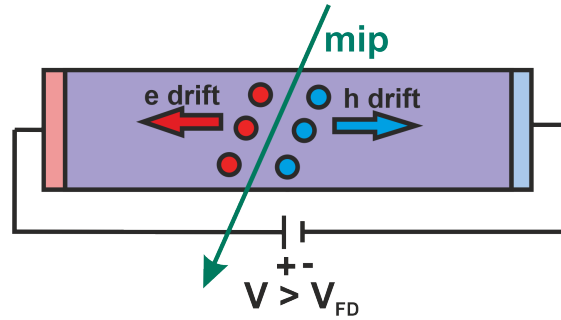


FIGURE 1.5: schematic of the drift of electrons and holes generated by a mip in the space-charge region of a fully depleted PN junction.

In silicon, and at moderate intensities of the electric field (up to $|\vec{\epsilon}| = 10^4 \text{ V/cm}$ [13]), the drift velocity is proportional to the field and can be described as [14]:

$$\vec{v}_d = (\mu_n + \mu_p) \vec{\epsilon} \quad (1.15)$$

where μ_n and μ_p are, respectively, the carrier mobility of electrons and holes. In a nutshell, the mobility is a parameter that gives information about the probability of collision of a carrier with a scattering center, and it strongly depends on temperature and doping concentration: the higher the both of them, the greater the collision probability, hence the lower the mobility either for electrons or holes [15]. When the intensity of the electric field is high enough, the collision probability is enhanced within the lattice, so mobility is no longer an increasing function of the reverse bias. In fact, it's been observed and widely proven that the drift velocity in silicon saturates at a given value of $|\vec{\epsilon}| > 10^4 \text{ V/cm}$ [8].

It is worth mentioning that the fact that the mobilities are different for electrons and holes arises from the very nature of the carriers. A conduction electron is excited from the outermost atomic shells of the dopant atom. Once this happens, such electron is free to move towards the N electrode under the application of the external field, being its motion only perturbed by random collisions with the scattering centers. In contrast, the motion of a conduction hole starts when a Si-Si bond breaks and its electron occupies the vacancy left behind by the electron that firstly drifted. This bond breaking and vacancy occupation mechanism continues until the hole (vacancy) has been pushed away from the depletion region to the P electrode. In short, either electron and hole drift is caused by the motion of electrons, but they are not free in the latter case. Transitioning between vacancy states is not as fast or straightforward as freely drifting, hence conduction holes move slower than electrons.

As we will discuss in detail in Chapter 2, a silicon based detector generally operates at voltages such that both electrons and holes drift at their saturation velocity. This is done to minimize, as much as possible, the signal pileup phenomenon [8]. In real-world experiments, silicon sensors do not detect a single particle but a great number of them over a specific period of time. The rate of this particle flux is known as *luminosity*. Certain applications in HEP experiments aim to be able to detect and identify separately every particle that has generated a signal in the silicon detector, for which the timing response of the sensor is crucial. The faster the generated signal is collected, the lower the probability of consecutive signals from different particles

piling up, which would prevent them from being distinguished. Figure 1.6 depicts a representation of the pile-up phenomenon. Two identical particles pass through the detector under the same incidence conditions, thus creating two identical output signals in terms of amplitude and generated charge (e.g. integral of the pulse). The time between events is set to 0.25 ns. If the time response of the detector is fast enough (A in Figure 1.6), the events can be genuinely distinguished in the compound output signal. However, if the time response is poor with respect to the time between events (B in Figure 1.6), it will not be possible to make such a distinction.

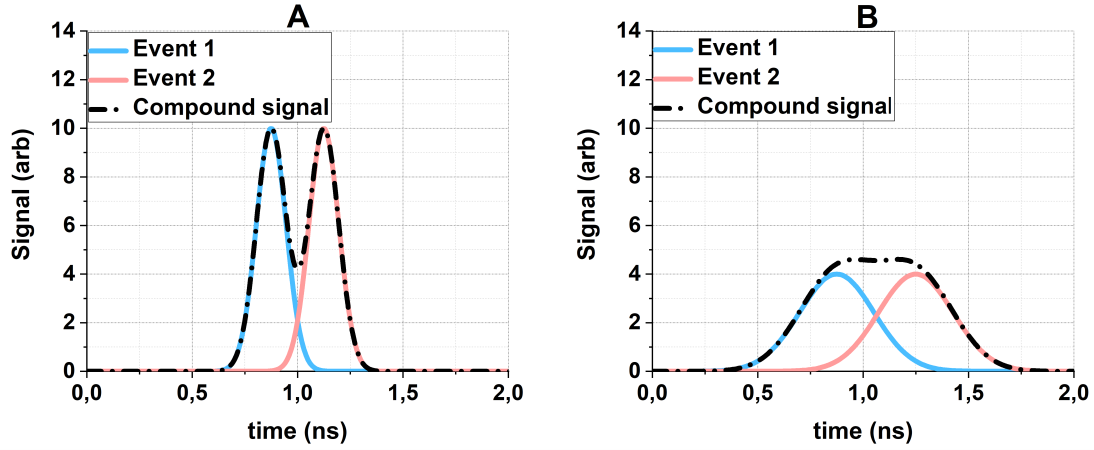


FIGURE 1.6: Representation of the pileup phenomenon.

1.6 Leakage current in silicon detectors

As we have already seen, in order to detect ionizing radiation using a semiconductor detector it is essential to have a charge-depletion region large enough for the impinging particle to generate an electrical signal that can be measured. Nevertheless, it is also crucial that such signal can be genuinely distinguished from the background noise intrinsic to any electrical setup. In order to achieve this, the so-called signal-to-noise ratio (SNR) must be maximised.

Excluding any other components composing the detection measurement setup as a whole (cables, amplifiers, oscilloscopes, etc), the noise of a silicon sensor is fully determined by its *leakage current*. Also referred to in the literature as *dark current*, it is the current that naturally flows through a silicon detector when it is operated in reverse bias mode. Despite most charge carriers are swept away when the detector is fully depleted, a small number of them can still be excited from the valence to the conduction band to contribute to the leakage current. The magnitude of it can vary depending of several factors.

1.6.1 Temperature dependence

The most straightforward is the strong *temperature dependence* of leakage current, which is exponential and approximately described as [8]:

$$I \propto \left[\exp \left(-\frac{eV}{kT} \right) - 1 \right] \quad (1.16)$$

where e is the electron charge, V the reverse bias, k is the Boltzmann constant and T the very temperature. Typical values of the reverse bias and temperature for most of the radiation detection applications are on the order of 100 V and tens of degrees Celsius (both below and above zero), respectively. Within this range of values, $\exp(-\frac{eV}{kT}) \ll 1$ and Equation 1.15 can be approximated by

$$I \propto \frac{kT}{eV} \propto T \quad (1.17)$$

1.6.2 Impurity concentration dependence

As aforementioned, doping with impurities is an essential technique in silicon detectors fabrication for constructing the PN junction. However, an undesired excess of donors or acceptors in the active volume of the detector can significantly increase its leakage current. This effect is due to the rise in available charge carriers that can easily transition between the valence and the conduction bands when the Fermi level gets close to any of them. (Figure 1.2).

Moreover, the presence of other unintended impurities (apart from the desired acceptor and donors to create the PN junction) can also have adverse effects on the leakage current. These impurities not only may add extra charge carriers available for conduction, but also alter the semiconductor's crystalline lattice, introducing new energy levels within the bandgap. Particularly critical are those that introduce energy levels close to the middle of the bandgap (the so-called deep-level impurities), as they serve as stepping stones for charge carriers to transition between bands (Figure 1.7). An extensive study of such impurities can be found in [16].

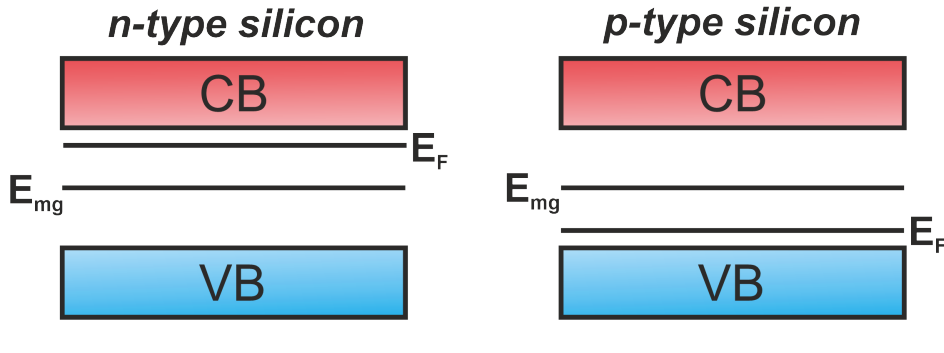


FIGURE 1.7: Illustration of mid-gap energy states (E_{mg}) within the bandgap.

It is worth mentioning that not only the SNR is diminished in the presence of undesired impurities due to the leakage current increase, but also the time resolution of the detector. Mid-gap energy levels can temporarily trap any charge carrier regardless of it being thermally excited or generated by the particle that the silicon sensor aims to detect. Consequently, the signal that apprise us of the passage of such particle experiences a delay on its path to the electrodes, increasing the likelihood of pileup between detection events.

To minimize the risk of contaminating the semiconductor by these deep-level impurities, all fabrication processes for silicon detectors are performed in clean-room environments with controlled levels of particulate contamination.

1.6.3 Geometrical effects

Despite Figure 1.5 being an intuitive schematic of the silicon detector functionality, it does not give us information about the physical edge of them. At the microscopic level, silicon surfaces on any of the three-dimensional directions have imperfections and dangling bonds (e.g. micro-cracks due to dicing processes or physical manipulation during the fabrication). This alters the crystalline lattice periodicity of the sensor, that in turn may modify the energy levels within the bandgap on the detector surfaces. As in the case of unwanted impurity contamination, such surface defects may serve as leakage paths for charge carriers, reducing both the SNR and the time response of the detector. Minimization of these surface effects is seriously taken into account during fabrication, as we will discuss in Chapter 3.

In addition, another geometrical parameter that increase the leakage current is the very active volume of the detector: the bigger it is, the greater the number of available charge carriers that can cause conduction. In terms of the SNR, reducing the entire volume of the detector is crucial to minimize the leakage current. Nonetheless, the time response is mostly determined by the thickness of the detector, proportional to the physical length from the charge generation points to the electrodes. This is the reason why silicon detectors are fabricated with an active thickness on the order of micrometers, while their active area varies on a wider range depending on the application.

1.6.4 Radiation damage dependence

Last but not least, the very purpose of a silicon sensor (detecting radiation) causes an impact on its leakage current and overall performance. As in the previous cases, this is due to the introduction of energy levels within the bandgap. However, they are not due to impurities occupying lattice sites or surface defects, but as a result of the so-called *displacement damage*. The term refers to the structural damage and its resulting introduction of defects in the crystalline lattice caused by the interaction of high-energy particles with the atoms composing such lattice. That is, if the particle to be detected has sufficient energy when traversing the sensor, it will be able to physically displace the atoms from their lattice sites, hence modifying the energy band structure where the damage has taken place.

The means by which the damage occurs depends on the nature of the very radiation, namely [9]:

- *Heavy charged particles*, such as protons or alpha particles, typically cause displacement damage via Coulomb interactions with the nuclei of the lattice atoms, creating vacancies (e.g. when the interaction is strong enough to push the atom away from its lattice site) and interstitials (atoms located in positions between lattice sites). In much less frequent occurrences, nuclear interactions can also take place between the impinging particle and the nuclei of the lattice atom, fragmenting them or creating unstable isotopes. Either case, that results in the creation of additional charged particles within the semiconductor which can cause further damage as they pass through it.
- *Electrons* do not undergo nuclear interactions but, if they are energetic enough, their Coulomb interaction with the nuclei can displace atoms from their lattice positions just as heavy charged particles do.

- While *x* and *Gamma* rays are not charged, they are highly energetic and ionize atoms in their path through the detector. The resulting ejecting electrons can lead to displacement damage if they are energetic enough. Moreover, Gamma rays can trigger nuclear reactions that lead to new damaging particles being created within the semiconductor.
- *Neutrons* are not charged either, but they can cause displacement damage in two different ways. As they have mass, they are able to undergo scattering with the nuclei of the lattice atoms, displacing them and creating vacancies and interstitials just as heavy charged particles do. On the other hand, neutrons can be captured by lattice atoms nuclei, forming unstable isotopes that will decay in other ionizing radiation fragments that may cause damage.

The extent of radiation damage caused by any of the mentioned particles depends on several factors such as their energy and flux, the duration of exposure and, most importantly for this work, on the specific strategy in designing and manufacturing the silicon detector. It is important to highlight that, conventionally, the radiation damage in silicon is scaled to irradiating with 1 MeV neutrons [9]. The reasons behind that will be addressed in Chapter 5.

1.7 The choice of Silicon

As the reader may have noticed, we started this chapter discussing the role of semiconductors as radiation detectors without focusing in any semiconductor in particular. However, as the sections progressed, the discussion has become focused on silicon. That is not trivial, since silicon is undeniably the most widely used material for detecting neutrons, charged particles and photons over a wide range of energies [9]. Other semiconductors, such as germanium and gallium arsenide (GaAs) are widely employed in the detection of those particles to which silicon is not so sensitive to, such as gamma radiation, soft x-rays or low-penetrating charged particles [8]. However, in the realm of R&D (Research and Development), there is always an effort to make silicon-based semiconductor detectors increasingly versatile. Particularly interesting are those approaches where the goal is to enhance their performance beyond the detection of particles that traditional silicon detectors are naturally sensitive to.

As an illustration, Chapters 6 and 7 offer an overview of how silicon detectors can be upgraded to be more sensitive to low energetic charged particles and x-rays, a scope traditionally dominated by germanium detectors. The challenge of developing silicon sensors able to compete in terms of performance with germanium ones has several benefits. The most straightforward is the ease of processing. Silicon is a well-established material with mature fabrication techniques and has a moderately large bandgap ($\approx 1.1\text{eV}$), making it easy to process in clean-room environments. Conversely, germanium fabrication is more challenging due to its lower bandgap ($\approx 0.7\text{eV}$), that makes it more sensitivity to impurities. Not only this difference in bandgap makes silicon easier to process high-purity semiconductor substrates, but it also makes an impact on the thermal noise once the detector is integrated with a readout electronics. Germanium detectors can be integrated with electronics as well as silicon ones, but they generally require additional precautions due to its sensitivity to thermal noise (e.g. by cooling them during operation in order to reduce their leakage current and improve the SNR). These arguments can be applied to other semiconductors detectors beyond germanium (GaAs, CdTe, diamond, etc).

Despite their bandgap varies up and down with respect to silicon's [8], processing and integrating in a read-out electronics is generally simpler for the latter from an engineering standpoint.

Apart from the pure technical benefits of using silicon, there is another advantage, last in line, but not in significance. It is the production cost. Tracing back to the very extraction of the materials, understood as natural resources, that comprise the detector, we find that silicon constitutes about 28% of Earth's crust. In contrast, the other semiconductors (Ge) or composing elements of them (Ga, As, Cd, Te, etc) are rare elements with a relative abundance down to 0.001% and below. As an integral part of society as a whole, science R&D is not exempt of being affected by the most well-established economical premises, being two of them the law of supply and demand and the optimization of the total factor productivity (that is, the efficiency of labor and capital resources in generating a market output.) Long story short, the scarcity of other semiconductors compared to silicon makes the latter much cheaper to obtain. Along with it, the ease of process and integration in readout systems makes the manufacturing of silicon detectors more profitable than other semiconductors when having the same investment. While this argument opens a discussion that goes beyond the scope of this thesis, not mentioning it would partially misconceive the actual range of R&D.

Chapter 2

The Low Gain Avalanche Detector (LGAD)

2.1 Introduction

In Chapter 1 we have established the fundamental concepts for what a silicon detector is and its intended purpose. That is, to be capable of detecting particles with high sensitivity (e.g having an optimal SNR) and with a time response that is suitable for the specific application.

As we discussed in previous sections, having a thin detector is determinant to improve the time response and reduce the leakage current. However, thinning devices does not translate by itself into improving the SNR since, depending on the particle absorption depth or range, the less the silicon atoms that the impinging particle interacts with, the smaller the amount of charge of the composing output signal. Moreover, the electronics of the detector read-out system or its inner capacitance value are also a source of noise. Thus, when the average noise introduced by the leakage current falls below the level of these other contributions, it does not matter how much further the device thickness is reduced for an improvement of the time response. The challenge of overcoming this drawback was the motivation of conceptualizing and developing Low Gain Avalanche Detectors (LGAD). To understand why that is so and what are their performance features, one needs to start introducing silicon detectors from the simplest structure: the PiN diode.

2.2 The PiN diode

From this section and the ongoing ones in this chapter, only the active volume of the detector will be addressed. That is, only the part of the device that is sensitive to detect radiation will be discussed, while the periphery of it and its optimization to reduce leakage current and early breakdown will be treated in Chapter 3.

The principle of operation of a PiN diode is intuitively represented in Figure 1.5. The term PiN refers to having intrinsic silicon (the zone that gets depleted) within low resistivity p-type and n-type silicon that serve as the P and N electrodes, respectively. In reality, the depletion region cannot be merely intrinsic, and the purest obtainable silicon has an active charge carrier concentration that exceeds one of two orders of magnitude the intrinsic value of $n_i \sim 10^{10} \text{ at/cm}^3$ [8]. The discussion in this section will be focused on the performance of a n-type PiN diode of an active area and thickness of $1.3 \times 1.3 \text{ mm}^2$ and $50 \text{ }\mu\text{m}$, and an doping concentration of the order of 10^{11} at/cm^3 , which corresponds to a resistivity of $\sim 10 \text{ k}\Omega \cdot \text{cm}$. The choice of these parameters is not arbitrary, but most of the silicon detectors studied in this

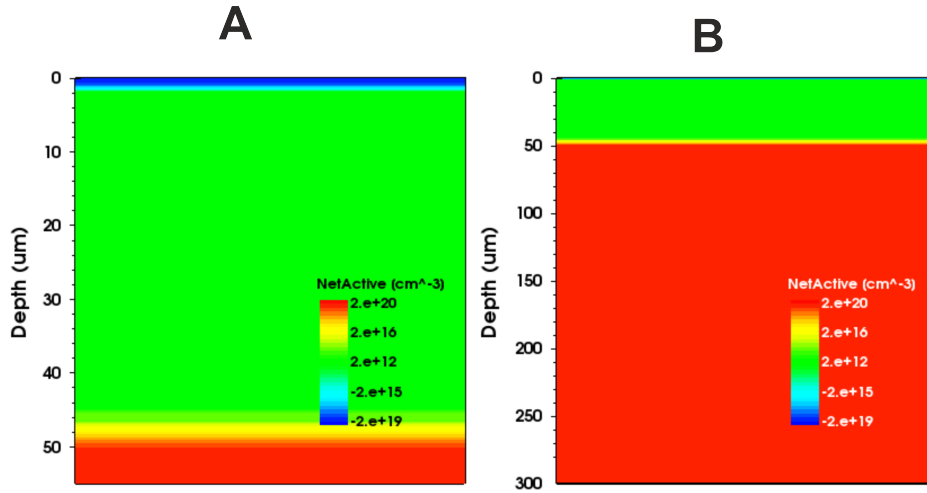


FIGURE 2.1: 2D TCAD Sentaurus simulation of the net active doping concentration of a n-type PiN diode of $1.3 \times 1.3 \text{ mm}^2$ of active area and $50 \mu\text{m}$ thickness.

thesis (either on p or n-type silicon) were built up having such geometry and conductivity. Picture (A) in Figure 2.1 depicts the active doping concentration of a 2D cross-section of the mentioned PiN diode, simulated with TCAD Sentaurus.

While on Figure 1.5 we have an impinging particle traversing the detector in a random direction, in practical applications the silicon sensors are positioned with the active area (of bigger dimension than the active thickness) facing the radiation source direction. That is done to geometrically enhance the sensor sensitivity. The electrode that serves as the entrance window for the radiation depends on both the conductivity type of the active thickness (n or p) and the type of wafer used as the substrate for the detectors fabrication. Let us talk through it.

When manufacturing thin silicon detectors, make it on wafers of thickness under $300 \mu\text{m}$ is not reliable from a mechanical point of view, since such slim wafers can easily break when being handled. Instead, the commercially available wafers have a greater thickness than the one of the desired active thickness, which provide mechanical protection from potential crack. This "excess" of silicon wafer is often called in literature *handle wafer*, and it is growth with a very low resistivity (e.g. a very high doping concentration) to aid having a good contact between the actual metalized electrode and the edge of the active area. Regardless of it being p or n-type, the handle wafer never gets depleted, hence it does not modify the preferred silicon detector thickness. This is illustrated in Figure 2.1 (picture (B)), where we depict a $50 \mu\text{m}$ n-type PiN diode built up on wafers having a handle wafer thickness of $250 \mu\text{m}$.

Thus, the entrance window is always chosen as the opposite face to that of the handle wafer **as long as the impinging particle does not have enough energy to completely traverse the full thickness of the sensor**. Otherwise, the charge generated by it will be partially recombined and lost within the handle wafer. Conversely, if the target particle to be detected has enough energy to traverse the full thickness of the detector, the entrance window can be either electrode.

Refocusing on the matter, let us now evaluate the response of the n-type PiN diode displayed in Figure 2.1, along with other with the same active area but larger

active thickness ($300\ \mu\text{m}$), when being traversed by ionizing radiation. To do so, we will continue being aided by TCAD Sentaurus simulation. While the nature of the impinging particle do cause an impact on how the charge composing the detectable signal is generated, it is much more intuitive to asses the response of PiN diodes of different thicknesses from the point of view of the depth at which the particle is likely to generate that charge. That is, two scenarios will be considered, one in which the impinging particle(s) are completely stopped or absorbed close to the entrance window (let us call them *low-penetrating particles*), and another in which the particle(s) can traverse the full thickness of the sensor (*high-penetrating particles*).

To illustrate this, we will simulate the irradiation of the PiNs with a focused photon-beam pulse of $0.25\ \text{mm}$ width and intensity $I_0 = 5 \cdot 10^{18}\ \text{photons}/(\text{cm}^2 \cdot \text{s})$, impinging perpendicularly to the P electrode during $0.5\ \text{ns}$ and for two different wavelengths: $404\ \text{nm}$ (blue light close to the UV range) and $1064\ \text{nm}$ (near-IR light). It is worth reminding that photons of such wavelength create charge carriers in silicon via electric photo-effect.

A visible photon of $404\ \text{nm}$, with an absorption depth of $\sim 0.1\ \mu\text{m}$ in silicon [17], will be either absorbed within the N electrode (not causing any detectable signal) or close to the PN junction. However, an IR photon of $1064\ \text{nm}$, with an absorption depth of $\sim 1\ \text{mm}$ in silicon [17], will be absorbed at any depth of the $50\ \mu\text{m}$ LGAD with the same probability. The same applies for a sensor with a thickness of $300\ \mu\text{m}$. Thus, the IR pulse will generate a uniform distribution of e^-h^+ pairs within the active depth of the detector. In a nutshell, **all photons from the $404\ \text{nm}$ beam will be absorbed within the detector, while most of the photons from the $1064\ \text{nm}$ beam will traversed the detector without noticing it**, being only few of them photo-absorbed to create e^-h^+ pairs. Figure 2.2 shows a 2D TCAD Sentaurus simulation of the optical generation (number of e^-h^+ pairs generated by unit volume and time) of light-beam pulses of different wavelength in our n-type PiN diode of $1.3 \times 1.3\ \text{mm}^2$ of active area and $50\ \mu\text{m}$ thickness. In such figure, the straight brown line represents the PN junction.

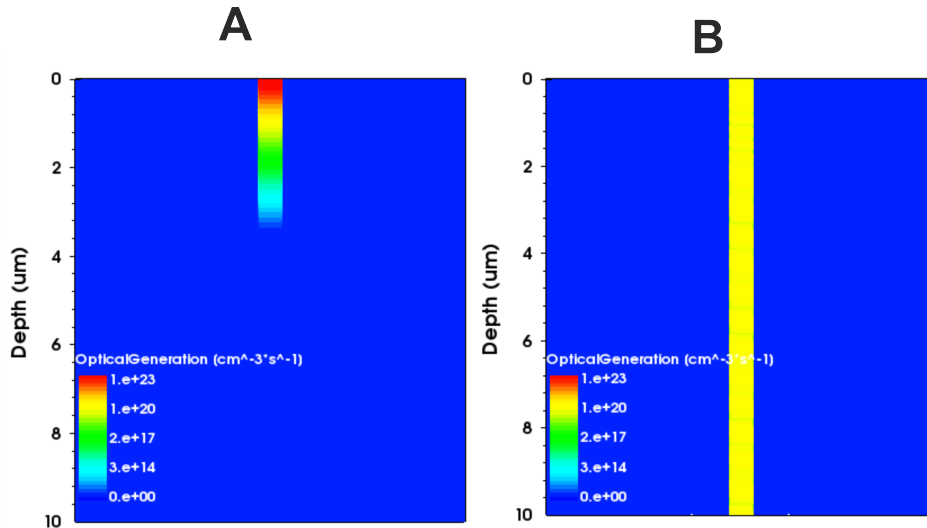


FIGURE 2.2: 2D TCAD Sentaurus simulation of the optical generation for light pulses of $404\ \text{nm}$ (A) and $1064\ \text{nm}$ (B) wavelength in an n-type PiN diode of $1.3 \times 1.3\ \text{mm}^2$ of active area and $50\ \mu\text{m}$ thickness

In our evaluation, we work at room temperature (20°C) and the n-type PiNs are reverse biased at 450 V to ensure having the devices fully depleted while keeping the electric field always above 10^4 V/cm (Figure 2.3), hence securing that the charge carriers are drifting at or close to their maximum velocity in silicon (Equation 1.15). On the other hand, since the leakage current of a 2D simulated PiN diode is never going to resemble the one of a real 3D device, for our analysis we will scale the leakage current to that of a 50 μm PiN. This is also displayed in Figure 2.3, showing that the leakage current is directly proportional to the active thickness.

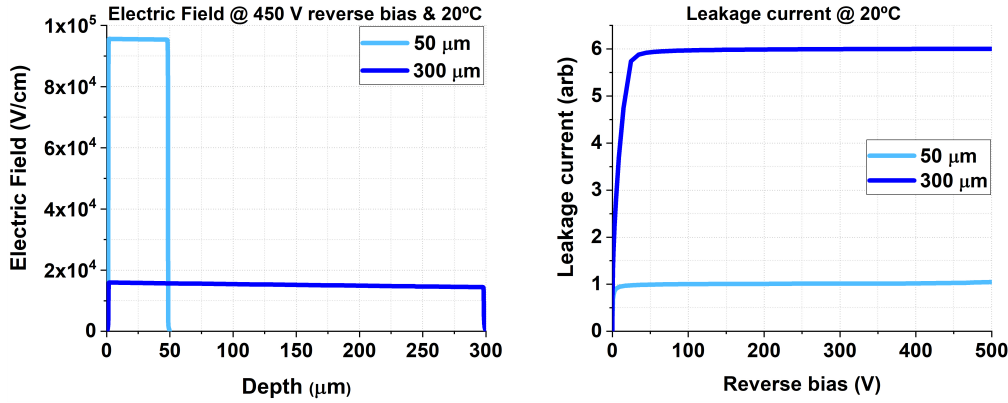


FIGURE 2.3: TCAD Sentaurus simulation of the electric field (at 450 V reverse bias and 20°C) and leakage current dependence on active thickness for an n-type PiN diode.

Figure 2.4 shows the simulated output signals when two beam-pulses (being its features mentioned above) of wavelengths 404 and 1064 nm impinge on the detector as shown in Figure 2.2. The signal current is scaled so the leakage current of a 50 μm PiN is 1. To study the quality of the signals as we reduce the active thickness from 300 μm to 50 μm , the SNR will be evaluated.

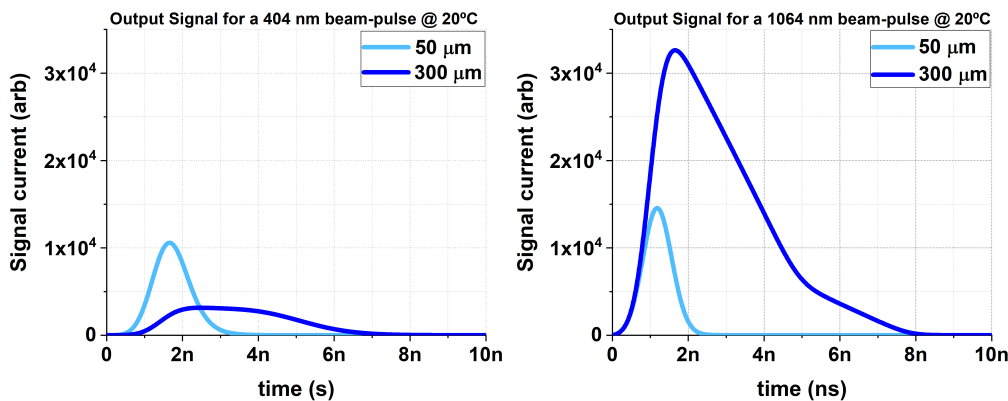


FIGURE 2.4: TCAD Sentaurus simulation of the output generated signal, at 450 V reverse bias and 20°C, dependence on active thickness for an n-type PiN diode when illuminated with light pulses of 404 and 1064 nm wavelength.

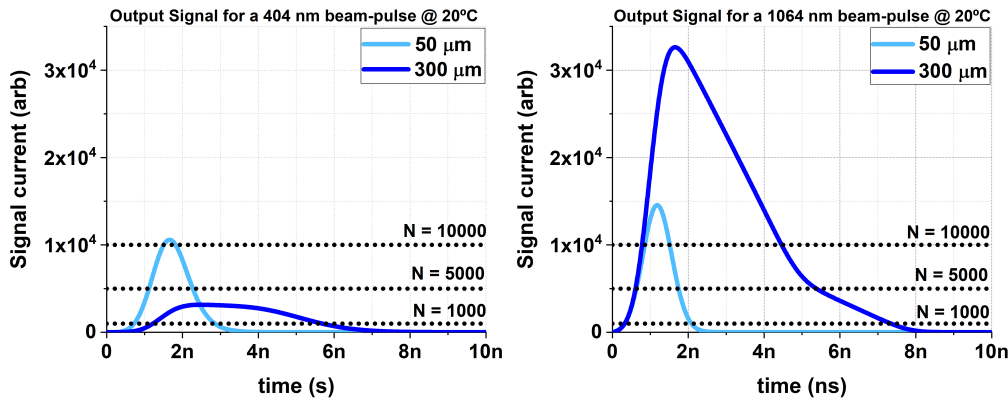


FIGURE 2.5: Generated output signals displayed along with different noise levels $N \gg 1$. If N exceeds certain limit, some of the signals cannot be processed.

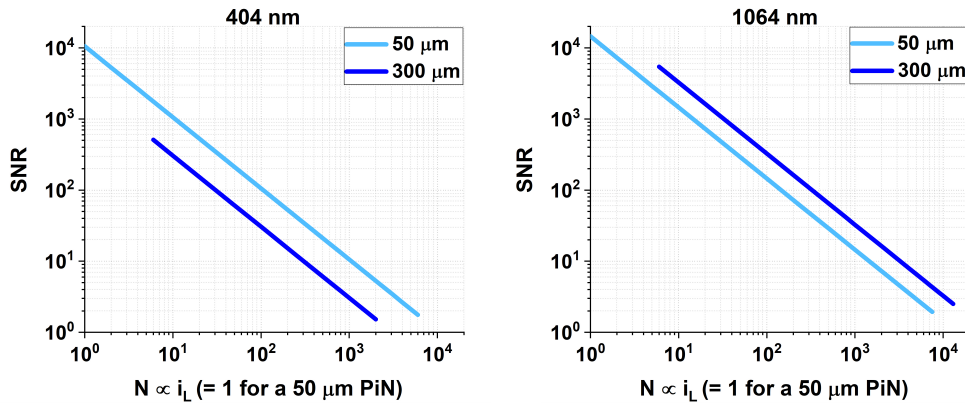
The *SNR* (signal to noise ratio) is a measure of the quality of the signal generated in the detector in relation to the level of noise N . It can be estimated as $SNR \sim S/N$, being S the signal amplitude and N the total noise. Considering the leakage current as the sole source of noise, the *SNR* of the signals displayed in Figure 2.4 can be estimated as $SNR \sim S(d)/[d/50]$ being d the thickness of the PiN diode in μm .

In very ideal conditions, the leakage current (i_L) would be the sole source of noise and $N = i_L$ (recalling that we have defined $i_L = 1$ for the $50 \mu\text{m}$ n-type PiN diode displayed in Figure 2.1, at 450 V and 20°C). This idealization is far away from reality, in which the read-out electronics noise contribution generally exceeds the leakage current a few orders of magnitude. That is, in the real case, $N \gg 1$, which can significantly alter the signal processing analysis as schematically depicted in Figure 2.5.

While the total noise present during the measurements can be affected by many factors, let us generalize so the noise is divided in three contributions, one dependent on the sensor capacitance (N_C), other dependent on the leakage current (N_{i_L}) and other depending on the electronics (N_e). Thus, $N^2 = N_C^2 + N_{i_L}^2 + N_e^2$ [18].

It has been shown that $N_C \propto C \propto d^{-1}$ [18]. Thus, in general, **a thin silicon detector will contribute more to the total noise level than a thick one**. Studies have reported that for thicknesses under $50 \mu\text{m}$, the decrease in *SNR* due to an increase of N_C does not trade-off for a better time response of the silicon detector [19]. That is the reason why our evaluation will be narrowed to sensors of $300 \mu\text{m}$ (standard in silicon detector fabrication) and $50 \mu\text{m}$, being the latter the specified thickness for the HEP applications that will be discussed in Chapter 5.

Let us assume that $N_C, N_e \ll N_{i_L}$ (so $N \approx N_{i_L} \propto i_L$) and evaluate how the *SNR* changes for every sensor thickness. With this approximation, we can estimate an upper limit to the *SNR* for a given noise level set by the leakage current, as long as the experiments are conducted under the same conditions. Figure 2.6 shows $SNR \sim S/N$ as a function of $N \approx N_{i_L}$ for the two different wavelengths. The *SNR* was inferred by analysing the signals shown in Figure 2.4. For the low-penetrating 404 nm beam, the *SNR* is greater for a $50 \mu\text{m}$ PiN. This results is a direct consequence of the increasing physical distance that the charge carriers (electrons in this case) have to go through till they reach the N electrode. The thicker the device, the longer such distance, hence the amplitude of the output signal decreases at a given N .

FIGURE 2.6: SNR dependence on the background noise level $N \approx N_{i_L}$

On the other hand, for the 1064 nm beam, the result is just the opposite. In contrast to the 404 nm case, the charge carriers are not generated within the first few microns of the device, but all along the active thickness with the same probability. Thus, the amplitude of the signal is greater for 300 μm devices.

If now N_C and N_e are included within N , the SNR values displayed in Figure 2.6 **can only be further reduced, and such reduction will be greater for a 50 μm PiN due the relationship $N_C \propto C \propto d^{-1}$** . For a low-penetrating particles, the SNR for a 50 μm PiN might or might not be poorer than for a 300 μm PiN depending only on the specific N_C value as N_e is assumed to be identical for both sensor thickness values (i.e. the same electronics is assumed). However, for a high penetrating particle, we can assure that the SNR for a 300 μm PiN will always be larger than for a 50 μm one.

This result lead us to conclude that for high-penetrating particles, the SNR is degraded when reducing the active thickness from 300 μm to 50 μm . In another words, **for a PiN detector, it is not possible to enhance both the SNR and the timing response for high-penetrating particles by means of active thickness reduction from 300 to 50 μm** . The idea of developing a silicon detector that enhances both the SNR and time response simultaneously for high-penetrating particles was the germ of the LGAD conception.

The discussion in this section has been limited to n-type PiN detectors, so it is worth pointing out the existing differences with respect to p-type ones. **For high-penetrating particles, such as 1064 nm wavelength IR photons, a p-type and an n-type detector will have the exact same performance as long as they are identical in terms of absolute conductivity of the active thickness, P and N electrode construction and device volume**. This is due to the inherent symmetry in the optical generation for light beam pulses of such kind (Figure 2.2).

For low-penetrating particles, such as 404 nm wavelength photons, the main difference in the generated signal is the type of charge carrier that has to cover a longer distance while drifting to the electrode opposing the entrance window. For an n-type PiN, these are electrons, that drift to the N electrode (Figure 2.1) while for p-type PiNs, they are holes drifting to the P one. As we will discuss in section 2.3.4, holes have smaller mobility than electrons which, in a nutshell, means that their motion to the electrodes is slower. This translates into longer signals with smaller amplitudes so, for a given value of N , the degradation in SNR and time response for a thick 300 μm is greater when using a p-type PiN rather than an n-type one.

From this point forward, the discussion will focus on strategies to **enhance the SNR of a 50 μm thin p-type silicon detector for high-penetrating particles.**

2.3 Silicon detectors with intrinsic multiplication: LGAD concept

Let us address another issue regarding particle detection with PiN diodes. The analysis carried out in the previous section do not contemplate changes in the beam-pulse intensities, that is, in the number of electron-hole pairs generated by the ionizing radiation. However, this is also crucial to be able to obtain an output generated signal given a noise level. This is depicted in Figure 2.7.

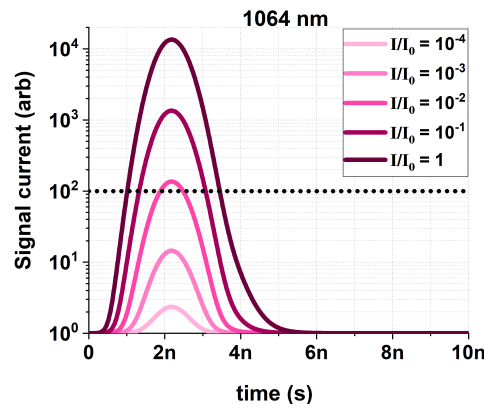


FIGURE 2.7: TCAD Sentaurus simulation of the signal dependence on IR beam intensity, at 450 V and 20°C. I_0 corresponds to the intensity used in the simulations shown in Figures 2.5 and 2.6.

As the number of ionizing radiation particles reduces, so does the amount of generated charge carriers, hence the SNR with it. The amount of charge generated by the impinging particles can be inferred as the *Collected Charge* (CC), defined as the integral of the signal pulse. If the beam intensity is too low, the signal will not be distinguishable for a given noise level. This is illustratively shown in Figure 2.7), where $N = 100$, being 1 the leakage current at 450 V and 20°C. It is worth noting that in this evaluation, N_C and N_e are assumed to be constant so N depends only on $N_{i_L} \propto i_L$. Nevertheless, Figure 2.7 has to be understood as an informative illustration rather than an actual example with realistic N values.

Let us focus to find the solution of having a p-type silicon sensor that is sensitive to a low intensity (picking the value $I = 10^{-3}I_0 \sim 10^{15} \text{ photons/cm}^2\text{s}$ in Figure 2.7) 1064 nm IR beam pulse. Let us also toss the timing response aside and empathising on SNR and CC. As we pointed out, the discussion on the previous section was considering the beam-pulse intensity as a fixed parameter, but also was the reverse bias. While the response of a p-type PiN diode is linear in SNR with reverse bias [13], there is a voltage point at which such linearity is broken to start an exponential behavior.

This is depicted in Figures 2.8 and 2.9. In both cases, and to avoid losing comparability with previous figures, the signal current is scaled to the leakage current at 450 V and 20°C. As the reverse bias rises from 450 V in steps of 25 V, the generated

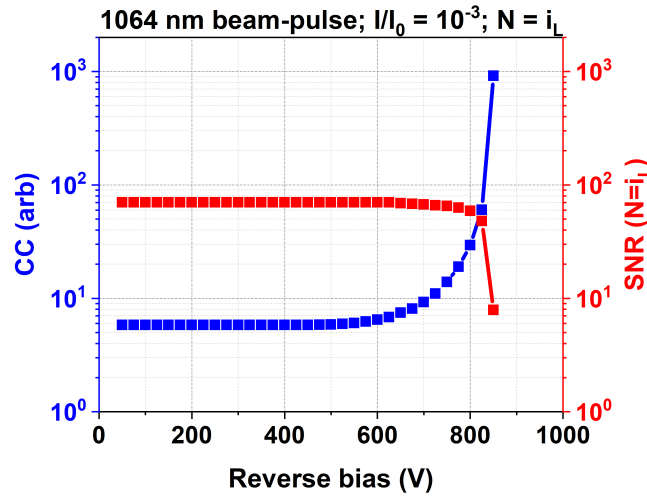


FIGURE 2.9: TCAD Sentaurus simulation of the CC and SNR dependence on reverse bias for an p-type PiN diode illuminated with a low intensity 1064 nm IR pulse-beam.

signal shape barely changes, while the SNR and CC slightly increases and decays linearly, respectively. After $\approx 750\text{V}$, the leakage current starts exponentially growing, the signal shape drastically changes and the CC boosts while the SNR plummets. In semiconductors argot, we say that **the PiN detector transitions from linear mode to Geiger or Avalanche mode** [13].

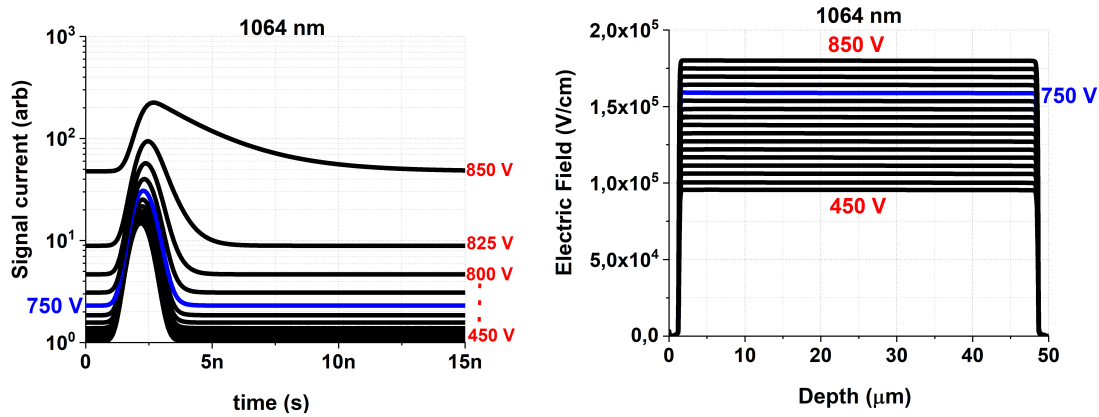


FIGURE 2.8: TCAD Sentaurus simulation of the generated signal and electric field dependence on reverse bias for an p-type PiN diode illuminated with a 1064 nm IR pulse-beam and at 20°C .

When the PiN detector is operated in Geiger mode, the electric field is so high ($E \gtrsim 1.5 \cdot 10^5 \text{ V/cm}$ in Figure 2.9) that the charge carriers generated by the impinging ionizing radiation have enough acceleration (i.e. energy) to ionize the silicon atoms that they encounter on their way to the electrodes. This causes a cascade or avalanche of generated and hence collected charge. In turn, the SNR is drastically reduced, since the charge (either generated thermally or by radiation) is being multiplied all along the active thickness of the detector. The avalanche phenomenon can

be mathematically described with the so-called impact ionization rate [13]:

$$\alpha \propto \exp\left(-\frac{\beta}{E}\right) \quad (2.1)$$

where α is defined as the number of electron-hole pairs that a charge carrier (electron or hole) can generate when traversing 1 cm of silicon. For low values of the electric field, $\alpha \propto E$ and we are working on the linear mode: the carriers are not accelerated enough to ionize many (if not any) silicon atoms. In the case of the simulated PiN results shown in Figure 2.9, $\alpha = 0$ up to ≈ 500 V (e.g. CC is constant). However, for $V > 500$ V, E exceeds a certain value in contrast to β (parameter that depends on temperature and charge carrier type, among others), the exponential function cannot longer be approximated by a linear function of E , and we enter the Avalanche or Geiger mode. **Despite the CC is boosted in this regime, the SNR degrades due to the high leakage current present all along the device.**

This last drawback can be solved by re-designing the PN junction so α has a smoother transition from 0 to Geiger values. As said, having a high electric field all along the active thickness of the detector causes the leakage current to boost when operated in Geiger mode. However, we can tune our sensor so the electric field is only high in a small restricted region of such thickness (this is called the *multiplication layer*), so charge carriers get multiplied only when they traverse it. This can be achieved by diffusing a thin and highly doped layer of boron in between the N electrode and the active thickness, as Figure 2.10 shows. The addition of such layer creates a very high electric field region around the PN junction, that drops below avalanche values ($E \gtrsim 1.5 \cdot 10^5$ V/cm) as soon as we reach low values of the doping concentration, hence avoiding a boost of leakage current all along the active thickness. The resulting device is a *silicon detector with intrinsic amplification*.

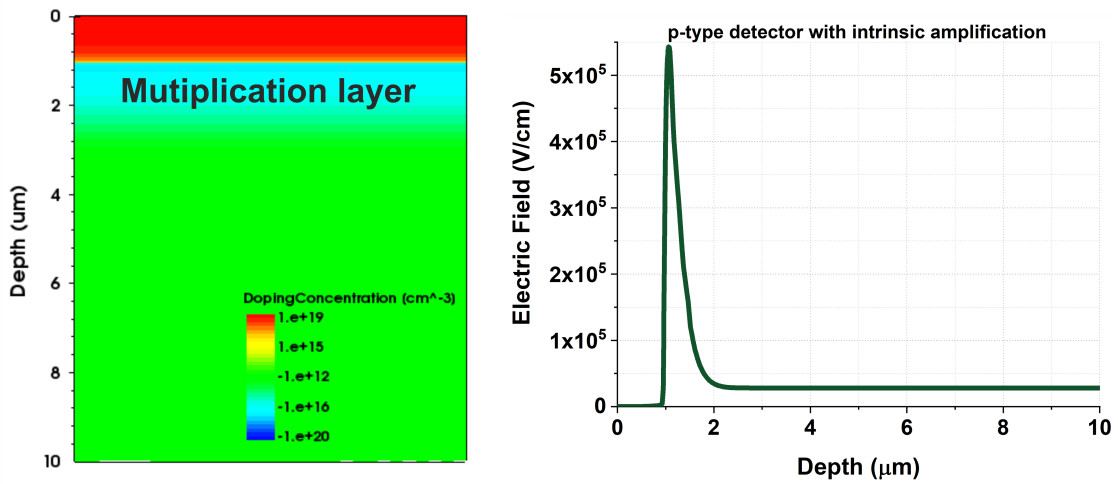


FIGURE 2.10: TCAD Sentaurus simulation of the doping profile of an p-type detector with intrinsic amplification and its electric field.

Instead of the CC, let us start evaluating a crucial parameter for silicon detectors with intrinsic amplification: the so-called *gain*. Given a noise level for every voltage point (picked as $N = i_L$ in the discussion), the gain is defined as the **ratio between the CC of a detector with intrinsic amplification and a PiN**. Figure 2.11 shows the simulated gain of the detector displayed in Figure 2.10 when being illuminated by our low intensity IR beam-pulse. For the voltage range shown in the graph, the

detector works in linear mode (with $\alpha > 0$ in this case) to a certain bias, to then starting to exhibit Geiger behavior at ≈ 500 V. In contrast to the p-type PiN, this detector as a larger operational voltage range for which both the SNR and gain (\propto CC) increase due to a moderate level of α . In this regime, the detector is working on *Low Gain Avalanche* mode. Conversely, for $V > 500$ V, the device starts working in *Avalanche Photodetector* (APD) mode.

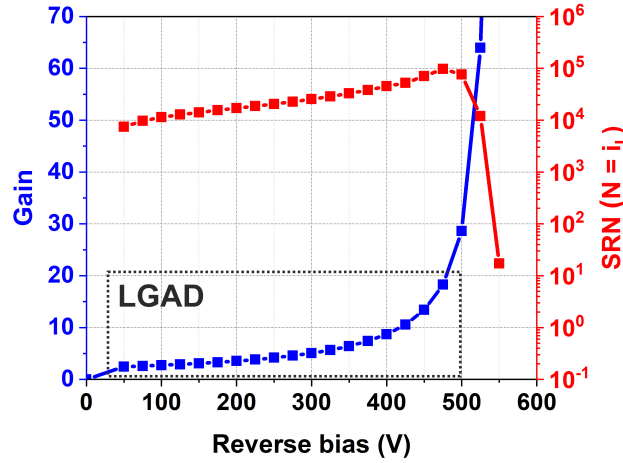


FIGURE 2.11: TCAD Sentaurus simulated gain and SNR for a p-type silicon detector with intrinsic amplification.

Thus, the SNR for low-intensities of a high-penetrating photon beam in $50 \mu\text{m}$ thin p-type detectors can be improved by means of operating them in LGAD mode. Despite the means of ionization are different, the results shown in Figure 2.11 can be extended for a mip, which also generate small signals in thin p-type silicon detectors. Thus, **p-type LGAD devices of $50 \mu\text{m}$ active thickness were chosen by the HEP community as the baseline for tracking and timing application for LHC experiments at CERN.** This will be fully addressed in Chapter 5.

2.3.1 Gain and shot noise

In the previous sections, only the leakage current, detector capacitance and electronics were considered as a source of noise. For detectors with intrinsic amplification, their inner gain supposes an extra source of noise by itself. This is defined as *shot noise*, and will be briefly addressed in this section. To introduce the shot noise, we first need to bring up the concept of mobility and understand it fully from its roots. Mobility is a physical constant of charge carriers that gives information about a probabilistic event: the collision with a silicon atom. Introducing the impact ionization rate in LGAD devices, such probabilistic event involves the ionization of a silicon atom within the collision. In the very mathematical context of statistics, a probabilistic event does not have an exact outcome, and there is always some degree of uncertainty or randomness involved with it. To cut to the chase, the drift of an electron through the multiplication layer of an LGAD can result in two possible outcomes, each with an associated probability of occurring during the carrier journey to the N electrode. The choices are: either the electron ionizes a silicon atom, causing impact ionization, or it simply does not. Moreover, in the absence of intrinsic amplification (e.g a PiN detector), the shot noise is also present during the particle

detection, since the ionizing radiation might or may not generate an electron-hole pair tied to a certain probability of such event occurring.

This uncertainty is translated into a fluctuation of the output generated current signal in a silicon sensor when detecting ionizing radiation. In turn, this introduces a noise contribution that is what we call *shot noise*. Statistically, it can be described as [20], [21]:

$$N_{shot} \propto i_L \sqrt{2QG^2F} \quad (2.2)$$

where i_L is the leakage current, G the gain of the detector, Q the number of radiation generated electron-hole pairs (before they trigger impact ionization) and F is a gain dependence correction factor described as [20]:

$$F = G \frac{\alpha_h}{\alpha_e} + (2 - \frac{1}{G})(1 - \frac{\alpha_h}{\alpha_e}) \quad (2.3)$$

where α_h and α_e are the impact ionization rate of holes and electrons, respectively. We may notice that, for $G = 1$ (the case of a PiN diode in linear mode), $F = 1$ and the gain contribution disappears from the shot noise.

For a given photon beam intensity, Q is defined as the number of photo-generated electron-hole pairs in the active volume. For a mip, the evaluation of Q is different due to the nature of its interaction with silicon. As stated, a charged particle generates electron-hole pairs all along its track within the sensor. In this case, the shot noise is related to the fluctuations in the number of charge carriers that the impinging particle is able to generate to cause impact ionization. Assuming that the ionizing particle direction is perpendicular to the entrance window surface, a minimum ionizing particle (mip) will be able to generate $Q \approx 5 \cdot 10^3$ electron-hole pairs [8].

Being all that set forth, we can define the LGAD shot noise for the detection of a mip as:

$$N_{shot}^{mip} \sim 70.7 i_L \sqrt{2G^2F} \quad (2.4)$$

Thus, the replace of a PiN for an LGAD brings with it a source of noise that is directly proportional to the nominal gain. Not only the SNR will be affected by it, but also the CC and the time response. This shortcoming also discarded silicon detectors with intrinsic amplification to work in APD mode.

Figure 2.12 shows an actual example of this issue. All the features of the displayed measurement will be explained in Chapter 5 so, for now, let us just hold onto the main result. The gain of the LGAD shown in Figure 2.12 was tested when irradiated with a high-flux ($Q \gg 1$) 15 keV x-ray beam. Photons in this energy range have a penetration depth in silicon of the order of the mm [22], so it is a high-penetrating particle just as a 1064 nm IR photon or a mip. The error bars in the plot are the standard deviation when performing five gain measurements per bias point. The LGAD gets fully depleted at ≈ 30 V and, as long as it is working on linear mode (up to ≈ 100 V), the gain is well defined with a negligible error. Nevertheless, as soon as the detector enters Geiger mode, the shot noise gets boosted and the precision of the gain measurement worsens, which is due to the boost of shot noise.

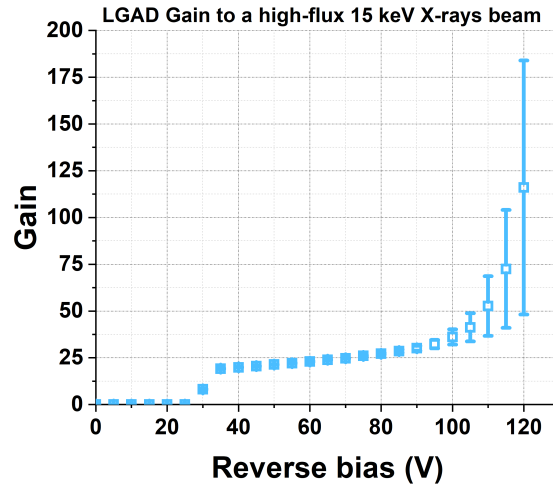


FIGURE 2.12: Gain measurements on a 50 μm thick LGAD when irradiated with a high-flux 15 keV X-rays beam at Diamond Lightsource [23].

2.3.2 Time resolution in LGADs

As stated, LGAD detectors with a moderate gain supposes and upgrade on the performance of high-penetrating charged particles detection in terms of SNR. Let us now address how the time response is also improved using such silicon detectors for high-penetrating particles.

For any kind of silicon detector, the time resolution can be expressed as [24]:

$$\sigma_t^2 = \sigma_{jitter}^2 + \sigma_{Landau}^2 + \sigma_{Distortion}^2 + \sigma_{TDC}^2 \quad (2.5)$$

where every term takes into account a time uncertainty arisen from different contributions:

- σ_{jitter} : this term represents the time inaccuracy due to the presence of noise (either coming from the detector or the electronics used during a measurement). It can be expressed as $\sigma_{jitter} \approx t_{rise} / \text{SNR}$ [24], where the risetime t_{rise} is defined as the time it takes for a signal to go from 10% to 90% of its net maximum value (amplitude)
- σ_{Landau} : the Landau term is directly related to the nature from which the shot noise arises. The number of electron-hole pairs (Q in Equation 2.4) that a charged particle or a photon pulse beam generate in the detector can vary from one detection event to another. Such variations in Q produce fluctuations in the output signal (the so-called Landau noise [24]) that in turn degrade the time resolution.
- $\sigma_{Distortion}$: the generated current inside the detector depends on drift velocity v (Equation 1.15) and electric field E as $i \propto vE$. Hence, non-uniformities of v and E along the active volume of the detector implies a distortion of the signal between successive detection events. As discussed earlier, an uniform drift velocity can be achieved by biasing the detector so the charge carriers move

with their saturation velocity in silicon. In terms of electric field, their non-uniformities are more related to fabrication features, such as non-homogeneity of the boron concentration in the multiplication layer.

- σ_{TDC} : the time resolution is lastly limited by the precision of the time-to-digital (TDC) converter that digitizes the output signal. This term is directly proportional to the time bin width of the TDC system $\sigma_{TDC} \propto \Delta T$.

TCAD Sentaurus simulation calculates the output generated signal in very ideal conditions. That is, the shot noise is not taken into account and the drift velocity and the electric field are completely uniform during successive events. Also, the time bin width can be picked as small as we wish. Thus, the evaluation of the time response of an LGAD will be illustrating not by TCAD Sentaurus, but by using an actual example. This is shown in Figure 2.13, where a IMB-CNM fabricated LGAD from the 6LG3-v1 run was tested. Information about these measurements can be found in [25], and the features of 6LG3-v1 detectors will be discussed in Chapter 5.

For the moment, we can focus on the important result: **LGADs improve time resolution (specifically, the jitter term in Figure 2.13) for high-penetrating particles as their inner gain increases within moderate values.**

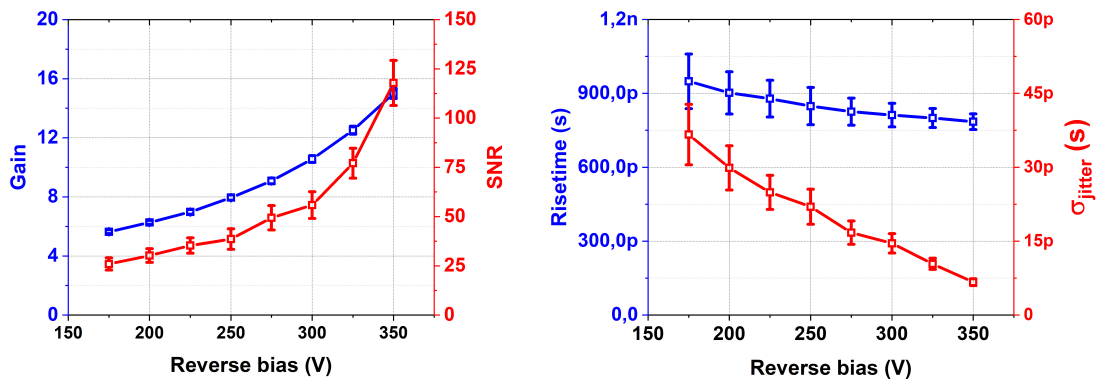


FIGURE 2.13: Gain, SNR, risetime and σ_{jitter} for an LGAD while being illuminated with a 1064 nm beam pulse of high intensity ($Q \gg 1$).

2.3.3 Breakdown and depletion voltages: finding the best trade

The discussion presented so far include the features of an LGAD when detecting a certain type of high-penetrating particle. However, the first filter that an LGAD must pass to confirm its reliability after manufacturing is the determination of its *voltage operation range*. While this range varies depending on the target experiment, we may define it plainly as the difference between the breakdown and the full depletion voltage of the detector.

The breakdown voltage (V_{BD}) is determined as the bias at which a significant increase in the leakage current occurs due to the avalanche multiplication of charge carriers. In another words, it is the bias point at which the detector performance switches from linear (LGAD) to Geiger (APD) mode. Measurements of the leakage current vs reverse bias help easily determine the breakdown voltage, as Figure 2.14 shows.

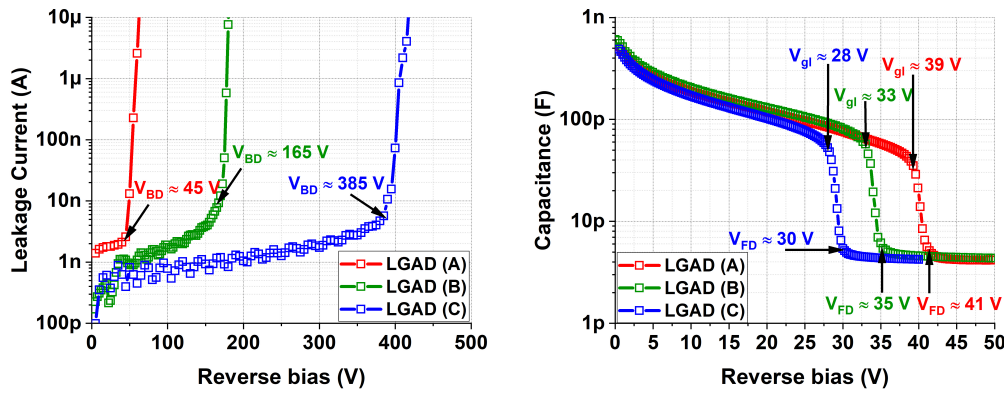


FIGURE 2.14: Leakage current and capacitance vs reverse bias measurements, at 20°C, for three IMB-CNM manufactured LGADs, each one corresponding to a different fabrication batch.

On the other hand, the full depletion voltage (V_{FD}) determines the bias at which the entire active volume of the detector is fully depleted of free charge carriers. Operating an LGAD over full depletion voltage ensures that the electric field extends across the entire thickness of the detector, enabling optimal performance in terms of particle detection. Another key parameter is the multiplication layer depletion voltage, often labelled as V_{gl} in the literature. It is defined as the bias at which the multiplication layer gets fully depleted of charge carriers. The multiplication layer always gets depleted before the high-resistivity layer, as it has a higher dopant concentration. To put it another way, V_{FD} is always greater than V_{gl} , so the high-resistivity active thickness will never get depleted if the multiplication layer has not.

Generally, greater values of V_{gl} lead to lower values of V_{BD} (Figure 2.14), as it implies that either the multiplication layer is wider or has a higher doping concentration, hence leading to a higher electric field peak at a given reverse bias. Finding a good trade between V_{gl} and V_{BD} is crucial in LGAD design and fabrication in order to optimize the voltage operation range. To illustrate this, we may analyse the curves in Figure 2.14. For the LGAD labelled as (C), the difference between V_{BD} and V_{FD} is great enough to ensure an operation voltage range of about 300 V. For LGAD (B), V_{BD} is closer to V_{FD} , but the device is still operational within a voltage range of about 100 V. The actual problem arises when we have a look at the results for LGAD (A), as its full depletion voltage is so close to V_{BD} that the voltage operation range is practically none.

Both V_{gl} (V_{FD}) and V_{BD} depend on a great deal of fabrication parameters that have to be carefully chosen to optimize the voltage operation range. This will be discussed in Chapter 4.

2.3.4 Avalanche mechanism for electrons and holes

To close this section, it is worth making a brief stop to address how the LGAD avalanche mechanism differs for electrons and holes. In Chapter 1, we discussed how electrons have a greater mobility than holes (Equation 1.15). Such fact translates into the electrons having a bigger likelihood to collide with a silicon atom lattice when drifting inside silicon. The impact ionization rate, α (Equation 2.1), is directly linked to mobility, since the greater the probability of collision, the bigger the chance for a charge carrier of ionizing a silicon atom. It has been widely proven that **the**

impact ionization rate is smaller for holes than electrons. An extensive analysis about this topic can be found in [26]. With this knowledge, it appears to be that an LGAD will work more efficiently to improve their SNR and time response when the radiation-generated electrons (and not the holes) are the main contributors to trigger the avalanche mechanism.

To illustrate this, let us evaluate the electron drift when a 404 nm and a 1064 nm wavelength photon beam impinges on a n-type LGAD and on a p-type LGAD (both of 50 μm active thickness) through the electrode located at the opposite side of a thick handle wafer (Figure 2.15). For a n-type LGAD, the entrance window will be the P electrode (where holes drift to be collected), while for a p-type LGAD it will be the N electrode (where electrons do).

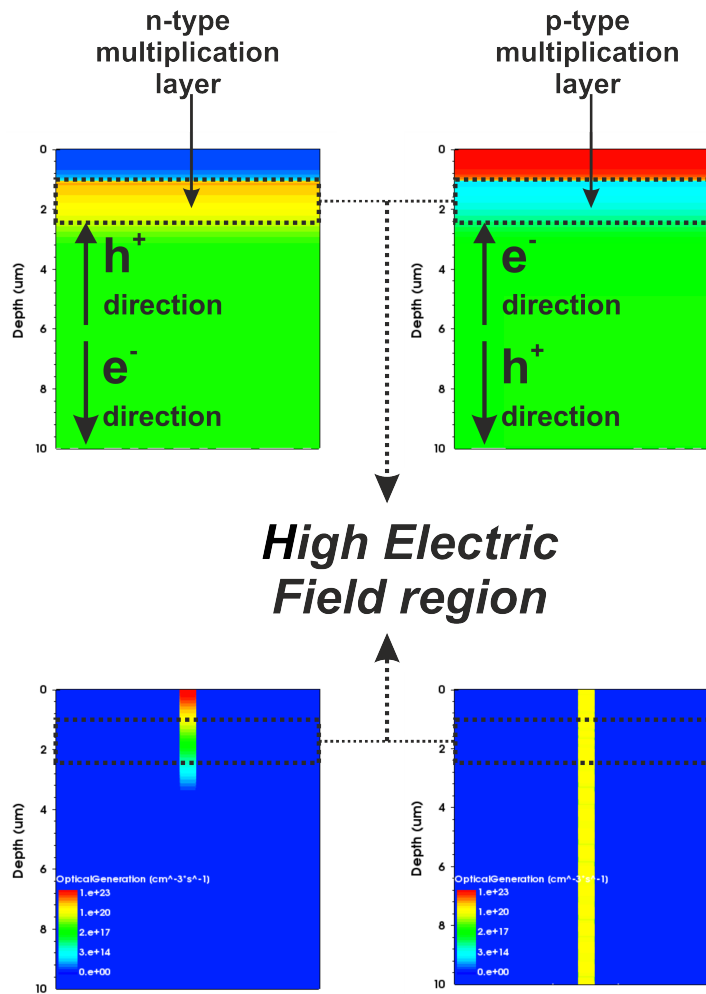


FIGURE 2.15: 2D TCAD Sentaurus simulation of the active doping concentration profiles of an n a p-type LGAD. The optical generations for a 404 nm and 1064 nm beam-pulse are also displayed.

While the IR photons will be absorbed with the same probability all along the active thickness of a 50 μm LGAD (regardless of its type), the generated electrons will always chose to drift to the N electrode. This is displayed in Figure 2.15. For a n-type LGAD, electrons will drift opposing the multiplication layer side (close to the P electrode) with independence of the depth at which the IR photon got absorbed and hence the carrier generated. In contrast, for a p-type LGAD, electrons will always

drift towards the multiplication layer (close to the N electrode). Since, for a IR beam, electrons are equally generated all along the thickness of the sensor, the number of electrons traversing the high electric field region will be much greater for a p-type LGAD than for a n-type LGAD. Let us change the IR photons for another high-penetrating particles with the same generated-charge distribution. The qualitative results will be the same.

In short, **for high-penetrating particles, the SNR is enhanced for a p-type LGAD rather than an n-type one.** Conversely, **the opposite of the latter statement is true for low-penetrating particles**, such as 404 nm wavelength photons (Figure 2.15). Since they are absorbed close to the PN junction surface, more photo-generated electrons will cross the multiplication layer for a n-type LGAD. Let us remark that, for low-penetrating particles, this argument is only valid if we are constructing thin 50 μm LGADs on thick low resistivity handle wafers with an entrance window on the PN junction side.

2.4 Applications

2.4.1 Tracking and timing in High Energy Physics experiments

The first Low Gain Avalanche Detector (LGAD) were designed and fabricated at the IMB-CNM [5]. Since then, the LGAD technology has been gradually established as the baseline technology for certain High Energy Physics experiments.

Regarding those, the most noteworthy and ambitious are indeed the experiments carried out in the Large Hadron Collider (LHC) at CERN [27]. Apart from being the largest particle collider ever built, it is also powerful enough to accelerate charged-particles to energies of the order of few TeV . For a proton (the most common particle used at the LHC) that supposes having relativistic velocities asymptotically akin to the speed of light in vacuum. By colliding protons at such unprecedented energies, the LHC experiments aim to bring about extreme conditions that lead to the discovery of new particles (such as the forever-sought dark matter [28] or the already found Higgs Boson [29]) or contribute to a better understanding of the underlying physics right after the Big Bang [30]. The probabilities of having collision events involving such zealous endeavors are derisory, hence the LHC has recently planned an upgrade, to be implemented by 2025, to increase its luminosity by a factor of 10. As defined in Chapter 1, the luminosity is directly proportional to the number of particle collisions occurring per unite time. Thus, by increasing it by a factor of 10, we are also multiplying the probability of a non-likely collision event to happen by such factor.

Nevertheless, striving to make such rare collision events happened is useless if there are no means to properly record and analyse them. In order to do so, we do need to be able to detect the remnants of the proton-proton collisions in both time and space. That is, we need to locate in space and time the fragments of the collision to reconstruct the event. For high luminosity values, this needs to be done with a very precise timing resolution to avoid pile-up phenomena and fail to record the desired events. Moreover, as discussed in Chapter 1, high radiation fluences (also linked to luminosity) lead to a degradation of conventional silicon detectors by increase of their leakage current (hence their SNR). Such radiation damage may imply a complete insensitivity of the silicon sensors over a range of the experiment lifespan.

With all that set forth, it appears evident that the LHC experiments do need particle detectors with a great time resolution and radiation hardness, so the probability

of missing out an already non-probable event is further reduced. LGADs are the best candidate for such venture. The discussion and measurements presented in the previous section remark the outstanding time resolution and SNR that can be achieved by an LGAD before being irradiated (Figure 2.13). Furthermore, the presence of intrinsic amplification counterbalances the loss of SNR by radiation damage, increasing their sensitivity over a longer period of the experiment lifespan in comparison to a standard PiN detector. It is worth remarking that the enhancement of the LGAD radiation resistance for very high fluences is still a current work, and means to improve it will be discussed in Chapter 5.

2.4.2 Detection of low-penetrating particles in silicon

Discarding some remnants from particle decays, sensors for the LHC at CERN are mainly sought to detect high-energetic ions (mips), which are high-penetrating particles in silicon. Nevertheless, detecting low-penetrating particles in silicon is of vital importance for a wide range of applications in the fields of industry, medicine, and pure research, such as x-ray monitoring in synchrotron facilities [25], alpha particle sensing for indirect neutrons detection [31] or radiation therapy dosimetry [32].

As discussed earlier in this chapter, LGADs built up on n-type silicon (nLGAD for short) point out to be promising on the detection of low-penetrating particles. As well as traditional p-type LGADs, nLGADs were first conceptualized and fabricated at the IMB-CNM [6]. Although their manufacturing was not tied to a project as specific as the LHC one, the great performance of the first nLGADs prototypes to low-penetrating particles detection opens the door to countless applications. This will be addressed in Chapter 6.

Chapter 3

Design and fabrication of LGADs

3.1 Introduction

As pointed out in previous chapters, the manufacturing of silicon devices, regardless its intended application, is a well-established engineering technique. In the particular case of the LGADs studied in this work, they are fabricated using a method known as *planar technology* [33]. The term refers to a manufacturing technique in which all layers composing the device are constructed on the flat, or nearly flat, surface of a substrate: the silicon wafer. The manufacturing of such layers require the use of several sub-techniques comprised within planar technology, including photolithography, material deposition and etching or ion implantation. They will all be addressed in section 3.2. The Institute of Microelectronics of Barcelona (IMB-CNM) offers, since its opening in 1985 [34], a clean-room environment with all necessary equipment for planar technology fabrication. All LGADs studied in this thesis were manufactured at the IMB-CNM and their fabrication process will be fully discussed in sections 3.3 and 3.4.

The symmetry that working with flat structures offers (i.e., without the presence of complex three-dimensional structures) not only facilitates the fabrication of detectors from a technical standpoint, but also makes their simulation design simpler from a mathematical point of view. This will be discussed in Chapter 4, along with the calibration of TCAD Sentaurus simulation with actual fabricated detectors at the IMB-CNM.

3.2 Engineering fabrication techniques for planar technology

Every silicon detector batch that is fabricated begins with a silicon wafer of any sort. The IMB-CNM does not count with the necessary equipment to manufacture silicon wafers, so they are always purchased from an external vendor. Nevertheless, it is worth giving a brief description of the process. For a more extensive one, the reader may refer to [33].

3.2.1 From crust to silicon wafer: an overview

It all starts with a relatively pure piece of the so-abundant SiO_2 (quartzite when referring to it as a mineral), that undergoes a series of chemical reactions that help removing the majority of its impurities by distillation. The result is a piece of bare silicon, that is then melted in a vessel to start the so-called Czochralski (CZ) process (Figure 3.1), which is hereunder summarized.

A specific amount of dopant (typically boron or phosphorus) is introduced into the melt to obtain the desired doping concentration and conductivity type of the

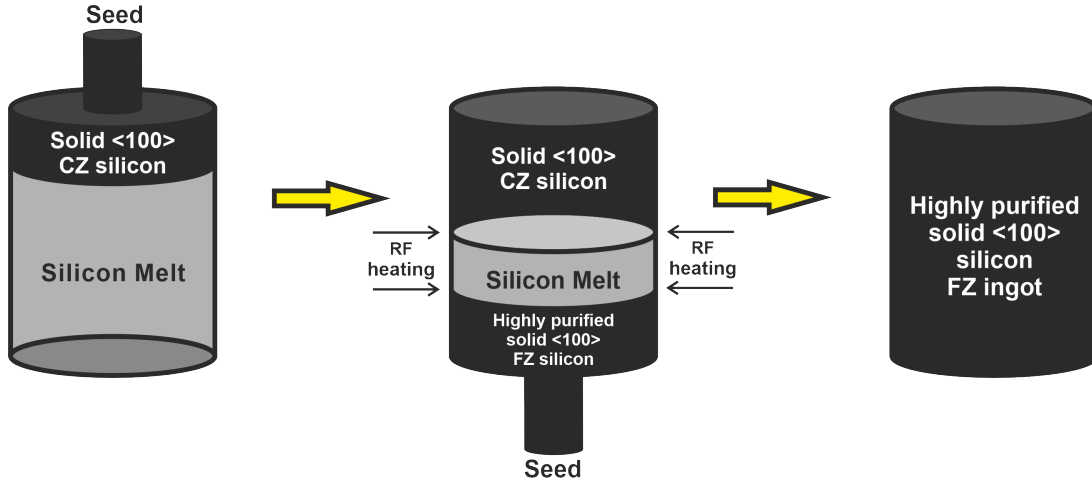


FIGURE 3.1: schematic of how a CZ ingot is created, to thereafter go through a FZ process and obtain a high-purity silicon ingot.

final wafers. Subsequently, a *seed* is brought into contact with the melt to start growing a silicon ingot. The seed is a small piece of silicon of a certain orientation that serves as a starting point for the growth of the ingot. In other words, the seed can be understood as a template for the orientation of the growing crystal. At the microscopic level, the first silicon atoms from the melt that interact with the seed align with the orientation of the latter, to be further solidified. This process continues as the crystal grows and it is pulled out of the equipment vessel. The outcome is a silicon ingot with a certain conductivity, that can be either diced to obtain wafers or further purified via Flat Zone (FZ) technique.

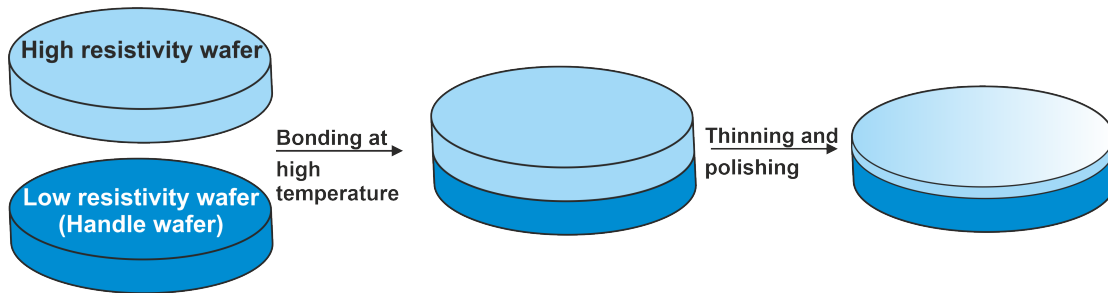
The first step of such technique is holding the CZ silicon ingot downside from the seed (Figure 3.1) within an inert atmosphere (typically argon). Then, a mobile radiofrequency heating system is swept from the seed upwards, locally melting the CZ silicon as it passes through. Many of the silicon impurities, either electrically neutral as carbon or oxygen, or critical for the semiconductor conductivity as nikel, iron or copper, tend to stay in liquid silicon rather than solid. Thus, as the molten zone moves through the silicon ingot, such impurities are swept along with the liquid phase and concentrated at the top of the ingot. In a nutshell, a great number of impurities can be squeezed out of the original CZ ingot by applying the FZ technique to it. As a result, a high-purity silicon of a certain conductivity ingot is created, that can be further diced in wafers. It is worth remarking that the molten zone has been oversized in Figure 3.1 for clarification of the process, and such zone is generally quite narrow when compared to the CZ ingot length. An extended review of the CZ and FZ methods can be found in [33].

Silicon wafers for LGAD manufacturing at the IMB-CNM are always fabricated with the FZ technique and a seed orientation of (100), which is known for providing a better charge carrier mobility compared to other crystal orientations [35]. Since silicon detectors rely on the movement of charge carriers generated by incident radiation, a higher mobility is advantageous for faster signal collection. This is particularly important for application where the timing response is crucial, such as the ones mentioned in section 2.3.3. As discussed in Chapter 1, the carrier mobility is inversely proportional to its recombination probability. That is, the higher the latter, the smaller the amount of charge that, once generated by an external ionizing

particle, can reach the electrodes. Moreover, the number of dangling bonds existing in the surface of a silicon detector manufactured on a (100) oriented wafer is the smallest when compared to any other crystal orientation [36]. As we will address in section 3.2, the latter statement translates into having a smaller leakage current at the $Si - SiO_2$ interfaces existing in the detector. Thus, having a silicon sensor with a crystal orientation of (100), with a relative higher mobility, not only provides a better time response, but also enhances the amount of charge that can be collected to compose the radiation-generated signal while reducing the leakage current. In other words, silicon detectors with a crystal orientation of (100) also provide a better SNR.

As discussed in Chapter 2, most of the wafers that were used as a substrate for LGAD fabrication at the IMB-CNM had a $\approx 50 \mu m$ high resistivity active thickness plus a handle-wafer of low resistivity to offer protection from potential mechanical crack (Figure 2.1). The thickness of the handle-wafer varies depending on the manufacturing batch, but it is selected so that the total wafer thickness is always greater than $300 \mu m$. The first paragraph of this section describes how a silicon ingot of a certain doping concentration and conductivity can be manufactured to then be diced in wafers. However, we have not yet address how to engineer wafers with $\approx 50 \mu m$ high resistivity active thickness plus a handle-wafer of low resistivity (that is, a wafer with two layers of different thickness, doping concentration, or even conductivity). Let us talk through it.

Si-Si Wafers



Epitaxial Wafers

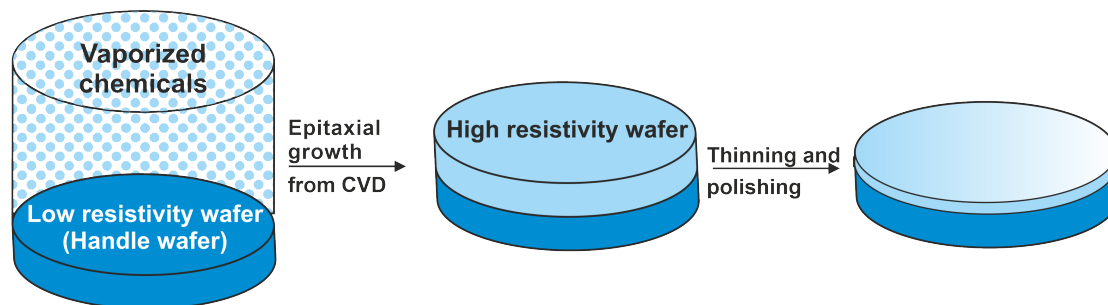


FIGURE 3.2: schematic of how Si-Si and epitaxial wafers are processed.

The most straightforward method to do so is by fusing two already processed wafers of different doping concentration. Such pair of wafers is brought into contact at high temperature, close to the melting point of silicon, to ensure a solid bond

between them (Figure 3.2). The final wafer can be then thinned by any of their sides to achieve the desired thickness of its layers, which are further polished to enhance planarization. The high-resistivity side is the one typically undergoing the thinning process if we aim to obtain a $\approx 50 \mu\text{m}$ active thickness in the fabricated detectors. In the literature, wafers processed with this method are referred to as *Si-Si wafers*.

Another known technique to obtain wafers with layers of different doping concentration is by epitaxial growth, that is, by physically tailoring one of the layers onto another wafer (Figure 3.2). This is typically achieved through a process called *Plasma Enhanced Chemical Vapor Deposition (PECVD)* [37]. In a nutshell, the PECVD technique consists in introducing the handle-wafer in a reactor chamber containing a combination of vaporized chemicals, including both silicon and acceptor/donor compounds in a certain concentration. By bringing the system to a sufficiently high temperature, the plasma aids the vaporized compounds in undergoing reactions that result in the deposition of a layer with controlled thickness and doping concentration onto the handle wafer. An advantage of this technique, in compared to wafer bonding, is that the deposited layer can be grown to the desired thickness, so no further thinning is typically needed. However, a polishing is generally carried out to assure planarization. As a result, one obtains a so-called *epitaxial wafer*.

The techniques described in this section give as a result a set of wafers that mark the starting point of the manufacturing process of silicon detectors at the IMB-CNM. Let us now address the engineering steps that take us from a raw wafer to a detectors wafer.

3.2.2 Outline of engineering techniques for silicon detector fabrication at the IMB-CNM

Figure 3.3 shows a very simplistic but illustrative depiction of the beginning and the end of a silicon detector wafer fabrication process. By starting with a raw wafer of a certain size and conductivity type of the substrate (generally p-type for standard LGADs), one ends with a wafer containing several detectors. While the geometry of the latter is typically varied along the wafer, for the seek of simplicity we have picked a detector wafer where most of its sensors have an area of $3.3 \times 3.3 \text{ mm}^2$. The choice is not trivial, but one the first LGAD wafers fabricated at the IMB-CNM had such geometry configuration [25].

The color code in Figure 3.3 indicates different layers manufactured on top of the high resistivity p-type layer (SiO_2 , metal, doped silicon, etc). Nevertheless, let us forget about the nature of such layers for a moment and focus on an evident but very important feature. When fabricating a detector wafer, one starts with a blank pattern on the surface (in Figure 3.3, the high-resistivity p-type silicon) to end with a specific pattern that repeats across the wafer and shapes the structure of the devices ($3.3 \times 3.3 \text{ mm}^2$ sensors). We may notice that every layer reading a color code in Figure 3.3 has a precise design that also repeats for every individual detector on the wafer. Drawing such patterns on an original raw wafer is achieved through an engineering technique called photolithography.

Photolithography

Figure 3.4 shows an outline of a photolithography process to create a pattern on the surface of a wafer. Firstly, a thin layer ($1\text{--}2 \mu\text{m}$ thickness) of *photoresist* is deposited on top of the wafer surface (step 2 in Figure 3.4). A photoresist is a light-sensitive material that can change its chemical properties when illuminated with photons of a

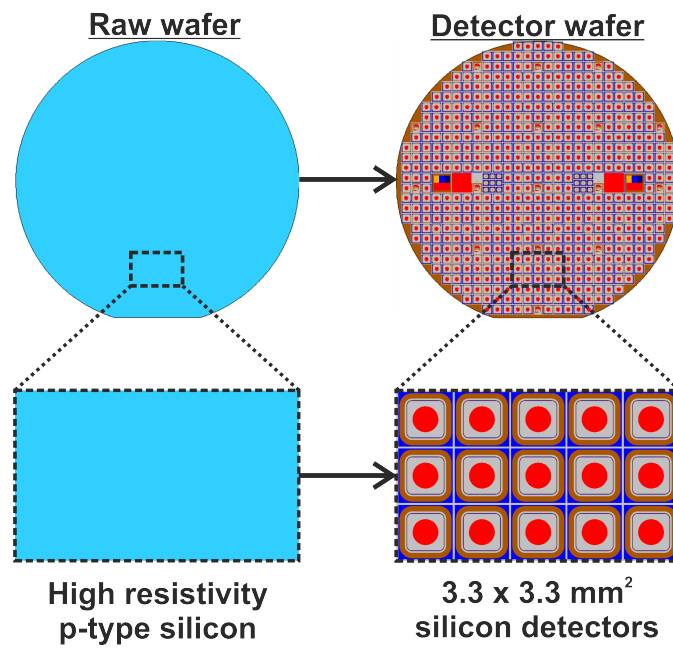


FIGURE 3.3: Illustration of the beginning and end of a silicon detector wafer fabrication process.

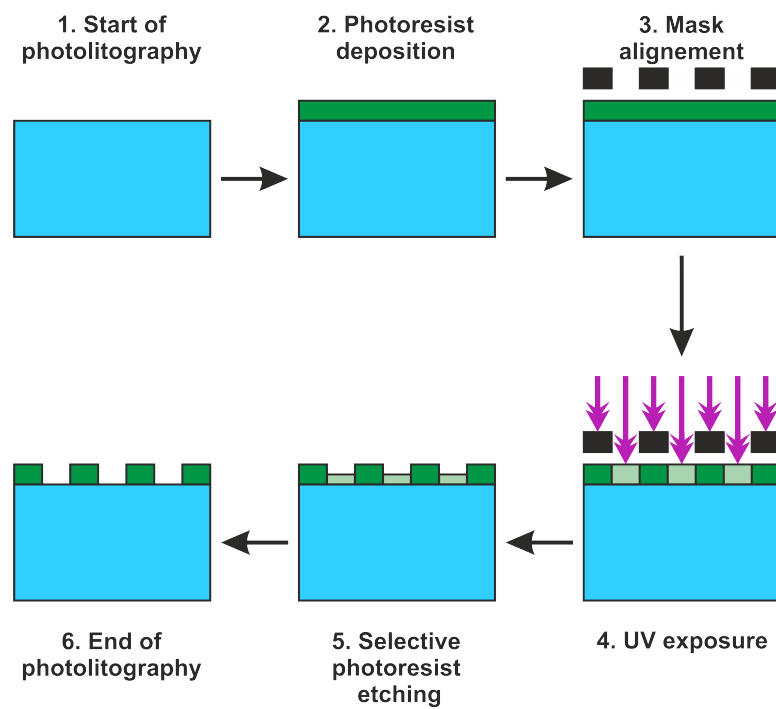


FIGURE 3.4: Outline of a photolithography process to create a pattern on the surface of a silicon wafer.

certain wavelength (typically in the UV range) [33]. Then, a *mask* designed with the desired pattern is aligned onto the wafer surface (step 3 in Figure 3.4). The mask is made of materials highly absorbent to photons of wavelength which the photoresist is sensitive to. Subsequently, the surface is illuminated with light of such wavelength (step 4 in Figure 3.4) through the mask. Here is where the pattern is physically created on the surface, as the photoresist will change its chemical properties only in those parts where the mask allows the light to pass through. In those sites hit by the incident light, the photoresist will be either more (positive photoresist) or less (negative photoresist) soluble to a chemical solution developed to selectively etch it (step 5 in Figure 3.4). Ultimately, one ends up with a pattern on the wafer surface in which some sites are covered with the photoresist, while others are not.

It is worth noting that masks are not fabricated at the IMB-CNM clean-room. While they are designed at the IMB-CNM, their manufacturing is outsourced to an external vendor, as is the case with raw wafers. However, apart from wafer and mask fabrication, the IMB-CNM facilities have all the necessary equipment to develop silicon detectors.

Deposition/oxidation and selective etching

Despite Figure 3.4 shows a photolithography process made on the raw high-resistivity silicon layer, in reality it is always made to create a pattern on an already existing layer of a different material type. Such layers, regardless its nature, are typically created by *deposition* (a review of deposition techniques can be found in [33]), with the exception of SiO_2 layers. When tailoring a SiO_2 layer onto a silicon surface, it is common to do it with a thermal process called *oxidation*. Essentially, it consists in placing the wafers on a clean furnace, at a certain temperature and gas flow (oxygen of water vapour) and for a given time, so a layer of SiO_2 can naturally be grown in the surface of the silicon wafer. It is worth mentioning that SiO_2 layers may also be deposited, particularly when it has to be done onto layers that do not only contain silicon but other materials (e.g. metal).

Once a layer is deposited (or growth) onto the wafer, a photolithography process is carried out to create the desired pattern on it (Figure 3.5). The use of chemicals that can selectively etch a layer without affecting others is here critical. For instance, the solution used in step 6 in Figure 3.5 to etch the illuminated photoresist has to be inert to SiO_2 and the non-illuminated photoresist. Subsequently, the chemicals used to etch SiO_2 in step 7 must be unreactive to the bare silicon of the high-resistivity layer and the non-illuminated photoresist. A review of the most common chemical solutions for selective etching can be found in [33].

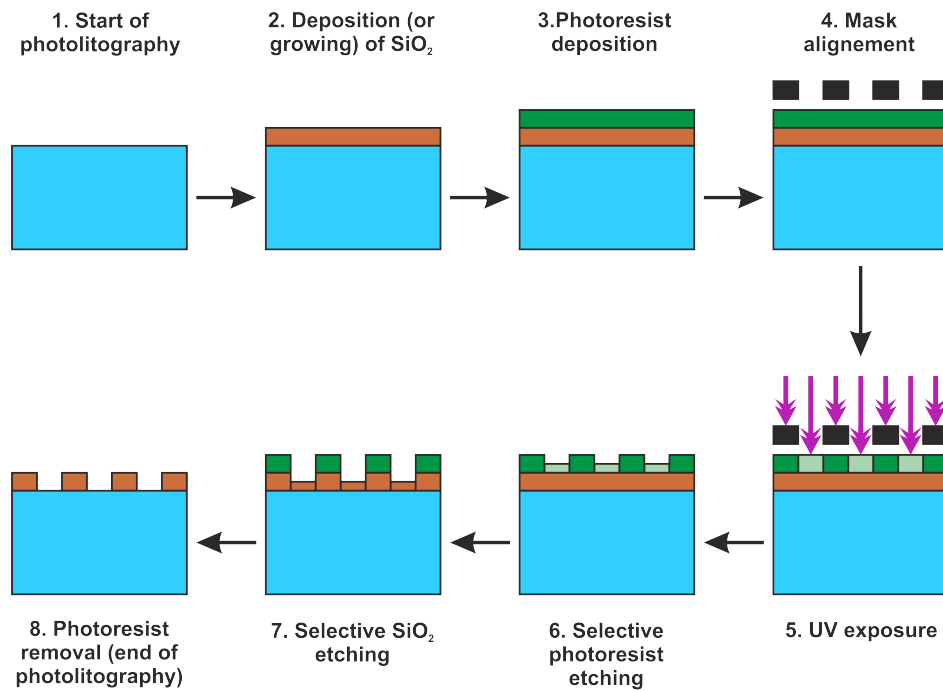


FIGURE 3.5: Outline of a photolithography process to create a pattern on a deposited/growth SiO_2 layer tailored onto the surface of a silicon wafer.

Dopant implantation

When a layer of silicon of different doping concentration or conductivity type that the one of the high-resistivity layer is needed, the most common technique is the *ion implantation* [33]. The method consist on accelerating a beam of ions of the desired dopant (typically boron for p-type silicon and phosphorus for n-type one) that impinges on the wafer surface, traverses it and is stopped at a certain depth. By tuning the ion energy and dose (number of ions per unit area) of the beam, a layer of doped silicon of a certain active doping concentration, conductivity type and thickness is created from the wafer surface inward.

The ion implantation technique always involves pre-implantation photolithography processes to grow a relatively thick SiO_2 layer where the creation of the doped silicon layer is not desired (step 1 in Figure 3.6). Such oxide layer serves as a shielding mask to stop the accelerated ions before they reach the high-resistivity layer, so its thickness depends on the energy and dopant species of the implantation beam. It is worth mentioning that using SiO_2 as a shielding mask for ion implantation is the technique generally used at the IMB-CNM, but not the only one. Another typical method consists in using the very photoresist as a mask. Nonetheless, this can be counterproductive from a technical view, as some photoresist materials (such as the ones used at the IMB-CNM) tend to change its chemical properties when doped after irradiation with ions, making its subsequent etching quite difficult. Conversely, doped SiO_2 generally has a smaller etching resistant when compared to SiO_2 , avoiding the aforementioned technical issue.

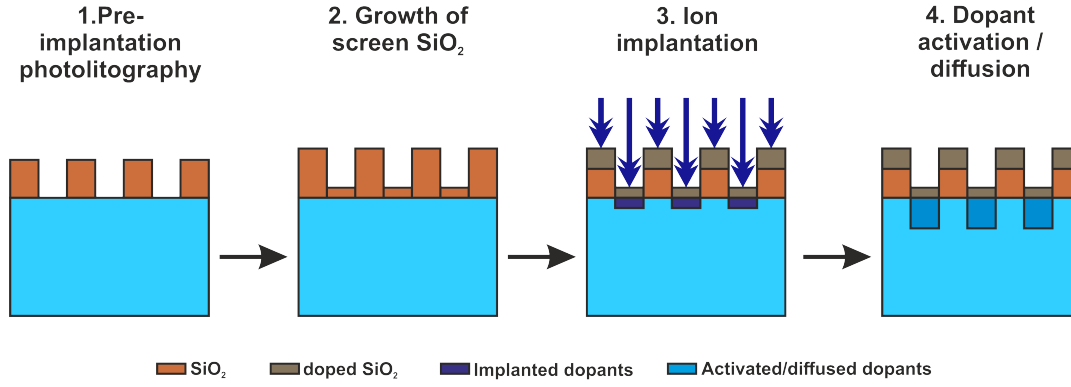


FIGURE 3.6: Outline of the dopant implantation and activation/diffusion onto the surface of a silicon wafer.

On the other hand, ion implantation is typically carried out through a thin layer of SiO_2 (referred to as *screen oxide* in the literature) at the wafer surface sites where the doped silicon layer is aimed to be built (steps 2 and 3 in Figure 3.6). The utilization of a screen oxide instead of implanting directly into the high-resistivity layer has its justification. Firstly, the screen oxide serves as a barrier that prevents contamination from the ion implantation process itself [38], [39]. Some parts of acceleration chambers contain metallic elements (such as Fe or Ni) that can be sputtered during the implantation process and reach the silicon wafer surface. Such metallic elements suppose critical impurities for silicon, as they tend to create midgap energy levels when introduced into the crystal lattice [40]. As discussed in Chapter 2, the addition of midgap energy levels alters the electrical properties of the final fabricated detector, increasing its leakage current and reducing the carriers mobility. By using a screen oxide, most of the sputtered metallic elements are stopped within it before reaching the high-resistivity layer, so they can easily be removed from the wafer by SiO_2 etching.

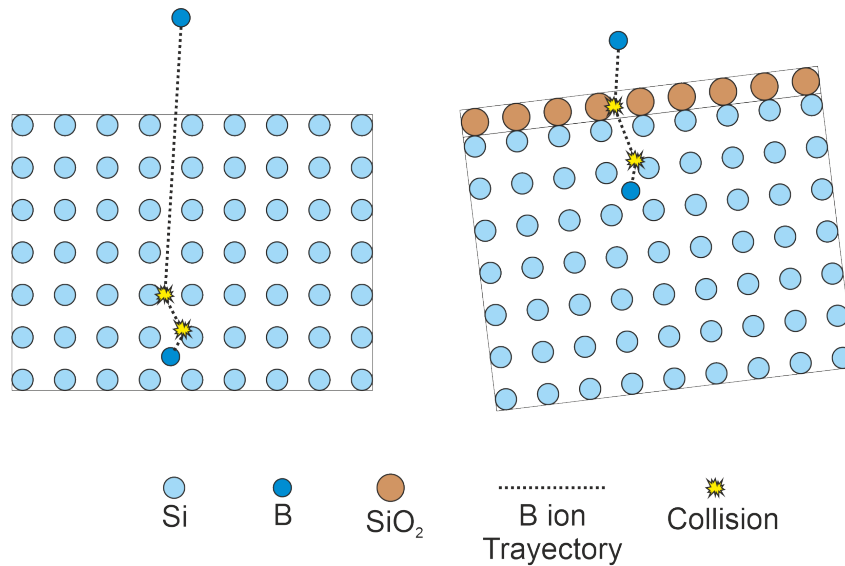


FIGURE 3.7: schematic of a boron ion implantation on a $\langle 100 \rangle$ silicon wafer, with a growth screen oxide and a tilt of 7° and without.

Following that, the presence of a thin screen oxide helps preventing the *chanelling* effect during ion implantation [33], [41]. The term channelling refers to a phenomenon where implanted ions penetrate more deeply into certain directions within the crystalline silicon lattice. For instance, if an accelerated ion impinges on the bare $\langle 100 \rangle$ silicon surface perpendicularly (or almost) to it, there is a probability for the ion to go through the space between two atomic rows in the lattice (Figure 3.7). In the presence of a screen oxide, such probability is reduced, as the ion can be scattered by a SiO_2 molecule (bigger than a silicon atom) before entering the high-resistivity layer. The scattered dopant ion will change its direction, so the likelihood of colliding with a Si atom once in the silicon bulk is also enhanced. Moreover, and despite this is not displayed in Figure 3.6 to avoid losing simplicity, ion implantation is normally carried out with the wafer slanted at a certain angle (traditionally 7° [33]). This tilt, along with the use of a screen oxide, reduces even more the probability of an ion being channelled during implantation (Figure 3.7). As a direct consequence of it, the doped silicon layers that are built are more uniform, both in doping concentration and depth [38], [41], [42]. The latter fact is crucial if we aim to reduce the dispersion in the electrical performance of the silicon detectors along the wafer, as such performance mainly depend on the conductivity (e.g. physical shape) of its layers. Ultimately, the use of a screen oxide also mitigates the silicon crystal damage that involves the ion implantation process itself. That is, part of the beam energy is absorbed within the screen oxide by ion- SiO_2 atom collisions (Figure 3.7), reducing the number of radiation-induced defects on the silicon lattice.

Annealing and activation/diffusion of dopants

Let us make a pit stop to address the nature and effects of the cited radiation-induced defects that ion implantation brings with it. When a charged particle (e.g. a boron ion) traverses matter (e.g. silicon), it can lose its energy by colliding with electrons (via Coulomb interaction) or atomic nuclei (via both Coulomb or nuclear interaction). As discussed in Chapter 2, only the latter involve sufficient energy transfer so that the silicon atoms may be displaced from its lattice positions. Furthermore, the recoil atom may even have enough energy to dislodge other silicon atoms, generating a cluster of displacements. When such phenomenon happens in abundance, as often in the case of ion implantation, the *displacement damage* (i.e. the ratio of radiation-induced dislodge atoms) is significant enough to degrade the quality of the silicon where such damage has taken place. Such degradation is linked to a rise of mid-gap levels introduced in the energy band structure of the crystal, and is translated into an increase of leakage current and a reduction of the carrier mobility [33]. While having a thin layer of SiO_2 helps to mitigate this effect, it is often not enough to reduce it to a reasonable level. In order to do so, the silicon wafer needs to be annealed.

An *annealing* process, as in the previously mentioned oxidation, is no more than a thermal process in a clean furnace at a given temperature, time and gas flow, but with a different purpose: the repair of the implantation damage. In simple terms, maintaining an implanted wafer in a furnace for a given time and temperature helps silicon atoms to move back to their lattice positions, recovering the original crystal structure. For boron and phosphorus, core dopants for LGAD fabrication at the IMB-CNM, an annealing at $T \sim 1000^\circ\text{C}$ and $t \sim 1\text{h}$ is sufficient to repair more than 90% of the displacement damage, regardless of the implantation dose [33]. The use of this thermal step is not only necessary to mitigate damage effects, but also to activate dopants.

When implanted, dopants do not generally occupy an optimal lattice site to function as donors or acceptors. In other words, they are not bonded to other silicon atoms in a way that they are able to give away a electron or hole to conduct. An *activation* (e.g. an annealing) helps such dopant atoms to move to interstitials or vacancies where the atomic bond to the silicon atoms ensure their functioning as donors or acceptors, hence achieving the aim of their preceding implantation: to construct a doped silicon layer with a different conductivity. Furthermore, an activation/annealing can also be understood as a dopant *diffusion*. This is schematically represented in Figure 3.6 (step 4). Doped silicon layers frequently need their depth and doping concentration to be tuned in order to achieve their desired performance. The motion of the dopant atoms do not stop once they have encountered a lattice site to be activated, but can keep jumping into activation sites based deeper in the high-resistivity layer. As a result, the doping concentration of the layer is redistributed within a certain depth, that strongly depends on the time and temperature of the thermal process [33].

As we will discuss in Chapter 5, there are certain applications that require doped silicon layers to be activated while avoiding dopant diffusion as much as possible. In those cases, the implanted wafers are treated with thermal processes of times of the order of seconds instead of hours (a so-called Rapid Thermal Annealing or RTA [33]). In order to have both the dopants activated and the implantation damage reasonably repaired with such short annealing, a trade-off has to be made with temperature. That is, the temperature of an RTA tends to be greater than that of an annealing that also implies diffusion.

Wafer cleaning

Every planar technology process addressed so far involves the physical contact of the wafers with certain equipment that may add impurities to their surfaces. Moreover, and despite the safety measures to maintain a clean-room environment are extensive, there is always a non-zero chance of organic contamination, either from the very operators or from outside the facilities. In order to avoid that, wafers undergo several cleaning processes during the detectors fabrication.

Just as the aforementioned etching techniques, cleaning methods consist of immersing the wafers in a chemical solution for a certain period of time. The most common cleaning solution is a mixture of sulfuric acid and hydrogen peroxide, also known as *piranha* etch in the literature [43]. Such chemical is able to oxidize and dissolve most organic contaminants. Also, it helps removing photoresist residues that may have kept adhered to the wafer surface during the photolithographic processes. Ultimately, the piranha solution oxidizes some metals such as aluminum and copper (typical elements composing engineering equipment), facilitating their removal in the event of contamination.

Other techniques for quality control during fabrication

Last but not least, it is important to mention a few techniques available at the IMB-CNM clean room that facilitate quality control during the fabrication process. As aforementioned, wafers for LGAD manufacturing are purchased from an external vendor. Typically, wafer features such as its thickness and the resistivity of their layers are given within a certain range. On the other hand, the thickness of the oxide layers that are thermally grown during the fabrication play a crucial role when tailoring the different elements of a detector. This is particularly critical regarding

the screen oxide prior to implantation. As we will address in section 3.4, knowing the actual values of these parameters before the fabrication process is essential to make accurate predictions of the LGAD performance by means of TCAD simulation. The IMB-CNM clean room counts with equipment able to measure these important parameters.

The wafer thickness is determined at the IMB-CNM with a Proforma 300 equipment, which has a micrometer able to measure the distance between probes when they touch both sides of the wafer. The resistivity is determined with a Chang Min Tech 4-probe station, that measures the surface current-voltage of the wafer and calculates the sheet resistance R_s , that can be further translated into resistivity by applying the formula $\rho = R_s \cdot D$, being D the thickness previously measured with the Proforma 300. Lastly, the oxide thickness after an oxidation or deposition is measured with a Nanospec 6100 equipment. This is done via interferometry, that is, by analyzing light reflected off the wafer surface to determine the thickness of oxide films over it.

3.3 Fabrication process of single-pad LGADs at the IMB-CNM

Let us start by describing the fabrication process that lead us to manufacture an p-type LGAD wafer containing only single-pad diodes (Figure 3.8), which are the simplest form of detector. From a basic classification perspective, a single-pad detector has two parts: the *active volume* or *core* and the *periphery*. In a nutshell, the active volume is the device element where a current will flow when the particle to be detected impinges on the detector, while the periphery serves as the termination element. Typically, the periphery sub-elements and the core are designed and optimized independently, but their manufacturing is carried out simultaneously.

Despite the periphery does not play a role in the particle detection, its fabrication is crucial for the device functionality as a whole. Their main elements are the *channel stopper*, the Junction Termination Extension (*JTE*) and the *guard ring*. In the event of manufacturing LGADs for high-energy physics applications, a *p-stop* will also be needed in the periphery. On the other hand, the active area is composed of the *multiplication layer*, the *bulk* and the *ohmic contacts*. There is a last element that covers both the periphery and the core. These are the *passivation* layers, that serve as a back-end element to prevent degradation from the ambient. All these device elements and their fabrication processes are described in this section.

It is worth remarking that the mask used to didactically addressed the features of IMB-CNM LGAD fabrication was design to fulfill the specific requirements of the CMS experiment at the LHC. LGADs fabricated this way will be comprehensively studied in Chapter 5. Thus, any single-pad LGAD parameter numerically indicated in this section is subjected to change with dependence on the specific application. An example of it can be seen in Figure 3.8, where the active area of the detectors is $1.3 \times 1.3 \text{ mm}^2$. The numerical value of such area is a requirement for the CMS experiment sensors, so a different application may require larger or smaller pad areas. Nevertheless, the main aspects of how an LGAD must be manufactured to be functional are hereunder addressed.

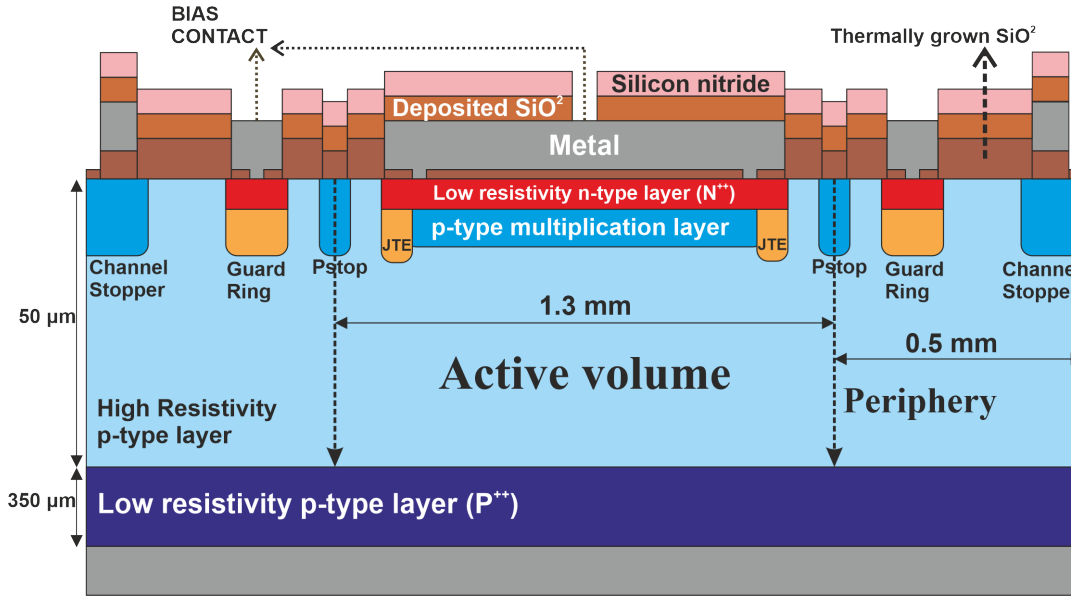


FIGURE 3.8: Cross section of a single-pad LGAD of active volume $1.3 \times 1.3 \text{ mm}^2 \times 50 \text{ } \mu\text{m}$ fabricated on a high resistivity p-type wafer on a low-resistivity handle wafer of $350 \text{ } \mu\text{m}$. The device elements are not scaled in order to better distinguished each part.

3.3.1 The field oxide

The first step in the fabrication process is the growth of a field oxide of $8000 \text{ } \text{\AA}$ thickness all along the wafer surface. This is done by placing the wafer in a furnace during a certain time, temperature and gas flow. On one hand, the field oxide serves as a protective layer on the surface of the silicon wafer, passivating the underlying silicon and reducing surface defects, as well as blocking potential contaminants from reaching the silicon surface. On the other hand, it also acts as a barrier that impedes ions from subsequent implantation processes to reach regions where they are not desired. It is worth mentioning that the field oxide is always constructed in two steps. First, a thin layer of oxide of the order of $\sim 100 \text{ } \text{\AA}$ is grown at the $\text{SiO}_2\text{-Si}$ interface via *dry oxidation*, that is, in an atmosphere of bare O_2 flow. The rest of the field oxide is grown on top of it via *wet oxidation* (within a water vapour atmosphere). The reasons for that are hereunder summarized.

On one hand, oxide layers grown by dry oxidation typically have a higher density and quality, which is beneficial for the inner part of the field oxide, where the primary concerns are insulation and isolation. On the other hand, wet oxidation tends to introduce more defects in the oxide layer due to the incorporation of hydrogen, which may in turn disrupt the quality of the $\text{SiO}_2\text{-Si}$ interface and introduce leakage current paths on the device surface. However, the growth of SiO_2 via wet oxidation is way faster than doing so in a dry environment. Moreover, the outer part of the field oxide is generally aimed to just isolate from the ambient. Hence, a thick enough ($8000 \text{ } \text{\AA}$) field oxide growth by wet oxidation is sufficient to play its role, despite the lower quality of the grown SiO_2 .

3.3.2 The Channel Stopper and the P-stop

As previously discussed, it is always desirable to operate silicon detectors at reverse biases above the full depletion value. This ensures that the entire active volume is available for particle detection and, in the case of LGADs, also guarantees having an electric field high enough to trigger the avalanche mechanism so a certain gain is obtained. However, working an LGAD at overdepletion biases may induce leakage current problems if the periphery is not optimized to do so.

On one hand, a silicon detector does not only deplete its charges vertically (that is, from N^{++} to P^{++} in Figure 3.8) as a bias is applied, but it also does it laterally. On the other hand, when an LGAD is cut and removed from the wafer, its dicing edge contains a great amount of defects (i.e. dangling bonds or even conductivity inversion) that can serve as paths or channels for leakage current to flow. These two statements together translate as it follows: if the depletion region in the bulk reaches the dicing surfaces, the defects present on them will induce an extra source of leakage current. In order to prevent that, masks for LGAD fabrication are designed so the core is sufficiently far from the edges. As Figure 3.8 shows, in the examples given in this section the core is 0.5 mm away from the edges. An overview of how such distance was optimized can be found in [13].

Furthermore, the leakage current path from cutting edge defects to the bulk is also blocked by implanting and activating a highly-doped layer of dopants of the same type as the high-resistivity layer. In doing this, any carrier that is generated in the very periphery of the LGAD has a higher probability of being recombined before reaching the core. Such layer is known as the *channel stopper*. The first photolithographic step in any LGAD fabrication run at the IMB-CNM is done to construct this element on the device periphery (Figure 3.9). To sum it up, in the event of the depletion region laterally extending to the outermost periphery, the channel stopper acts as a barrier to prevent the aforementioned defect charges carriers from reaching the core.

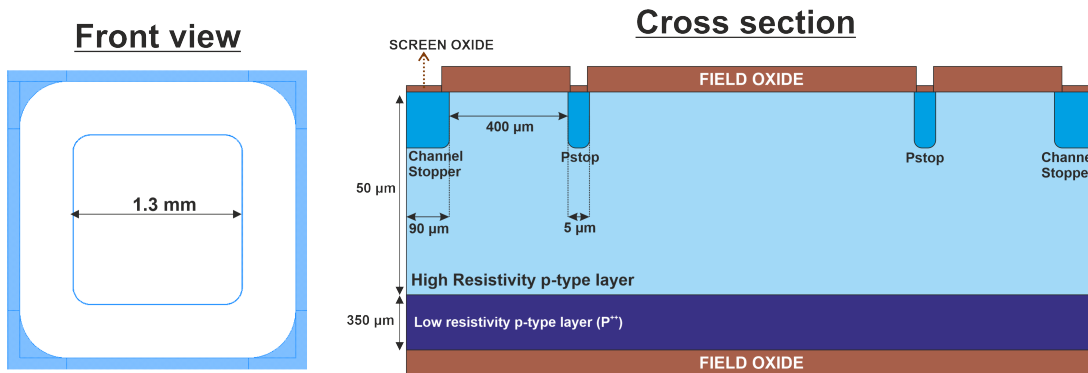


FIGURE 3.9: Front view and cross section of a single-pad LGAD where a channel stopper and a p-stop have been constructed.

This first manufacturing step has an extra purpose in the event of fabricating detectors to be used in harsh radiation environments. If that is the case, a narrow window around the active area is also opened in the field oxide for the implantation of a highly-doped boron layer (Figure 3.9) of the same characteristics as the channel stopper. This device element is the *p-stop*, and helps preventing the generation of an effective n-type conductivity layer by the SiO_2 - Si interface by means of high levels of irradiation [44]. The physics that lead to such phenomenon will be comprehensively

addressed in Chapter 5. In order to understand why this can suppose a problem in the device functionality, it is intuitive to discuss it along the next periphery elements: the JTE and the guard ring.

On the other hand, the channel stopper also has a p-stop intent when the detector is irradiated. This is due to a phenomenon known as *conductivity type inversion*, an effect occurs when the majority carrier type in a region of the detector changes due to the presence of high levels of irradiation induced defects [45]–[47]. As n-type silicon more readily to be converted to p-type than vice versa when irradiated [45]–[47], any LGAD mean to be used in harsh radiation environments is fabricated on p-type wafers rather than n-type ones. Along with other radiation damage phenomena, the conductivity type inversion will be addressed in Chapter 5.

3.3.3 The Junction Termination Extension (JTE) and the guard ring

As discussed in previous chapters, a high value of the leakage current can degrade the performance of an LGAD, as it introduces noise and reduces the detector sensitivity. The periphery current (also known as surface current) is an important source of noise that needs to be separated from the total leakage current during particle detection measurements. To do so, a *guard ring* is constructed in the second photolithographic step (Figure 3.10). It withdraws the surface current of the sensor while biased along with the active area (Figure 3.8), reducing the baseline noise level.

Along with the guard ring, a *Junction Termination Extension (JTE)* is also manufactured at this photolithographic level. This extension creates a graded doping profile at the edges of the PN junction that will be constructed in the next fabrication steps (multiplication and N^{++} layers in Figure 3.8). By extending the PN junction and creating a gradual drop from the highly doped region (N^{++}) to the lightly doped JTE region, a smoother transition for the electric field is reached around the active area, which in turn reduces the risk of early voltage breakdown at the edge of the core [13]. Thus, the JTE is not a distinctive element for LGADs, but standard PiN detectors also need it to avoid edge breakdown. In other words, no PN junction can be manufactured without having a proper termination around it, as the absence of one will unavoidably lead to an increase in leakage current and a likely early breakdown of the device as a whole.

It is worth remarking that the term *guard ring*, despite often used in high energy physics detectors argot, may be misleading. Historically, JTE elements were not implemented in silicon detectors to avoid edge breakdown. Such task (along with the one of subtracting the periphery current) was given to ring elements manufactured around the active area, as the one depicted in Figure 3.10. That is the reason why the term *guard* was coined to them, as they were "guarding" the potential effects of high electric fields at the device edge. However, the avoidance of edge breakdown was delegated from guard rings to the JTE as the latter was introduced in detectors fabrication, leaving the first with the sole task of extracting the periphery current. In a nutshell, while the term *guard ring* has been established within the argot, its actual function is to serve as a surface current *extraction ring*, as long as a JTE is properly manufactured to avoid edge breakdown.

The presence of the guard ring and the JTE gives a sharper insight of the p-stop purpose (Figure 3.10). This highly-doped p-type layer helps preventing the creation of the aforementioned n-type conductivity layer by the $\text{SiO}_2\text{-Si}$ interface in between the core and the guard ring when the device is irradiated, assuring a good isolation between them during high-energy physics experiments. To put it another

way, the p-stop helps maintaining the guard ring functionality (withdrawing the surface current from the bulk one) even in harsh radiation environments [13].

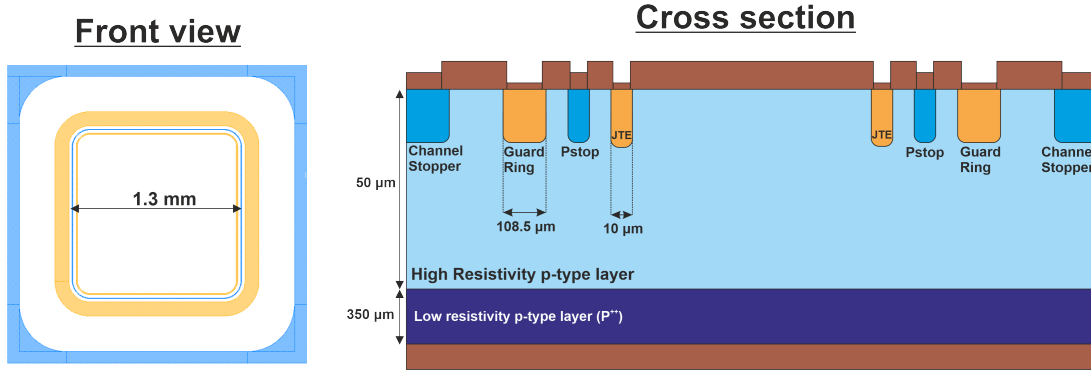


FIGURE 3.10: Front view and cross section of a single-pad LGAD where a JTE and a guard ring have been constructed.

Last but not least, it is important to mention that the implantation of a narrow p-stop is not the only technique to preserve the guard ring functionality. Particularly, a method known as *p-spray* [48] is also commonly used in LGAD detector manufacturing [49]. In short, the p-spray technique consists in implanting a shallow boron layer all over the raw wafer surface (and not only at the narrow areas typical of p-stop) before starting the fabrication. While implementing the p-spray method would save ourselves from a photolithographic step, it was discarded for its use at the IMB-CNM due to non-uniformities observed in its shallow boron concentration layer [48].

3.3.4 The multiplication layer

Following the aforementioned periphery elements, the next photolithographic step is to build the key active volume element of an LGAD: the multiplication layer. Traditional IMB-CNM LGADs have the multiplication layer implanted at 100 keV and $1.9 \cdot 10^{13}$ at/cm² and annealed at 1100°C for 180 min. This creates a moderately doped p-type layer that extends a few micrometers into the bulk. As Figure 3.11 shows, this photolithographic level and the previous have a 3 μm lateral overlap. This is done to promote an inter-diffusion between boron and phosphorus at the active area periphery that ensures the JTE functionality [13].

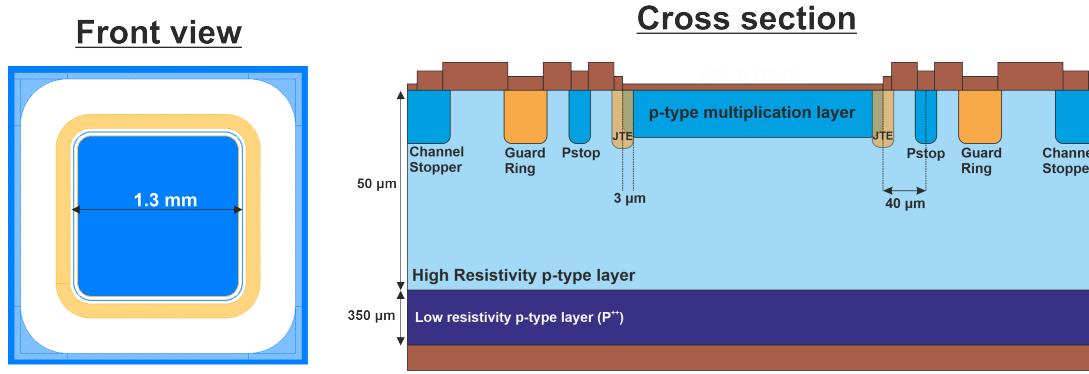


FIGURE 3.11: Front view and cross section of a single-pad LGAD where a multiplication layer has been constructed.

On the other hand, another important parameter in LGAD periphery optimization is the distance between the edge of the multiplication layer and the middle of the p-stop ($40\ \mu\text{m}$ in Figure 3.11). In the case of pixelated detectors, the parameter to optimize is the distance between the edge of the multiplication layers in adjacent pixels. The importance of such parameter will be addressed in section 3.3, while the optimization of the multiplication layer fabrication will be discussed in section 3.4.

3.3.5 The electrodes

Following the multiplication layer, the next fabrication step is the construction of the electrodes. For the N^{++} layer, phosphorus is implanted at relatively high doses ($\sim 10^{15}\ \text{at}/\text{cm}^2$) to ensure having a layer with a sufficiently low resistivity so a good ohmic contact can be built in the following photolithographic steps. An annealing is then carried out at 1000°C for 30 min in order to activate and diffuse the phosphorus. This procedure is done both in the active area and the guard ring, which are the elements that get biased during measurements (Figure 3.12). In the example given in this section, the P^{++} electrode is already present in the device (handle wafer). In the event of manufacturing the P^{++} from scratch, the strategy is the same as in the case of the N^{++} but exchanging the dopant type.

In the case of standard PiN detectors, there is little more to say about the N^{++} function. However, such layer has an additional purpose when manufacturing LGADs. As Figure 3.11 displays, traditional IMB-CNM LGADs have its multiplication layer implanted and annealed just by the very surface of the active area. As we move to Figure 3.12, we notice that there is a portion of such layer that has been covered by the N^{++} one. The selection of the phosphorus implantation dose and energy, along with the annealing time and temperature of the layer, are key parameters to ensure having a device with linear gain. In other words, the way that the N^{++} covers the multiplication layer may determine whether we have an LGAD, and APD or even a device with no gain at all. A discussion about this will be held in section 3.4.

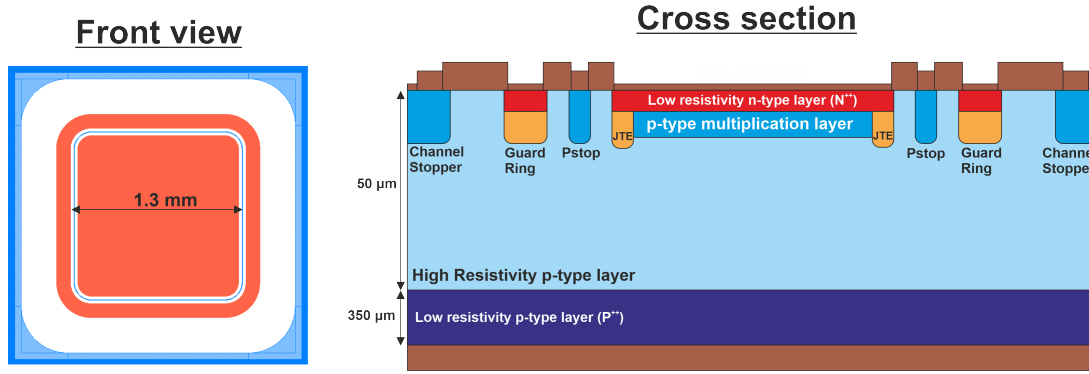


FIGURE 3.12: Front view and cross section of a single-pad LGAD where an N^{++} electrode has been constructed.

Once the N and P electrodes have been constructed, an extra photolithographic step has to be made to etch the oxide where the metal and the mentioned layers will make physical contact. This is depicted in Figure 3.13. While the oxide in the P^{++} (uniform and without structural elements) is completely etched, the one of the guard ring and the N^{++} is only selectively etched with a specific pattern. The technological reasons for that are the following.

First, this selective removal helps to preserve the integrity of the oxide layer in the remaining regions, maintaining its insulating properties and protecting the underlying silicon. Also, with a patterned etch it is easier to precisely define the dimensions and shapes of the contact openings. Along with that, the etch time is additionally reduced, minimizing over-etching in critical areas such as the gap between the active area and the periphery. This accuracy is crucial for ensuring proper alignment and spacing of metal contacts, minimizing the risk of short-circuiting the core and the guard ring after metallization.

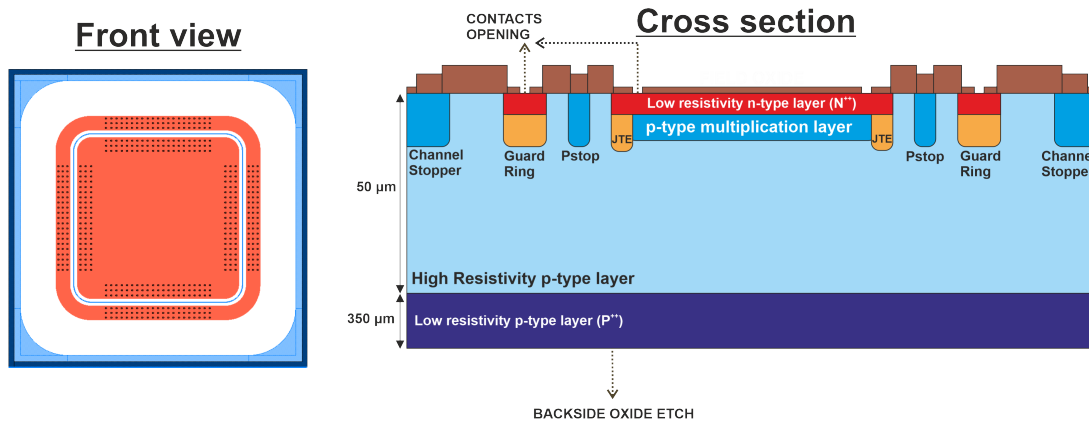


FIGURE 3.13: Front view and cross section of a single-pad LGAD where contacts have been opened on the electrodes and the guard ring.

3.3.6 Metallization: the ohmic contacts

After the contacts have been opened, the entire wafer is metallized with a 1.5 μm layer of an alloy of aluminum (99.5%) and copper (0.5%). This process is done via

sputtering. A review of this technique can be found in [33]. In a nutshell, it is a process where a target material (Al and Cu as the case in point) is bombarded with energetic ions in a vacuum chamber. These ions are generally of a chemically inert species such as argon, that does not react either with the target material or silicon. The collisions eject atoms from the target, which then condense onto the wafer surface to form a thin, uniform metal layer.

The doping of aluminum with a small portion of copper is a common technique in semiconductor devices fabrication, and has few reasons to be. Firstly, it enhances the electrical conductivity of the aluminum, which is always desirable for ohmic contacts creation. Secondly, the addition of copper improves the mechanical strength of the aluminum film and aids to avoid micro-cracks on it during wafer handling or even further LGAD operation after fabrication. Lastly, the presence of copper within the metal layer helps reducing the effects of *electromigration* [33]. In short, electromigration is a phenomenon where the electrons drifted to the electrodes transfer enough energy to the metallic atoms so they are displaced. To put it another way, the very passage of current through the metal layer can push away the aluminum atoms to certain regions. The higher the current and the thinner the metal layer, the more critical this effect will be, even causing aluminum atoms to pile up in some regions while leaving voids in others. This may result in local short-circuits within the metal layer, which in turn will increase the leakage current of the fabricated LGAD. The addition of copper, even in small amounts down to 0.5%, makes the metal layer much more resistant to suffer electromigration, as it reduces the aluminum atoms mobility and blocks diffusion paths for them. Furthermore, the choice of depositing a metal layer of 1.5 μm is not trivial, as electromigration is further prevented by using such a relatively large thickness.

Following the Al:Cu film deposition, a thermal process of 20 minutes at 350°C is performed. During such annealing, a slight inter-diffusion of aluminum into silicon and vice versa occurs, forming a thin Al-Si alloy layer at their interface that enhances the electrical connectivity, hence the quality of the ohmic contacts. It is important to point out that, once the metal has been annealed, any further thermal process at temperatures beyond 400°C should be avoided, due to a phenomenon known as *spiking* [33]. In a nutshell, spiking refers to the formation of deep, pyramid-like bulges of aluminum into the silicon (or the N^{++} layers, as the case in point) by diffusion of Al atoms during a thermal process. The depth of these spikes is an increasing function of temperature, and they start to appear at Al-Si interfaces at temperatures of 400°C and beyond. This phenomenon can locally short-circuit the ohmic contacts if the spikes traverse completely the highly-doped N^{++} layers (either in the core or the guard ring), hence boosting the leakage current of the manufactured LGAD.

Back to the matter at hand, the Al:Cu alloy deposition is followed by another photolithographic step to selectively etch the metal on the front side of the device. The result is depicted in Figure 3.14. Apart from the bias contacts (backside and N^{++} in the core and guard ring), the metal is also maintained close to the outermost periphery, which helps to visually determine the dicing edge between adjacent devices.

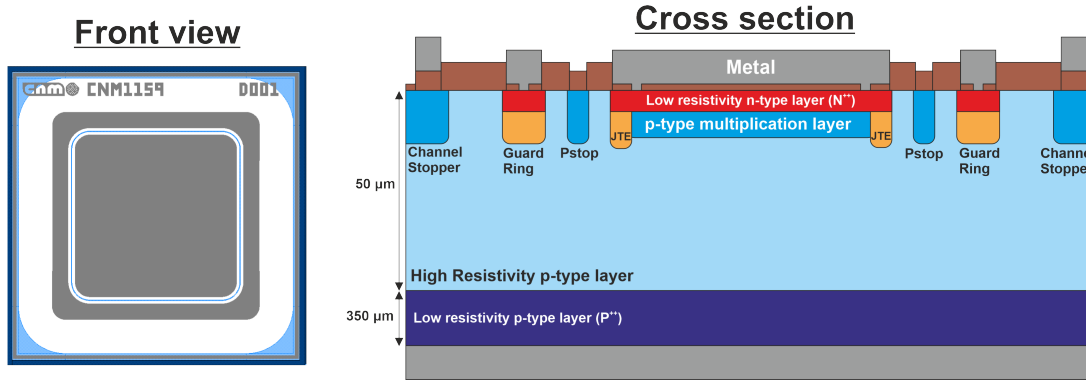


FIGURE 3.14: Front view and cross section of a single-pad LGAD where the metallization process has been done.

The regions where the metal is physically touching the low resistivity electrodes form the *ohmic contacts* of the LGAD. That is, these are the parts where the interface between the metal and the semiconductor allows a low-resistance, bidirectional connection with linear I-V characteristics, which ensures that the signal generated by any impinging particle can be withdrawn and analyse.

3.3.7 Passivation

The final step in the fabrication process is the construction of the *passivation* layers on the metal surface. A thin layer deposition of silicon dioxide (4000 Å) and silicon nitride (7000 Å) is carried out all over the wafer surface via Plasma-Enhanced Chemical Vapor Deposition (PECVD). A review of this technique can be found in [33]. In short, in the PECVD process gaseous precursors of the desired layers are introduced into a vacuum chamber, and a plasma is generated by applying a high-frequency electric field. Having such precursors in the plasma phase provides the energy needed so they can react and form a thin film onto the silicon. While the passivation layers can also be deposited via Chemical Vapor Deposition or CVD (addressed in Section 3.2), it is not feasible to use such technique when the wafers are metallized.

On one hand, the Al:Cu alloy previously deposited has its melting point at around $\sim 660^{\circ}\text{C}$, while the CVD process has an operational temperature in the range 700°C - 800°C for nitride deposition and 450°C - 900°C for oxide deposition. Thus, a chemical vapour deposition of the nitride layer will unavoidably damage the Al:Cu layer, as the latter will melt during the process. Conversely, the PECVD technique allows for such layer deposition onto the metal within a lower temperature range ($<400^{\circ}\text{C}$), maintaining the integrity of the metal layer. Despite oxide layers might be deposited using a CVD method at 450°C (away from the melting point of the Al:Cu alloy), it is not recommended to expose metal-silicon interfaces to temperatures over 400°C due to the spiking phenomenon explained in the last subsection. Consequently, the oxide passivation layer is always deposited via PECVD technique at temperatures below 400°C .

After the passivation layers have been deposited, they are selectively etched in the last photolithographic step (Figure 3.15), opening bias points in the active area and the guard ring. As in the metal photolithographic step, the passivation layers are not etched close to the outermost periphery to properly demarcate the dicing

edges. The reasons of using silicon dioxide (4000 Å) and silicon nitride (7000 Å) for the passivation layers are hereunder summarized.

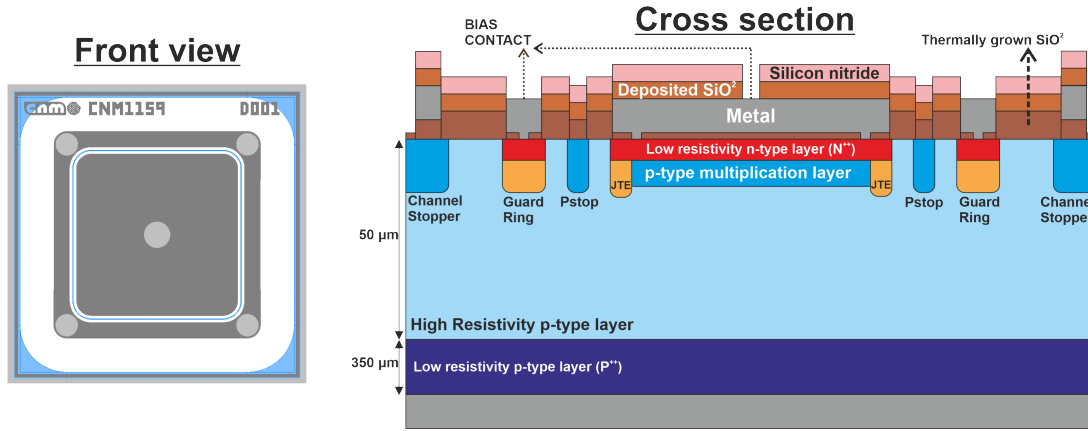


FIGURE 3.15: Front view and cross section of a single-pad LGAD where the passivation process has been done.

The SiO_2 layer protects the metal surface from external contaminants. Particularly critical are those that can oxidize the metal, as it can degrade the ohmic contact performance over time. The Si_3N_4 further enhances this protection with its properties against moisture. Furthermore, the Si_3N_4 layer adds mechanical strength to the passivation layer as a whole, protecting the metal and underlying silicon from physical damage and mechanical stress during the LGAD handling and operation.

3.3.8 Overview of the etching techniques at the IMB-CNM

All along this section, we have been claiming that the different layers (growth or deposited) are etched to create the desired pattern on the LGAD upper surface. However, it is worth making a last brief stop to briefly discuss the etching techniques that are used depending on the nature and purpose of such layers. For a more extensive review, the reader may refer to [33]. To wrap it up, the manufacturing of a single-pad LGAD involves the etch of photoresist, oxide (either thermally grown or deposited), Al:Cu and silicon nitride layers. From a basic classification perspective, an etching process may be *wet* or *dry*. In wet etching, the wafers are immersed into a liquid chemical solution that selectively dissolves and removes the components of the desired layer. In dry etching, the wafers are placed in a vacuum chamber where reactive gases or ions etch away the target layer. While there are few dry etching techniques [33], the one used in LGAD manufacturing at the IMB-CNM for photoresist, oxide and nitride layers is plasma etching (PE).

As long as it is possible, PE is always desirable than wet etching. The main reason for that is the inherent isotropic nature of wet etching in contrast to PE. In other words, the PE technique etches in a preferred direction (vertically), while the immersion into a liquid solution etches uniformly in all directions. This is schematically depicted in Figure 3.16. When immersed into the chemical solution, the oxide layer suffers an unavoidable lateral etch, that is drastically reduced when placing the wafer in a PE chamber. Controlling the lateral etch is critical in photolithographic steps that involve implantation/annealing in narrow areas, such as the p-stop ($\sim 5 \mu\text{m}$) or the JTE-Multiplication layer overlap ($\sim 3 \mu\text{m}$), as the doping concentration

may extend beyond the desired zone by dopant diffusion and cause device malfunctioning.

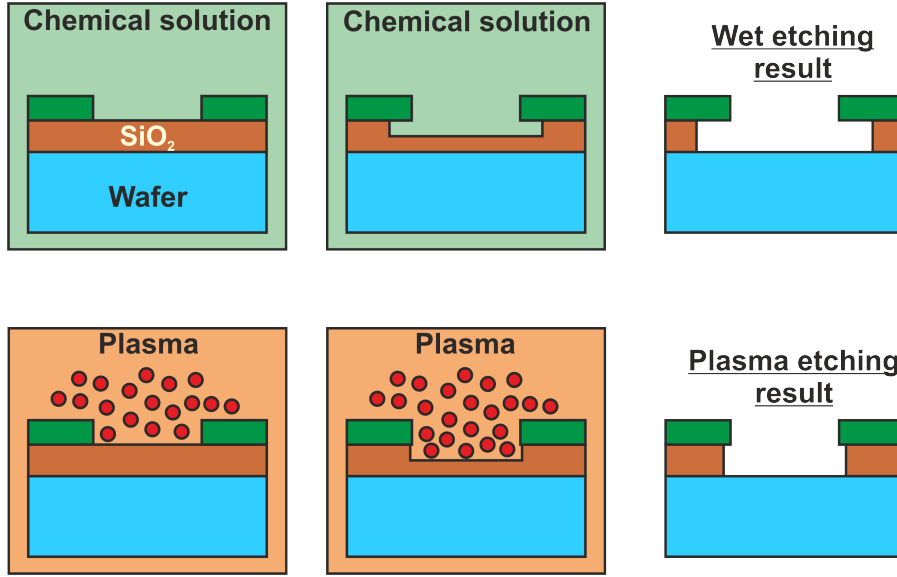


FIGURE 3.16: schematic of how the lateral etch changes from wet to plasma etching.

Conversely, wet etching is always picked for the metal layer. On one hand, the chemicals used for aluminum and copper etching are well studied, so they are extremely selective. That is, the damage to the underlying silicon or oxide is highly reduced when compared to PE for metal. On the other hand, such chemicals are able to etch the $1.5\ \mu\text{m}$ of Al:Cu alloy with an exceptional etch rate (of the order of $\sim 1\ \text{min}$). Moreover, even though lateral etch always takes place in wet etching, the areas where the metal is aimed to remain (guard ring and N^{++}) area large enough to consider this effect negligible.

3.4 Fabrication process of pixelated LGAD detectors

Now that we have addressed in detail how to fabricate a single-pad LGAD, we can extend the discussion to a pixelated one. For the seek of simplicity, we would consider a matrix of 2×2 LGAD pixels (Figure 3.17). As discussed in section 2.3.3, LGADs with a pixel array are the backbone technology for some high energy physics experiments. This will be comprehensively covered in Chapter 5.

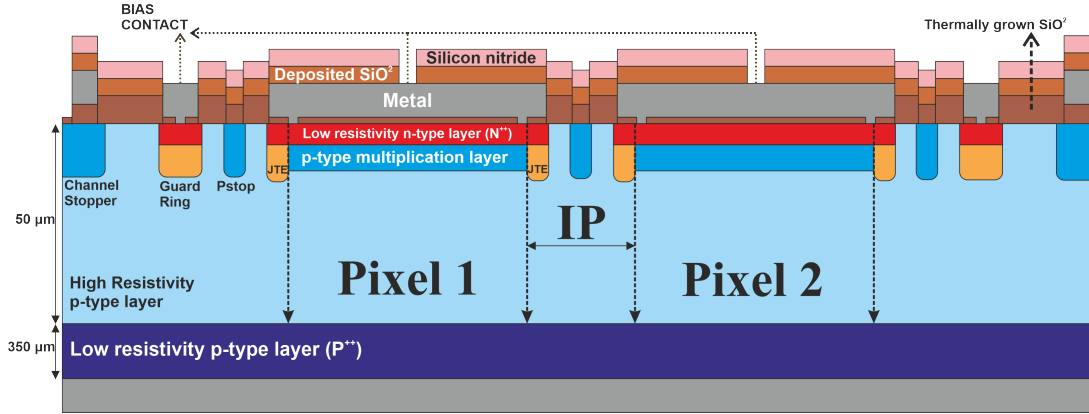


FIGURE 3.17: Cross section of a detector of 2 x 2 LGAD pixels.

In essence, the periphery elements and the photolithographic steps for a pixelated LGAD (Figure 3.18) are the same as in the case of a single pad. The only difference is that now we have a new region to consider for optimization: the interpad (IP), defined as the distance between the multiplication region in adjacent pixels. In order to understand the importance of the IP region, we need to introduce the *fill factor* concept. In the context of LGADs, it is defined as the ratio between the active area where the multiplication layer takes shape and the total active area. In other words, the fill factor is the percentage of LGAD active area able to provide gain in a particle detection measurement. Ideally, one would want to have a fill factor of 100%, but such goal is impossible when fabricating pixelated detectors as the ones depicted in Figures 3.17 and 3.18, as it will lead to having a single-pad LGAD. While there are other LGAD fabrication techniques that lead to pixelated detectors with 100% fill factor, this discussion will be left for Chapter 7. Studies on how the IP region design has an impact on an LGAD performance can be found in [25], [50]–[52]. Its main features are reviewed in this section.

In regard to the detector stability during operation, a limitation when shortening the IP distance to optimize fill factor is found. If the p-stop is too close to the JTE surrounding the active area of adjacent pixels, a leakage current channel is formed between these periphery elements that lead to an early breakdown of the detector. The phenomenon responsible for such event is known as *punch-through* [53]. In a nutshell, its mechanism is as it follows. The electric field existing between the JTE and the p-stop increases as both the doping concentration of the bulk and the IP distance decrease. This unavoidably lead to an early breakdown of the device if such electric field value is sufficiently high so a large leakage current can flow through the IP surface. Increasing the doping concentration of the high-resistivity layer wafer would be counterproductive to avoid this problem since, for particle detection applications, we need a bulk that "easily" depletes of charge with a relatively low reverse bias. This leaves us with the IP distance as the parameter to enlarge to elude punch-through. Studies about that were reported in [50], [52], finding safe operational bias ranges (far from breakdown) for pixelated LGADs when $IP \geq 30 \mu\text{m}$.

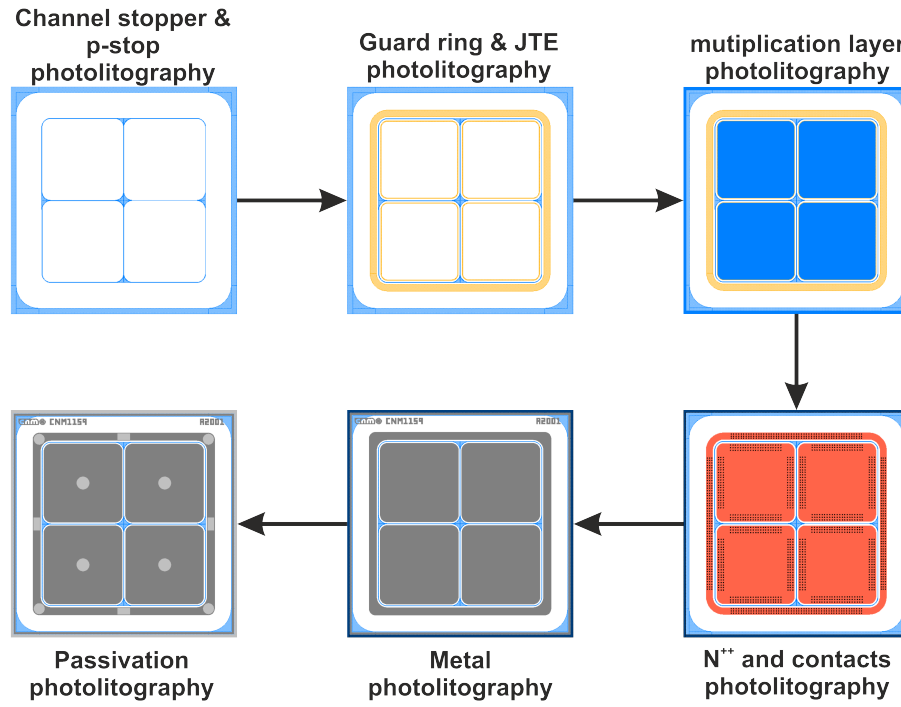


FIGURE 3.18: schematic of the photolithographic steps for the manufacturing of a detector of 2×2 LGAD pixels.

The stability during operation is not the only concern when optimizing the IP region. Even though an early breakdown of the LGAD can be avoided with an IP distance of about $30 \mu\text{m}$, some charge carriers may still punch through from the JTE to the p-stop, generating spurious signal-like pulses that increase the baseline noise level and degrade the particle detection measurement. This is known as *popcorn noise* [50] and is strongly dependent on the IP distance. As a case in point, IMB-CNM LGADs with an IP of $47 \mu\text{m}$ were tested before and after being irradiated, founding high levels of popcorn noise before their breakdown voltage in both cases [51]. In addition, an increase in the boron concentration peak in the p-stop layer also enhances the punch-through effect [52]. Reducing such boron peak during fabrication may look like a plausible solution to avoid this issue. However, for devices thought to be operated in harsh radiation environments, it can be counterproductive. This is due to the aforementioned radiation-induced effect, that generates a n-type conductivity layer by the $\text{SiO}_2\text{-Si}$ interface. That is, if the p-stop boron concentration peak is too low, the IP region may invert from p to n-type during irradiation, short-circuiting adjacent pixels. Being all that set forth, one can conclude that the IP region needs to be carefully optimized for particle detection applications, so a good trade-off is found between fill factor, detector stability, popcorn noise and (avoiding) conductivity type inversion. This is an ongoing hot topic in the field of detector fabrication for HEP experiments (at the juncture when this thesis is being written) [52].

Refocusing on the subject of manufacturing pixelated LGADs of a certain array, the discussion presented in this section can be extended to any pixel array beyond a 2×2 matrix.

Chapter 4

Optimization of LGAD core using TCAD Sentaurus

4.1 Introduction

TCAD Sentaurus simulation is a powerful tool when testing the LGAD functionality before starting its fabrication. This was thoroughly studied in [13] and [25] to optimize all the periphery elements present in single-pad LGADs. A contribution of how to optimize and calibrate TCAD simulation for a good prediction of the LGAD core performance is presented in this chapter. Thus, from now on, just the active volume of the detector will be considered. Additionally, only 2D simulations will be addressed, as the inherent symmetry of the planar technology of LGADs allows for it.

4.2 TCAD Sentaurus simulation of dopant activation and diffusion in silicon

To understand the potential of TCAD in predicting the electrical behavior of an LGAD, we first need to halt for a bit to discuss how the layers that make up its core are formed during the fabrication process. These are the N^{++} and the multiplication layer (Figures 3.11, 3.12), which form the PN junction responsible of triggering the avalanche mechanism when the LGAD is reverse biased. As presented in the previous section, such layers are formed by ion implantation, that get further annealed to activate and diffuse its dopants in a certain manner. The steps that lead us to construct the core of a traditional IMB-CNM LGAD are listed below. This procedure was optimized in [13] and [25].

- Growth of a screen oxide of ~ 100 Å via thermal process (85 minutes at 950°C) during the multiplication layer photolithography level.
- Boron implantation at 100 keV, $1.9 \cdot 10^{13}$ at/cm^2 and 7° wafer tilt to avoid the channeling effect (Figure 3.7).
- Annealing of the implanted boron with a thermal process at 1100°C for 3 hours.
- Once again, growth of a screen oxide of ~ 100 Å via thermal process (85 minutes at 950°C) during the N^{++} layer photolithography level
- Phosphorus implantation at two different energies and doses: 70 keV and 10^{15} at/cm^2 , and 150 keV and $5 \cdot 10^{14}$ at/cm^2 . The wafer is also tilted 7° to avoid the channeling effect.

- Annealing of the implanted phosphorus with a thermal process at 1000°C for 30 minutes.

Figure 4.1 shows the TCAD Sentaurus simulation of the impurity concentration after the implantation and annealing processes for such traditional IMB-CNM LGAD core. It is important to notice that, while phosphorus for the N^{++} is only annealed once (30 minutes at 1000°C), boron for the multiplication layer suffers a few consecutive annealing steps: 3 hours at 1100°C (*Annealed Boron* in Figure 4.1 (A) and *Annealed Boron (1)* in Figure 4.1 (B)) and 84 minutes at 950°C plus 28 minutes at 1000°C (*Annealed Boron (2)* in Figure 4.1 (B)). As a result, one obtains an overlap of a n and p-type silicon layers which charges compensate around the PN junction to give a certain profile to the multiplication layer (Net Active in in Figure 4.1 (B)). As long as the device periphery is well optimized, it is precisely such net active doping profile that is responsible for determining the electrical performance of the LGAD core. The physical phenomena that gives shape to this impurities concentration during a thermal annealing are the dopant diffusivity and activation.

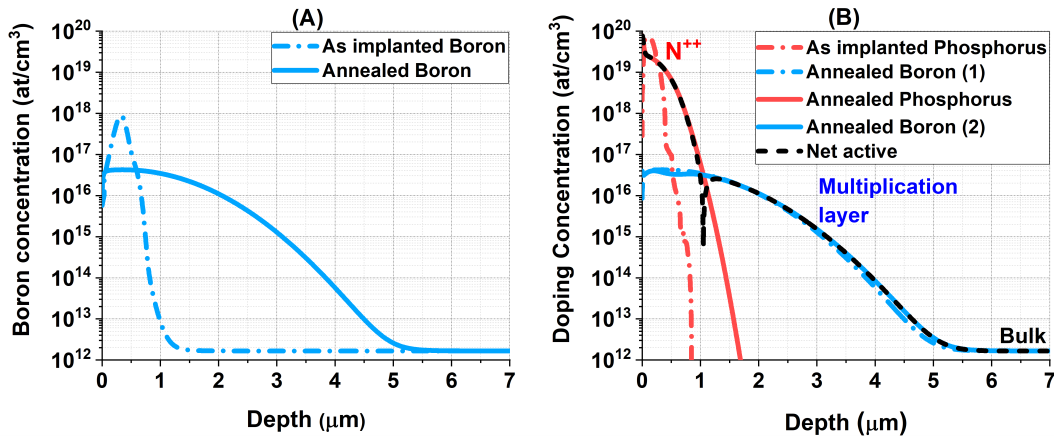


FIGURE 4.1: TCAD simulation of the net active doping concentration of an LGAD core.

Dopant diffusivity [54] refers to the ability of impurity atoms to move within the silicon lattice when subjected to high temperatures. This motion occurs as a consequence of the thermal energy provided to the wafer during the annealing process. The phenomenon is highly temperature-dependent, following an exponential relationship with it described as [54]–[56]:

$$\frac{\partial N_j}{\partial t} = D_j \exp\left(-\frac{E_j}{kT}\right) \frac{\partial^2}{\partial x^2} [n_{bulk}(x, t) N_j] \quad (4.1)$$

The solution of equation 4.1, where N_j is the active doping concentration of the species j (typically boron or phosphorus), k is the Boltzmann constant, T is the temperature, t is the time, n_{bulk} is the net number of charge carriers in the bulk and x is the depth in the silicon wafer, are strongly dependent on two parameters that are empirically obtained by fitting experimental data [54]–[56]. These are the *diffusivity pre-factor* D_j and the *activation energy* E_j of the species j . It is worth noticing that, if there is only one impurity diffusing into high-purity silicon, $n_{bulk}(x, t)$ can be approximated by the average doping concentration of the bulk, eliminating the dependence of this factor on time and depth. However, if two species of different

type are co-diffusing in silicon, as is the case during LGAD fabrication (Figure 4.1) $n_{bulk}(x, t)$ will be strongly dependent on time and space around the PN junction. To put it simply, the diffusion of boron through the LGAD fabrication will be subjected to the presence and amount of phosphorus (and viceversa) at any instant and depth during the annealing process, as both impurities are competing to move through activation sites.

On the other hand, *dopant activation* [54], [55] refers to the process by which dopant atoms become electrically active, contributing to the conductivity of the silicon layer where they are present. In order to do so, the impurity atoms need to locate (by diffusion) in lattice sites, such the aforementioned vacancies or interstitials, where they are able to ionize and contribute to the generation of charge carriers (electrons in the case of donors, and or holes in the case of acceptors). Regardless of the chosen annealing time and temperature, TCAD Sentaurus always assumes that 100% of the dopant atoms get activated. This approximation is very close to reality considering the temperatures and times involved in the IMB-CNM core fabrication process. Regarding diffusivity, TCAD Sentaurus features advanced calibrated models fitted with experimental data. However, these models are adjusted to diffusion processes carried out in clean-room equipment that are not those of IMB-CNM [56]. As a result, they do not accurately reproduce the electrical characterization of LGADs fabricated at the IMB-CNM, and adjustment and calibration of the models are necessary for TCAD Sentaurus to be a reliable prediction tool.

4.3 Optimization of the LGAD core design

A real example of a IMB-CNM traditional LGAD batch will be used in order to illustrate this fact. Such LGADs correspond to the 6LG2-v2 fabrication run, that will be extensively studied in Chapter 5. The detectors were manufactured on 150 mm Si-Si wafers with a 50 μm active thickness on 350 μm low resistivity handle wafer. Figure 4.2 shows the predicted leakage current and capacitance vs reverse bias, along with actual measurements, at 20°C, for 20 samples of the aforementioned LGAD batch. A quick look is enough to determine that none of the used Advanced Calibration versions of Sentaurus is able to reproduce the actual results.

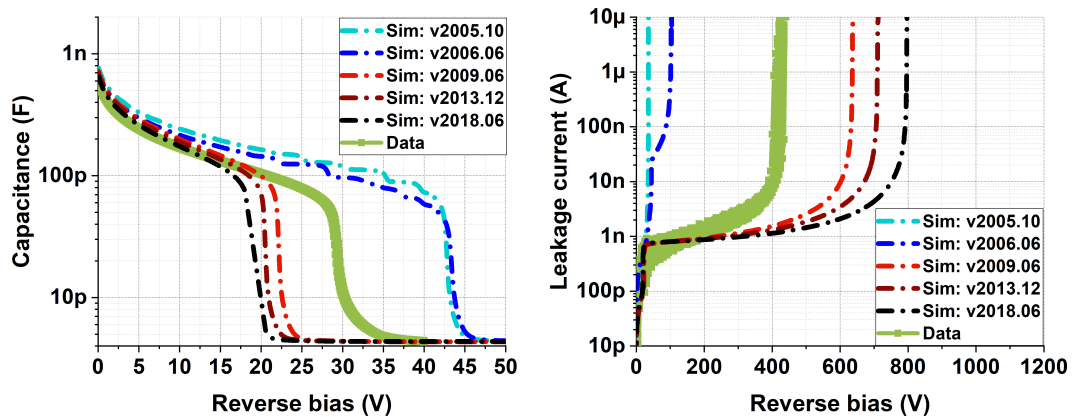


FIGURE 4.2: TCAD Sentaurus simulation prediction, for different Advanced Calibration version and at 20°C, of the IV and CV curves for LGADs of the 6LG2-v2 fabrication run.

Every one of such versions counts with a set of calibrated values for D_j and E_j (4.1), among many other parameters. They are listed in Table 4.1. As we may notice, E_B and E_P barely change from version to version, while D_B and D_P may suffer major changes. Phenomenologically, the activation energy has always been found to fit experimental data in a narrower range than the diffusivity pre-factor does. In the case of boron and phosphorus, values for E_B and E_P were reported in the range [3.25 - 3.87]eV and [3.3 - 3.7]eV, respectively [54]–[56], while values for both D_B and D_P may span within few orders of magnitude in the range [~ 0.01 - ~ 10]cm²/s [54]–[56]. Taking such fact into account, the calibration of diffusivity parameters with actual measurements was first approached by tuning the pre-factor. Additionally, it is important to point out the difference in the physical meaning attributed to both parameters. The activation energy represents the minimum thermal energy required for dopant atoms to migrate from one site in the silicon lattice to another, while the pre-factor is defined as the maximum diffusivity that such dopant can achieve when $T \rightarrow \infty$. In other words, while the activation energy represents a threshold, the pre-factor represents an asymptote.

Sentaurus Advanced Calibration - Diffusivity values				
Version	D_B (cm ² /s)	E_B (eV)	D_P (cm ² /s)	E_P (eV)
2005.10	0.297	3.57	0.453	3.482
2006.06	0.291	3.57	0.6	3.482
2009.06	0.123	3.57	1	3.55
2013.12	0.123	3.57	0.34	3.4
2018.06	0.123	3.57	0.23	3.35

TABLE 4.1: Diffusivity pre-factor and activation energy of boron and phosphorus for different Sentaurus Advanced Calibration versions.

Figure 4.3 shows a 2D sweep on the difference between the simulated and measured V_{gl} (depletion voltage of the multiplication layer), for IMB-CNM LGADs of the 6LG2-v2 fabrication batch, for values of $[D_B, D_P]$ in a subrange of the span reported in [54]–[56]. While a great deal of $[D_B, D_P]$ sets lead to Geiger (breakdown voltage $> V_{gl}$) or PiN behavior, a clear linear trend $D_B \propto D_P$ is observed, which values reasonably predict the measured V_{gl} . A selection of these $[D_B, D_P]$ are listed in Table 4.2. Furthermore, also the capacitance curves as a whole (and not only the V_{gl}) are well predicted for values within such linear trend, as Figure 4.4 shows.

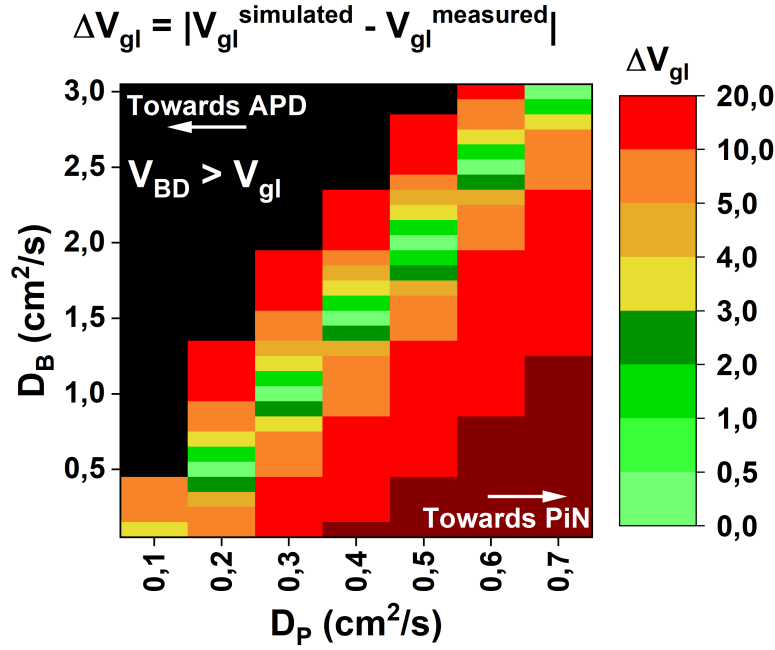


FIGURE 4.3: Color code mapping of the D_B , D_P sets that better fit the measured V_{gl} for IMB-CNM LGADs of the 6LG2-v2 fabrication batch.

A distinction on how a set of values $[D_B, D_P]$ can predict the V_{gl} (or the overall capacitance) and the V_{BD} (or the overall leakage current) is also highlighted in Figure 4.4. While different values of $[D_B, D_P]$ result in similar capacitance curves, the same is not true for leakage current and breakdown voltage V_{BD} . The nature of this effect can be understood by examining Figure 4.5.

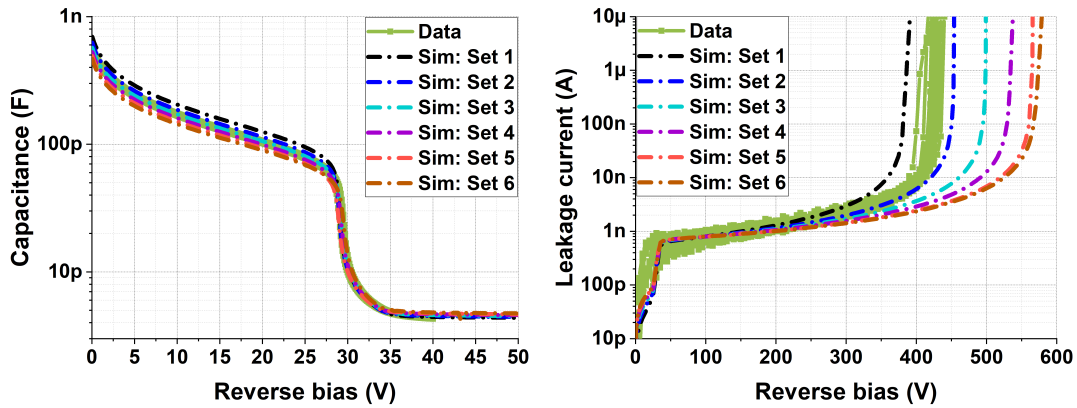


FIGURE 4.4: TCAD Sentaurus simulation prediction, for different diffusivity sets (listed in Table 4.2) and at 20°C, of the IV and CV curves for LGADs of the 6LG2-v2 fabrication run.

Sentaurus IMB-CNM Calibration - Diffusivity values				
Version	D_B (cm^2/s)	E_B (eV)	D_P (cm^2/s)	E_P (eV)
Set 1	0.5	3.57	0.2	3.35
Set 2	1.0	3.57	0.3	3.35
Set 3	1.51	3.57	0.4	3.35
Set 4	2.01	3.57	0.5	3.35
Set 5	2.48	3.57	0.6	3.35
Set 6	3.0	3.57	0.7	3.35

TABLE 4.2: Diffusivity pre-factor and activation energy of boron and phosphorus that predict the V_{gl} of CNM-6LG2-v2 LGADs.

On one hand, the depletion voltage of the multiplication layer depend on the trade between the peak of active boron and the width of such layer. As the diffusivity of the dopants increase (i.e. D_B or D_P increase), the peak of boron gets reduced which, in principle, should reduce the voltage at which the layer gets depleted. However, the increase in diffusivity is also translated into a widening of the multiplication layer, that raises the depletion voltage. As a result, a zero-sum outcome is obtained, and the V_{gl} is kept constant for different shapes of the multiplication layer. In Figure 4.5, the widths are calculated as the difference between the position of the PN junction and the position at which the doping concentration reach the bulk one.

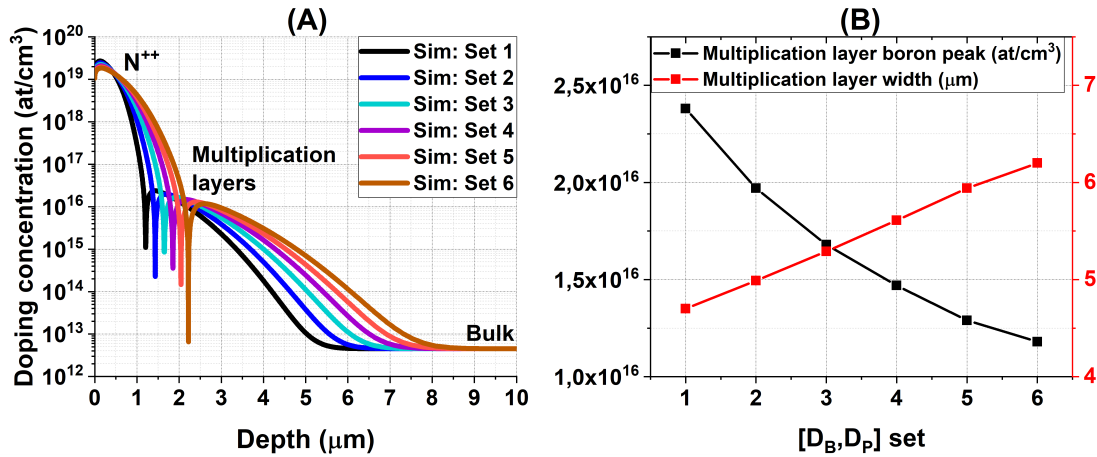


FIGURE 4.5: (A): Simulated doping profiles for the different $[D_B, D_P]$ sets listed in Table 4.2. (B): peak of active boron and width of the multiplication layer as a function of the $[D_B, D_P]$ set.

On the other hand, the charge integral of the multiplication layer (that is, the actual amount of net charge within it) do changes for every one of the $[D_B, D_P]$ sets, as Figure 4.6 shows. This has a direct effect on the electric field present around the PN junction when the detector is reverse biased: the higher the integral of charge, the higher the electric field for a given bias. As a result, the transition between linear and Geiger mode (e.g. the V_{BD}) is reached at a lower voltage for higher charge integrals.

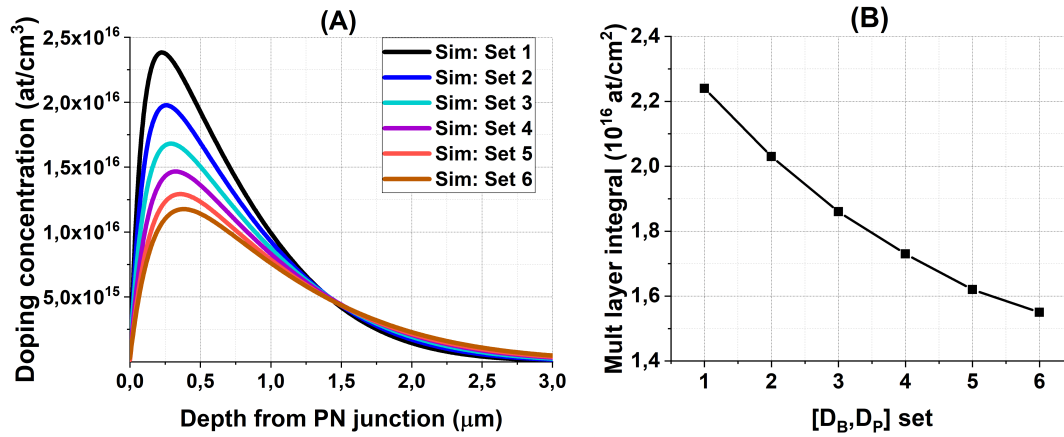


FIGURE 4.6: (A): Simulated boron concentration in the multiplication layer for the different $[D_B, D_P]$ sets listed in Table 4.2. (B): Charge integral of the multiplication layer as a function of the $[D_B, D_P]$ set.

Having discussed this, we may conclude that the breakdown voltage and the charge integral of the multiplication layer are directly related to the avalanche phenomenon. However, the V_{gl} is a geometric parameter that is not necessarily linked to the detector's gain. Thus, a fit of the diffusivity parameters with the CV measurements only tell us a part of the story. In order to properly calibrate simulation and reality, we need to have an idea of how the shape and the charge integral of the multiplication layer is. If our LGAD is modelled as a parallel plate capacitor, this information can be inferred from the capacitance vs reverse bias measurements as [57]:

$$N(w) = \frac{2}{e\epsilon A^2} \left[\frac{\partial(1/C^2)}{\partial V} \right]^{-1}; w = \frac{\epsilon A}{C} \quad (4.2)$$

where N is the doping concentration of the layers that get depleted in the parallel plate capacitor (the multiplication layer and the bulk for LGADs), w is the depletion width, A is the area of the capacitor, C is the capacitance, e is the electron charge and ϵ is the dielectric permittivity of silicon. It worth remarking that this approach does not allow us to know the depth or the doping concentration of phosphorus in the N^{++} layer, as it never gets depleted.

Figure 4.7 shows the average multiplication layer profile, extracted via Equation 4.2, for IMB-CNM LGADs of the 6LG2-v2 fabrication batch. The CV curves used to obtain the profiles are the ones depicted in Figure 4.4. Along with it, the simulated multiplication layer profiles for the $[D_B, D_P]$ sets listed in Table 4.2 are also shown. Both graphs display the same data but in linear scale and logarithmic scales. The profiles are scale in depth so the doping peaks are all shown at the same depth position.

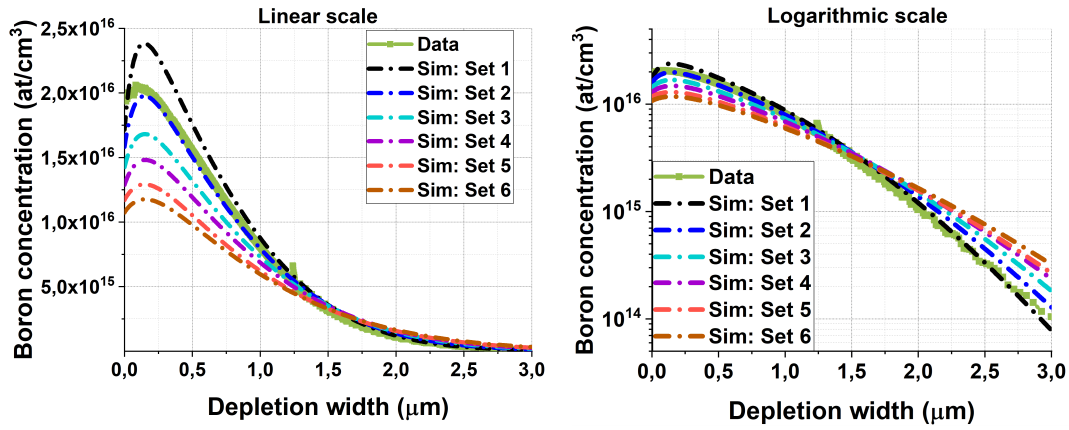


FIGURE 4.7: CV extracted boron profiles (via Equation 4.2) for LGADs of the 6LG2-v2 fabrication batch, shown along with the simulated profiles obtained via TCAD Sentaurus with the $[D_B, D_P]$ value sets listed in Table 4.2.

By examining how the simulated leakage current and doping profiles fit with the measured (Figure 4.4) and the CV-extracted ones (Figure 4.7), respectively, we may infer that a good prediction is likely to be obtained with a set of diffusivity parameters $[D_B, D_P]$ in between set 1 and set 2 (Table 4.2). A proper tuning of such parameters by following the color code map shown in Figure 4.3 gives away that the set $[D_B, D_P] = [0.82, 0.26] \text{ cm}^2/\text{s}$ is able to predict the V_{gl} , the breakdown voltage V_{BD} and the shape of the multiplication layer for IMB-CNM LGADs of the 6LG2-v2 fabrication batch. The results are shown in Figures 4.8 and 4.9.

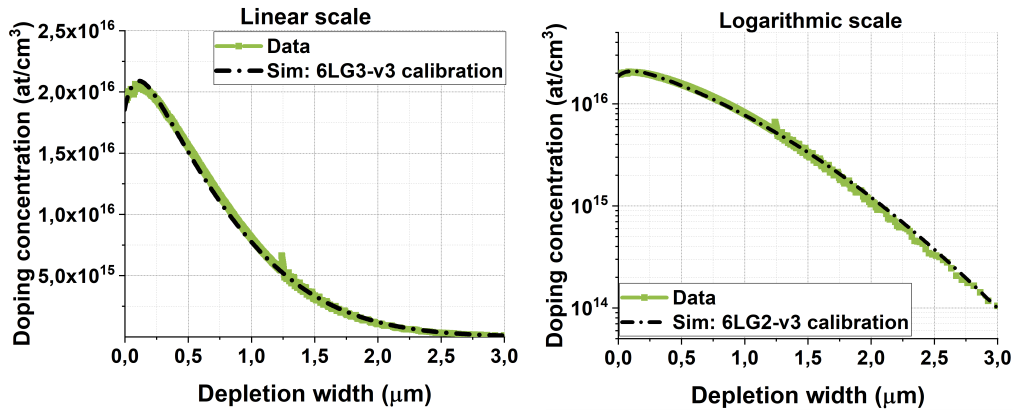


FIGURE 4.8: CV extracted boron profiles for LGADs of the 6LG2-v2 fabrication batch, shown along with the TCAD Sentaurus simulation obtained with the calibrated set $[D_B, D_P] = [0.82, 0.26] \text{ cm}^2/\text{s}$.

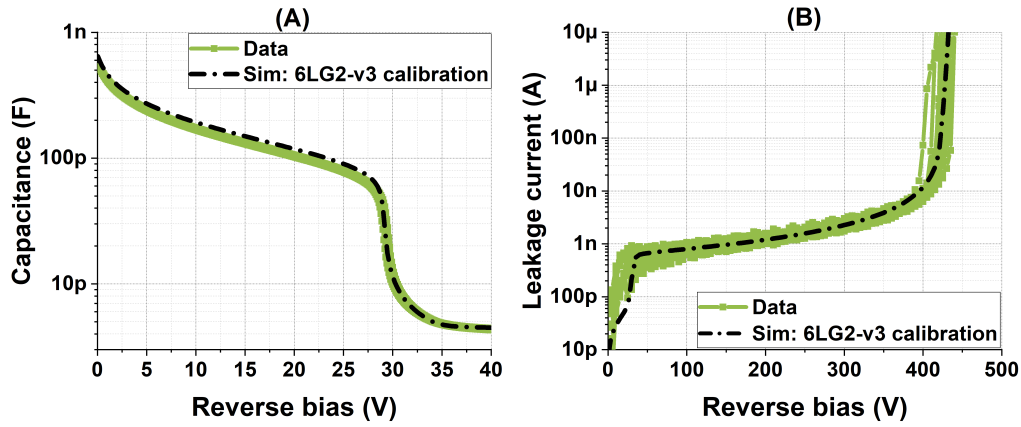


FIGURE 4.9: IV and CV measurements, at 20°C, for LGADs of the 6LG2-v2 fabrication batch, shown along with the TCAD Sentaurus simulation obtained with the calibrated set $[D_B, D_P]=[0.82, 0.26]cm^2/s$ and the Van Overstraeten - De Man avalanche model.

For the simulation of the leakage current and breakdown voltage V_{BD} , TCAD Sentaurus offers different avalanche models fitted with experimental data [56]. While each model may have added or scaled parameters, the avalanche phenomenon is modeled in each of them with the mathematical expression described in equation 2.1. That is, $\alpha_i \propto \exp(-\frac{\beta_i(T)}{E})$, where i refers to the charge carrier type (electrons or holes), E is the electric field at a given bias, $\beta_i(T)$ is a temperature dependent parameter, and α_i is the impact ionization rate, defined as the average number of electron-hole pairs that are created within the detector via avalanche mechanism by unit length.

In all the figures shown in this section, including the calibration displayed in Figure 4.9, the avalanche model used is the one by default in TCAD Sentaurus: the Van Overstraeten - De Man model. An overview of how such model was parameterized and fitted with experimental data can be found in [26]. Despite all avalanche models in Sentaurus follow the same qualitative behavior (e.g. the higher the boron peak in the multiplication layer, the lower the predicted V_{BD}), the Van Overstraeten - De Man model is the only one able to predict all the IMB-CNM experimental data presented in Figure 4.9. Moreover, the parameters of such model did not need to be tuned, as it was the case of the diffusivity model parameters. It is worth remarking that this is not a common occurrence, and typically the avalanche model parameters need tuning from its original fitted values in order to predict the behavior of LGADs. An great review of how this is done can be found in [58]. The difference between the fit of the avalanche parameters found in such studies and the one presented in this section (e.g. no fit) lies solely on the experimental data it was done through. While in both cases the starting point is a CV-extracted boron profile of the multiplication layer, in [58] such fit was done by using the measured gain response to IR light illumination under certain conditions, while in here we are just adjusting the breakdown voltage.

Having said all that, one may conclude that the fitted parameters in any simulation model (either diffusivity or avalanche) is always subjected to the experimental data we are trying to reproduce. In other words, TCAD Sentaurus is a tool that needs to be fed with data in order to give away a reasonable prediction of what to expect of future measurements of the same kind.

4.4 The importance of quality control during the fabrication process

The work presented in the previous section becomes meaningless if we do not know in advance certain parameters related to the manufacturing process. In particular for the LGAD core performance, the screen oxide prior implantation, the wafer thickness and the temperature ramps during the annealing steps are the most critical. As stated in section 3.3, the construction of the multiplication and N^{++} layers is done via ion implantation through a screen oxide of a certain thickness (typically of the order of 100 Å). The presence of the screen oxide helps to mitigate surface damage and the channeling effect, but it can also change the shape of the LGAD PN junction with dependence on its thickness. For the IMB-CNM LGADs of the 6LG2-v2 fabrication batch that were studied in the previous section, the average screen oxide thickness across the wafer was 206 Å for boron implantation (multiplication layer) and 105 Å for phosphorus implantation (N^{++}). Figure 4.10 shows how the doping profile, breakdown voltage at 20°C and V_{gl} for such IMB-CNM fabricated LGADs can change as a function of the screen oxide growth prior to the multiplication layer implantation when the one of the N^{++} is kept fixed at 105 Å.

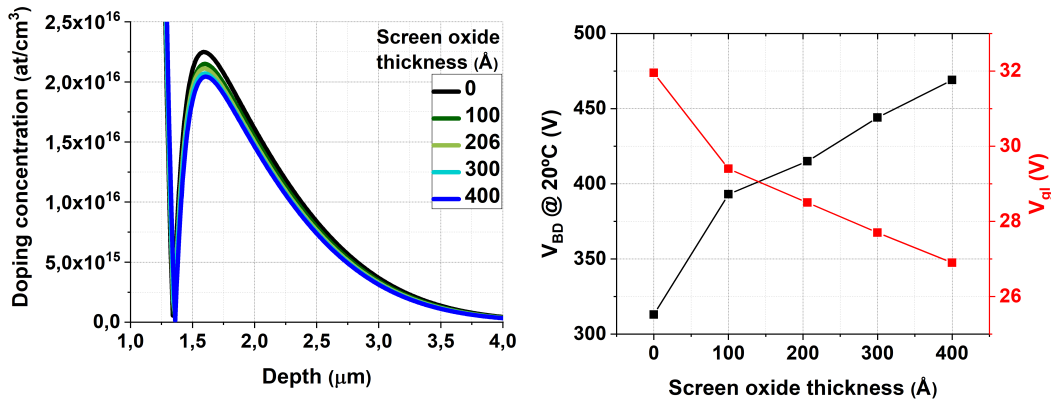


FIGURE 4.10: TCAD Sentaurus simulation of the doping profile, breakdown voltage at 20°C and V_{gl} for IMB-CNM LGADs of the 6LG2-v2 fabrication batch, as a function of the screen oxide growth prior to the multiplication layer implantation.

The simulation shown in Figure 4.10 (and all the upcoming in this subsection) was performed with the diffusivity calibrated set $[D_B, D_P] = [0.82, 0.26] \text{ cm}^2/\text{s}$ and the Van Overstraeten - De Man model avalanche model. Let us discuss the results in such figure.

Thicker screen oxide causes the implanted boron ions to lose more energy through it before they reach the silicon. Thus, their penetration depth into the bulk gets reduced or, in another words, the implanted boron ions will be more piled-up near the oxide-silicon interface for thicker screen oxide windows. As a result, the following annealing will lead to boron profiles that are more peaked near such oxide-silicon interface. Given this scenario, the subsequent implantation and diffusion of phosphorus (N^{++}) into the multiplication layer will neutralize the boron p-type effect in a greater extent, effectively reducing the peak of boron concentration around the

LGAD PN junction. In short, a thicker screen oxide for the multiplication layer implantation will reduce the boron peak of the further fabricated PN junction, hence reducing the V_{gl} and increasing the V_{BD} of the manufactured LGAD.

The opposite occurs in the case of the N^{++} layer implantation. As thicker screen oxides will stop the phosphorus ions closer to the wafer surface, the neutralization of the boron p-type effect is less pronounced in this case. As a result, a thicker screen oxide for the N^{++} will enhance the boron peak in the multiplication layer, hence increasing the V_{gl} and reducing the V_{BD} of the manufactured LGAD. This is depicted in Figure 4.11, where the screen oxide growth prior to the multiplication layer implantation was kept fixed at 206 Å while the one for the N^{++} was swept.

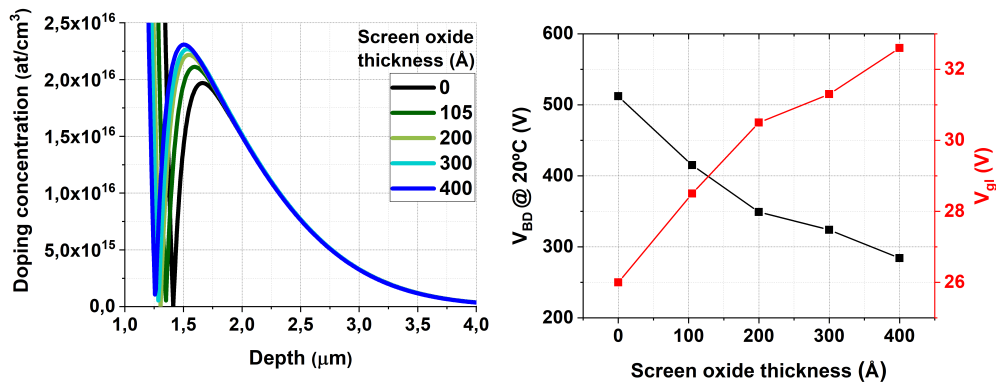


FIGURE 4.11: TCAD Sentaurus simulation of the doping profile, breakdown voltage at 20°C and V_{gl} for IMB-CNM LGADs of the 6LG2-v2 fabrication batch, as a function of the screen oxide growth prior to N^{++} layer implantation.

The thickness of the raw wafer (i.e. before fabrication) is also a key parameter to determine before planning the manufacturing process. As thinner detectors require a smaller bias to reach the same electric field intensity compared to thicker detectors, the first will tend to have a lower breakdown voltage than the latter when they are fabricated in the same way. This is shown in Figure 4.12.

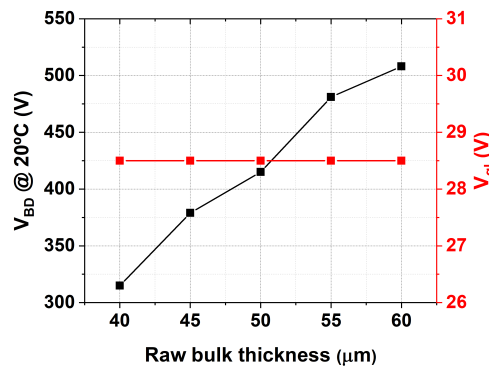


FIGURE 4.12: TCAD Sentaurus simulation of the breakdown voltage at 20°C and V_{gl} for IMB-CNM LGADs of the 6LG2-v2 fabrication batch, as a function of the high-resistivity layer thickness.

It is worth noticing that the V_{gl} , in contrast to the breakdown voltage, is not dependent on the high-resistivity layer thickness. The wafers used for the IMB-CNM 6LG2-v2 fabrication batch had an average high-resistivity bulk of $50\ \mu\text{m}$.

Throughout the chapter, we have been stating that the annealing processes are carried out for a certain temperature and time (i.e. the annealing of the multiplication layer, at 1100°C for 3h). Nevertheless, we have overlooked a very important detail about these processes, which are the time ramps for heating up and cooling down. The shape of the diffused PN junction is highly sensitive to such ramps, as implanted dopants will diffuse for longer or shorter depending on the time that it takes to reach the desired annealing temperature. This is depicted in Figure 4.13, where the ramp time to 1100°C for the multiplication layer annealing is evaluated vs the electrical performance of the manufactured LGAD. While every furnace may operate with specific ramps provided by the manufacturer, knowing them in advance is essential to make a good simulation prediction. The time ramp during the annealing of the multiplication layer for the IMB-CNM 6LG2-v2 fabrication batch was $10^\circ\text{C}/\text{min}$.

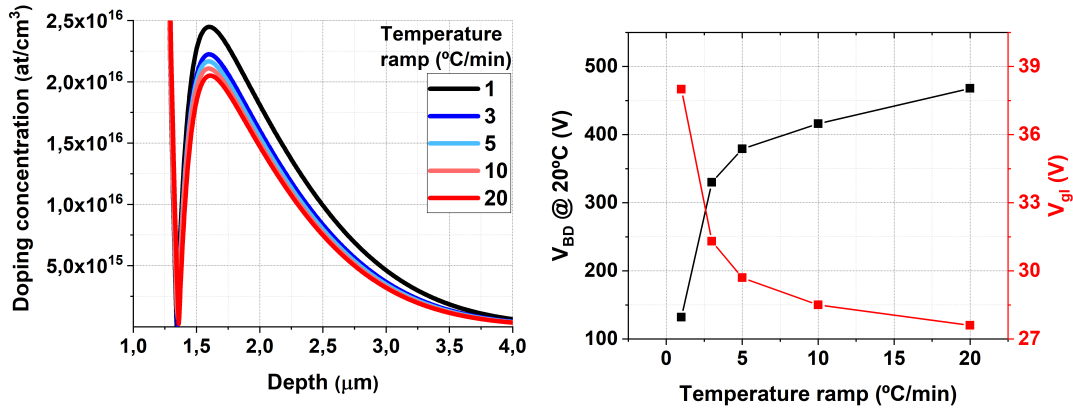


FIGURE 4.13: TCAD Sentaurus simulation of the doping profile, breakdown voltage at 20°C and V_{gl} for IMB-CNM LGADs of the 6LG2-v2 fabrication batch, as a function of time ramp to reach 1100°C in the multiplication layer annealing of 3h.

4.5 Future work on TCAD Sentaurus simulation

So far we have covered the means to calibrate TCAD Sentaurus simulation models for it to become a reliable prediction tool. However, it is worth highlighting that the content presented in this section is merely a first stepping stone for future work.

The furnaces at the IMB-CNM were replaced with new equipment during the period 2020-2022. As aforementioned, the tune of parameters included in physical models (e.g. diffusion) with experimental data is highly subjective to the fabrication conditions. In other words, we may empirically obtain the same result twice only if the same conditions are replicated twice. LGADs of the 6LG2-v2 batch have been the first manufactured with this new IMB-CNM furnace equipment and for which all the fabrication parameters stated in the last subsection are known. That is, the validation of the calibrated diffusivity parameters presented in Figures 4.8 and 4.9 will have to be tested with new LGAD productions fabricated in the same way as the 6LG2-v2 batch was. Moreover, LGADs from such batch were carbonated, a typical

technique for High Energy Physics experiments that will be discussed in the following chapter. For the moment, we will just point out that the addition of carbon within the PN junction alters the diffusivity of both boron and phosphorus through interstitials. Consequently, the diffusivity parameters tuned during Section 4.3 correspond only to those of boron and phosphorus diffusion through interstitial lattice sites. In the event of evaluating the electrical performance of LGADs via TCAD Sentaurus, the calibrated simulation shown in Figures 4.8 and 4.9 may be obsolete if either the devices are not carbonated or the implantation strategy for carbon is not identical as the one used for the 6LG2-v2 batch.

Lastly, not only the manufacturing conditions can determine the trustworthiness of an empirical tune of diffusivity or avalanche models. The sort and the conditions of the measurements to do so are also crucial. In particular, only leakage current at 20°C, capacitance and CV-extracted doping profile measurements were evaluated in the simulation calibration presented in the previous section. The availability of more data, such as gain response to different particle species, leakage current dependence on temperature or doping profiles extracted by other means different of CV-extraction may re-adapt such calibration for it to portray a more consistent prediction tool.

Chapter 5

LGADs for High Energy Physics experiments

5.1 Introduction

In Chapter 2, the importance of LGAD technology in the field of HEP experiments was briefly discussed. In this chapter, we will delve deeper into this topic, with special emphasis on how IMB-CNM fabricated LGADs have gradually improved their hardness for high-radiation environments. Before we get into it, it is worth to itemize the reasons why LGAD technology is highly valued for HEP experiments. It is important to note that all the enhancements listed below are attributed to an LGAD when its performance is compared with that of a standard PiN detector (see section 2.2).

LGADs employ the avalanche multiplication mechanism to increase the number of radiation-generated charge carriers, hence amplifying the output signal. Additionally, LGADs are designed to operate at a moderate gain (5-30), which minimizes the excess noise factor associated with higher levels of charge multiplication (e.g. APD-like detectors). Having an amplified radiation-generated signal without a striking noise increase results in an *improvement of the SNR*. In contrast, PiN detectors do not have this internal amplification mechanism, resulting in a lower output signal for the same incident radiation, which often cannot be resolved when compared to the noise contribution from external electronics.

As the SNR improves, so does the ability of an LGAD to precisely determine the location where particles interact, which leads to an enhancement of the *space resolution*. In another words, the chances of missing the signal that pinpoints the location (i.e. the pixel) of an interaction event within a pixelated LGAD are diminished when compared to a pixelated PiN detector.

Furthermore, the charge multiplication mechanism inherent to LGADs allows us to reduce the thickness of its active volume without compromising its SNR performance in a drastic manner. For instance, a typical LGAD has a thickness of $\simeq 50 \mu\text{m}$, while standard PiN detector are generally $300 \mu\text{m}$ thick. A reduced thickness of the detector allows a swifter collection of the radiation-generated charges as, in average, they have to cover less distance to the electrodes. Additionally, the high electric field present in an operational LGAD enables an acceleration of such charges, fastening the signal collection ever further. As a result, an improvement on the *time resolution* is obtained, which is a key parameter to avoid the pile-up phenomena between interaction events (see section 1.5).

Lastly, LGADs suppose a great improvement in terms of *radiation hardness*. It is worth emphasizing that, while there are strategies to further enhance it, LGADs are more radiation resistant than PiNs by very design. In order to understand why

is that so, we need to address the nature and effects of radiation damage in silicon detectors.

5.2 Radiation damage in LGAD and PiN detectors

As discussed in Chapter 1, the semiconductor properties of silicon make it one of the best candidates for particle detection applications, and its features can be fully understood in terms of the band theory of solids (see section 1.2). In short, it is the specific bandgap of silicon, along with the particular energy levels that certain impurities (such as boron or phosphorus) add within such bandgap, that make it effective to create PN junctions able to deplete and function as a radiation-generated signal collectors. These properties have its nature on how the silicon atoms, or its added impurity ones, arrange in the semiconductor crystalline lattice. If such arrangement is altered, the potential of silicon as a particle detector material may be drastically cut down. Its exposure to high levels of irradiation has this precise effect, as it induces physical changes in the crystalline lattice that lead to the degradation of the detector functionality. This phenomenon is the so-called *radiation damage*, and its main effects in an LGAD or a PiN performance are briefly discussed in this section. Typically, radiation damage is categorized in *bulk* and *surface* damage, understanding the first as the one suffered at the very silicon bulk and the latter as the one suffered at the interfaces of silicon with other materials (mainly at the SiO₂-Si interfaces). From a microscopic point of view, the nature of radiation damage is as it follows.

On one hand, bulk damage is caused by the collision of the incident radiation particles with the silicon atoms, displacing them from their regular sites in the crystalline lattice (the so-called *displacement damage*). Elastic nuclear collisions of impinging charged ions or neutrons with the silicon nuclei are the most damaging reaction for detectors [59], [60]. In a lesser extent, high energetic electrons may also displaced silicon atoms from its lattice sites. This high energy particles may be primary, understood as being the radiation aimed to be detected by the sensor, or secondary, as the products of another reaction occurring within the bulk of silicon under the incidence of primary radiation. A few examples are listed below, and a more comprehensive reading of the matter can be found in [59]–[61].

- *Remnants of inelastic nuclear reactions.* Light charged ions (typically protons and alpha particles) or neutrons may be absorbed by the silicon nuclei, generating unstable isotopes within the crystalline lattice. When they decay into a more stable isotope, other high energy particles are emitted within the silicon bulk, including protons, neutrons, alpha particles, electrons or even x and gamma-rays.
- *Remnants of gamma-ray reactions.* While silicon detectors are not generally used for gamma-ray detection (see Chapter), they can be generated in some inelastic nuclear reactions. The presence of gamma rays in the silicon bulk may trigger nuclear reactions that lead to the generation of other high energy particles, such as electron-positron pairs, neutrons, protons or alpha particles.
- *Ejected electrons from x-ray absorption.* As stated, some inelastic nuclear reactions lead to the emission of x-rays, that can be absorbed by electrons in an atomic orbit, that are in turn ejected from it. It is worth remarking that these electrons are often not energetic enough to trigger displacement damage in the lattice, so they typically represent a negligible contribution to bulk damage compared to the previous examples.

To summarize, **any impinging particle that has enough energy to displace a silicon atom from its position in the crystal lattice** (either directly, as in the case of protons or neutrons, or indirectly, as in the case of gamma rays) **is a source of bulk damage** for the detector. These displaced atoms are often referred in the literature as *defects* in the crystalline structure. In short, the main consequence of having a large number of radiation induced defects within the bulk is that the original high-quality silicon changes its band structure properties. In detail, it translates into several changes in the detector's electrical performance, whether we are talking about a PiN or an LGAD.

On the other hand, surface damage at the SiO₂-Si interface is caused by the same means of bulk damage. In particular, **it is due to the introduction of radiation-induced defects on it that act as acceptors** [44]–[47]. That is, such induced defects are traps for electrons, hence reducing the number of them within the interface and generating a layer of positive fixed charge on it. As a consequence, an electric field is created, which extends into the silicon beneath the oxide. In response to it, electrons accumulate in the silicon bulk close to the interface, generating an effective n-type conductivity layer all over the silicon surface. This phenomenon explains the need for p-stop or p-spray construction during LGAD fabrication for HEP experiments (see section 3.2). It is mandatory to point out that the aforementioned phenomenon can happen at the SiO₂-Si interface even in the absence of displacement damage within it. Such interface intrinsically has a higher density of acceptor-like defects [44], so any radiation, primary or secondary, capable of ionizing SiO₂ in a sufficient extent (e.g. x-rays) can lead to hole-trapping within it. In another words, displacement damage boosts the generation of a acceptor-like defects at the SiO₂-Si interface, with the subsequent creation of an n-type conductivity layer on the silicon surface. However, a certain density of such defects is always already present at the interface due to the very nature of it. As a result, any pixelated silicon detector (LGAD or PiN) built up on high-resistivity p-type silicon needs a p-stop or p-spray structure to assure isolation between pixels, as long as the sensor has a chance to be exposed to radiation able to ionize SiO₂.

Finally, it is worth mentioning that radiation damage in silicon is typically scaled to 1 MeV neutron equivalent (n_{eq} for short), that is, to the damage caused by fluxes of neutrons of 1 MeV. Such standard provides a consistent and comparative measure of the effects of different types and energies of radiation on silicon [60]. The reason of picking 1 MeV neutrons to scale the effects of radiation damage is not trivial but, historically, neutrons were one of the first types of radiation studied for its effects on materials and electronic devices, resulting in a large and comprehensive set of data, particularly around the 1 MeV range [62].

5.2.1 Leakage current increase

As discussed, the displacement damage caused by high-energy particles introduces mid-gap energy levels in the semiconductor energy band. This facilitates thermal excitation of charge carriers to the conduction band and increases the bulk leakage current of the devices. Such increase has been found to be quasi-linear with the irradiation fluence for PiNs [63]. However, the same does not always apply for LGADs. If the inner gain of the device is sufficiently high, the leakage current may decrease as a function of the irradiation fluence [64]. The reason behind that relies on a counterbalance between the radiation-induced increase in leakage current and the loss of gain by the same means. The physical phenomena behind this effect are the conductivity type inversion and the acceptor removal, which will be addressed

in the following subsections. On the other hand, the surface damage at the $\text{SiO}_2\text{-Si}$ interface also facilitates surface leakage current paths. However, its effects are less pronounced than bulk current if a p-stop or p-spray has properly been constructed during the LGAD fabrication (see section 3.2).

The drawbacks that the radiation-induced increase of leakage current cause on the devices are the following. The inner amplification mechanism inherent to LGADs aims to detect small signals generated by any impinging particle, which implies that a good SNR and timing resolution between events is crucial for its role. Since it contributes to the noise level, a high leakage current may reduce the possibility of distinguishing between the generated signal and the very noise. Thus, the lower the leakage current, the better the sensitivity of the detector. Also, the leakage current causes an impact on the power consumption of an LGAD. The higher it is, the more the power that is dissipated within the detector. As a result, an increase on heat generation takes place that might require supplementary cooling mechanisms over the extended periods that LGADs require to be operational during some HEP experiments.

5.2.2 Conductivity type inversion

Displacement damage can also cause conductivity type inversion in silicon by introducing the aforementioned midgap energy states. In short, high levels of irradiation may convert p-type silicon into n-type one and vice-versa, depending on the charge state of the introduced defects (acceptor or donor-like). While this effect depends strongly on the initial doping concentration of the silicon layers under irradiation, p-type to n-type inversion is less prevalent to occur than the other way around [45]–[47]. That is the reason why any LGAD meant to be used in harsh radiation environments is fabricated on p-type wafers. N-type to p-type inversion is more prevalent when silicon is irradiated primarily due to the nature of the defects created by the irradiation process and their interaction with the dopants in silicon. The key factors for this phenomenon are hereunder detailed.

Irradiation tends to introduce defects in the silicon lattice that act as acceptors [45]–[47]. That is, such defects act as traps for free electrons, thereby reducing the number of them within the semiconductor and effectively creating a p-type region. This is more effective in n-type silicon, where the majority carriers are electrons. Following that, the impinging high-energy particles can displace donor atoms (phosphorus) from their active lattice sites, neutralizing their donor effect. This results in a reduction of the donor concentration in n-type silicon, which decreases the number of free electrons, hence pushing the material towards p-type behavior even further.

In p-type silicon, acceptor atoms (boron) may also be displaced or neutralized by irradiation. This is the so-called *acceptor removal effect*, key phenomenon in LGADs for hard radiation environments. Nevertheless, the resultant defects from acceptor removal do not compensate in p-type silicon as effectively as they do for donor removal in n-type silicon. The reason behind that is a counterbalance between acceptors being neutralized (via boron-particle interaction) and acceptor-like defect states being created (via silicon-particle interaction).

5.2.3 Acceptor removal effect

Another known effect of high levels of irradiation in silicon sensors is the aforementioned *acceptor removal effect* [65], which is directly linked to the conductivity type

inversion phenomenon happening in the multiplication layer. As discussed in previous chapters, the high electric field that allows the charge multiplication mechanism in LGADs depends directly on the active doping concentration of boron in the multiplication layer. Thus, and even though such layer is so doped that hardly gets fully neutralized, a reduction of its active boron will straightforward cause a decrease on the achievable electric field for a given bias, hence degrading both the SNR and the timing performance of the device. In terms of their electrical performance, this effect will translate into an increase of the breakdown voltage and a decrease of the gain layer depletion voltage (V_{gl}) [64].

5.2.4 The role of carbon

From a physical standpoint, acceptor removal has its effects on the *interstitials-like defects* introduced in the crystalline lattice by displacement damage. In a nutshell, an interstitial site (either already existing in the lattice of radiation generated) are empty spaces between the regular lattice points where silicon atoms are usually located [55]. These sites can be occupied by another atom species that typically are smaller in size than the silicon atoms, as they can be arranged into the interstitial spaces without causing significant lattice distortion. As boron atoms are indeed smaller in size than silicon ones, a striking increase of interstitial-like defects by irradiation act as a trap for these acceptors, removing them for its substitutional active sites and neutralizing them by forming defects complexes, mainly within interstitial silicon or oxygen atoms naturally present in the lattice [65].

Carbonation of LGADs is a known technique to mitigate the acceptor removal effect [66]. Despite carbon being a neutral impurity for silicon (that is, it acts neither as an acceptor nor as a donor), its atoms, smaller in size than silicon's, compete with the boron ones when occupying the interstitials introduced within the multiplication layer by displacement damage [65]. Moreover, carbon can also interact with interstitial oxygen to compete with boron in the formation of the aforementioned defect complexes [65]. Therefore, implanting and diffusing a carbon layer alongside with the multiplication layer helps reducing the deactivation of boron during high irradiation experiments [66].

Conversely, the introduction of carbon on the active volume of an LGAD may imply an increase of the leakage current. This effect has a similar nature as irradiation at high energies. When present in high concentrations, carbon atoms alter the structure of the silicon lattice, introducing mid-gap levels that permit charge carriers to reach the conduction band. However, the mitigation of the acceptor removal effect by carbon addition can positively balance the reduction of the SRN and timing performance by increase of leakage current due to carbonation [67].

Furthermore, the silicon defects intrinsically introduced in the lattice by the very process of carbon implantation can serve as active sites for boron. This added effect, known as *carbon co-doping silicon amorphization* [68], allows boron to get activated in lattice sites closer to the surface of the detector, modifying the shape of the PN junction and enhancing the boron peak in the multiplication layer, hence amplifying the electric field of the LGAD at a given bias and the charge multiplication mechanism along with it.

Last but not least, it has been observed that, in carbon-implanted silicon, the diffusion of boron and phosphorus is altered during the manufacturing process. In particular, the presence of interstitial carbon within the lattice blocks one of the main diffusion paths for these dopants (their motion through empty interstitial spaces), forcing them to be activated in sites that are closer to the detector surface. This

effect is known as *carbon enhanced suppressed diffusion* [69], [70], and its outcome is a modification of the charge compensation between phosphorus and boron around the PN junction when diffusing. The displacement of the N^{++} layer towards the sensor surface allows for the boron partially buried behind it to get de-neutralize (Figure 5.1). As a result, the peak of boron in the multiplication layer is enhanced in the presence of carbon, hence increasing the electric field peak of the device around the PN junction for a given bias. The simulation in Figure 5.1 was carried out to replicate the fabrication of IMB-CNM LGADs of the 6LG2-v3 batch (Section 4.3). The effects of the carbon enhanced suppressed diffusion are clear for both dopants, which indicate that TCAD Sentaurus takes such phenomenon into account.

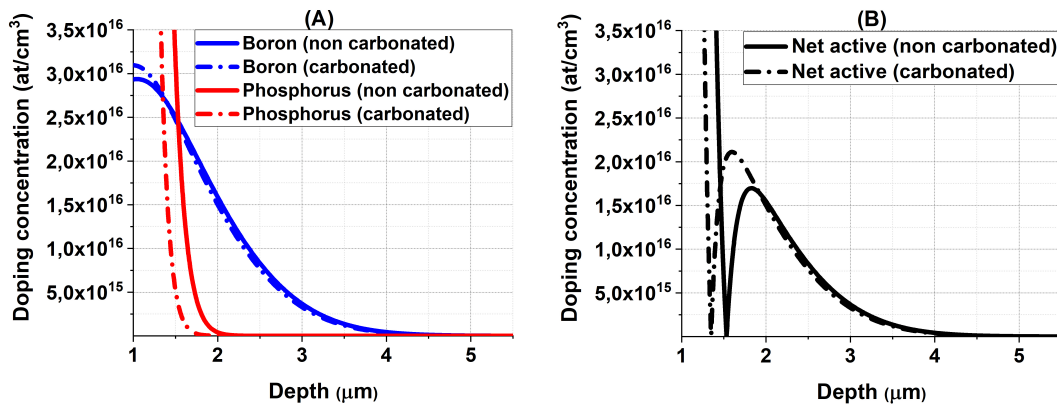


FIGURE 5.1: (A) TCAD Sentaurus simulation of the boron and phosphorus doping profiles around the PN junction, in a IMB-CNM fabricated LGAD, with and without the presence of a carbon layer. (B): Same as (A) but showing the net active doping profiles.

In summary, **implanting a carbon layer around the LGAD PN junction act as a mitigator for the acceptor removal effect inherent to irradiation.** In addition, the combination of carbon co-doping silicon amorphization and carbon enhanced suppressed diffusion results in having LGADs with a higher peak of boron in the multiplication layer, thus having a better performance in terms of charge multiplication.

LGADs with carbon co-doping have been the baseline for the ATLAS and CMS experiments phase-II upgrade at CERN, one of the biggest and more ambitious HEP experiments of the decade. The IMB-CNM has actively participated in the manufacturing of LGADs for such experiments under the RD50 collaboration [2]. Before getting into the fabrication and characterization of the IMB-CNM carbonated LGADs, let us first briefly discuss the main features of the ATLAS and CMS experiments phase-II upgrade.

5.3 The ATLAS and CMS experiments phase-II upgrade

The sought to answer questions about the origins of mass, the nature of dark matter, and the fundamental forces governing the universe led to the creation of CERN (Geneve, Switzerland) and the Large Hadron Collider (LHC), the world's most powerful particle accelerator [1]. Operative since 2008, it consist of a 27-kilometer ring where protons are accelerated close to the speed of light and then smashed together

in high-energy collisions. These collisions recreate conditions similar to those just moments after the Big Bang, allowing scientists to explore the fundamental components of matter.

Two of the flagship experiments designed to take on this zealous task are ATLAS (A Toroidal LHC ApparatuS) and CMS (Compact Muon Solenoid). The primary goal of ATLAS is the search for new particles (including the Higgs boson, discovered within this experiment in 2012 [29]) either within or beyond the Standard Model [1]. CMS focuses on similar scientific goals as ATLAS, and the differences between the two experiments relies mainly on their size and magnet type. On one hand, ATLAS is a largest experiment, being 46 m long and 25 m in diameter, while CMS is more compact, with a length of 21 m and a diameter of 15 m. On the other hand, ATLAS employs a toroidal magnetic field generated by eight large superconducting magnet coils arranged in a cylinder around the beamline, while CMS accelerates the protons using a magnetic field produced by a single large superconducting solenoid magnet [1].

Despite ATLAS and CMS were designed with different focuses, such differences make them complementary rather than one being better than the other. As a case in point, the larger size of ATLAS, particularly its extensive muon spectrometer, provides greater coverage and the ability to track muons more effectively over a larger volume. This can be particularly beneficial to identify certain types of particle decays that involve muons. Conversely, the more compact design and stronger magnetic field of CMS allow for more accurate measurements of charged particle momenta, which is crucial for many physics analyses, including detailed studies of radioactive decays and searches for new particles. Most importantly, having the same experiment with different designs allows for independent verification of results. Additionally, the differing designs mean that each experiment has its systematic uncertainties, so cross-checking results between ATLAS and CMS helps to identify and reduce them. A great example of this can be found in [71], where the uncertainty in the measurements of the top quark mass was highly reduced when combining ATLAS and CMS data.

Both experiments were constructed by international collaborations involving thousands of scientists, engineers, and technicians from institutions worldwide. One of them is the aforementioned RD50 collaboration [2], which started on 2001, years before the first operational date of the LHC, and finished on early 2024. It aimed to cope with the operational limits of standard silicon detectors to the harsh radiation environments inherent to the LHC particle energies and fluxes. In particular, part of the RD50 collaboration where the IMB-CNM has been involved with targeted to design, fabricate and test LGADs for the ATLAS and CMS phase-II upgrade [3], [4], which aimed at preparing these detectors for the High-Luminosity Large Hadron Collider (HL-LHC), set to start in the late 2020s'. In short, the HL-LHC will significantly increase the proton-proton collision rate (often referred to as *luminosity* in the literature) by a factor of ~ 10 [3], [4], allowing for more data to be collected in shorter times and enhancing the potential for discovering new physics.

Increasing the luminosity of the ATLAS and CMS experiments has two direct consequences on the silicon sensors composing the inner layers of the detector. On one hand, the radiation fluences that they have to suffer over the operational period of the experiment is increased. On the other hand, having a higher collision rate unavoidably raise the probability of pile-up during consecutive events. Overall, the challenges that silicon detectors have for the ATLAS and CMS experiments phase-II upgrade is the optimization of both their radiation hardness and timing resolution. In particular, the High Granularity Timing Detector (HGDT) [72] and the Endcap

Timing Layer (ETL) [73] of the ATLAS and CMS phase-II upgrade, respectively, are the ones where this chapter is entirely focus. They are schematically depicted in Figures 5.2 and 5.3

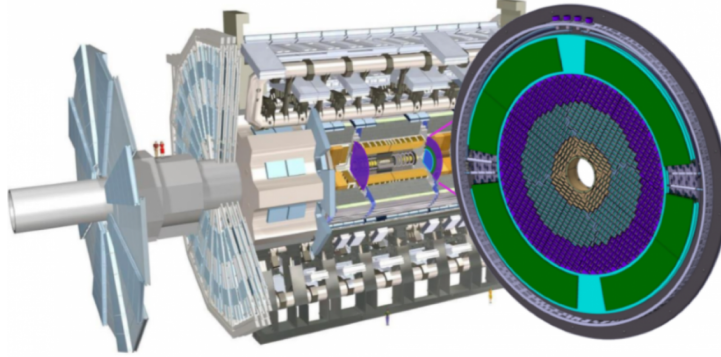


FIGURE 5.2: schematic of the HGDT within the ATLAS detector [72]

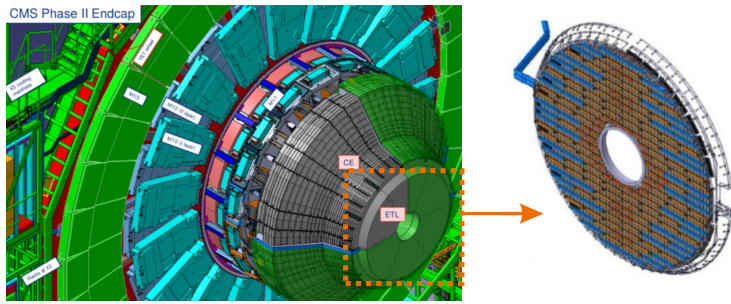


FIGURE 5.3: schematic of the ETL within the CMS detector [4]

Both the HGTD and the ETL are an arrange of timing sensors composing one of the innermost layers of the HL-LHC detection system (Figures 5.2 and 5.3). That is, such sensors are very close to the beamline, which translates into being the ones receiving most of the irradiation dose inherent to the experiment. Furthermore, the sensors within the HGTD and ETL disk that are closer to the beamline take the worst part, as the expected irradiation fluences for them exceed $10^{15} n_{eq}/cm^2$ [72], [73]. Although there are particular requirements depending on whether the LGAD will be integrated into the HGTD or the ETL, it is worth emphasising some general challenges common to both detectors.

- *Technology long-term reliability.* The fabricated LGAD must fulfil acceptable operational characteristics from the beginning to the end of the experiments. Before irradiation, LGADs have to maintain a good trade between their breakdown voltage V_{BD} and their full depletion voltage V_{FD} . This translates into having an operational voltage range (see section 2.3.3) large enough so the LGADs can function at the desired gain (i.e. desired Collected Charge or CC and timing resolution for a mip), at full depletion and at biases not very close to their breakdown voltage. During and after high irradiation fluences, the trade-off has to be maintained between the CC and timing resolution, both degraded due to the loss of gain via acceptor removal effect, and the maximum

operational voltage. Such maximum was consensually chosen as $11\text{ V}/\mu\text{m}$ (550 V for a $50\text{ }\mu\text{m}$ detector) [72], [73], far enough from the average electric field at which the Single Event Burnout (SEB) effect takes place. In short, SEB refers to a phenomenon where a single particle or ionizing event causes permanent damage or destruction of a pixel or localized region within the detector. This effect was observed to be particularly relevant for highly irradiated detectors [74].

- *Large scale manufacturing yield.* HGTD and ETL require pixelated LGAD detectors of relatively large area (of the order of $\sim 1\text{ cm}^2$) with an exceptional uniformity and yield of 100% (that is, without any malfunctioning pixel). This supposes an outstanding challenge from a technological standpoint, as maintaining uniformity across a large silicon detector is arduous. Variations in doping concentrations, layer thicknesses, and material properties can result in non-uniform performance or even local malfunction. Furthermore, pixels near the edges of the wafer are more prone to defects due to edge processing issues (e.g. the very handling of it).
- *Optimized fill factor.* For pixelated LGAD devices, the fill factor refers to the ratio of the active area, where avalanche multiplication occurs, to the total detector area. Ideally, a fill factor of 100% is desirable, but for traditional IMB-CNM pixelated LGADs as the ones described in Chapter 3 this is not possible. Periphery elements such as the guard ring and the JTE unavoidably take up area where the charge deposited by an impinging particle will not be multiplied. The interpad distance may indeed be optimized to reduce the non-multiplication area. Nevertheless, a good trade-off has to carefully be maintained between such distance and the appearance of the popcorn noise (see section 3.3). While there are innovative LGAD designs to achieve a 100% fill factor, they are not contemplated for the ATLAS and CMS experiments phase-II upgrade. Such designs will be addressed in Chapter 7.

The particular specifications for the HGTD and the ETL in terms of sensor geometry and electrical performance before and after irradiation (with 1 MeV neutrons) are presented in Table 5.1. **It is worth remarking that the specifications for the ATLAS HGTD and CMS ETL sensors have changed through the years, and those detailed in Table 5.1 are the most up to date (2023 for ATLAS and 2024 for CMS). For every LGAD run to be addressed in the chapter, the ATLAS HGTD and CMS ETL requirements will be specified for those applicable at the time of each fabrication batch completion.**

CMS ETL LGAD sensor specifications (May 2024)	
Geometrical sensor properties	
Active thickness D	$D = 55 \pm 5 \mu\text{m}$
Pad array	16x16 pixels
Pad size	$1.3 \times 1.3 \text{ mm}^2$
Interpad distance (IP)	$40 \mu\text{m} < IP < 70 \mu\text{m}$
Unirradiated sensors performance at 20°C	
V_{gl}	$20 \text{ V} < V_{gl} < 55 \text{ V}$
Full depletion voltage V_{FD}	$V_{FD} < V_{gl} + 10 \text{ V}$
Operation voltage V_{op} (definition)	$V_{op} > 180 \text{ V}$. Bias at which the sensor provides 15 fC of CC for a mip
Breakdown voltage V_{BD}	$V_{BD} < 330 \text{ V}$
Maximum voltage of operation V_{MaxOp}	$V_{op} + 30 \text{ V} < V_{MaxOp} < V_{BD} - 10 \text{ V}$
Pad leakage current	$I_{pad} < 200 \text{ nA}$ up to V_{MaxOp}
Total leakage current	$I_{Tot} < 20 \mu\text{A}$ up to V_{MaxOp}
Time resolution at V_{op}	$< 50 \text{ ps}$
Time resolution at V_{MaxOp}	$< 40 \text{ ps}$
Irradiated sensors at $1.5 \cdot 10^{15} \text{ n}_{eq}/\text{cm}^2$ and -25°C	
Maximum voltage of operation V_{MaxOp}	$V_{MaxOp}/D < 11 \text{ V}/\mu\text{m}$
Total leakage current at V_{MaxOp}	$I_{Tot} < 400 \mu\text{A}$
CC at V_{MaxOp}	$> 8 \text{ fC}$
Time resolution at V_{MaxOp}	$< 50 \text{ ps}$
ATLAS HGTD LGAD sensor specifications (May 2023)	
Geometrical sensor properties	
Active thickness D	$D = 50 \pm 5 \mu\text{m}$
Pad array	15x15 pixels
Pad size	$1.3 \times 1.3 \text{ mm}^2$
Interpad distance (IP)	$IP = 50 \pm 10 \mu\text{m}$
Unirradiated sensors performance at -30°C	
V_{gl}	$V_{gl} < 60 \text{ V}$
Full depletion voltage V_{FD}	$V_{FD} < V_{gl} + 90 \text{ V}$
Operation voltage V_{op} (definition)	$V_{op}/D < 11 \text{ V}/\mu\text{m}$. Bias at which the sensor provides $> 10 \text{ fC}$ of CC for a mip
Maximum voltage of operation V_{MaxOp}	$V_{MaxOp}/D = 11 \text{ V}/\mu\text{m}$
Breakdown voltage V_{BD}	$V_{BD} > V_{FD} + 30 \text{ V}$. $(V_{BD} - V_{gl})/D > 0.7 \text{ V}/\mu\text{m}$
Pad leakage current	$I_{pad} < 200 \text{ nA}$ at V_{op}
Total leakage current	$I_{Tot} < 2 \mu\text{A}/\text{cm}^2$ at V_{op}
Time resolution at V_{op}	$< 40 \text{ ps}$
Irradiated sensors at $2.5 \cdot 10^{15} \text{ n}_{eq}/\text{cm}^2$ and -30°C	
Maximum voltage of operation V_{MaxOp}	$V_{MaxOp}/D < 11 \text{ V}/\mu\text{m}$
Total leakage current for $D = 50 \mu\text{m}$	$I_{Tot} < 160 \mu\text{A}/\text{cm}^2$
CC at $V < V_{MaxOp}$	$> 4 \text{ fC}$
Time resolution at $V < V_{MaxOp}$	$< 50 \text{ ps}$

TABLE 5.1: Technical and geometrical specifications for the CMS ETL and ATLAS HGTD LGAD sensors

5.4 Review of previous IMB-CNM LGAD runs

Prior to the beginning of this thesis, three LGAD fabrication runs for the ATLAS HGTD and CMS ETL phase-II upgrade were manufactured at the IMB-CNM within the scope of the RD50 collaboration. The electrical performance of such LGADs was extensively studied in [25], [75]–[78] and a brief review of its main results is given in this section. The technology code for every LGAD manufacturing batch will read as $x_1LGx_2 - vx_3$, where x_1 is the size in diameter of the raw wafer (4 for 4 inches or 100 mm and 6 for 6 inches or 150 mm), x_2 labels the type of wafer (1 for thick FZ wafers, 2 for Si-Si and 3 for epitaxial wafers) and x_3 indicates the number of times that the run was produced under the previous conditions (e.g. the version of it). The different IMB-CNM LGAD fabrication batches and their technology code can be found in Appendix A.

Additionally, the measurements of the CC and time resolution for a mip presented in this section were carried out at the Institut de Física d'Altes Energies (IFAE, Barcelona) and the Instituto de Física de Cantabria (IFCA, Santander) with a radioactive Sr-90 source. All the data shown in this section's tables and figures was extracted from [25], [75]–[78]. In particular, the methodology to infer such data can be found in [77], [78].

5.4.1 Non-carbonated IMB-CNM LGADs

The first LGAD fabrication run for the ATLAS HGTD and CMS ETL upgrade was the 4LG2-v2 batch, fabricated on 100 mm high-resistivity p-type Si-Si wafers. It was followed by the 6LG3-v1 batch, fabricated on 150 mm high-resistivity p-type epitaxial wafers. Both LGAD productions are extensively studied in [25], [77]. The 4LG2-v2 run mask was composed of single-pad and pixelated structures, while the 6LG3-v1 one was solely comprised of single-pad LGADs. Nevertheless, the characterization to determine the reliability of the productions to fulfill the ATLAS HGTD and CMS ETL requirements was carried out on single-pad LGADs only. As previously mentioned, the ATLAS HGTD and CMS ETL sensors specifications have changed through the years, so the 4LG2-v2 and 6LG3-v1 runs were targeted to fulfilled the official requirements by the time of their manufacturing. Table 5.2 shows a compilation of such specifications, along with a summary of the characterization of single-pad LGADs from the 4LG1-v2 and 6LG3-v1 runs.

Let us discuss the overall results shown in such tables. On one hand, 4LG2-v2 devices turned to have a very narrow operational voltage range as produced. Their V_{FD} was about 42 V, while their breakdown voltage at the temperature fixed by the experiments was just a few volts above V_{FD} (≈ 55 V at -25°C and ≈ 50 V at -30°C). This excluded the detectors from fulfilling the requirements before irradiation for both ATLAS HGTD and CMS ETL. On the other hand, 6LG3-v1 sensors turned to fulfill all specifications before irradiation for both experiments. In short, the 4LG2-v2 devices had such high inner gain that they were not functional before irradiation, whereas the 6LG3-v1 sensors exhibited a moderate inner gain that allowed them to be operational as produced. However, neither of the fabricated LGADs was radiation-hard enough to be functional at the high fluences expected at the end of the experiments lifespan. Such result highlighted that **increasing the inner gain of LGADs up to operational limits as produced (as the case of 4LG2-v2) was not a methodology that helped mitigate the radiation damage to a greater extent**. In fact, the operational voltage (V_{op}) at high fluences differed only ≈ 100 V for both runs and experiments, while such difference was >250 V before irradiation. By then, studies

had already reported an enhancement in LGAD radiation resistance by carbonation. [79]. Consequently, the next IMB-CNM fabrication run for the ATLAS HGTD and CMS ETL started to investigate the effects of carbonation to mitigate the radiation damage.

CMS ETL specifications (2021)		4LG2-v2	6LG3-v1
Geometrical sensor properties			
Thickness D (μm)	45 – 65	40	55
Pad size (mm^2)	1.3x1.3	1.3x1.3	1.3x1.3 & 3.3x3.3
IP (μm)	≤ 80	47 & 57	47
Unirradiated sensors performance at -25°C			
V_{gl} (V)	< 60	38	30
V_{FD} (V)	$V_{FD} < V_{gl} + 10$	42	34
V_{op} (V)	8 fC for a mip	≈ 45	300
V_{BD} (V)	$> V_{op} + 30$	55	380
Time resolution at $V < V_{BD} - 30$ V	< 50 ps	Fulfilled but $V < V_{BD} - 30$ V	Fulfilled at $V_{op} = 300$ V
Pad leakage current (nA)	$I_{pad} < 200$	~ 10	~ 10
Irradiated sensors at $1.5 \cdot 10^{15} \text{ n}_{eq}/\text{cm}^2$ and -25°C			
V_{op} (V)	8 fC for a mip	< 700	≈ 800
V_{op} requirement	$V_{op} < 11(V/\mu\text{m}) \cdot D$	Not fulfilled	Not fulfilled
Time resolution at V_{op}	< 50 ps	Fulfilled but $V_{op} > 11D$	Fulfilled but $V_{op} > 11D$
ATLAS HGTD specifications (2023)			
Geometrical sensor properties			
Thickness D (μm)	$D = 50 \pm 5$	40	55
Pad size (mm^2)	1.3x1.3	1.3x1.3	1.3x1.3 & 3.3x3.3
IP (μm)	50 ± 10	47 & 57	47
Unirradiated sensors performance at -30°C			
V_{gl} (V)	< 60	38	30
V_{FD} (V)	$V_{FD} < V_{gl} + 90$	42	34
V_{BD} (V)	$> V_{op} + 30$	50	375
V_{op} (V)	10 fC for a mip	≈ 45	340
V_{op} requirement	$V_{op} < 11(V/\mu\text{m}) \cdot D$	Fulfilled but $V_{op} < V_{BD} - 30$	Fulfilled.
Time resolution at V_{op} (ps)	< 40	50	32
Pad leakage current (nA)	$I_{pad} < 50$	~ 10	~ 10
Irradiated sensors at $2.5 \cdot 10^{15} \text{ n}_{eq}/\text{cm}^2$ and -30°C			
V_{op} (V)	4 fC for a mip	≈ 680	≈ 750
V_{op} requirement	$V_{op} < 11(V/\mu\text{m}) \cdot D$	Not fulfilled	Not fulfilled
Time resolution at V_{op}	< 50 ps	Fulfilled but $V_{op} > 11D$	Fulfilled but $V_{op} > 11D$

TABLE 5.2: Technical and geometrical specifications for the CMS ETL (2021) and ATLAS HGTD (2023) sensors, along with the characterization of 4LG1-v2 and 6LG3-v1 detectors [25], [77].

5.4.2 Carbonated IMB-CNM LGADs

The first carbonated LGAD run for the ATLAS HGTD and CMS ETL phase-II upgrade was fabricated at the IMB-CNM on 150 mm high-resistivity p-type epitaxial wafers (6LG3-v2 technology). An extensive review of this run can be found in [25], [75], [78]. 6LG3-v2 devices had its multiplication and N^{++} layers constructed with the same implantation and annealing strategy as for the 6LG3-v1 detectors previously discussed. Thus, the idea for this run was to replicate the good results of the 6LG3-v1 sensors before irradiation (Table 5.2) while studying the radiation hardness introduced by the addition of a carbon layer covering the multiplication layer. Also, it is important to point out that the 6LG3-v2 was the first LGAD batch fabricated with the new furnaces installed at the IMB-CNM clean-room by 2022 (see section 4.5). Thus, **this the ATLAS-CMS 6LG3-v2 was also an engineering run that helped to calibrate manufacturing results of the new equipment in compared to the old one.** While many LGAD wafers were introduced in this run, only two of them showed a reliable performance to be tested for the ATLAS HGTD and CMS ETL upgrade. Their fabrication features are detailed in Table 5.3.

	6LG3-v1	6LG3-v2	6LG3-v2 carbonated
Carbon implantation dose in multiplication layer (10^{14} at/cm^2)	-	-	1
Carbon implantation energy in multiplication layer (keV)	-	-	150
Boron implantation dose in multiplication layer, implanted after carbon (10^{13} at/cm^2)	1.9		
Boron implantation energy in multiplication layer, implanted after carbon (keV)	100		
Annealing of boron (and carbon) in multiplication layer	180 min at 1100°C		
Phosphorus implantation dose in N^{++} (10^{14} at/cm^2)	5 & 10		
Phosphorus implantation energy in N^{++} (keV)	150 & 70		
Annealing of phosphorus in N^{++}	30 min at 1000°C		
Screen oxide for all implantations (Å)	~100		

TABLE 5.3: Fabrication features for the 6LG3-v1 and 6LG3-v2 LGAD runs.

The 6LG3-v2 mask contained pixelated structures required for the ATLAS HGTD and CMS ETL upgrade (e.g. 15x15 and 16x16 pixels of $1.3 \times 1.3 \text{ mm}^2$) but, as in the 4LG2-v2 and 6LG3-v1 case, the characterization was carried out solely on single-pad devices. This is shown in Table 5.4.

CMS ETL specifications (2021)		6LG3-v2	6LG3-v2 (carbonated)
Geometrical sensor properties			
Thickness D (μm)	45 – 65	55	55
Pad size (mm^2)	1.3x1.3	1.3x1.3	1.3x1.3 & 3.3x3.3
IP (μm)	≤ 80	57	57
Unirradiated sensors performance at -25°C			
V_{gl} (V)	< 60	29	30
V_{FD} (V)	$V_{FD} < V_{gl} + 10$	33	34
V_{op} (V)	8 fC for a mip	≈ 180	≈ 180
V_{BD} (V)	$> V_{op} + 30$	350	300
Time resolution at $V < V_{BD} - 30$ V	< 50 ps	Fulfilled at $V_{op} = 230$ V	Fulfilled at $V_{op} = 230$ V
Pad leakage current (nA)	$I_{pad} < 200$	< 1	< 1
Irradiated sensors at $1.5 \cdot 10^{15} \text{ n}_{eq}/\text{cm}^2$ and -25°C			
V_{op} (V)	8 fC for a mip	> 700	≈ 680
V_{op} requirement	$V_{op} < 11(V/\mu\text{m}) \cdot D$	Not fulfilled	Not fulfilled
Time resolution at V_{op}	< 50 ps	Not measured	Fulfilled but $V_{op} > 11D$
ATLAS HGTD specifications (2023)			
Geometrical sensor properties			
Thickness D (μm)	$D = 50 \pm 5$	55	55
Pad size (mm^2)	1.3x1.3	1.3x1.3	1.3x1.3 & 3.3x3.3
IP (μm)	50 ± 10	47	47
Unirradiated sensors performance at -30°C			
V_{gl} (V)	< 60	29	30
V_{FD} (V)	$V_{FD} < V_{gl} + 90$	33	34
V_{BD} (V)	$> V_{op} + 30$	350	300
V_{op} (V)	10 fC for a mip	≈ 220	≈ 220
V_{op} requirement	$V_{op} < 11(V/\mu\text{m}) \cdot D$	Fulfilled	Fulfilled.
Time resolution at V_{op} (ps)	< 40	Fulfilled at 260 V	Fulfilled at 260 V
Pad leakage current (nA)	$I_{pad} < 50$	< 1	< 1
Irradiated sensors at $2.5 \cdot 10^{15} \text{ n}_{eq}/\text{cm}^2$ and -30°C			
V_{op} (V)	4 fC for a mip	Not measured	≈ 700
V_{op} requirement	$V_{op} < 11(V/\mu\text{m}) \cdot D$	Not measured	Not fulfilled
Time resolution at V_{op}	< 50 ps	Not measured	Fulfilled but $V_{op} > 11D$
Acceptor removal constant c ($10^{-16}/\text{cm}^2$)	Not specified. The lower the better	8.25	4.95

TABLE 5.4: Technical and geometrical specifications for the CMS ETL (2021) and ATLAS HGTD (2023) sensors, along with the characterization of 6LG3-v2 detectors [25], [75], [77], [78].

As expected, both ATLAS HGTD and CMS ETL specifications were fulfilled for

non-irradiated 6LG3-v2 devices, regardless they were carbonated or not. An outcome to highlight is the low leakage current levels achieved in this run (< 1 nA per pad) when compared to the previous (~ 10 nA). While this upgrade in leakage current may be multifactorial, it is worth remarking that 6LG2-v2 sensors were manufactured in new furnaces, which are less likely to have particulate contamination from several years of previous processes.

On the other hand, the specifications after high levels of irradiation were not met for 6LG3-v2 detectors. Nevertheless, their radiation tolerance study brought with it some fundamental results. The first evidence of radiation resistance improvement by carbonation was inferred by studying how the V_{gl} dropped as the LGADs were irradiated with 1 MeV neutrons. It can be shown that $V_{gl}(\phi) \propto \exp(-c\phi)$ [80], being c the so-called acceptor removal constant and ϕ the 1 MeV neutron irradiation fluence. With independence on the as produced V_{gl} (e.g. before irradiation), the acceptor removal effect discussed in section 5.2 leads to a decrease of the original V_{gl} as ϕ increases. Thus, the determination of c gives an insight of the LGAD radiation hardness, as smaller values of c are translated into a mitigation of the acceptor removal effect. This was investigated in [25], finding that 6LG3-v2 devices had values of $8.25 \cdot 10^{-16}/\text{cm}^2$ (non-carbonated) and $4.95 \cdot 10^{-16}/\text{cm}^2$ (carbonated). Furthermore, it could be shown that the operation voltage for CMS ETL specifications (V_{op} at which 8fC of CC is reached for a mip) after irradiation was smaller if the LGAD was carbonated. This is displayed in Figure 5.4, where it can also be inferred that V_{op} at the target irradiation fluence ($1.5 \cdot 10^{15} n_{eq}/\text{cm}^2$) would lie closer to the upper voltage limit of $11(\text{V}/\mu\text{m}) \cdot D$ when the 6LG3-v2 LGAD is carbonated.

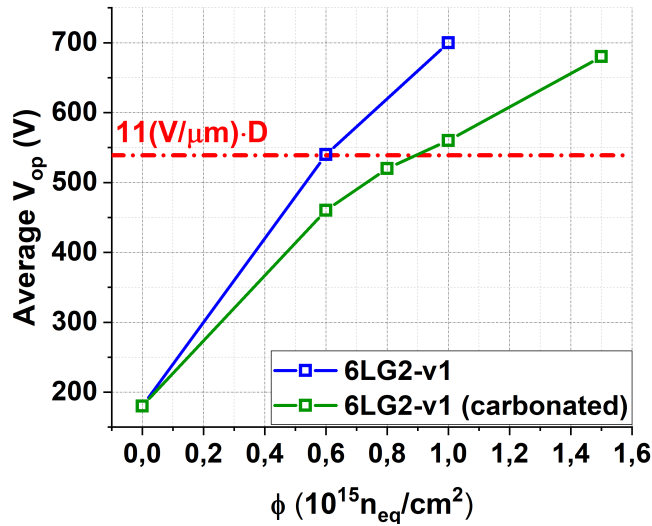


FIGURE 5.4: V_{op} (CMS ETL specifications) dependence on n_{eq} irradiation fluence for 6LG2-v2 detectors. Data extracted from [75], [78].

With all that set forth, it could be demonstrated that **the addition of a carbon layer over the multiplication one mitigates the effect of acceptor removal** in IMB-CNM LGADs. This outcome was the seed to design the next IMB-CNM LGAD fabrication run, which constitute one of the main parts of this thesis.

5.5 ATLAS HGTD LGAD 6LG2-v1 run and its comparison to the ATLAS-CMS Engineering 6LG3-v2 run

The IMB-CNM 6LG2-v1 run was based on the previously discussed ATLAS-CMS engineering run. It relied on the hypothesis that increasing the doping concentration of carbon around the PN junction would translate into an enhance of the LGAD radiation tolerance. It was fabricated on 150 mm high-resistivity p-type Si-Si wafers with the CNM1139 mask, mainly comprised by LGADs of 15×15 $1.3 \times 1.3 \text{ mm}^2$ pixels (26 devices per wafer), as specified by the ATLAS HGTD requirements for its phase-II upgrade. Nevertheless, the radiation tolerance characterization was performed on single-pad detectors, so its findings are further applicable to the CMS ETL specifications. Figure 5.5 shows a photograph of a fabricated wafer from 6LG2-v1 run, and Figure 5.6 depicts a schematic view of a carbonated single-pad LGAD from such run.

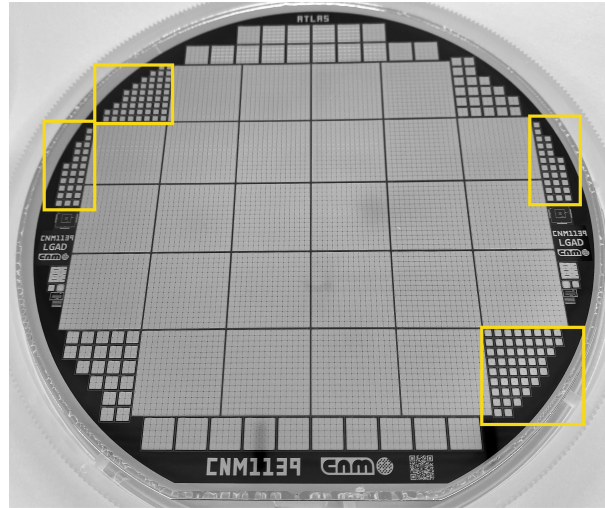


FIGURE 5.5: Photograph of a manufactured wafer from the 6LG2-v1 run. The single-pad LGADs for testing are located within the yellow boxes.

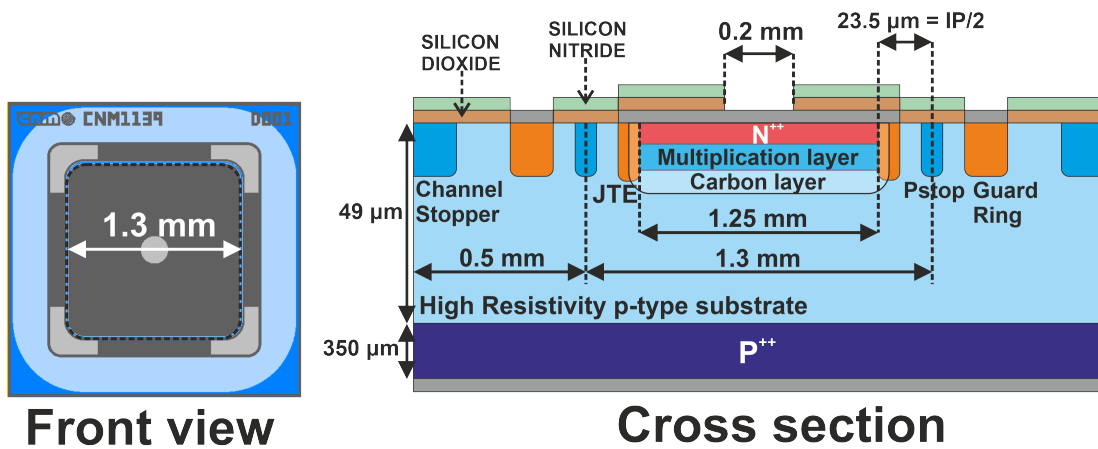


FIGURE 5.6: schematic of the front view and cross section of a carbonated single-pad LGAD from the 6LG2-v1 run.

Table 5.5 shows the implantation and annealing strategy for this fabrication run. The major change compared to the 6LG3-v2 run was (apart from the type of wafer) the use of different carbon doses in the range $1\text{-}9\cdot 10^{14} \text{ at/cm}^2$.

	W1	W2	W3	W4	W5	W6
Carbon implantation dose in multiplication layer (10^{14} at/cm^2)	-	1	2	3	6	9
Carbon implantation energy in multiplication layer (keV)	-	150				
Boron implantation dose in multiplication layer, implanted after carbon (10^{13} at/cm^2)	1.9					
Boron implantation energy in multiplication layer, implanted after carbon (keV)	100					
Annealing of boron (and carbon) in multiplication layer	180 min at 1100°C					
Phosphorus implantation dose in N^{++} (10^{14} at/cm^2)	5 & 10					
Phosphorus implantation energy in N^{++} (keV)	150 & 70					
Annealing of phosphorus in N^{++}	30 min at 1000°C					
Screen oxide for all implantations (Å)	~100					

TABLE 5.5: Fabrication features for 6LG2-v1 LGAD run.

5.5.1 TCAD Sentaurus simulation of carbonated LGADs

Despite the aim of the 6LG2-v1 run was to enhance the radiation tolerance of LGADs by means of carbonation, studies of the devices stability as a function of the carbon implantation dose needed to be carried out before starting the fabrication. This was necessary due to the carbonation effects described in section 5.2.4. To summarize, the presence of carbon within the PN junction of an LGAD alters the dopant diffusivity during fabrication (carbon-enhanced suppressed diffusion [69], [70]), as well as the number of activation sites for such dopants (carbon co-doping silicon amorphization [68]). The direct effect of such phenomena is that **the higher the carbon concentration, the higher the inner gain of the LGAD for a given reverse bias**. Since the latter statement also indicates that a higher carbon implantation dose results in a lower breakdown voltage and a higher V_{gl} , such dose needs to be kept at a low enough level to ensure a reasonable operational voltage range for the fabricated detectors.

With all that set forth, the research of the dependence between carbon implantation dose and V_{BD} , V_{gl} was carried out via TCAD Sentaurus simulation. Figure 5.7 shows such simulation when performed with the default models of Sentaurus (that is, without adjusting any parameter as it was done in section 4.3). The results highlight that the aforementioned carbonation phenomena are taken into account when the default parameters of the implantation and diffusivity models of Sentaurus are used. Such parameters correspond to the latest version available at the IMB-CNM: v2018.06.

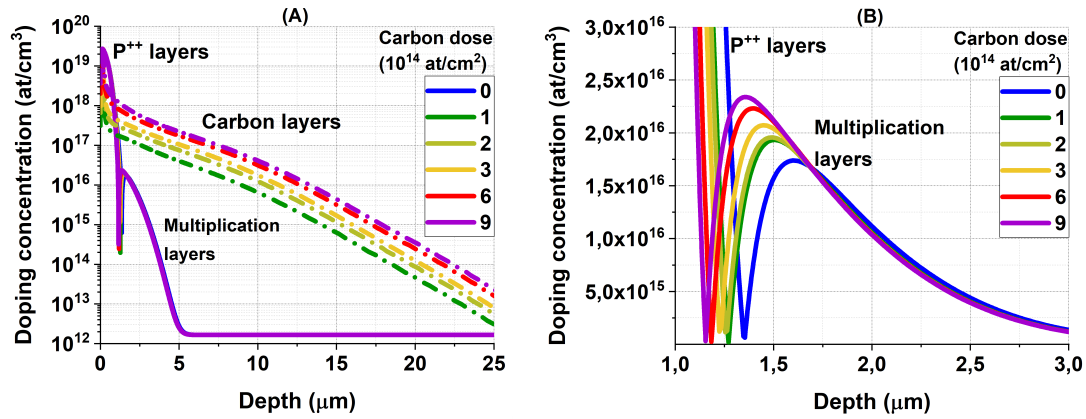


FIGURE 5.7: TCAD Sentaurus simulation of LGAD doping profiles dependence on the carbon implantation dose. (A): profiles in logarithmic scale to distinguish the carbon layers. (B): profiles in linear scale and narrowed around the PN junction.

Nevertheless, the default parameters set by any of the available TCAD versions were not able to predict well the electrical performance of IMB-CNM LGADs (see section 4.3). The manufacturing of the ALTAS-CMS engineering 6LG3-v2 run (addressed in the last section) gave away two data points in terms of carbon dose (0 and 10^{14} at/cm^2). Such data was used to adjust the diffusivity parameters of TCAD Sentaurus in order to fit, to a reasonable extent, the average V_{gl} and V_{BD} (at -30°C) of 6LG3-v2 detectors. In particular, the boron and phosphorus diffusivity through interstitials was adjusted, as previous works pointed out that the presence of carbon in silicon alters the diffusion of such dopants through interstitial sites [68], [69]. The dopant diffusivity is modelled as $D \propto D_j \exp(-f(T))$, that is, as the product of a constant parameter (the diffusivity pre-factor D_j , where j is the dopant species) and an exponential function dependent on temperature. The adjustment of the Sentaurus parameters was carried out solely on the diffusivity pre-factor for boron and phosphorus through interstitials. A sweep of these parameters was carried out until the V_{gl} of 6LG3-v2 sensors was well predicted by TCAD Sentaurus. These tuned values for the diffusivity pre-factor of boron (D_B) and phosphorus (D_P) are listed in Table 5.6.

	$D_B \text{ (cm}^2/\text{s)}$	$D_P \text{ (cm}^2/\text{s)}$
Default values of Sentaurus v2018.06	0.123	0.23
Tuned values to fit the V_{gl} of 6LG3-v2 detectors	0.5	0.3

TABLE 5.6: Diffusivity pre-factor of boron and phosphorus through interstitials.

Figure 5.8 shows the simulated LGAD doping profiles as a function of the chosen diffusivity pre-factor parameters shown in the table above. Figure 5.9 shows how the V_{gl} and V_{BD} (at -30°C) dependence on such parameters, as well as on the carbon implantation doses chosen for the 6LG2-v1 run, along with actual data from 6LG3-v2 devices. The results in both figures highlight that the default diffusivity parameters of TCAD Sentaurus v2018.06 give away LGAD profiles which inner gain is lower than the actual IMB-CNM fabricated, a result already discusses in section 4.3.

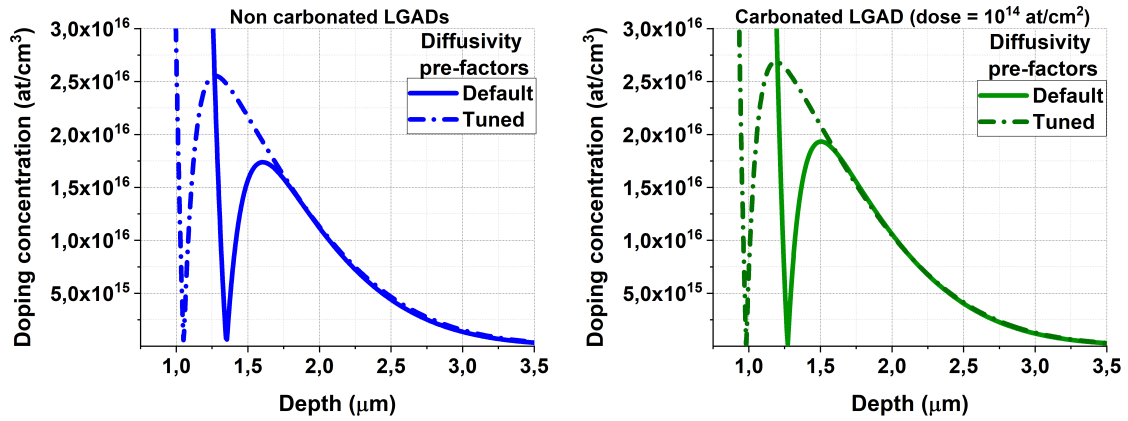


FIGURE 5.8: TCAD Sentaurus simulation of an LGAD doping profile (as fabricated in the 6LG3-v2 run) dependence diffusivity pre-factors choice (Table 5.6).

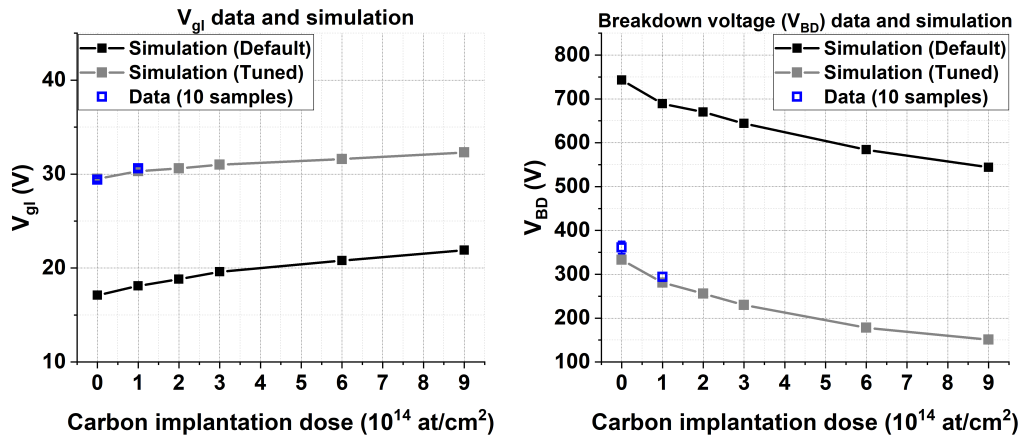


FIGURE 5.9: TCAD Sentaurus simulation of V_{gi} and V_{BD} at -30°C dependence on the carbon implantation dose and diffusivity pre-factors choice.

Nevertheless, it is important to note that the methodology for tuning the diffusivity parameters was not as rigorous as the one presented in section 4.3. The parameters presented in Table 5.6 was obtained solely by fitting the V_{gi} of 6LG3-v2 sensors. As discussed in section 4.3, this procedure is generally not enough to have a reliable prediction tool, as different diffusivity pre-factors may result in similar predicted V_{gi} values. This is highlighted by having a look at the predicted IV and CV curves shown in Figure 5.10. While the V_{gi} is accurately predicted, the CV and IV shapes, along with the V_{BD} and full depletion voltage V_{FD} , are not. Moreover, not all the fabrication parameters were well controlled during the fabrication. Specifically, the thickness of the screen oxide prior to implantation of carbon, boron and phosphorus was uncertain within $[100-400]\text{\AA}$. In short, the calibration of Sentaurus parameters with 6LG3-v2 data left some degrees of freedom unaccounted for. The outcome of such fact will be soon addressed in the next subsections.

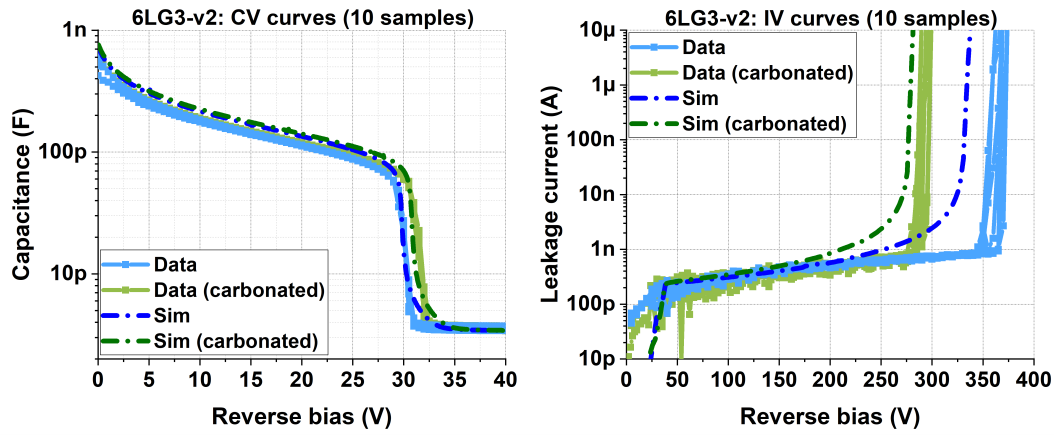


FIGURE 5.10: TCAD Sentaurus simulation of IV at -30°C and CV curves of 6LG3-v2 detectors, shown along with actual data. The diffusivity pre-factors is the one labelled as "tuned" in Table 5.6.

5.5.2 Basic electrical characterization: IV and CV measurements

Since the ATLAS phase-II upgrade experiment is expected to be conducted at -30°C , the basic electrical characterization of 6LG2-v1 sensors was carried out at that temperature. Such basic electrical characterization consisted in leakage current and capacitance vs reverse bias measurements, to determine the average V_{gl} , V_{FD} , V_{BD} and average leakage current within the voltage operation range.

Leakage current vs bias (IV) measurements were carried out on over 30 devices per carbon dose. The samples were distributed across different sections of the wafers. The guard ring (Figure 5.6) was connected in every measurement to separate the periphery current from the leakage current in the active region of the detector. Figure 5.11 depicts the averaged IV curves for every carbon dose at -30°C . The leakage current of the devices (regardless of the carbon dose) was found to be smaller than the current precision of the equipment (Keithley 2410, with a precision of 1 nA for biases over 20 V). On one hand, that highlights that the leakage current of the studied LGADs is low enough to fulfill the ATLAS and CMS experiments phase II upgrades specifications when unirradiated (Table 5.1). On the other hand, it allowed us to determine the avalanche breakdown voltage (V_{BD}) of every device by defining it as the voltage at which the IV curve abandons a quasi-linear trend and starts exhibiting an exponential behavior. This is shown in Figure 5.11 (B).

Alongside, capacitance vs bias (CV) measurements were performed on 20 devices per carbon dose. As in the IV measurements, the devices were picked from different sections of the wafers. The CV curves were obtained with a Keysight Agilent 4284A LCR-meter in parallel mode, at 20°C , 10 kHz and 500 mV AC. The average CV curves are shown in Figure 5.12. The average V_{gl} was inferred as illustrated in Figure 5.13. That is, for every CV curve, linear fits were performed in voltage ranges before and within multiplication layer depletion. The intersection of such linear fits was picked as the V_{gl} of the device.

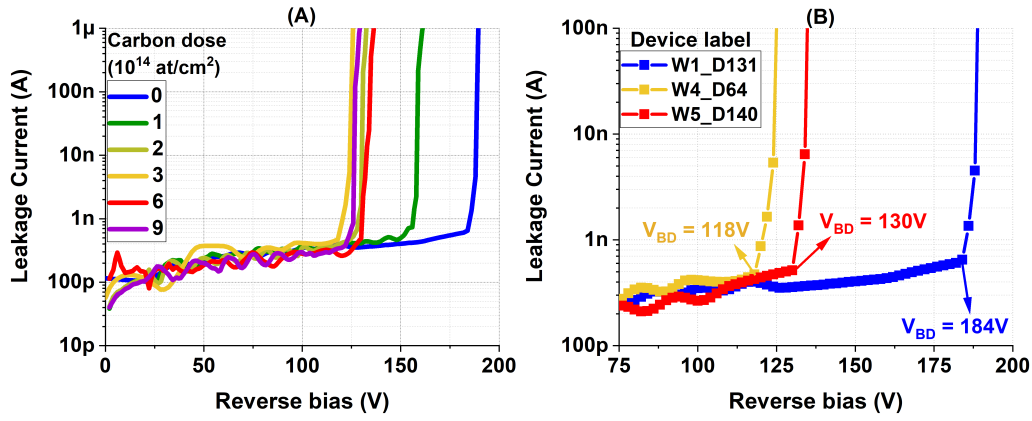


FIGURE 5.11: (A): Average IV measurements, at -30°C , of 6LG2-v1 detectors. (B): Method to infer the V_{BD} per device.

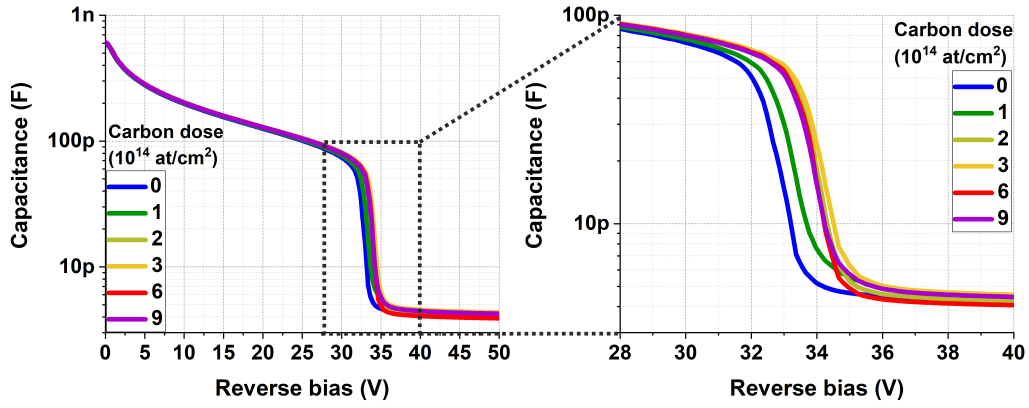


FIGURE 5.12: Average CV measurements, at 20°C , of 6LG2-v1 detectors.

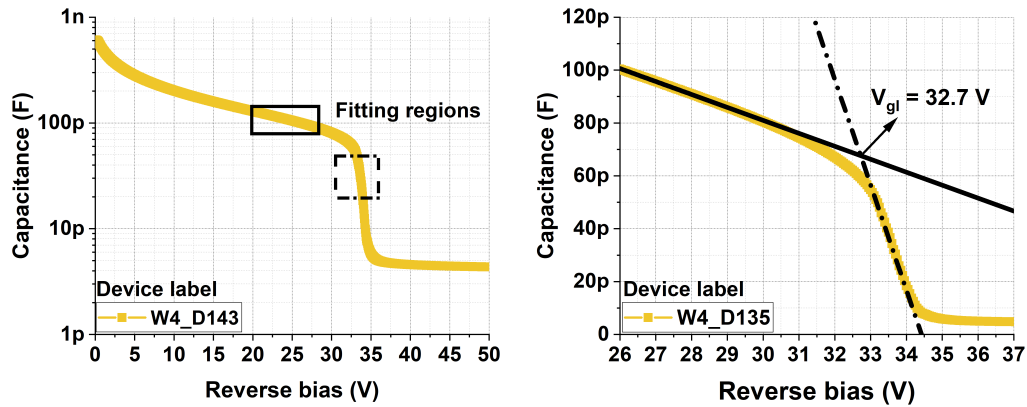


FIGURE 5.13: Methodology to infer V_{gl} .

Figure 5.14 depicts the V_{gl} and V_{BD} dependence on carbon dose for 6LG2-v1 devices, inferred by the methods displayed in Figures 5.11 and 5.13. The bar errors correspond to the standard deviation for each case. From 0 to $3 \cdot 10^{14} \text{ at/cm}^2$, the behavior is consistent with the carbon co-doping phenomena previously addressed. That is, V_{gl} increases and V_{BD} decreases with dose when carbon is implanted prior to boron (multiplication layer) and phosphorus (N^{++}). Since all dopants are diffused using the same temperature and annealing time, this result suggests that the greater the concentration of carbon, the greater the charge multiplication would be if the other fabrication parameters are kept fixed.

Nevertheless, a turning point for this effect is found when the carbon dose exceeds $3 \cdot 10^{14} \text{ at/cm}^2$. Not only do the results point out that the impact of the charge multiplication mechanism is diminished after such a dose, but it also appears to even out, showing only small variations between 6 and $9 \cdot 10^{14} \text{ at/cm}^2$. The existence of this turning point was not expected, as TCAD Sentaurus simulation predicted a quasi-linear behavior of the V_{BD} and V_{gl} dependence on carbon implantation dose (Figure 5.9). In contrast, Figure 5.14 demonstrate the non-linearity of the carbon co-doping amorphization and suppressed diffusion effects dependence on implantation dose.

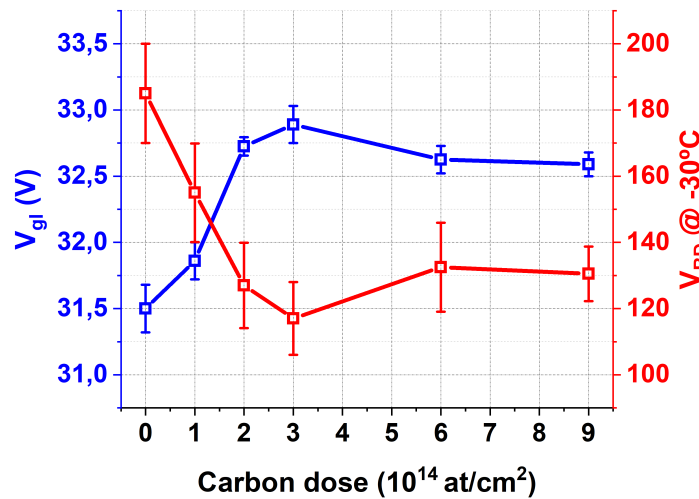


FIGURE 5.14: V_{gl} and V_{BD} (at -30°C) dependence on carbon implantation dose for 6LG2-v1 detectors.

This effect was also observed when extracting the boron doping profiles via CV measurements (see section 4.3). The results are shown in Figure 5.15. The peak of boron concentration is enhanced with carbon doses up to a value of $3 \cdot 10^{14} \text{ at/cm}^2$, to then drop for values of $6 \cdot 10^{14} \text{ at/cm}^2$ and $9 \cdot 10^{14} \text{ at/cm}^2$. Such tendency is consistent with the results shown in Figure 5.14, since higher peaks of boron concentration in the multiplication layer lead to higher V_{gl} and lower V_{BD} values. All the data presented so far seem to point in the same direction: the inner gain of 6LG2-v1 sensors increases with carbon dose up to a value of $3 \cdot 10^{14} \text{ at/cm}^2$, to then drop for values of $6 \cdot 10^{14} \text{ at/cm}^2$ and $9 \cdot 10^{14} \text{ at/cm}^2$. In order to prove such hypothesis, the gain response to 15 keV x-rays was investigated for 6LG2-v1 devices.

Nevertheless, it is mandatory to make a pit-stop before that, and discuss the evident differences found between the TCAD Sentaurus predicted V_{BD} and V_{gl} values and its actual ones.

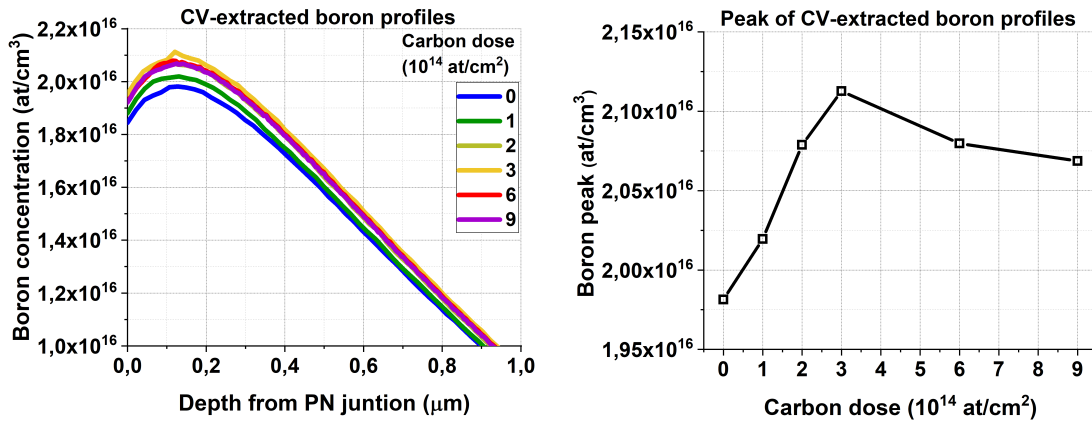


FIGURE 5.15: CV-extracted boron doping profiles for 6LG2-v1 detectors, along with the average boron concentration peak dependence on carbon implantation dose.

5.5.3 Stabilization of the LGAD technology at the IMB-CNM

LGADs from the 6LG3-v2 and 6LG2-v1 run were fabricated, in principle, under identical conditions. That is, they were manufactured with the same furnace equipment, annealing recipes, and dopant implantation scheme, among others. Nevertheless, their basic electrical characterization highlights a big difference between them in terms of V_{BD} and V_{gl} values. This is depicted in Figure 5.16.

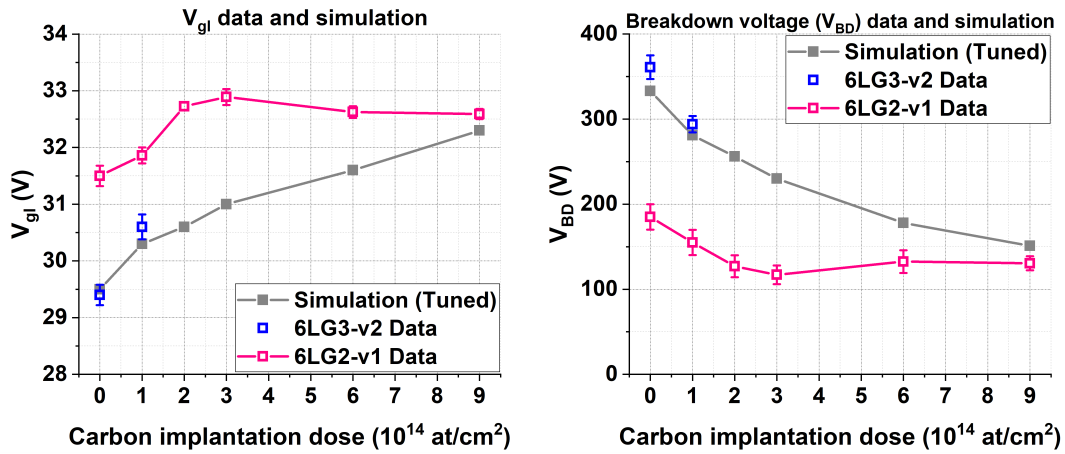


FIGURE 5.16: Average V_{gl} and V_{BD} data from 6LG3-v2 and 6LG2-v1 detectors, along with their Sentaurus predicted values using the tuned diffusivity parameters shown in Table 5.6.

From a technological standpoint, this result highlighted an anomaly in the reproducibility of IMB-CNM manufactured LGADs that needed to be addressed. The first indicator of these runs not being identical was inferred by evaluating the raw wafers. Despite the clean-room processes matched for both batches, the wafer type and manufacturer was different (epitaxial for 6LG3-v2 and Si-Si for 6LG2-v1). One single-pad LGAD per run was inspected via reverse engineering techniques. The

diced samples were inspected via optical microscopy to evaluate the thickness of silicon layers with different resistivity. The results are shown in Figure 5.17, highlighting that the high-resistivity layer of the 6LG2-v1 detectors was 6 μm thinner than the 6LG3-v2 ones.

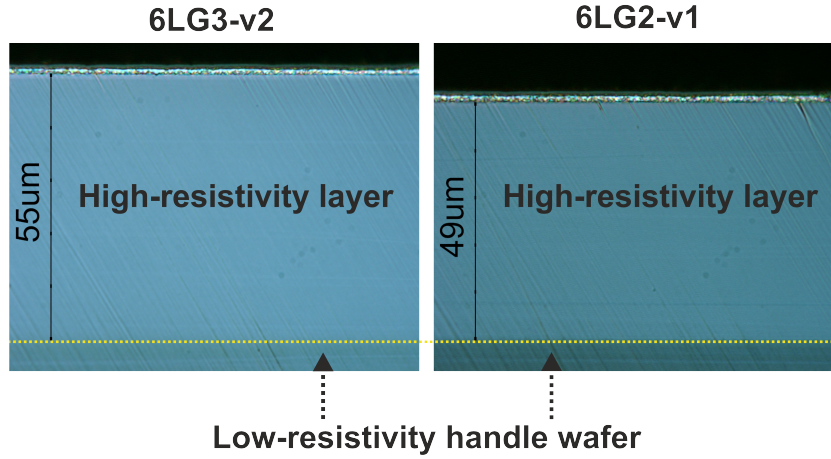


FIGURE 5.17: Optical view of a cross section of 6LG3-v2 and 6LG2-v1 LGAD samples.

The effects of the high-resistivity layer thickness difference between runs was investigated via TCAD Sentaurus simulation (Figure 5.18). Despite its results gave an insight on why 6LG2-v1 devices broke down at earlier biases than 6LG3-v2 ones, it was clear that the device thickness was not the only parameter involved in the LGADs performance differences. In particular, the V_{gl} of the devices is not subjected to changes for thicker or thinner detectors, but depends only on the shape of the multiplication layer.

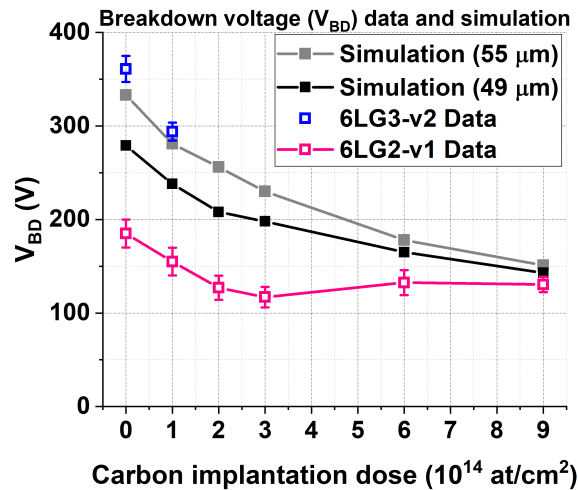


FIGURE 5.18: V_{BD} data from 6LG3-v2 and 6LG2-v1 detectors, along with their Sentaurus predicted values using the tuned diffusivity parameters shown in Table 5.6 and thicknesses of 49 and 55 μm .

This was evidenced by extracting the doping profiles for 6LG3-v2 and 6LG2-v1 sensors via CV measurements (Figure 5.19). Thus, the only means for the V_{gl} to be modified from run to run is an alteration of either the implantation or annealing processes.

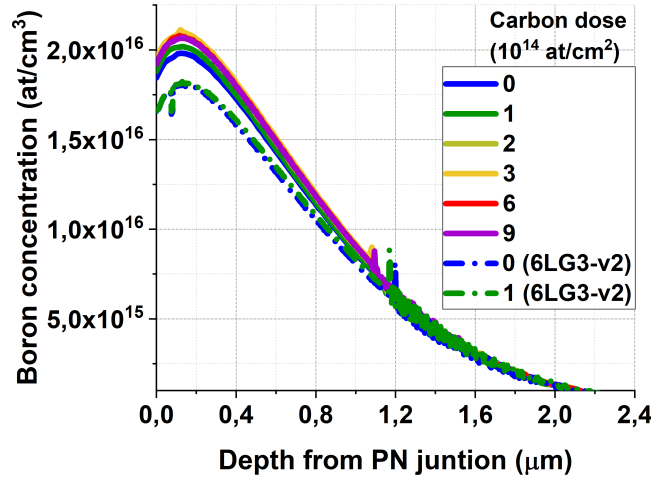


FIGURE 5.19: CV-extracted doping profiles for 6LG3-v2 (dashed line) and 6LG2-v1 (solid line) devices.

The implantation energies and doses, along with annealing ramps and temperatures, are carefully monitored and controlled during manufacturing. Therefore, it was quite unlikely that the non-reproducibility resulted from these processes. As previously stated, the only blind spot left during manufacturing was the thickness of the screen oxide prior to the multiplication and N^{++} layers implantation, so further investigation was led in that direction. The anomaly was soon spotted.

On one hand, TCAD Sentaurus (by default) assumes that the oxide growth during a certain annealing recipe is independent on wafer doping concentration. In particular, the simulated screen oxide with the IMB-CNM annealing recipe was fixed at 375 Å for all doping concentrations in p-type silicon below 10^{21} at/cm^3 . Such presumption clashed with studies where a relationship between thermal oxide and doping concentration had been reported [81]–[83]. With that in hand, the question of how the screen oxide prior to the multiplication layer implantation (grown on lightly-doped p-type silicon) could be identical to that prior to the N^{++} layer one (grown on highly-doped p-type silicon) arose. Furthermore, the quality of the oxidation processes at the IMB-CNM was conducted by measuring the oxide grown in a test wafer introduced in the furnace along with the ones meant for fabrication. Almost certainly by chance, the growth oxide on such test wafer was aligned to the one given by TCAD Sentaurus simulation, $\approx 375 \text{ Å}$, for all screen oxide processes during 6LG3-v2 and 6LG2-v1 manufacturing.

Nevertheless, the actual screen oxide had not been measured on the wafers under fabrication, so such information was lost. As comprehensively studied in section 4.3, differences in the screen oxide of the order of $\sim 100 \text{ Å}$ may result in great changes in the LGAD PN junction profiles, hence in their V_{BD} and V_{gl} . Without this information, investigation of the differences between the performance of 6LG3-v2 and 6LG2-v1 detectors and its dependence on fabrication features hit a dead end. Moreover, the

quality of Sentaurus V_{BD} and V_{gl} predictions by tuning the diffusivity pre-factors was also called into question, as such simulations had been carried out assuming a screen oxide of ≈ 375 Å.

Conversely, this result highlighted the importance of carefully controlling any manufacturing parameter, as well as examining the methodology to do so. Additionally, it led to a more rigorous scrutiny of the Sentaurus simulation models. From both a technological and R&D standpoint, stabilization of LGAD design (by means of TCAD Sentaurus) and fabrication evidenced to need a more rigorous approach to be fulfilled. This observation was, partially, the seed of the 6LG2-v2 fabrication batch, that will be address further in this chapter.

5.5.4 Gain response to 15 keV x-rays

Let us return to the subject at hand. As stated, the electrical characterization data presented in section 5.5.2 suggested that the inner gain of 6LG2-v1 devices increases with carbon dose up to a value of $3 \cdot 10^{14}$ at/cm², to then drop for values of $6 \cdot 10^{14}$ at/cm² and $9 \cdot 10^{14}$ at/cm².

In order to investigate such hypothesis, gain response measurements to 15 keV x-rays were conducted at the B16 beamline available at Diamond Light Source [23]. In contrast to the IV and CV results previously analysed, the measurements presented in this section were carried out at room temperature (20°C) instead of -30°C, as the experimental setup was not equipped with a cooling system. By using a crystal monochromator, this beamline offers ultra-fast monochromatic x-ray beams, in the range of 4-45 keV and generated from synchrotron radiation. Additionally, a compound refractive lens (CRL) was employed to achieve spot sizes of the beam of the order of 1 µm. Specifically, the beam spot size was measured to be 2.7 ± 0.1 µm FWHM (X direction) and 1.9 ± 0.1 µm FWHM (Y direction). For every measurement, the beam was projected around the center of the detectors (perpendicular to the beam direction) with the aid of a visible red laser available within the experimental setup of the beamline. The beam intensity (of the order of 10^8 photons/s when microfocused [23]) was monitored by an ionization chamber during the entire lifespan of the measurements (around 24 h). The energy of the x-rays in the beam was set at 15 keV for all measurements. X-rays of such energy have an absorption depth in silicon of the order of a millimeter [17], so the beam energy is partially deposited in the detector uniformly along its active thickness (of about 50 µm). In other words, 15 keV x-rays are high-penetrating particles for the studied LGADs (one per carbon dose).

For every measurement, the gain was extracted by dividing the photocurrent of the LGAD by the one of a reference PiN of the same fabrication batch. The photocurrent is defined as the current generated in the detector while irradiated with the x-ray beam around its center (called *Beam On* current from now on), minus the leakage current. The current was measured with a Keithley 2410 Source Measure Unit. Five measurements per device were carried out, and all plots presented in this section have error bars indicating the standard deviation of such measurements. It is worth remarking that, for every voltage point, the measurement time was always much longer than the beam pulses. The results are shown in Figures 5.20 and 5.21.

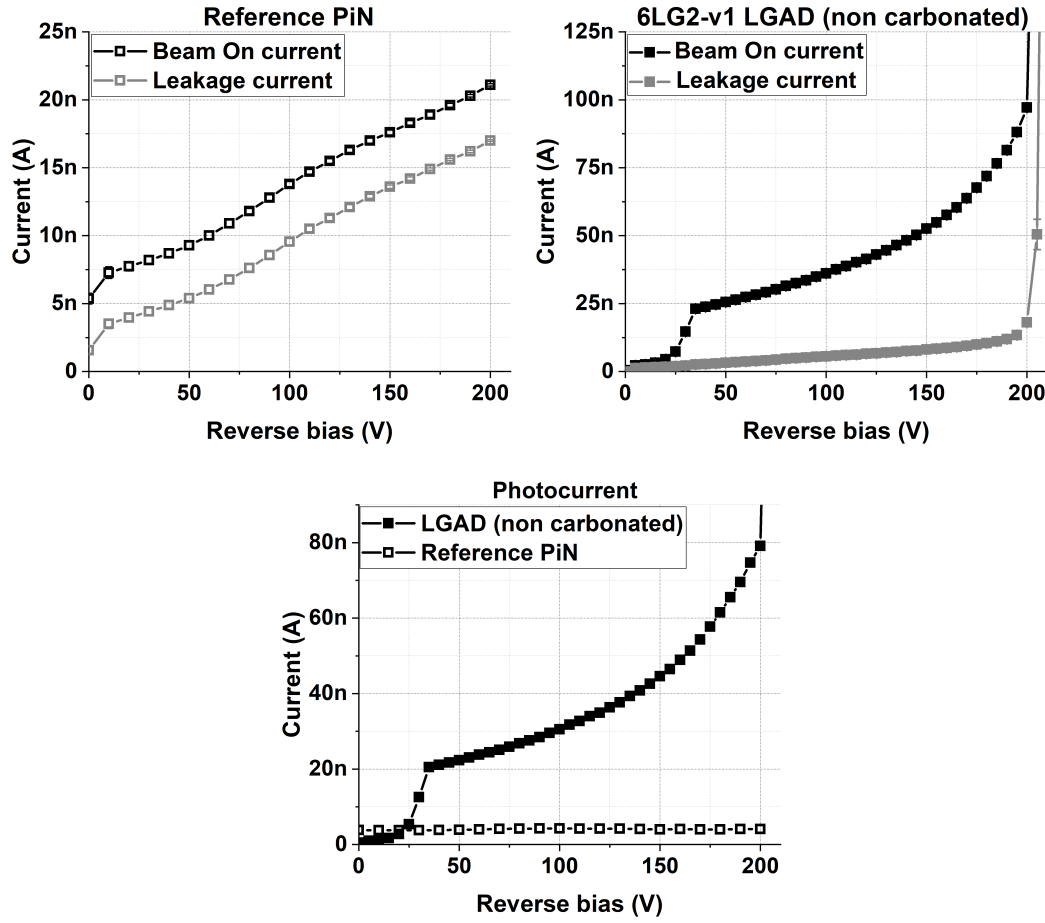


FIGURE 5.20: Example of photocurrent derivation for the non carbonated 6LG2-v1 LGAD and reference PiN.

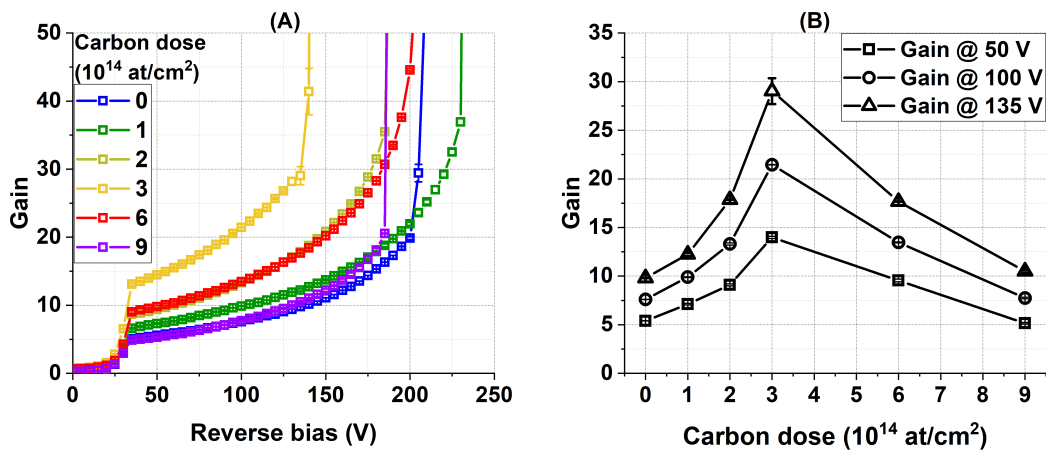


FIGURE 5.21: (A): Gain response vs bias, at 20°C, of 6LG2-v1 detectors to 15 keV x-rays. (B) Gain vs carbon implantation dose at different bias points.

As Figure 5.21 shows, the highest gain for a given bias is reached for a carbon

dose of $3 \cdot 10^{14} \text{ at/cm}^2$, to then drop for doses of 6 and $9 \cdot 10^{14} \text{ at/cm}^2$. This outcome is consistent with the electrical characterization results shown in section 5.5.2.

The B16 beamline at Diamond Light Source also offers the possibility to attenuate the x-ray beam intensity by means of pure aluminum layers of different thicknesses that can be introduced right before the CRL system. The set of attenuators enable the variation of the aluminum thickness that the beam passes through, before being microfocused, in steps of 0.5 mm.

Gain response measurements at 20°C were carried out for aluminum thicknesses of 0.5 and 1.0 mm, which correspond to an attenuation of $\approx 66\%$ and $\approx 88\%$, respectively, of the maximum beam intensity (labelled as $I_0 \approx 10^8 \text{ photons/s}$) in Figure 5.22. The ratios of beam attenuation for every aluminum thickness were estimated by using the attenuation coefficients found in [22]. Gain measurements with further beam attenuation were impossible, as for aluminum thicknesses of 1.5 mm and beyond, the photocurrent of the reference PiN fell below leakage current values. Five measurements per intensity value and carbon dose were conducted and the gain was extracted with the methodology aforementioned detailed. Figure 5.22 shows a cutline of the gain response dependence on beam intensity (A) and carbon dose (B) at 20°C and 100 V.

Once again, the results manifest that the highest gain at a given bias is reached for a carbon dose of $3 \cdot 10^{14} \text{ at/cm}^2$, regardless of the beam intensity. Also, and with independence of the carbon dose, *gain suppression* is observed for high intensities of the x-ray beam. Such phenomenon was already observed when evaluating the gain response of LGADs to IR beams of high flux [84] and 3 MeV protons [85]. Such reduction of gain is a consequence of the high ionization charge density (that is, the large number of electron-hole pairs) being created by the LGAD PN junction either by high photon fluxes or charged particles. In short, the presence of such a large number of charge carriers around the PN junction can locally and temporarily drop the effective electric field intensity, hence reducing the impact of avalanche mechanism during the gain response measurements.

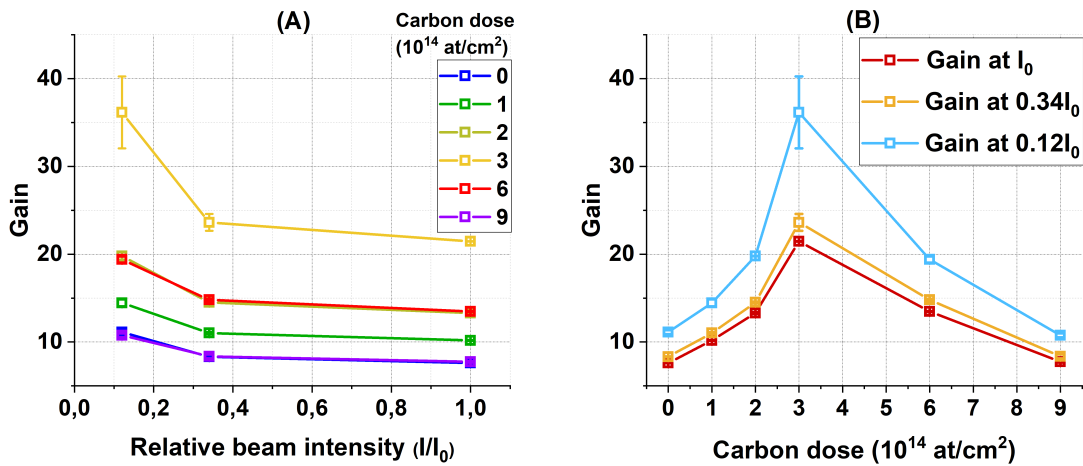


FIGURE 5.22: (A): Gain response vs relative intensity of the 15 keV x-ray beam, at 20°C and 100 V. (B) Gain vs carbon implantation dose, at 20°C and 100V, at different relative beam intensities.

Additionally, measurements at low-intensities of the 15 keV x-ray beam also

pointed out the importance of keeping a moderately low gain during particle detection experiments. The explanation lies in the shot noise we have discussed in Chapter 2 (see section 2.3.1), which is an increasing function of the nominal gain. This is shown in Figure 5.23. **As the gain suppression mechanism is reduced with low-intensities of the beam, the gain is enhanced and the shot noise with it.** As the latter is associated with fluctuations in the number of avalanche generated charge carriers, the gain response measurements lose accuracy and large standard deviation errors are observed.

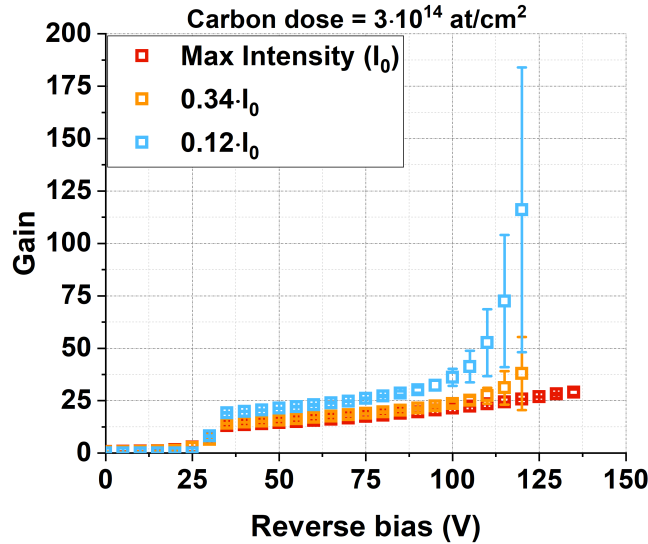


FIGURE 5.23: Gain response vs bias and relative intensity of the 15 keV x-ray beam, at 20°C, for the 6LG2-v1 device carbonated with a dose of $3 \cdot 10^{14} \text{ at/cm}^2$

In conclusion, all the measurements carried out on non-irradiated 6LG2-v1 sensors indicate that its carbonation has an impact on how they trigger the avalanche multiplication mechanism. In particular, such phenomenon is enhanced for carbon implantation doses up to $3 \cdot 10^{14} \text{ at/cm}^2$, to then drop at 6 and $9 \cdot 10^{14} \text{ at/cm}^2$. The underlying physics that may explain this effect is still under review, and a few hypothesis will be addressed in the last section of this chapter. For the time being, let us return to the matter at hand as, apart from the interesting results in terms of LGAD performance vs carbon concentration, 6LG2-v1 were designed and fabricated to fulfill the ATLAS HGTD and CMS ETL phase-II upgrade. Let us delve into that.

5.5.5 Radiation tolerance of 6LG2-v1 detectors

Studies of the acceptor removal constant of 6LG2-v1 devices were carried out at IFCA and Jozef Stefan Institute (JSI, Ljubljana, Slovenia). Their methodology and findings can be found in [51], [86], and the overall results are displayed in Figure 5.24, along with the acceptor removal constant of LGADs from the previous 6LG3-v2 run [25]. While the results indicate an improvement in the acceptor removal mitigation in the presence of carbon, this is observed up to a value of $3 \cdot 10^{14} \text{ at/cm}^2$. For a dose of $6 \cdot 10^{14} \text{ at/cm}^2$, the acceptor removal constant shows a slight increase, which seems to stabilize and align with the value for a dose of $9 \cdot 10^{14} \text{ at/cm}^2$.

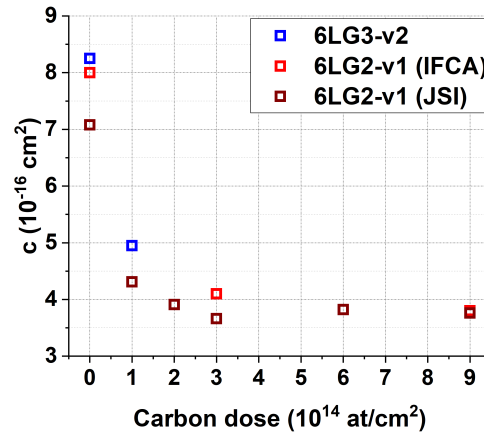


FIGURE 5.24: Acceptor removal constant c for 6LG3-v2 [25] and 6LG2-v1 detectors [51], [86].

On the other hand, IV measurements were carried out at the IMB-CNM for 6LG2-v1 irradiated detectors. As in the case of non irradiated samples, leakage current measurements were made at -30°C , with a Keithley 2410 and the guard ring biased at all times to withdraw the periphery current. The results are shown in Figure 5.25 and further analysed in Figure 5.26.

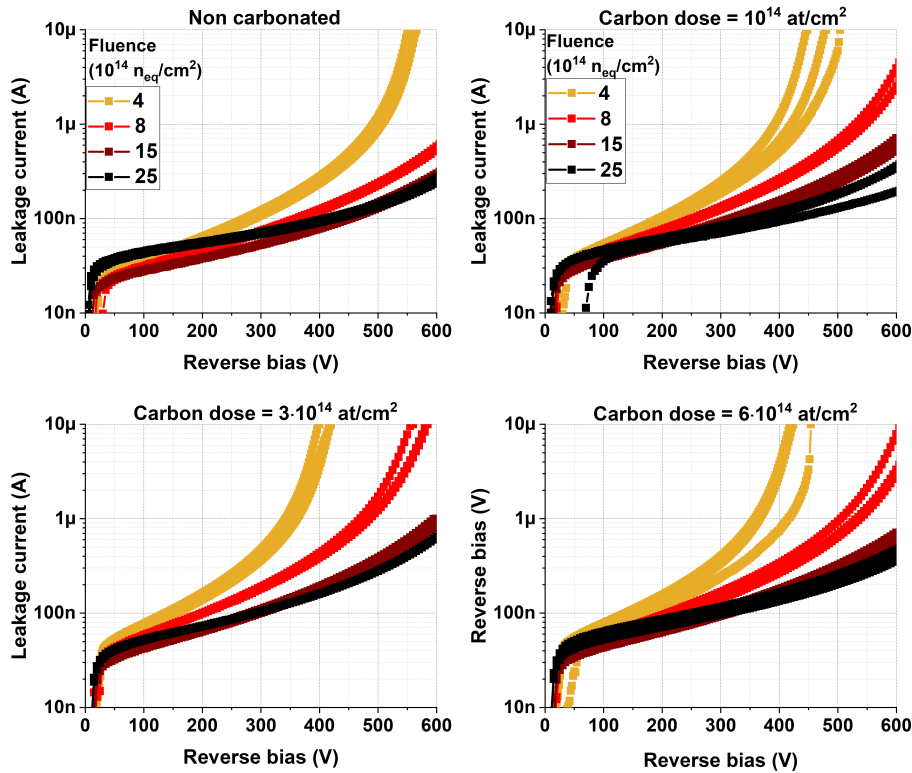


FIGURE 5.25: IV curves dependence on irradiation fluence for 6LG2-v1 detectors carbonated with implantation doses 0, 1, 3 and $6 \cdot 10^{14} \text{ at/cm}^2$.

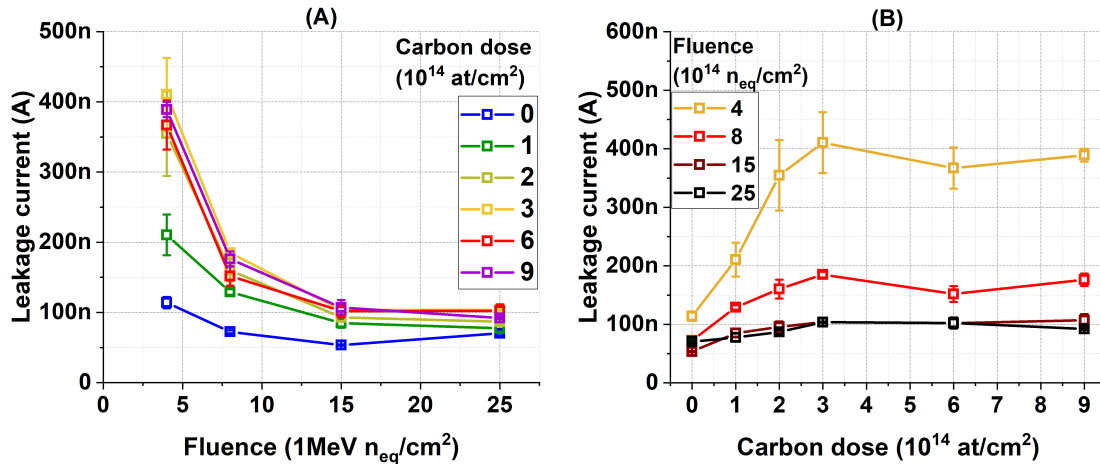


FIGURE 5.26: (A): Leakage current, at 300 V and -30°C dependence on irradiation fluence. (B): Same as (A), but analysing the dependence on carbon implantation dose.

Regardless of the carbon dose, a general trend was observed: a decrease of the leakage current as a function of irradiation fluence. Recalling that the pad current at -30°C when unirradiated was <1 nA for all carbon doses, Figure 5.26 shows that the leakage current of 6LG2-v1 suffers a great increase when irradiated at $4 \cdot 10^{14}$ n_{eq}/cm^2 . However, it then starts to drop with higher irradiation fluences, an effect likely originating from the loss of gain that LGADs experience with increasing fluence, which in turn counterbalances the rise in leakage current due to radiation-induced defects. On the other hand, for a given irradiation fluence, the leakage current increases with the carbon dose, but only up to $3 \cdot 10^{14}$ at/cm². Once again, a turning point is found at such value.

5.5.6 Fulfilment of ATLAS HGTD and CMS ETL phase-II upgrade specifications

In order to evaluate the fulfilment of ATLAS HGTD and CMS ETL requirements, measurements of the CC and time resolution for a mip were carried out at IFAE and IFCA with a radioactive Sr-90 source. The results are shown in Tables 5.7 and 5.8, which data was extracted from [51], [67], [78]. The experimental setup and methodology to infer such data can be found in [77], [78].

Table 5.7 highlights that the performance of 6LG2-v1 irradiated detectors has greatly improved in compared to previous IMB-CNM runs. In particular, the CMS specifications are fulfilled for measurements carried out in LGADs with a carbon dose of $9 \cdot 10^{14}$ at/cm², while it is worth pointing out that the requirements are met just at the upper voltage limit of $11(V/\mu\text{m}) \cdot D \approx 540$ V. On the other hand, another phenomenon was observed during the measurements reported in [51]. Spurious signal-like noise pulses were observed for half of the measured LGADs before their breakdown, which was an indicative of popcorn noise. As discussed in Chapter 3, the popcorn noise (see section 3.3) increases the baseline noise level, hence degrading the performance of an LGAD during particle detection. Also, its presence has been reported to be linked to having a low IP distance ($47 \mu\text{m}$ in 6LG2-v1 sensors). In order to study this phenomena and reduce the likelihood of popcorn noise, the

next IMB-CNM fabrication run was fabricated with an IP of $80 \mu\text{m}$ (upper limit for the CMS ETL specifications). This will be addressed in detail in the next section.

CMS ETL specifications (2021)		6LG2-v1	
Carbon dose (10^{14} at/cm^2)		3	9
Geometrical sensor properties			
Thickness D (μm)	45 – 65	49	
Pad size (mm^2)	1.3x1.3	1.3x1.3	
IP (μm)	≤ 80	47	
Unirradiated sensors performance at -25°C			
V_{gl} (V)	< 60	32.9	32.6
V_{FD} (V)	$V_{FD} < V_{gl} + 10$	≈ 38	
V_{op} (V)	8 fC for a mip	< 90	
V_{BD} (V)	$> V_{op} + 30$	≈ 120	≈ 130
Time resolution at $V < V_{BD} - 30 \text{ V}$	$< 50 \text{ ps}$	Fulfilled but $V > V_{BD} - 30 \text{ V}$	Fulfilled. 47 ps at 100 V
Pad leakage current (nA)	$I_{pad} < 200$	< 1	< 1
Irradiated sensors at $1.5 \cdot 10^{15} \text{ } n_{eq}/\text{cm}^2$ and -25°C			
V_{op} (V)	8 fC for a mip	> 540	$\approx 540 = 11D$
V_{op} requirement	$V_{op} < 11(V/\mu\text{m}) \cdot D$	Not fulfilled	$V_{op} = 11D$
Time resolution at V_{op}	$< 50 \text{ ps}$	Fulfilled but $V_{op} > 11D$	Fulfilled at $\approx 540 = 11D$

TABLE 5.7: Technical and geometrical specifications for the CMS ETL (2021) sensors, along with the characterization of 6LG2-v1 detectors [51].

ATLAS HGTD specifications (2023)		6LG2-v1	
Carbon dose (10^{14} at/cm ²)		2	3
Geometrical sensor properties			
Thickness D (μm)	45 – 55	49	
Pad size (mm ²)	1.3x1.3	1.3x1.3	
IP (μm)	40 – 60	47	
Unirradiated sensors performance at -30°C			
Specifications met for all carbon doses [78]			
Irradiated sensors at $2.5 \cdot 10^{15}$ n _{eq} /cm ² and -30°C			
V _{op} (V)	4 fC for a mip	> 600 V	
V _{op} requirement	V _{op} < 11(V/μm) · D	Not fulfilled	
Time resolution at V _{op}	< 50 ps	Not fulfilled for V<600 V	Fulfilled at V = 500 < 11D but CC(mip)< 2fC

TABLE 5.8: Technical and geometrical specifications for the ATLAS HGTD (2023) sensors, along with the characterization of 6LG2-v1 detectors [67], [78].

Table 5.8 shows the performance of 6LG2-v1 devices in terms of meeting of the ATLAS HGTD specifications. In this case, LGADs with all carbon implantation doses were studied, confirming that the requirements before irradiation were met

regardless the value of such dose [67], [78]. After irradiation, the studied LGADs (carbon doses of 2 and $3 \cdot 10^{14} \text{ at/cm}^2$) did not meet the specifications. Nevertheless, it is worth remarking that, for a carbon dose of $3 \cdot 10^{14} \text{ at/cm}^2$, a time resolution of 50 ps was obtained at a fluence of $2.5 \cdot 10^{15} \text{ n}_{eq}/\text{cm}^2$ and for biases under the voltage limit of $V_{op} < 11(V/\mu\text{m}) \cdot D$, a result that was never achieved for previous LGADs fabricated at the IMB-CNM.

5.5.7 IV measurements of ATLAS 6LG2-v1 pixelated detectors

As aforementioned, both the ATLAS HGTD and CMS ETL specifications require that all pixels on large-area segmented detectors are functional. That is, detectors with 15×15 or 16×16 pixels are required to achieve a 100% yield. In order to evaluate this, the wafers undergo a fabrication process at the IMB-CNM clean-room, where a *temporary metal* is deposited for the characterization of large segmented devices. The temporary metal consists of a $1 \mu\text{m}$ aluminum layer over a $0.03 \mu\text{m}$ titanium layer, deposited onto the existing $1.5 \mu\text{m}$ metal layer. After photolithography, the temporary metal is pattern-etched via wet etching to short all pixels in each segmented device on the wafer. An illustration of the temporary metal pattern on 6LG2-v1 segmented devices with 15×15 pixels is shown in Figure 5.27.

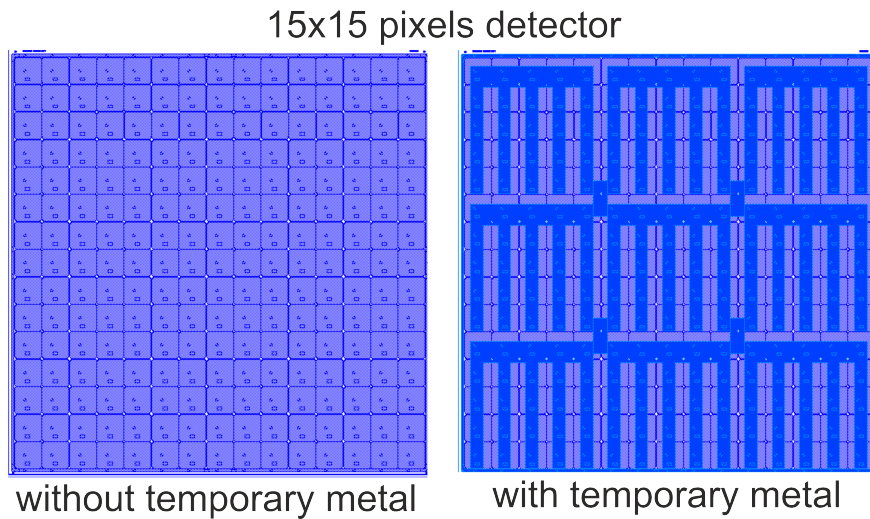


FIGURE 5.27: Mask design for the temporary metal in the 6LG2-v1 LGAD run.

By using this approach, we can detect malfunctioning pixels through the device's overall leakage current. That is, if any pixel experiences early breakdown, the leakage current measured with the temporary metal will reflect this breakdown. After performing IV measurements on large segmented devices, wet etching processes are used to selectively remove the temporary metal layers, hence recovering the wafers as originally manufactured.

It is important to mention that the leakage current measured with the temporary metal did not accurately represent the actual leakage current of the devices. This is shown in Figure 5.28, where a segmented LGAD of 2×2 pixels was measured with temporary metal and after its removal. As spotted from such figure, the sum of the leakage currents measured across each of the four pads does not match the total leakage current measured with the temporary metal. While the reasons for this effect

are still under investigation, it is suggested that the temporary metal layer may alter the electric field distribution across the device, potentially leading to higher leakage currents in certain regions.

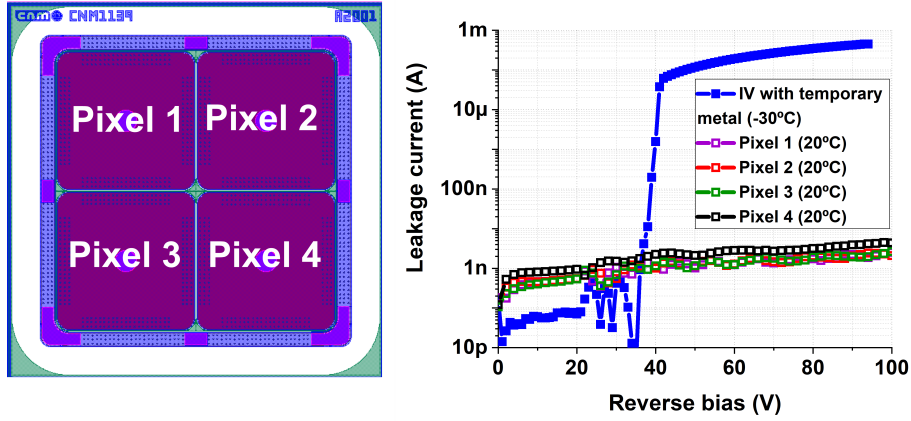


FIGURE 5.28: Leakage current of a 6LG2-v1 segmented LGAD of 2x2 pixels with and without the temporary metal.

Given all this, it is crucial to remark that IV measurements of pixelated detectors with a temporary metal layer do not provide a quantitative analysis of leakage current, **but only qualitatively indicate whether all pixels in the sensor are functional or not**. Figure 5.29 shows the IV measurements conducted on 6LG2-v1 segmented detectors of 15x15 pixels of 1.3x1.3 mm² and carbonated with an implantation dose of $3 \cdot 10^{14}$ at/cm². In the graph, 24 out of the 26 segmented devices on the wafers were shown to have 100% functional pixels, with leakage current increasing consistently above the full depletion voltage.

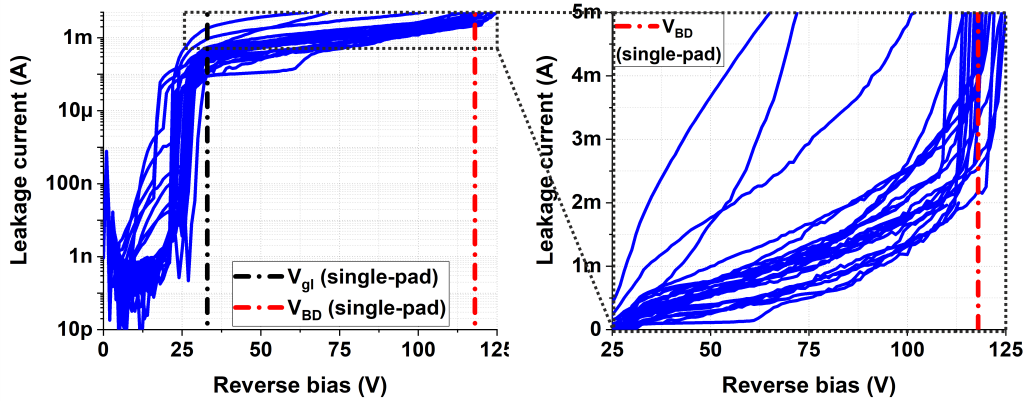


FIGURE 5.29: Leakage current of 6LG2-v1 segmented detectors of 15x15 pixels, measured with temporary metal at -30°C.

To determine the actual leakage current of the detectors, three were tested at the University of Science and Technology of China (USTC). The location of the tested devices on wafer is shown in Figure 5.30.

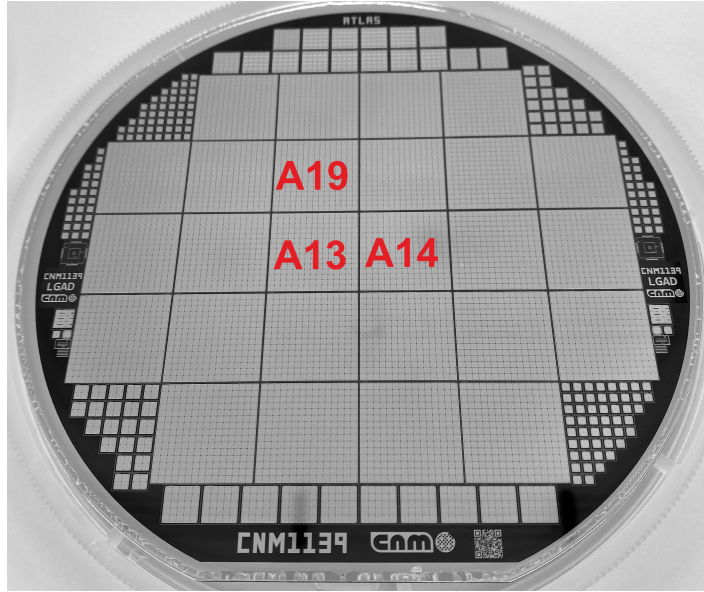


FIGURE 5.30: On wafer location of tested devices.

The measurements were performed using a probe card, enabling pixel-by-pixel IV measurements at 20°C [87]. The total leakage current for every tested devices is shown in Figure 5.31, alongside a comparison to the IV measurements conducted at the IMB-CNM using a temporary metal at -30°C. The results demonstrated that the presence of the temporary metal does increase the total leakage current of the segmented devices core.

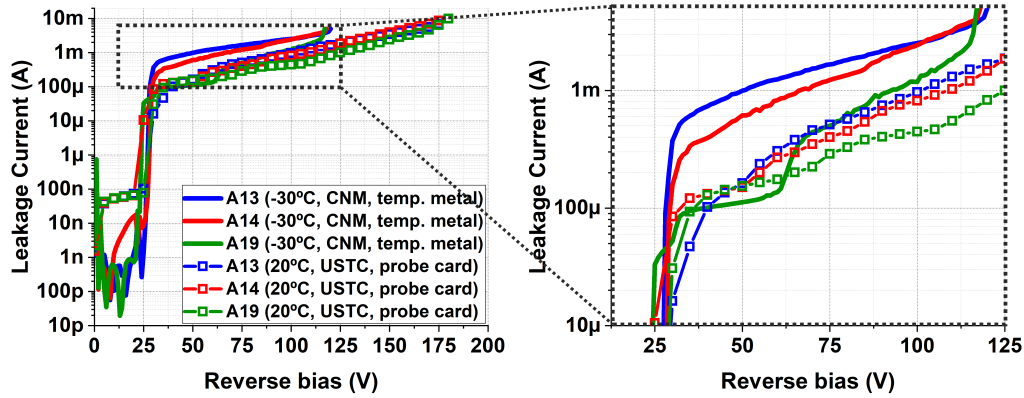


FIGURE 5.31: Leakage current of 6LG2-v1 segmented detectors of 15x15 pixels, measured with temporary metal at -30°C (IMB-CNM) and with a probe card at 20°C (USTC).

However, the actual leakage current measured with the probe card was still higher than expected. Specifically, the CMS ETL specifications require the average leakage current per pixel to be ≤ 200 nA at 20°C (see Table 5.1). As Figure 5.32 shows, such value is always greater than 1 μ A for the three tested 6LG2-v1 segmented detectors. However, the average leakage current drastically drops once the pixels that do not fulfill the criteria shown in Table 5.9 are discarded in the statistics. Moreover,

ATLAS HGTD sensors have the requirement of having an average pixel current below 200 nA at a temperature of -30°C . Since the IV measurements with a probe card were conducted at 20°C , it was not possible to determine whether the segmented 6LG2-v1 devices were suitable for the experiment.

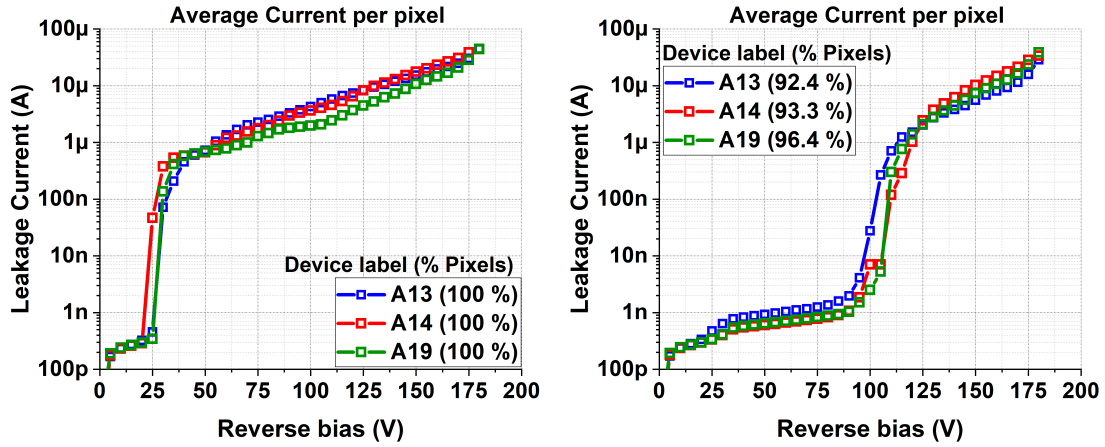


FIGURE 5.32: Average leakage current per pixel of 6LG2-v1 segmented detectors of 15x15 pixels, measured with a probe card at 20°C (USTC) [87].

As stated, the average leakage current per pixel does not provide a precise estimation of the detectors yield, as a few malfunctioning pixels can significantly affect the statistics. To obtain a more accurate estimation of the yield, pixel-by-pixel IV measurements were analysed. As stated in Tables 5.7 and 5.8, single-pad 6LG2-v1 detectors with a carbon dose of $3 \cdot 10^{14} \text{ at/cm}^2$ meet the CMS ETL and ATLAS HGTD specifications, before irradiation, at $V_{opCMS}=100 \text{ V}$ (-25°C) [51] and $V_{opATLAS}=80 \text{ V}$ (-30°C) [78], respectively. For both experiments and its target temperature, the leakage current per pixel is required to be $\leq 200 \text{ nA}$ before irradiation. Thus, and despite the IV measurements were conducted at room temperature, a rough estimation of the yield can be inferred by evaluating how many pixels per detector do not exceed 200 nA of leakage current up to V_{opCMS} and $V_{opATLAS}$ at 20°C . The results of such analysis is summarized in Table 5.9, and Figure 5.33 shows a color code mapping of the reverse bias at which every pixel reaches 200 nA of leakage current at 20°C .

6LG2-v1 Device Label	% Pixels with $i_L < 200 \text{ nA}$ at 100 V	% Pixels with $i_L < 200 \text{ nA}$ at 80 V
A13	92.4	94.6
A14	93.2	94.6
A19	96.4	96.9

TABLE 5.9: Percentage of pixels in segmented 6LG2-v1 detectors (measured at 20°C with a probe-card at USTC) that do not exceed 200 nA of leakage current up to V_{opCMS} and $V_{opATLAS}$.

On one hand, the results show that, for all studied devices, more than 90% of the pixels are functional and meet the ATLAS HGTD and CMS ETL leakage current specifications before irradiation. Furthermore, the yield values listed in Table 5.9

represent a lower limit for the device yield after irradiation, as the leakage current at -30°C and -25°C will be much lower than at room temperature.

On the other hand, the results also highlight the importance of improving the technology, as both ATLAS HGTD and CMS ETL require 100% yield for all the segmented devices that will be integrated for their phase-II upgrades. Nevertheless, it is important to note that, **from a technological standpoint, all segmented devices of 15×15 pixels are functional**. While some pixels of them exhibit higher leakage current levels at 20°C , none exceeds $\sim 10 \mu\text{A}$ within their operational voltage range ($\approx 30\text{--}100 \text{ V}$), and none experiences early breakdown before 100 V .

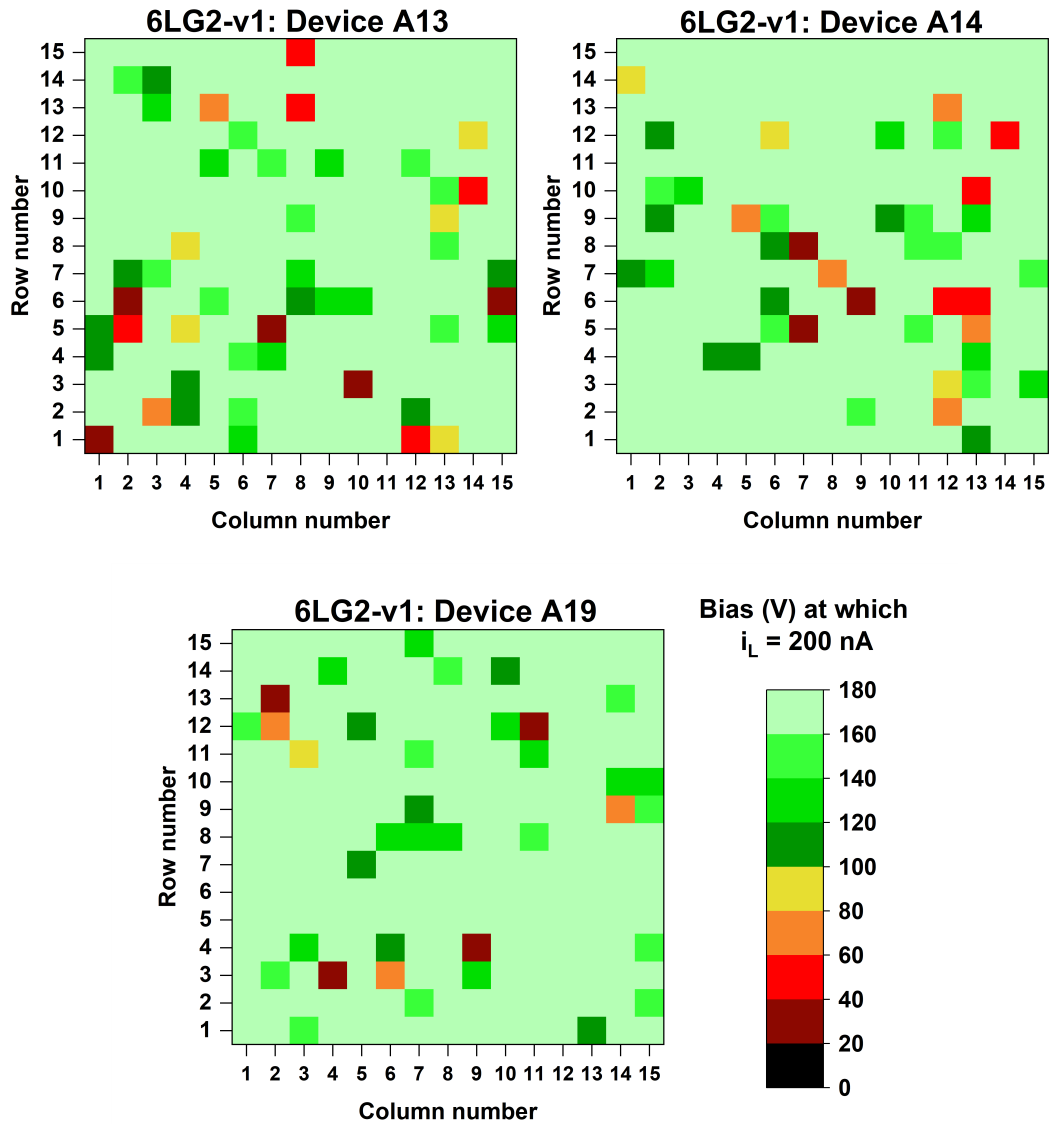


FIGURE 5.33: Color code mapping of the reverse bias at which every pixel reaches 200 nA of leakage current, for 6LG2-v1 segmented detectors IV measured with a probe card at 20°C .

5.5.8 Overview of 6LG2-v1 run results

Before introducing the next IMB-CNM LGAD run, let us make a brief stop to review the findings from the results of the 6LG2-v1 run. From a technological standpoint, there are a few aspects to highlight. On one hand, the **importance of carefully controlling the fabrication parameters was evidenced**. As information about the screen oxide prior to implantation processes was lost, the clear differences between the two IMB-CNM carbonated LGAD runs (6LG3-v2 and 6LG2-v1) could not be properly investigated via TCAD Sentaurus simulation. In turn, this posed a drawback to stabilizing the LGAD design and fabrication at the IMB-CNM, which needed to be addressed in future runs. On the other hand, the effects in fabrication of carbon doping was confirmed. An increase in carbon doping concentration around the PN junction was proven to lead to LGADs with higher inner gain. This is due to the carbon-enhanced dopant diffusion suppression and co-doping silicon amorphization, phenomena that have been covered during the chapter. Nevertheless, **an unexpected turning point at which such phenomena stops enhancing the gain of the detector (at a given bias) is found after an implantation dose of $3 \cdot 10^{14} \text{ at/cm}^2$** . Additionally, the actual carbon dose value at which such turning point occurs was not totally defined back then, as it was amidst 3 and $6 \cdot 10^{14} \text{ at/cm}^2$. Neither the underlying physics of the turning point were understood, as TCAD Sentaurus simulation did not predict it. Finally, the **IV measurements of 15x15 pixel detectors have demonstrated the viability of IMB-CNM technology for manufacturing large segmented LGADs. However, further improvements are required to achieve 100% yield.**

From the point of view of the ATLAS HGTD and CMS ETL phase-II upgrade requirements, the conclusions where as it follows. **In the CMS case, the requirements were met both before and after irradiation**, but they were at the very upper limit of the allowed operational voltage of $11(V/\mu\text{m}) \cdot D$. Additionally, the results suggested that an IP of $47 \mu\text{m}$ was not small enough to prevent the appearance of popcorn noise, with independence of the carbon implantation dose and irradiation fluence. **In the ATLAS case, the radiation tolerance needed to be enhanced in order to meet the LGADs specifications after irradiation.** The results presented in Figure 5.24 had shown that a carbon dose of $3 \cdot 10^{14} \text{ at/cm}^2$ was optimal in terms of mitigation of the acceptor removal effect. However, it was still not clear if dose values in between 3 and $6 \cdot 10^{14} \text{ at/cm}^2$ could lead to a higher radiation tolerance in such terms.

5.6 CMS LGAD 6LG2-v2 run

The arguments presented in the last section laid the groundwork for the CMS LGAD 6LG2-v2 run. It was manufactured on 150 mm high-resistivity p-type Si-Si wafers with the CNM1159 mask, that was mainly comprised by segmented LGADs of 16x16 pixels of $1.3 \times 1.3 \text{ mm}^2$ (21 devices per wafer), as specified by the CMS ETL requirements for its phase-II upgrade. Figures 5.34 and 5.35 show, respectively, a photograph of one of the fabricated wafers and a schematic view of a carbonated single-pad LGAD from this run. It is worth recalling that 6LG2-v2 devices were used as an example to illustrate the fabrication of single-pad LGADs in Chapter 3 (see section 3.3). This run was composed of three wafers.

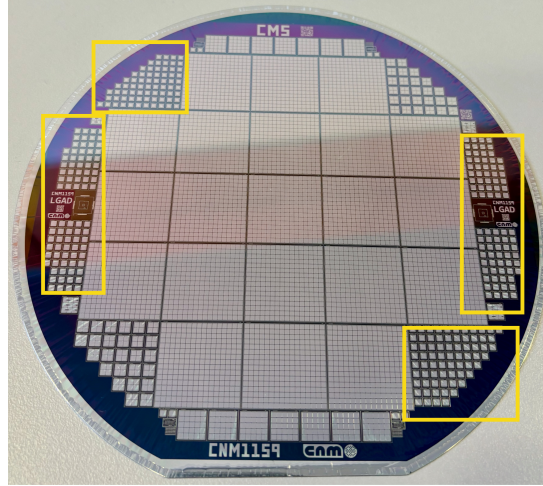


FIGURE 5.34: Photograph of a manufactured wafer from the 6LG2-v2 run. The single-pad LGADs for testing are located within the yellow boxes.

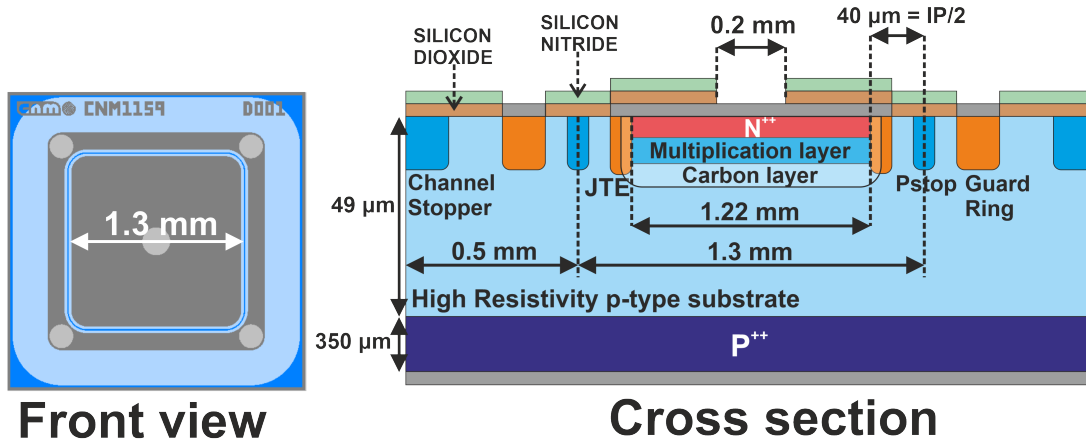


FIGURE 5.35: schematic of the front view and cross section of a carbonated single-pad LGAD from the 6LG2-v2 run.

The run was manufactured, in principle, under the same conditions as the 6LG2-v1 run. This includes using the same wafers (both in terms of type and provider), furnace and implantation equipment, annealing recipes, and dopant implantation strategies for boron and phosphorus. The main differences compared to the 6LG2-v1 run were the carbonation scheme and the IP of the devices. The carbon implantation doses were selected as $3, 4$ and $5 \cdot 10^{14} \text{ at/cm}^2$ for the following reasons. First, it would allow us to determine how reproducible the fabrication processes are, as a wafer with a carbon dose of $3 \cdot 10^{14} \text{ at/cm}^2$ had already been manufactured. Additionally, it would enable us to investigate the turning point for the carbon-enhanced phenomena described in the last section, which pointed out to be amidst 3 and $6 \cdot 10^{14} \text{ at/cm}^2$. Last but not least, an optimal value for the acceptor removal constant was also suggested to be within such carbon dose range. On the other hand, the devices IP was designed to be $80 \mu\text{m}$ instead of $47 \mu\text{m}$ to help avoid the appearance of popcorn noise and to evaluate its relationship with such distance.

The main features of 6LG2-v2 LGAD fabrication process are listed in Table 5.10.

	W1	W2	W3
Carbon implantation dose in multiplication layer (10^{14} at/cm ²)	3	4	5
Carbon implantation energy in multiplication layer (keV)	150		
Boron implantation dose in multiplication layer, implanted after carbon (10^{13} at/cm ²)	1.9		
Boron implantation energy in multiplication layer, implanted after carbon (keV)	100		
Annealing of boron (and carbon) in multiplication layer	180 min at 1100°C		
Phosphorus implantation dose in N^{++} (10^{14} at/cm ²)	5 & 10		
Phosphorus implantation energy in N^{++} (keV)	150 & 70		
Annealing of phosphorus in N^{++}	30 min at 1000°C		
Screen oxide prior to boron and carbon implantations (Å)	206±9		
Screen oxide prior to phosphorus implantation (Å)	89±50	117±18	108±17

TABLE 5.10: Fabrication features for 6LG2-v2 LGAD run.

For the 6LG2-v2 run, the screen oxide prior to the multiplication, carbon and N^{++} layers implantation was measured on different areas of the wafers, and the average values are found in Table 5.6. As in the previous IMB-CNM LGAD runs, the value of the screen oxide grown in the aforementioned test wafer was measured to be ≈ 375 Å. This result demonstrated a discrepancy that we had already anticipated, **as the screen oxide grown on the processed wafers was different to that of the test one**. Moreover, they also revealed an additional anomaly that did not align with previous reports. As discussed in section 5.5, studies had proven that the screen oxide grown under the same oxidation conditions is dependent on the wafer doping concentration [81]–[83]. In particular, it was reported that the thickness of such oxide was an increasing function of the doping concentration. That is, the more doped the silicon, the thicker the screen oxide. Nevertheless, the results detailed in Table 5.10 show otherwise. Prior to boron and carbon implantation, the silicon at the device core is lightly doped (as per raw wafer values). Conversely, before phosphorus implantation for the N^{++} layer, the multiplication layer has already been implanted and activated in such area. Consequently, the screen oxide grown in the first scenario was expected to be thinner (if not similar) than in the second one. However, the screen oxide grown in lightly-doped silicon was almost twice the one grown in highly doped-silicon. This mismatch opened the door to hypothesizing about the effects of carbonation not only on the diffusion and activation of dopants in the LGAD PN junction, but also on the implantation of such dopants through an alteration of the screen oxide. In order to address that, we need to take a moment to discuss the physics behind the growth of a SiO_2 layer on silicon.

5.6.1 Growing oxide in doped-silicon: an brief overview

As stated in Chapter 3, oxidation of silicon occurs by placing the wafers in a clean furnace during a certain annealing time, temperature and gas flow. For screen oxide

growth, this is done at the IMB-CNM for 84 minutes, at 950°C and via dry oxidation (see section 3.2), that is, with a gas flow of pure O_2 . When the annealing process starts, the silicon surface is quickly oxidized by direct reaction with the high temperature gas. At deeper levels, oxygen atoms from the gas need to diffuse through the semiconductor lattice to reach the underlying silicon. The motion of oxygen in silicon has proven to be carried out primarily via interstitial diffusion [88]–[90].

The latter result explains why thicker oxides can be thermally grown on highly boron-doped p-type silicon [81]–[83]. The smaller boron atoms (compared to silicon ones) create gaps and distortions in the regular pattern of the silicon lattice. In turn, this naturally leads to a higher concentration of interstitials lattice sites, defects that facilitate the diffusion of oxygen atoms, allowing for a more extensive oxidation process and thicker oxide layers to form at greater depths from the wafer surface. Nevertheless, this argument may be compromised in the presence of high concentrations of carbon by the silicon surface during the oxidation process. This is exactly the case during the growth of the screen oxide prior to the N^{++} implantation for 6GL2-v1 and 6LG2-v2 devices.

As previously addressed, carbon atoms can occupy interstitial sites, partially blocking interstitial diffusion paths for dopants such as boron and phosphorus (the so-called carbon enhanced suppressed diffusion [69], [70]). At sufficiently high doping concentrations, the presence of interstitial carbon might also cause a partial blockage of oxygen diffusion through interstitials during the oxidation process. Additionally, oxygen atoms can interact with interstitial carbon to form defect complexes, which would not contribute to oxidize silicon. Let us recall that the competition of such carbon-oxygen complexes formation with boron-oxygen ones was precisely the state-of-the-art of LGAD carbonation for harsh radiation environments [65].

With all that set forth, we could hypothesize that **higher levels of carbon concentration may lead to thinner screen oxides**. On one hand, this might explain the relatively low thicknesses of the screen oxide for 6LG2-v2 sensors prior to the N^{++} implantation when compared to those prior to the carbon and multiplication layer one. On the other hand, this might also explain the aforementioned turning point for the carbonation phenomena at an implantation dose value amidst 3 and $6 \cdot 10^{14} \text{ at/cm}^2$. If, at the carbon concentrations introduced in the device by such doses, the screen oxide is sufficiently reduced, phosphorus for the N^{++} layer would be implanted deeper into silicon, hence its subsequent annealing would neutralize more boron atoms in the multiplication layer. This effect was addressed in section 4.3 and recalled in Figure 5.36.

In a nutshell, the phosphorus implantation through a carbon-altered thinner screen oxide may counterbalance for the carbon enhanced suppressed diffusion (Figure 5.16), resulting in an LGAD with a lower boron peak in its multiplication layer, hence with a lower inner gain and V_{gl} and a greater V_{BD} .

Studies on oxygen diffusion reduction in carbon-doped silicon were reported in [89], [90]. However, these studies are based on thermal processes that are significantly different from the temperatures and times typically used for oxidations at the IMB-CNM. Furthermore, they were conducted at doping concentrations that were not representative of 6LG2-v2 devices, whether in terms of boron, carbon, or phosphorus. TCAD Sentaurus simulation were performed to investigate the growth of the screen oxide as a function of carbon concentration, finding no dependence at all. However, it is worth remarking that TCAD Sentaurus, by default, was neither able to predict the difference in screen oxide between the test wafer (highly-doped) and the process wafers (lightly-doped) of 6LG2-v2 detectors.

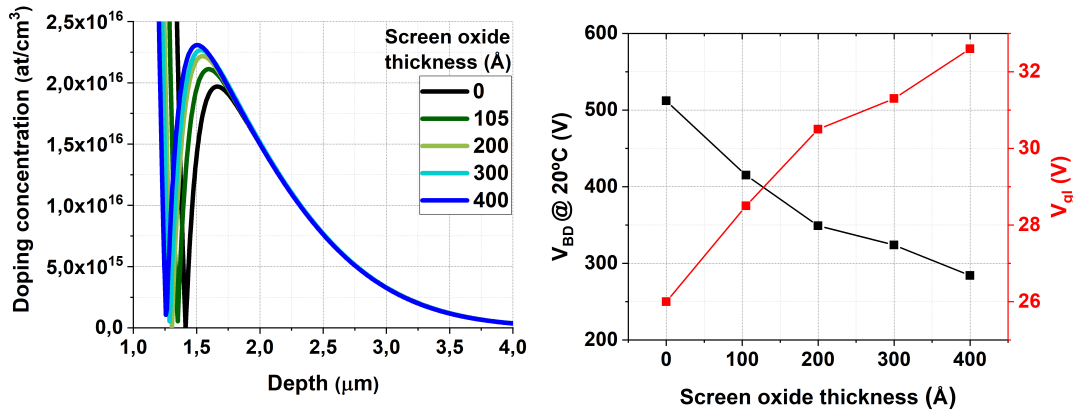


FIGURE 5.36: TCAD Sentaurus simulation of the doping profile, breakdown voltage at 20°C and V_{gl} for IMB-CNM LGADs of the 6LG2-v2 fabrication batch, as a function of the screen oxide growth prior to N^{++} layer implantation.

In light of this, it is crucial to rigorously challenge the hypothesis that high levels of wafer carbonation alter screen oxides and impact LGAD fabrication, as it may not hold true until actual scientific evidence is found.

5.6.2 Basic electrical characterization: IV and CV measurements at 20°C

To study the electrical characterization of 6LG2-v2 detectors, IV measurements were carried out on over 20 devices per carbon dose. The samples were analysed from various sections of the wafers. The guard ring was connected in every measurement to separate the surface from the bulk current. Figure 5.37 shows the averaged IV curves for every carbon dose at 20°C. It is important to highlight that, by the completion of the 6LG2-v2 run, CMS ETL requirements had been updated. The new specifications required LGAD performance measurements before irradiation to be conducted at 20°C (see Table 5.1). On the other hand, the V_{BD} of every device was inferred as in the 6LG2-v1 case (Figure 5.11). That is, by defining it as the voltage at which the IV curve abandons a quasi-linear trend and starts exhibiting an exponential behavior.

In addition, CV measurements were conducted on 20 devices for each carbon dose. Similar to the IV measurements, the devices were selected from various sections of the wafers. The CV curves were obtained with a Keysight Agilent 4284A LCR-meter in parallel mode, at 20°C, 10 kHz and 500 mV AC. The average CV curves are shown in Figure 5.38. The average V_{gl} was inferred using the same methodology as in for the 6LG2-v1 devices (illustrated in Figure 5.13). The average V_{gl} and V_{BD} dependence on carbon implantation dose for 6LG2-v2 sensors is depicted in Figure 5.39

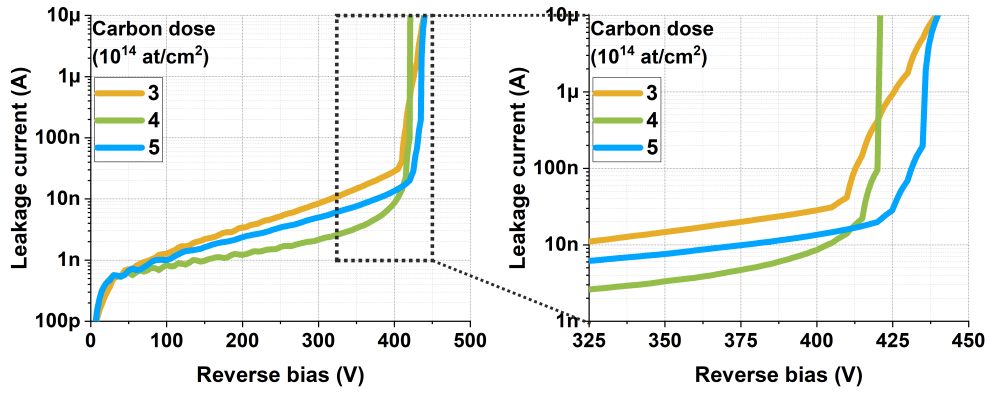


FIGURE 5.37: Averaged IV curves, at 20°C, of 6LG2-v2 detectors.

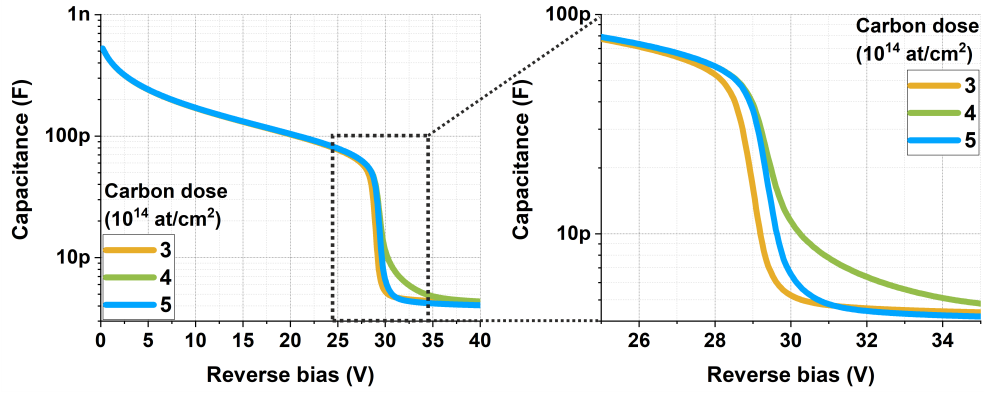
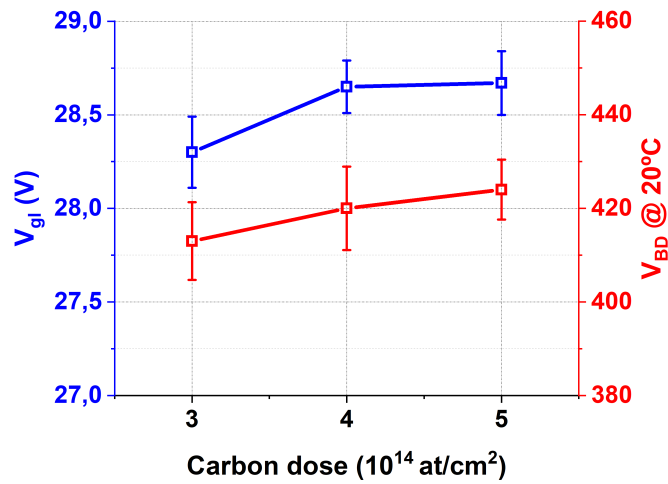


FIGURE 5.38: Averaged CV curves, at 20°C, of 6LG2-v2 detectors.

FIGURE 5.39: V_{gl} and V_{BD} dependence (at 20°C) on carbon implantation dose for 6LG2-v2 detectors.

For every carbon dose, the boron profiles in the multiplication layers were extracted from CV measurements, and their results are shown in Figure 5.40.

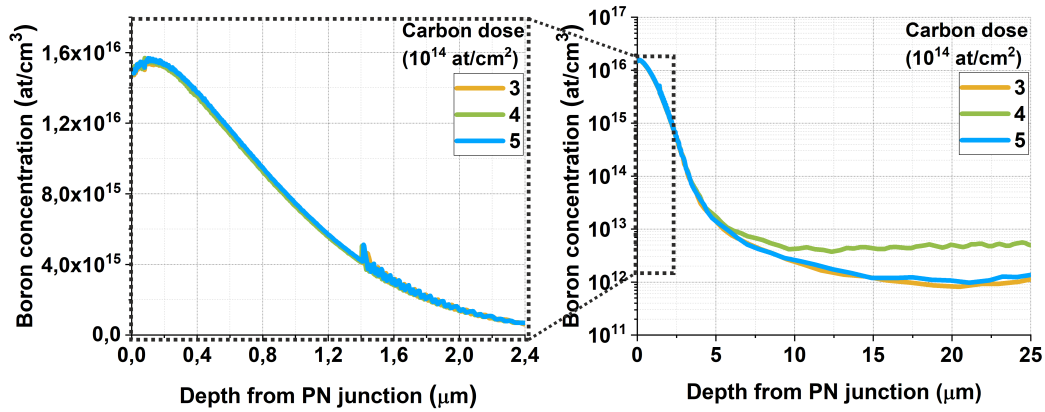


FIGURE 5.40: CV-extracted boron doping profiles for 6LG2-v2 detectors.

Let us review the main findings derived from the basic electrical characterization measurements. On one hand, the average V_{BD} and V_{gl} values do not confirm whether a turning point for the carbon-enhanced dopant suppression phenomenon exists. The differences between V_{BD} and V_{gl} as a function of carbon dose are slight, with some averaged values overlapping within the standard deviation bars. On the other hand, the boron peak extracted via CV measurements seem to be identical regardless of the carbon dose. As discussed earlier in this thesis, CV-extracted doping profiles do not offer information about the N^{++} depth or phosphorus concentration. Thus, an alternative technique is needed to effectively study the effects of carbon-enhanced diffusion suppression. The novel Spreading Resistance Profiling (SRP) equipment available at the IMB-CNM offers such an alternative. This method was used in LGADs to investigate this phenomenon. Before exploring SRP in detail, let us review the key basic electrical characterization results of 6LG2-v2 detectors and compare them to those from the 6LG3-v2 and 6LG2-v1 runs.

5.6.3 Comparative analysis of CMS 6LG2-v2 run with ATLAS-CMS engineering 6LG3-v2 run and ATLAS 6LG2-v1 run

In this section, the carbonation effects on LGADs will be set aside for a moment to provide a broader picture of how the different IMB-CNM LGAD runs have shown varying performance across each fabrication batch. Specifically, a comparison between the three carbonated IMB-CNM LGAD runs will be addressed. These include the ATLAS-CMS engineering 6LG3-v2 run (first in line when carbonation was added to the technology), the ATLAS 6LG2-v1 and the CMS 6LG2-v2 run, being the latter the matter at hand during the last sections.

IV measurements at -25°C were carried out in 20 6LG2-v2 devices (per carbon dose). These measurements were intended to study the leakage current versus irradiation fluence at the CMS ETL experiment temperature. Additionally, the inferred V_{BD} vs carbon dose at this temperature were also used to compare with the results from the 6LG3-v2 and 6LG2-v1 run. This is shown in Figure 5.41. In contrast to the IV measurements at 20°C for 6LG2-v2 sensors, a turning point for the V_{BD} at -25°C

seems to be spotted for a carbon dose of $4 \cdot 10^{14} \text{ at/cm}^2$. However, once again the differences are so slight that the values overlap within standard deviation errors.

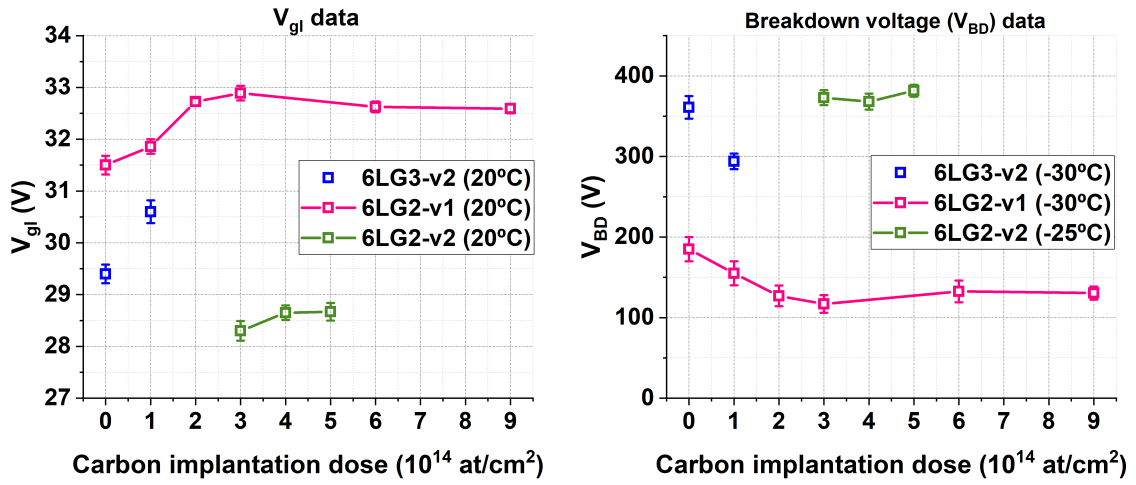


FIGURE 5.41: Average V_{gl} and V_{BD} data from 6LG3-v2, 6LG2-v1 and 6LG2-v2 detectors.

A comparison of CV-extracted doping profiles from these runs was also conducted. This is shown in Figure 5.42.

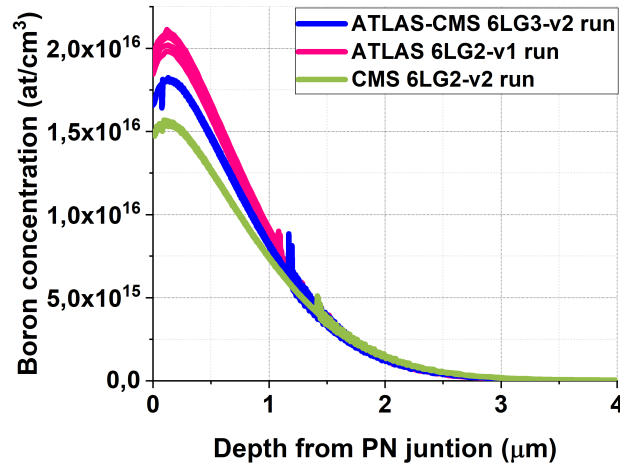


FIGURE 5.42: CV-extracted doping profiles for ATLAS-CMS 6LG3-v1, ATLAS 6LG2-v1 and CMS 6LG2-v2 IMB-CNM runs.

The results shown in Figures 5.41 and 5.42 lead to the same conclusion: **IMB-CNM LGADs from different runs fabricated under the same conditions do not result in identical devices.** While a dependence of LGAD performance on carbon implantation dose has been established, this effect alone cannot explain the variations observed among the different carbonated LGAD runs. Specifically, IMB-CNM fabricated LGADs under the same carbonation conditions have not demonstrated a consistent replicability. This highlights a missing point in a manufacturing process where, despite seemingly identical conditions, we have not consistently achieved the

same results due to certain factors not being accurately controlled or even accounted for. While monitoring the screen oxide points out to be a good starting point, there may be other parameters in the manufacturing process that also contribute to the observed variations and have yet to be fully understood.

However, the CMS 6LG2-v2 run is the first where all fabrication parameters, including the frequently mentioned screen oxide, were carefully controlled when using the new IMB-CNM furnace equipment. Therefore, calibrating its results with TCAD Sentaurus simulation represents a crucial first step toward stabilizing LGAD technology at the IMB-CNM. This will be addressed in section 5.6.5.

On the other hand, it is important to pause and make a few comments on the results shown in Figure 5.42. As stated in Chapter 4, the CV-extracted doping profiles are inferred with the formula [57]:

$$N(w) = \frac{2}{e\epsilon A^2} \left[\frac{\partial(1/C^2)}{\partial V} \right]^{-1}; w = \frac{\epsilon A}{C} \quad (5.1)$$

Conventionally in the literature, the LGAD area (A in Equation 5.1) is defined as the area enclosed by the p-stop, which is $1.3 \times 1.3 \text{ mm}^2$, as shown in Figure 5.35. Although this represents the depletion area when the device is operated over full depletion biases, only the multiplication layer is getting depleted before V_{gl} values are reached. As Figure 5.35 depicts, the effective area of this layer is $< 1.3 \times 1.3 \text{ mm}^2$, as it is limited to the adjacent JTE diffusions. For 6LG2-v2 detectors, such effective area is $1.22 \times 1.22 \text{ mm}^2$. As $N \propto A^{-2}$, using of $A = 1.3 \times 1.3 \text{ mm}^2$ (before V_{gl}) instead of the actual effective area results in an underestimation of the boron peak by a factor of ≈ 0.7 . Furthermore, the depletion width ($w \propto A^2$ in Equation 5.1) is overestimated by a factor of ≈ 1.2 . This is shown in Figure 5.43

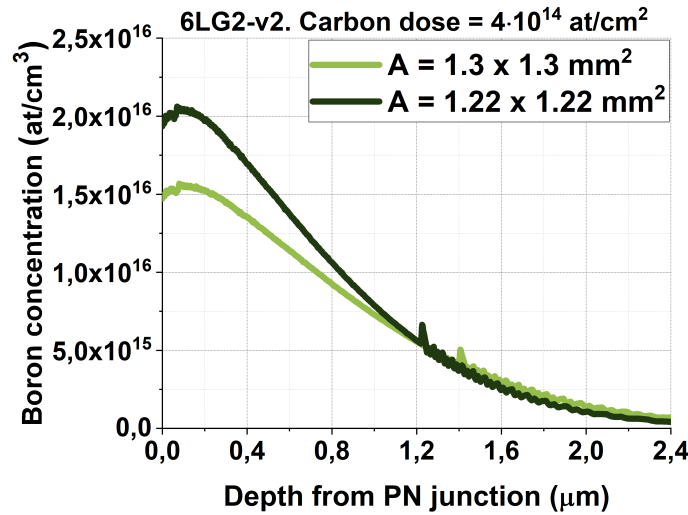


FIGURE 5.43: CV-extracted doping profiles for 6LG2-v2 detectors with a carbon dose of $4 \cdot 10^{14} \text{ at/cm}^2$.

It is important to note that this effect does not alter the qualitative results shown in Figure 5.42, as using a different value for A in Equation 5.1 would simply shift all the boron profiles together. This holds true as long as A does not vary significantly between devices, which is the case here. In another words, **it can be assured that ATLAS 6LG2-v1 detectors have the highest boron peaks, while CMS 6LG2-v2 sensors have the lowest.** Nevertheless, the results are not quantitatively accurate,

as demonstrated in Figure 5.43. Quantitative accuracy is crucial when comparing results with other techniques. Therefore, in section 4.3, TCAD Sentaurus simulated profiles were compared to CV-extracted ones using the actual effective area of the multiplication layer.

5.6.4 SRP of 6LG2-v1 and 6LG2-v2 samples

Another known approach to determine the doping profile of an LGAD sample is the aforementioned SRP. An overview of this reverse engineering technique can be found in [91], and is hereunder summarized.

To measure the doping profile as a function of depth, the device is diced at a specific angle, which exposes the internal layers of the sample. Two probes separated certain distance are placed on the surface of the diced sample. The probes are used to apply a small bias and measure the resulting current, from which the resistance can be inferred (Figure 5.44). Such resistance is influenced by the doping concentration at the depth through which the current flows.

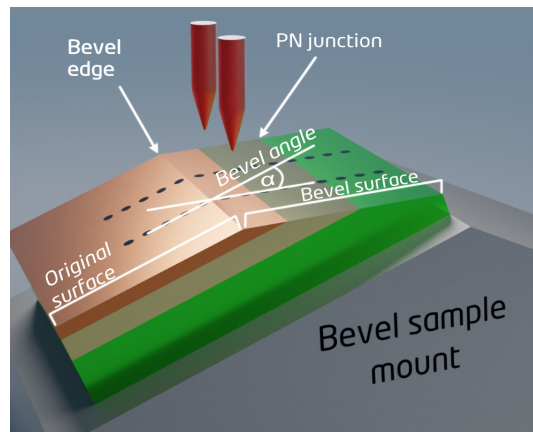


FIGURE 5.44: schematic of the SRP technique. Figure extracted from [92].

Calibration samples (which resistivity type and doping concentration are known) are measured prior to the sample under test. Thus, a relationship between the spreading resistance and the known resistivity and doping concentration is established. That is, a *calibration curve* is obtained, which is essential for converting the measured resistance of the sample into the actual doping concentration. An example of a P-type calibration curve is shown in Figure 5.45.

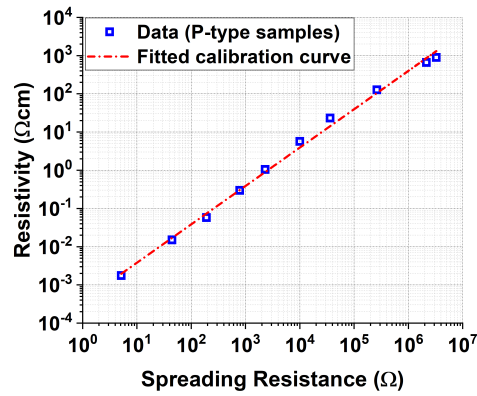


FIGURE 5.45: Example of a p-type calibration curve for SRP measurements. Such curve was used when studying the doping profiles of 6LG2-v1 detectors.

Additionally, an understanding of the conductivity type of the layers composing the sample is necessary beforehand. This information is crucial for determining the PN junction within the profile, which is manually identified in the raw spreading resistance data to apply the appropriate n-type or p-type calibration curves to each region. This process is illustrated in Figure 5.46.

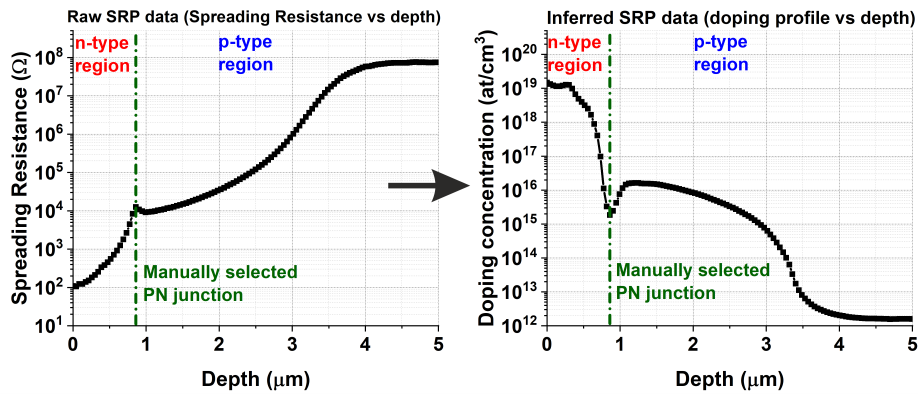


FIGURE 5.46: Example of doping profile extraction from raw spreading resistance data. The shown profile corresponds to a non-carbonated 6LG2-v1 LGAD.

It is important to note that the relationship between spreading resistance and resistivity presented in Figure 5.45 is valid for single-type samples (only p-type in the figure case). When inferring the resistivity of a PN junction sample via SRP, this calibration curve needs to be corrected to include *Junction Field* effects. Let us talk through it. In a PN junction, there is an intrinsic electric field due to the difference in doping concentrations between the p-type and n-type regions. This field can influence the distribution of charge carriers, particularly in the region close to the junction. When applying the SRP method to such a structure, the measured spreading resistance can be affected by this field, leading to inaccuracies in the inferred doping profiles, particularly near the junction. The software of the Semilab SRP-2100 equipment at the IMB-CNM accounts for junction field effects by incorporating

correction models derived from various studies [93]–[96]. Specifically, the software includes four models that can be selected to correct the spreading resistance around PN junctions. The quantitative values of the doping concentration depend on the model choice. This is illustrated in Figure 5.47, where the doping profile of a non-carbonated 6LG2-v1 device was obtained via SRP using each of the junction field correction models. In the figure, the *no model* plot corresponds to the doping profile inferred using the calibration curve in Figure 5.45 without any further correction.

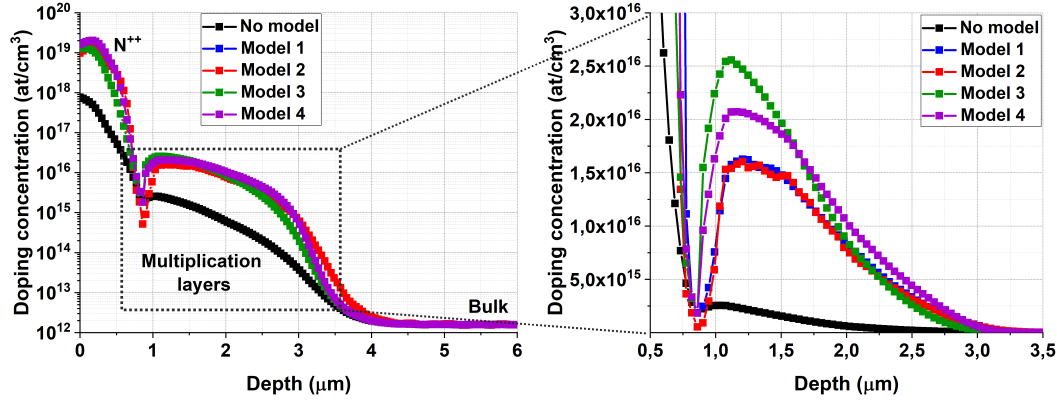


FIGURE 5.47: Doping profile around the PN junction for a non-carbonated 6LG2-v1 LGAD, obtained via SRP and with different junction field correction models.

As a novel technique, the appropriate junction field correction model to be applied to IMB-CNM LGADs was unknown at the time this thesis was completed. Thus, SRP doping profiles could not be quantitatively compared to those extracted using CV measurements or simulated using TCAD Sentaurus. Nevertheless, a qualitative approach could still be applied to extract some fundamental insights into the performance of carbonated LGADs. One ATLAS 6LG2-v1 LGAD per carbon dose and two CMS 6LG2-v2 LGADs per carbon dose were analysed using the SRP technique with the equipment Semilab SRP-2100. The results are shown in Figures 5.48 and 5.49. The profiles were obtained by using the junction field correction model labelled as *model 3* in Figure 5.47, which corresponds to the model labelled as *M1* if the reader refers to the Semilab SRP-2100 user guide [92].

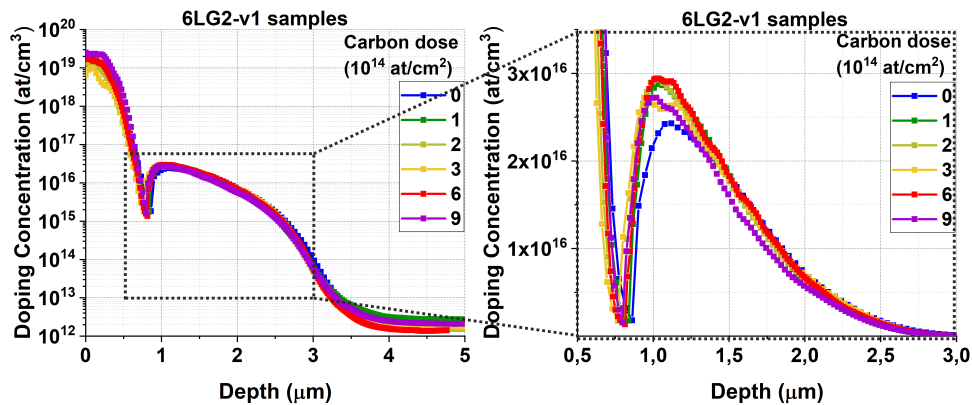


FIGURE 5.48: SRP doping profiles of ATLAS 6LG2-v1 LGAD samples.

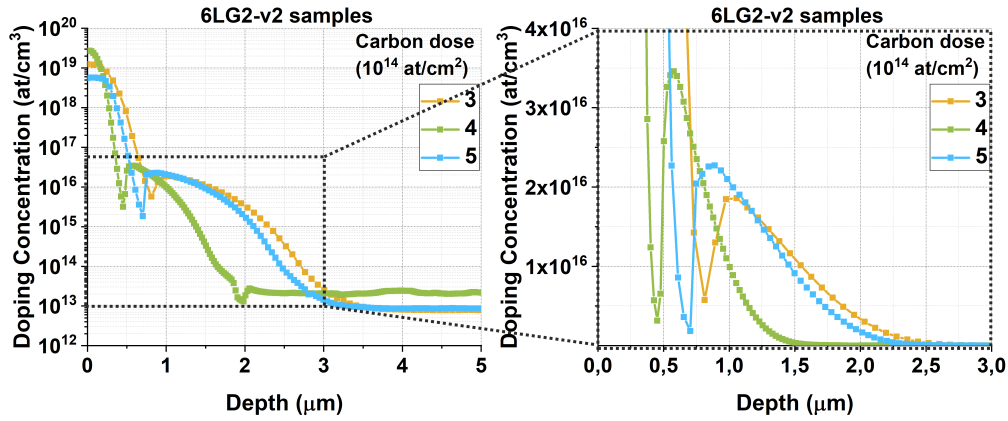


FIGURE 5.49: SRP doping profiles of CMS 6LG2-v2 LGAD samples.

As previously stated, in contrast to CV-extracted doping profiles, an SRP measurement allows us to infer the net active concentration including not only the depleted layers (multiplication and bulk), but also the N^{++} one. Additionally, the depth of such layers is accurately extracted from SRP measurements despite the junction field correction model used, which is inferred as it follows. The very surface of device (depth zero in Figures 5.48 and 5.49) is inferred by analysing the transition between the SiO_2 layer, where the software reads a spreading resistance virtually infinite, and the N^{++} , where the resistance drops from infinite to a certain value. The depth of such N^{++} layer (e.g. the PN junction depth) is then derived from the spreading resistance vs depth shape, as illustrated in Figure 5.46. As a result, an analysis of the PN junction depth dependence on carbon implantation dose can be carried out. The results are shown in Figure 5.50, indicating that a turning point in the carbon-enhanced suppressed diffusion effect for phosphorus is observed between implantation doses of 3 and $6 \cdot 10^{14} \text{ at/cm}^2$, consistent with previous measurements. Additionally, this turning point is estimated to occur around a dose of $4 \cdot 10^{14} \text{ at/cm}^2$. It is worth noting that, despite the significant difference in electrical performance between the 6LG2-v1 and 6LG2-v2 devices, their PN junctions for a carbon dose of $3 \cdot 10^{14} \text{ at/cm}^2$ are similar within error bars.

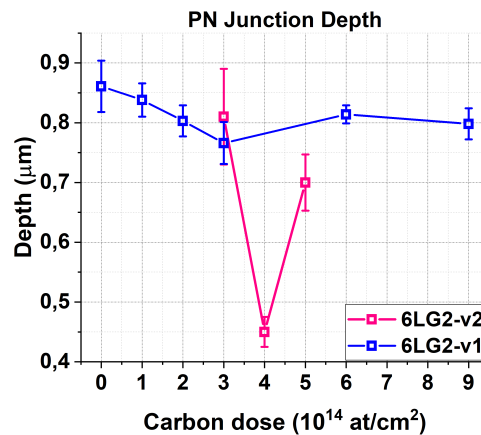


FIGURE 5.50: PN junction depth vs carbon implantation dose, extracted from SRP measurements.

The analysis of the SRP multiplication layer profiles is summarized in Figure 5.51. Specifically, the boron peak (which determines the maximum electric field at a given bias) and the charge integral (which shapes the electric field) were analyzed. As discussed in Chapter 4, the inner gain of an LGAD increases with both the multiplication layer's boron peak and its charge integral. To have qualitative insights into the LGAD performance inferred from SRP measurements, TCAD Sentaurus simulations of the V_{BD} and V_{gl} were conducted. In these simulations, the active thickness of the devices was fixed at $50\text{ }\mu\text{m}$ and the SRP PN junction profile was implemented for each case. The avalanche model used was the Van Overstraeten - De Man, set by default in TCAD Sentaurus, and the temperature was set at 20°C . The results are shown in Figure 5.52.

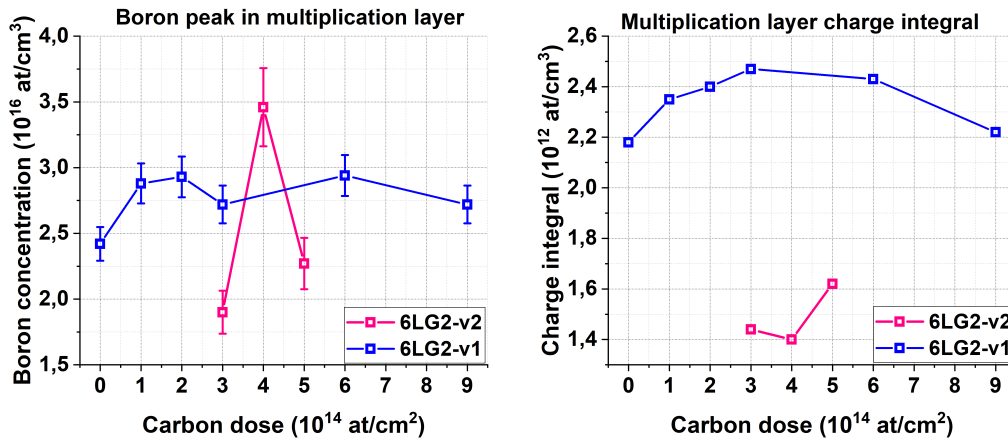


FIGURE 5.51: SRP extracted multiplication layer boron peak and charge integral for 6LG2-v1 and 6LG2-v2 detectors.

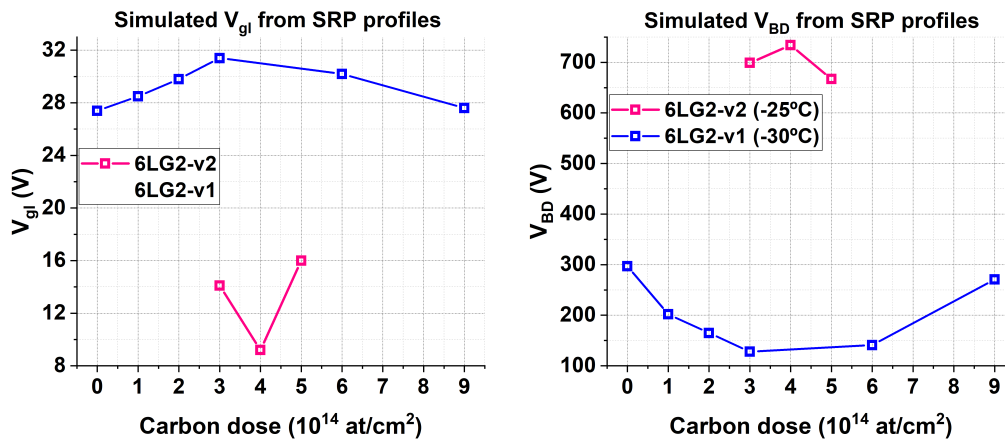


FIGURE 5.52: SRP-simulated V_{gl} and V_{BD} for 6LG2-v1 and 6LG2-v2 detectors, at 20°C .

The SRP-simulated electrical performance of ATLAS 6LG2-v1 sensors is phenomenologically identical to that extracted from actual IV and CV measurements. Specifically, the maximum V_{gl} and lowest V_{BD} at -30°C are achieved with a carbon

dose of $3 \cdot 10^{14} \text{ at/cm}^2$, where a turning point is observed. Conversely, the SRP-simulated performance of CMS 6LG2-v2 detectors does not match the results extracted from measurements, which suggested similar performance of the devices regardless the carbon dose. This underscores the importance of determining the appropriate junction field correction model for each manufacturing batch conditions.

In summary, the SRP analysis of 6LG2-v1 and 6LG2-v2 qualitatively demonstrated that **the carbon-enhanced suppressed diffusion of phosphorus shows a turning point around $4 \cdot 10^{14} \text{ at/cm}^2$** . However, further work is needed to refine the junction field correction models to better suit each fabrication scenario. This improvement will enhance the cross-checking of SRP results with actual measurements or TCAD Sentaurus simulations, which we are about to address.

5.6.5 TCAD Sentaurus simulation of CMS 6LG2-v2 detectors

In Chapter 4 (see section 4.3), a detailed overview was provided on how to fit TCAD Sentaurus models to predict the electrical performance of carbonated LGADs. Specifically, the electrical performance of 6LG2-v2 devices carbonated at an implantation dose of $4 \cdot 10^{14} \text{ at/cm}^2$ was studied. As mentioned, the 6LG2-v2 batch is the first to be fabricated at the IMB-CNM with the new furnace equipment and comprehensive knowledge of all fabrication parameters, which is crucial for adjusting TCAD Sentaurus models to match actual measurements. In particular, the diffusivity of boron and phosphorus through interstitials was tuned during the simulation calibration, as studies have reported that these diffusion paths are altered in silicon in the presence of carbon. These adjusted diffusivity parameters accurately predicted all V_{gl} , V_{BD} and CV-extracted boron profiles of 6LG2-v2 LGADs carbonated at a dose of $4 \cdot 10^{14} \text{ at/cm}^2$. However, the same parameters did not accurately predict the performance of 6LG2-v2 devices with different carbon doses, as shown in 5.53.

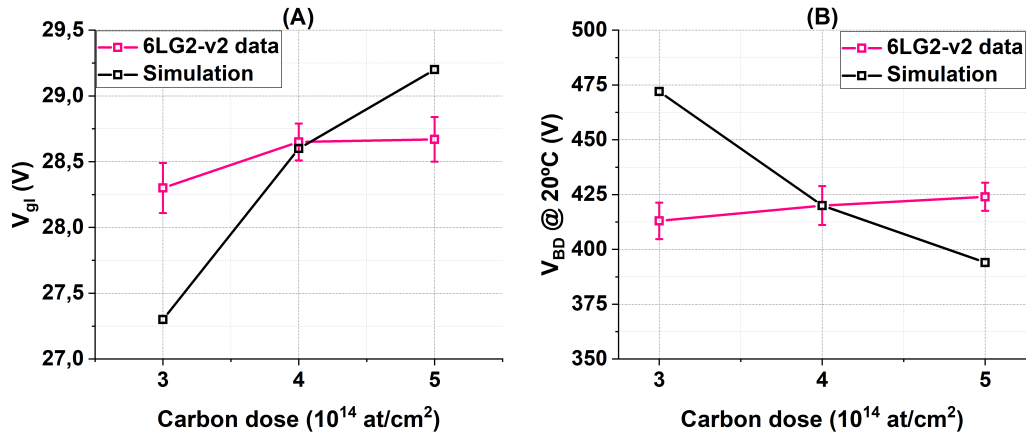


FIGURE 5.53: TCAD Sentaurus predicted V_{gl} (A) and V_{BD} , at 20°C , of 6LG2-v2 detectors after diffusivity model calibration.

This result suggests that **the diffusivity of boron and phosphorus is not only depend on the presence of carbon itself, but on its actual concentration around the PN junction**. Thus, further work is needed in order to understand how the diffusivity parameters can be parameterized in every LGAD fabrication scenario.

5.6.6 IV measurements of CMS 6LG2-v2 pixelated detectors

Five 6LG2-v2 segmented LGADs of 16x16 pixels were IV tested at the University of Science and Technology of China (USTC). The location on wafer of the tested devices is shown in Figure 5.54

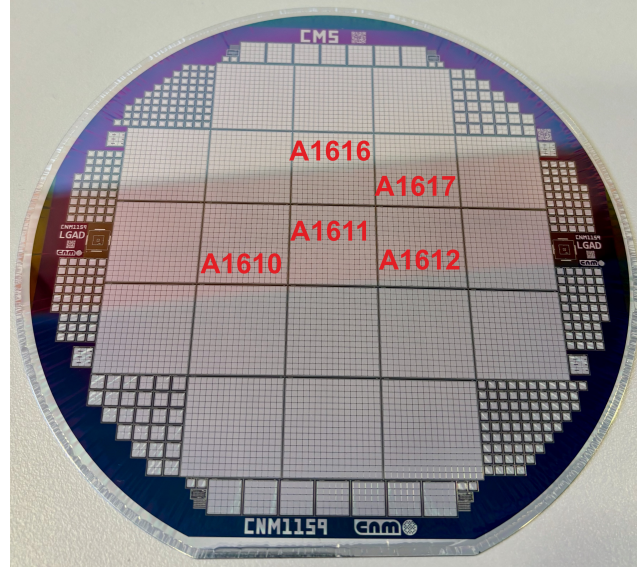


FIGURE 5.54: On wafer location of tested devices.

The measurements were performed as described for ATLAS 6LG2-v1 segmented detectors in section 5.5.7, obtaining pixel-by-pixel IV testing at 20°C. The total leakage current for every tested devices is shown in Figure 5.55 (A), along with the average leakage current per pixel (B). The first result that we can infer is that the average leakage current per pixel is lower for CMS 6LG2-v2 segmented detectors than those corresponding to the ATLAS 6LG2-v1 run.

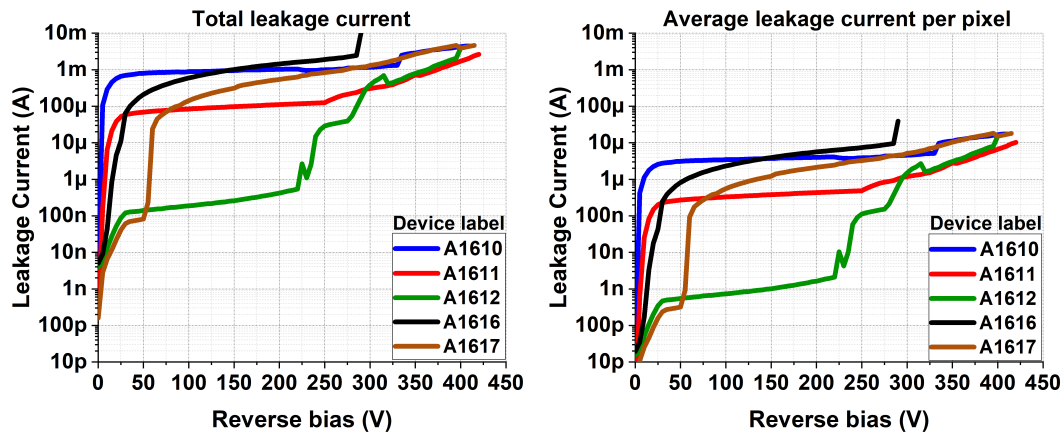


FIGURE 5.55: Total Leakage current (A) and average leakage current per pixel (B) of 6LG2-v2 segmented detectors of 16x16 pixels, measured with a probe card at 20°C in USTC.

Single-pad detectors from the 6LG2-v2 batch have yet to be tested for their timing response or CC for a mip before irradiation. Thus, their V_{op} to fulfill the ATLAS HGTD and CMS ETL specifications was not available at the time this thesis was completed. However, an estimation of the CMS 6LG2-v2 segmented detectors yield can be inferred by comparing to the same criteria as we did with ATLAS 6LG2-v1 detectors of 15x15 pixels. Specifically, by evaluating the number of pixels per device that, at 20°C and 100 V, have not exceeded the 200 nA leakage current limit set by ATLAS and CMS, we can directly compare how IMB-CNM technology has improved in fabricating large segmented detectors. The results are shown in Table 5.11 and Figures 5.56 and 5.57 highlighting that, under the same criteria, CMS 6LG2-v2 segmented LGADs have a better behavior than ATLAS 6LG2-v1 ones.

6LG2-v1 Device Label	% Pixels with $i_L < 200 \text{ nA at } 100 \text{ V}$	6LG2-v2 Device Label	% Pixels with $i_L < 200 \text{ nA at } 100 \text{ V}$
		A1610	98.4
A13	92.4	A1611	99.6
A14	93.3	A1612	100
A19	96.4	A1616	99.2
		A1617	99.6

TABLE 5.11: Percentage of pixels in segmented ATLAS 6LG2-v1 and CMS 6LG2-v2 detectors (measured at 20°C with a probe-card at USTC) that do not exceed 200 nA of leakage current up to 100 V.

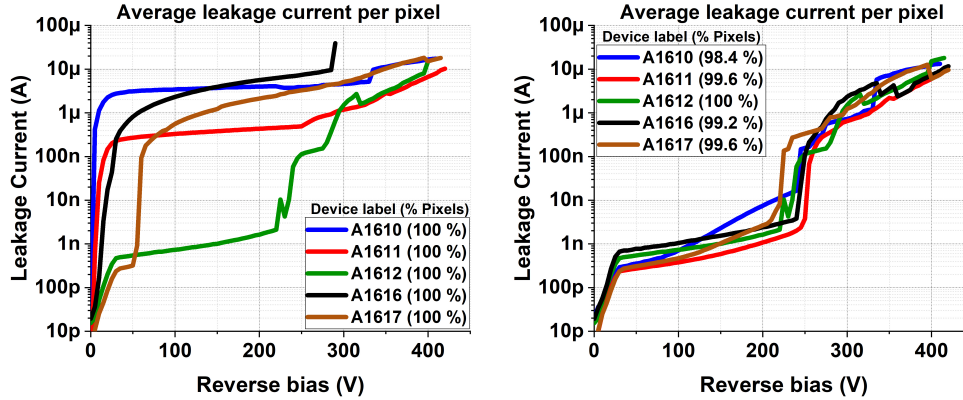


FIGURE 5.56: Average leakage current per pixel of 6LG2-v2 segmented detectors of 16x16 pixels, measured with a probe card at 20°C (USTC) [87].

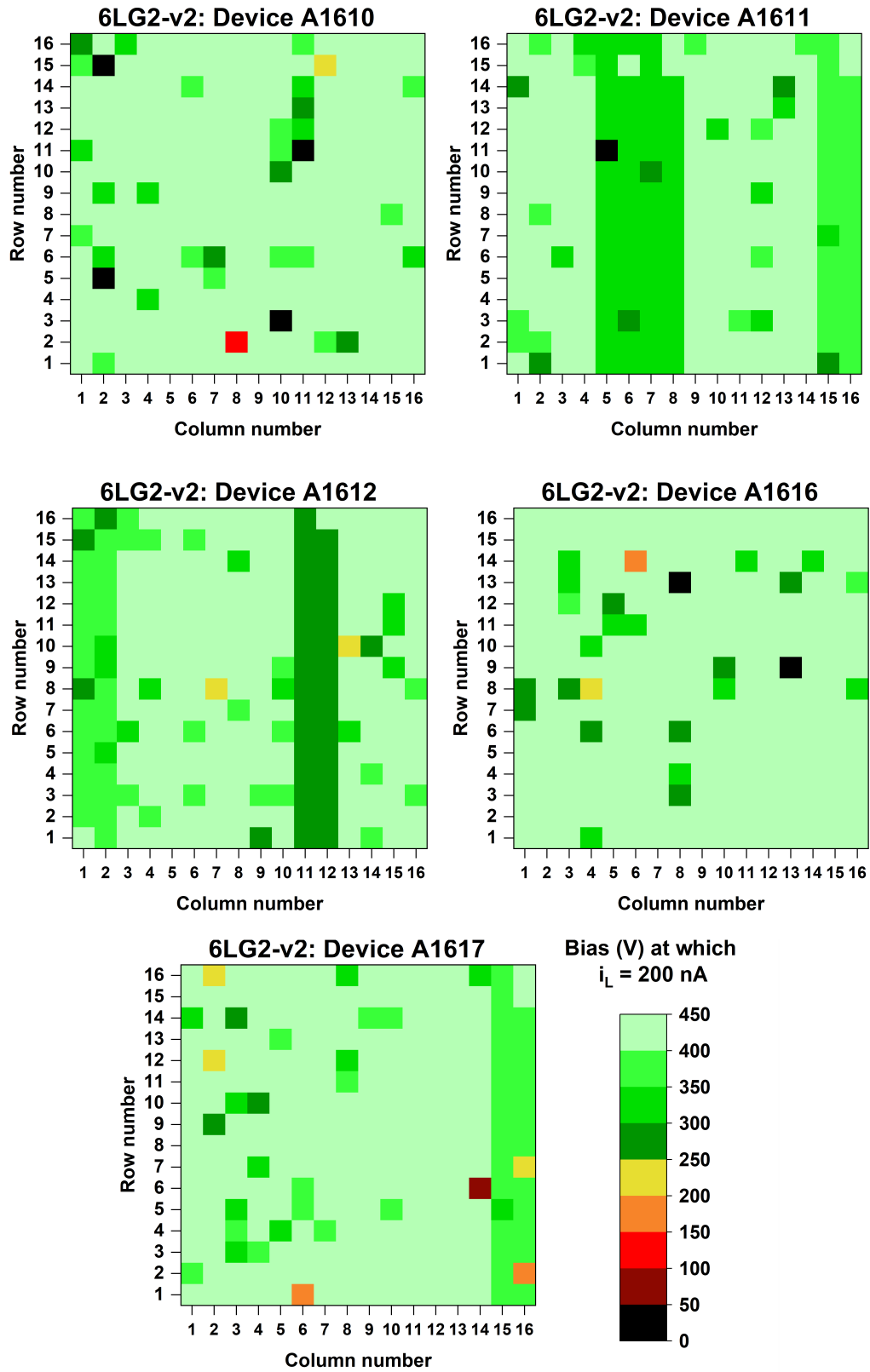


FIGURE 5.57: Color code mapping of the reverse bias at which every pixel reaches 200 nA of leakage current, for 6LG2-v2 segmented detectors IV measured with a probe card at 20°C.

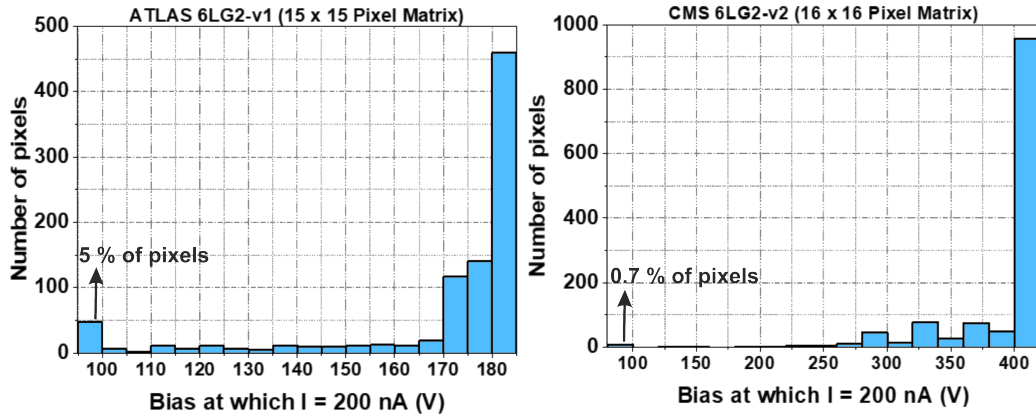


FIGURE 5.58: Histogram showing the number of ATLAS 6LG2-v1 and CMS 6LG2-v2 pixels that reach 200 nA of leakage current, at 20°C, and its dependence on reverse bias.

As displayed in Table 5.11 and Figures 5.56, 5.57 and 5.58, most of the tested 6LG2-v2 segmented detectors with 16x16 pixels exhibit yields approaching 100%. However, it is important to note that these yield values are only preliminary, as the operating voltage (V_{op}) for these detectors has not yet been determined. Additionally, the basic electrical characterization of single-pad 6LG2-v2 detectors suggests that their inner gain is lower to that of ATLAS 6LG2-v1 devices. If this is confirmed, V_{op} is expected to exceed 100 V, which could significantly reduce the yield values listed in Table 5.11. Thus, the measurements presented in this section can only confirm that **the CMS 6LG2-v2 segmented detectors exhibit a better performance (e.g. lower leakage current) than the ATLAS 6LG2-v1 ones from a technological standpoint**, but not to the extent of specifically fulfilling the ATLAS HGTD or CMS ETL requirements.

5.7 IMB-CNM 6DLG technology: Deep Profile LGADs

The results presented in the previous sections not only demonstrated the need for rigorous technological stabilization but also highlighted a limitation. Specifically, the radiation tolerance of traditional IMB-CNM LGADs seemed to be constrained by the carbon implantation dose turning point for the dopant suppressed diffusion phenomenon. In this section, we will present an overview of the developing *Deep Profile* LGAD technology (*dLGAD* for short) at the IMB-CNM. dLGADs have continuously demonstrated higher radiation tolerance compared to traditional IMB-CNM LGADs, with acceptor removal constant values below $2 \cdot 10^{-16} / \text{cm}^2$ [97]–[100]. Figure 5.59 schematically depicts what is meant by a deep profile. In a traditional LGAD, the N^{++} layer and the multiplication layer overlap, and their net charge distribution defines the profile. In a dLGAD, the multiplication layer is placed deeper relative to the N^{++} layer, resulting in a narrow separation between them where the doping concentration corresponds to bulk values. As a result, the overlap between the n-type N^{++} and the p-type multiplication layer is non-existent.

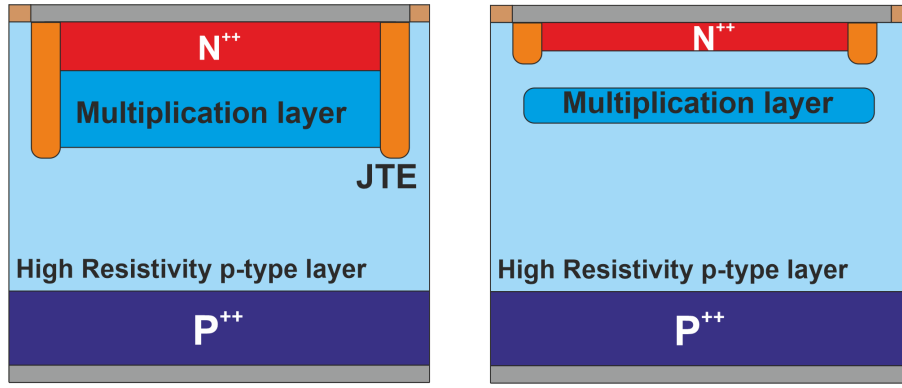


FIGURE 5.59: Schematically representation of the differences in the PN junction of an LGAD and a dLGAD.

While the term "deep profile" may be instructive, it is worth remarking that dLGADs typically have their N^{++} and multiplication layers located closer (shallower) to the device surface and not deeper into the bulk, as shown in Figure 5.60. This is a direct result of the difference in how such layers are implanted, diffused and activated when compared to a traditional LGAD, matter that will short be addressed.

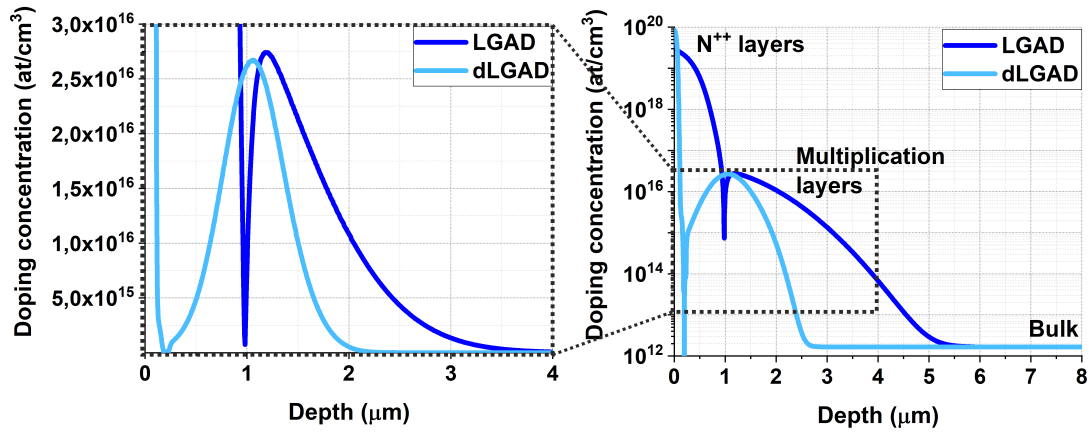


FIGURE 5.60: TCAD Sentaurus simulation of the typical doping profile of an LGAD and a dLGAD

Additionally, the electric field profile of a dLGAD deviates from the sharp peak shape of an LGAD, exhibiting a quasi-flat shape around the PN junction (Figure 5.61). However, the basic functioning of a dLGAD is the same as that of an LGAD. That is, both devices create an electric field around their PN junctions when reverse biased, which is strong enough to trigger the avalanche mechanism and cause charge multiplication during particle detection experiments.

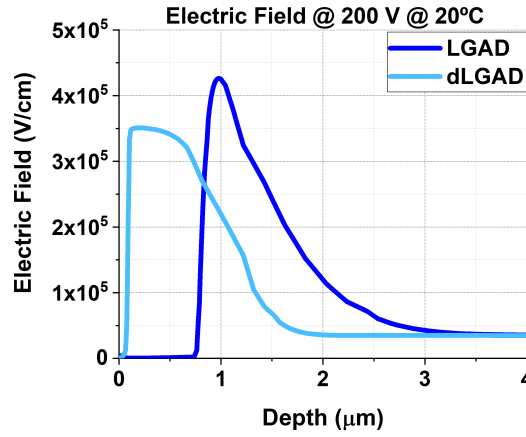


FIGURE 5.61: TCAD Sentaurus simulation of the electric field (at 20°C and 200 V) of an LGAD and a dLGAD

Table 5.12 shows the main differences in the implantation and annealing processes used to obtain an LGAD or a dLGAD at the IMB-CNM. Setting aside carbonation, the difference in implantation energy for boron and phosphorus must be much larger in dLGAD compared to LGAD devices to avoid the overlap between the multiplication and N^{++} layers. Additionally, the boron implantation dose in dLGAD sensors need to be reduced to prevent the doping profile from being high enough to cause Geiger mode behavior in the device. Lastly, the annealing time for a dLGAD is about 1 minute, so it is a so-called Rapid Thermal Annealing or RTA. This short annealing period helps to prevent the multiplication layer from spreading towards the N^{++} and also ensures that the boron peak remains sufficiently large to trigger the avalanche mechanism when biased, thereby avoiding to end up with a PiN detector.

	LGAD	dLGAD
Boron implantation dose in multiplication layer (at/cm^2)	$\sim 10^{13}$	$\sim 10^{12}$
Boron implantation energy in multiplication layer (keV)	100	> 400
Phosphorus implantation dose in N^{++} ($10^{14} at/cm^2$)	5 & 10	10
Phosphorus implantation energy in N^{++} (keV)	150 & 70	30
Annealing of boron in multiplication layer	180 min at 1100°C	≈ 1 min at 1100°C
Annealing of phosphorus in N^{++} layer	30 min at 1000°C	≈ 1 min at 1100°C
Screen oxide prior to boron implantation (\AA)	~ 100	
Screen oxide prior to phosphorus implantation (\AA)	~ 100	

TABLE 5.12: Overview of the differences in implantation and annealing processes for LGAD and dLGAD fabrication.

The reasons why dLGAD have higher radiation tolerance than LGAD detectors remain a hot topic in the HEP field. This thesis will focus on the technological challenges and advantages that dLGAD presents compared to traditional IMB-CNM LGAD.

5.7.1 Design and fabrication of the first dLGAD prototypes: CMS 6DLG2-v1 run

The first dLGAD prototypes at the IMB-CNM were manufactured on 150 mm high-resistivity p-type Si-Si wafers (6DLG2-v1 run) with the CNM1159 mask (Figures 5.34 and 5.35), which is mainly comprised by LGADs of 16×16 $1.3 \times 1.3 \text{ mm}^2$ pixels with an IP of $80 \text{ }\mu\text{m}$. As well as in the 6LG2-v2, the basic electrical characterization was performed on single-pad detectors. Table 5.13 shows the fabrication parameters for the 6DLG2-v1 PN junction. This manufacturing strategy was partially designed using TCAD Sentaurus simulations and partially reproduced from previous IMB-CNM productions. On one hand, the implantation scheme of multiplication and carbon layers was designed via TCAD Sentaurus by default (v2018.06), as the diffusivity parameters that were calibrated to predict the electrical performance of 6LG2-v2 devices had not yet been determined by the time this run was completed. On the other hand, the implantation parameters of the N^{++} , along with the RTA recipe to activate such layer and the multiplication one were based on previous strategies. These implantation and RTA techniques had demonstrated their ability to activate, at a sufficient extent to serve as electrodes, boron and phosphorus shallow layers in previous IMB-CNM fabricated detectors. It is worth remarking that the actual value of the screen oxide grown prior to the carbon, multiplication and N^{++} layers was not measured on the process wafers but only on the test wafer (yielding a typical value of $375 \text{ }\text{\AA}$).

One of the primary advantages of manufacturing dLGAD compared to traditional LGAD is the reduction in the number of thermal processes required for it. In conventional LGAD, carbon and boron are co-implanted and then annealed together at 1100°C for 180 minutes. Following this, phosphorus is implanted to create the N^{++} layer, which requires an additional annealing step at 1000°C for 30 minutes. In contrast, dLGAD follows a similar implantation sequence (carbon, boron, and phosphorus), but all dopants are activated in a single RTA process lasting just one minute. Furthermore, the short RTA times prevent boron and phosphorus from co-diffusing with carbon for extended periods. As a result, **the carbon-enhanced suppressed diffusion phenomenon is expected to be minimal in dLGAD** compared to traditional LGAD.

	W1	W2	W3
Carbon implantation dose in multiplication layer (10^{13} at/cm^2)	5		
Carbon implantation energy in multiplication layer (keV)	480		
Boron implantation dose in multiplication layer (10^{12} at/cm^2)	2.5	2.6	2.7
Boron implantation energy in multiplication layer (keV)	480		
Phosphorus implantation dose in N^{++} layer (10^{14} at/cm^2)	10		
Phosphorus implantation energy in N^{++} layer (keV)	30		
Annealing of boron (phosphorus) in multiplication (N^{++}) layer	30 s at 1100°C + 30s at 1050°C		
Screen oxide prior to boron and carbon implantations (\AA)	~ 100		
Screen oxide prior to phosphorus implantation (\AA)	~ 100		

TABLE 5.13: Fabrication features for 6DLG2-v1 run.

Figure 5.62 shows the TCAD Sentaurus prediction of the dLGAD carbon and PN junction profiles. Let us talk through them.

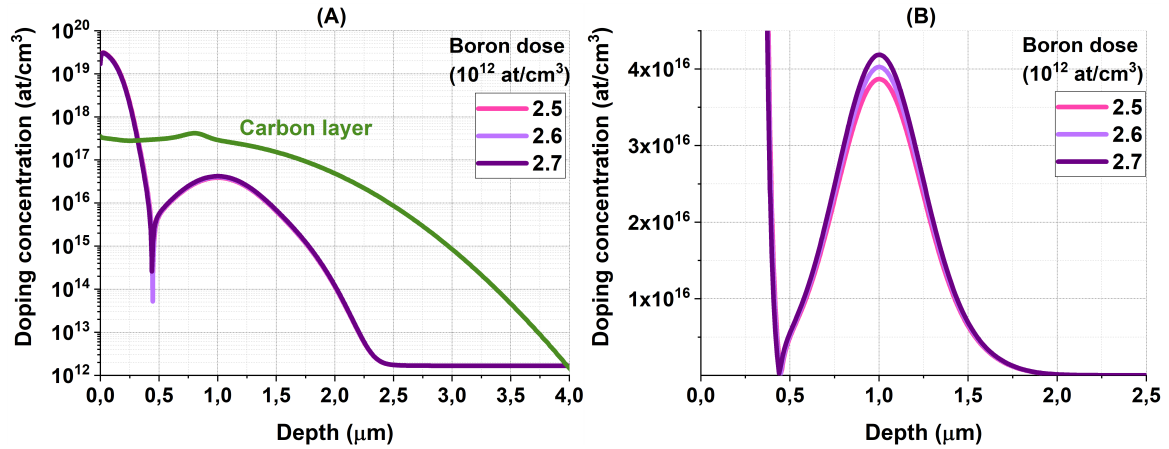


FIGURE 5.62: TCAD Sentaurus prediction of the PN junction and carbon layers of 6DLG2-v1 run. (A): PN and carbon layers in logarithmic scale. (B): Multiplication layer in linear scale.

On one hand, the carbon implantation dose was kept constant while the boron dose was varied. Since no dLGAD had been fabricated at the IMB-CNM before, this approach aimed to identify a boron implantation dose that would enable the production of a device with low inner gain, rather than optimizing the carbonation process for radiation tolerance. On the other hand, the ratios between carbon and boron doses were maintained as in the previous 6LG2 runs, ensuring that the carbon profile had a doping concentration of approximately one order of magnitude higher

than the boron concentration. As previously stated, the N^{++} layer was constructed such as previous IMB-CNM productions to ensure its reliability as an electrode.

Figure 5.63 shows the Sentaurus simulated V_{gl} and V_{BD} dependence on the chosen boron implantation doses. Such doses correspond to those where the simulated breakdown voltage was low enough to compensate potential *partial activation* of boron [101]. In short, this effect occurs when only some of the implanted boron atoms successfully locate in active lattice sites to contribute to p-type conductivity, while others remain in a non-active state due to incomplete annealing. Nevertheless, this approach was merely prudential, as several studies have reported full activation of boron at $T \geq 1000^\circ\text{C}$ with higher doses and shorter RTA times than those used in the 6DLG2-v1 run [102], [103]. Lastly, it is worth mentioning that the simulated V_{BD} and V_{gl} were independent on carbon implantation dose (over the range $1\text{-}10 \cdot 10^{13} \text{ at/cm}^2$) for a given boron dose, **which demonstrated, at least theoretically, that carbon-enhanced diffusion suppression did not operate for dLGAD devices as it does for LGADs.**

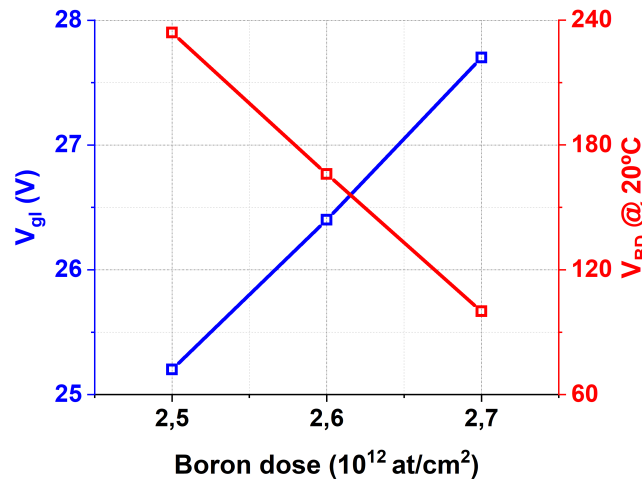


FIGURE 5.63: TCAD Sentaurus prediction of V_{gl} and V_{BD} for 6DLG2-v1 devices.

Before presenting the basic electrical characterization of 6DLG2-v1 detectors, it is worth making a pause to discuss some changes in the periphery elements construction that had to be addressed before starting the fabrication.

5.7.2 Optimization of the periphery elements in a dLGAD

On one hand, adjustments were required regarding the JTE thermal annealing process. For a traditional LGAD, the JTE is diffused at 1000°C for 30 min before starting the multiplication layer photolithography. This is sufficient for the JTE to perform its function effectively, given the full LGAD thermal load (Figure 5.64 (A)), that includes extra thermal steps at 1100°C for 180 min (multiplication layer annealing) and at 1000°C for 30 min (N^{++} annealing).

The substitution of such steps for an RTA could make insufficient a single annealing at 1000°C for 30 min for the JTE to work properly, as Figure 5.64 (A) depicts. Since dLGAD was a technology under development at the IMB-CNM, assuring a proper separation of the N^{++} and multiplication layer during fabrication was under question upon first prototypes manufacturing. With the standard annealing for

LGAD, the JTE profile does not fully cover the multiplication layer of a dLGAD, so it would be uncertain whether electric field edge effects are effectively mitigated or not. This setback was addressed by modifying the JTE annealing process from the typical 1000°C for 30 minutes (prior to the multiplication layer photolithography) to 1100°C for 180 minutes. As Figure 5.64 (B) shows, this would ensure the JTE functionality for a dLGAD.

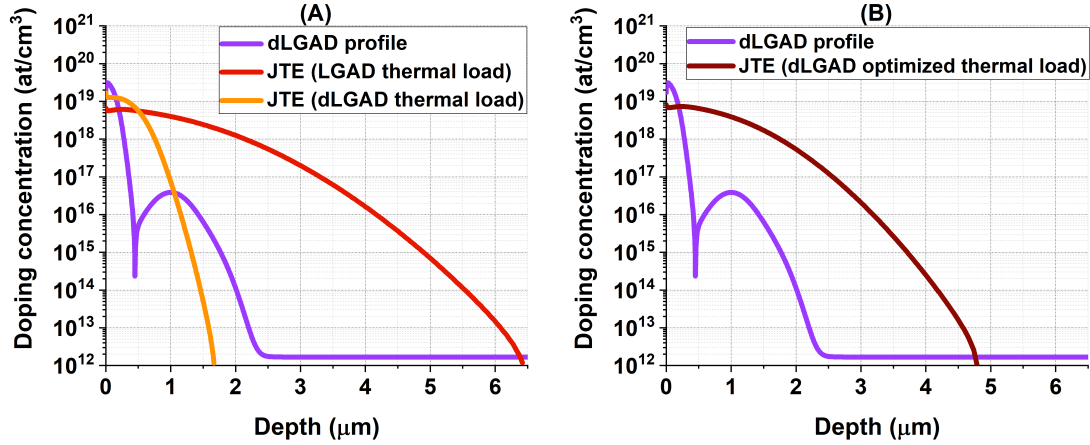


FIGURE 5.64: TCAD Sentaurus simulation of the JTE (at different thermal loads) and multiplication layer for 6DLG2-v1 detectors.

The modification of the full thermal load for dLGAD also affects the p-stop and channel stopper profiles. However, the optimized annealing process for the JTE in dLGAD devices compensates for this, maintaining reasonable values for these peripheral elements to function effectively (Figure 5.65).

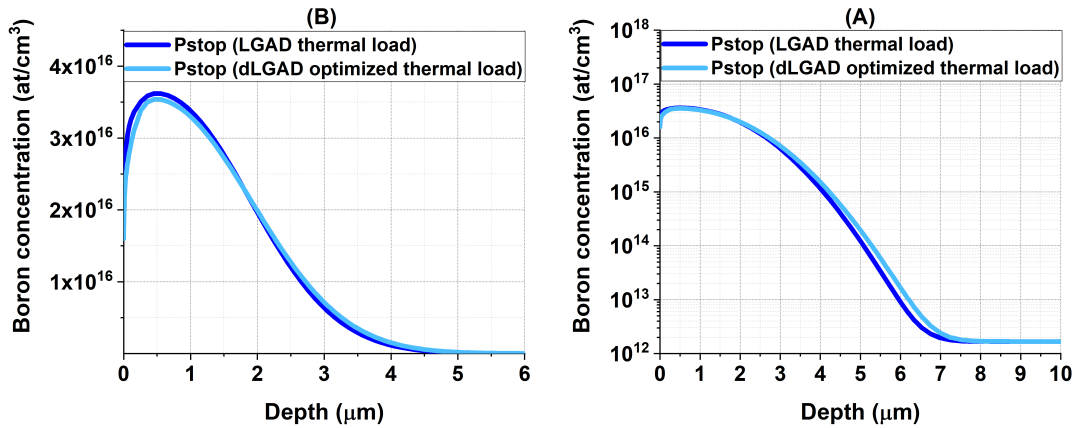


FIGURE 5.65: TCAD Sentaurus simulation of the p-stop and channel stopper profiles for 6LG2-v2 and 6DLG2-v1 devices. (A): logarithmic scale. (B): linear scale.

As stated in Chapter 3, the p-stop and JTE are manufactured prior to the core elements. For traditional LGAD devices, during the 100 keV boron and 150 keV carbon implantation in the active area, the oxide grown in previous thermal steps is

thick enough to block these ions from being implanted outside the core. This does not hold for dLGAD, as boron and carbon ions are implanted at much higher energy. In this case, an extra oxide layer is needed over the periphery elements to prevent them from being doped with unwanted impurities, which may, in turn, increase leakage current due to lattice distortion. As Figure 5.66 shows, about $1.5\ \mu\text{m}$ of oxide is needed to stop 480 keV boron and carbon ions. As the oxide thickness in the periphery elements was measured to be $\geq 0.6\ \mu\text{m}$ after the JTE optimized annealing, this setback was solved by depositing a $0.9\ \mu\text{m}$ of oxide just before the multiplication layer photolithography. The deposition technique was chosen over oxidation in a furnace to prevent both the loss of silicon thickness in the active volume and the alteration of the p-stop and JTE profiles close to the device surface.

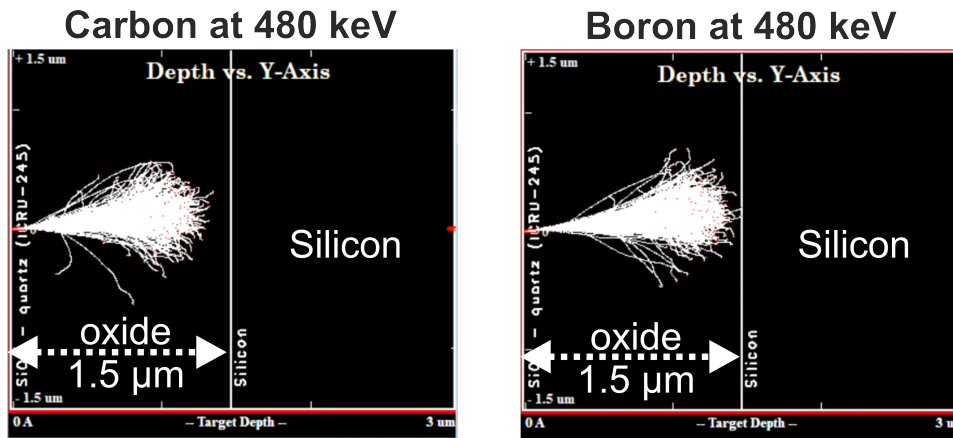


FIGURE 5.66: 480 keV carbon and boron ions distribution as they pass through a $1.5\ \mu\text{m}$ of oxide, obtained via Stopping and Range of Ions in Matter (SRIM) simulation [104].

A similar drawback is also encountered in dLGAD fabrication during the last implantation step: 30 keV phosphorus for the N^{++} and guard ring layers. In traditional LGAD, the annealing of the multiplication layer (1100°C for 180 min) grows a thick enough oxide layer ($\approx 0.6\ \mu\text{m}$) to completely prevent phosphorus ions from being implanted at the cutlines between adjacent devices on the wafer. In the original dLGAD design, there was no thermal step in between the multiplication and the N^{++} implantation steps, so the oxide at the cutlines remained close to its native thickness ($\approx 0.003\ \text{\AA}$). As Figure 5.67 shows, about $0.1\ \mu\text{m}$ of oxide is needed to stop 30 keV phosphorus ions. Thus, the implantation of phosphorus at the cutlines through the native oxide would create a floating PN junction, i.e. a PN junction not properly covered by a JTE element, around the edge of the device. This is undesirable, as it would fail to mitigate the punch-through phenomenon between the channel stopper and the guard ring, hence the device would be more likely to suffer early breakdown. Given the thinness of the oxide needed to prevent the 30 keV phosphorus ions from being implanted at the cutlines between adjacent devices, it was grown via oxidation in a furnace. The thermal process was performed in two steps: a wet oxidation at 800°C for 100 minutes, followed by a dry oxidation at 950°C for 84 minutes. At this relatively low temperature, the diffusion of dopants such as boron, phosphorus, and carbon in the already implanted regions remains minimal [54]. Additionally, the dry oxidation step served to re-grow a screen oxide for the subsequent phosphorus implantation for the N^{++} and guard ring.

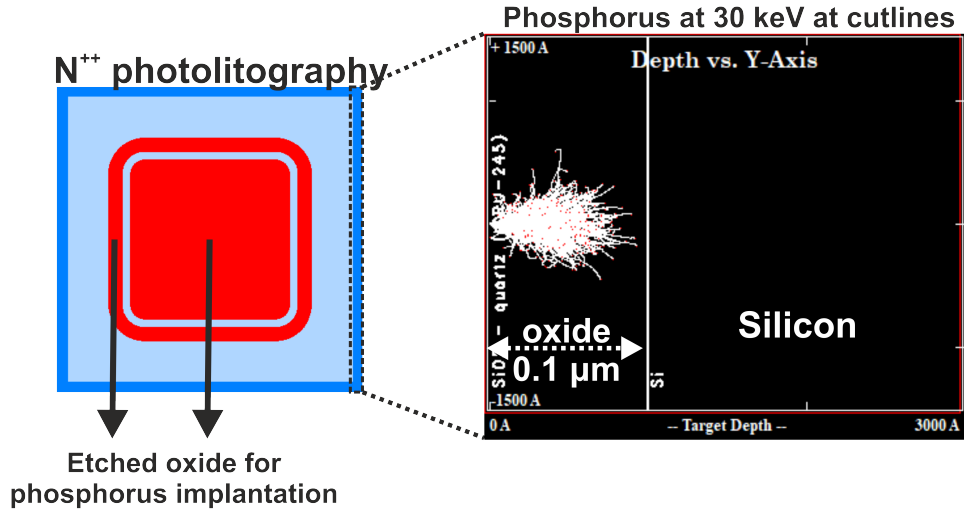


FIGURE 5.67: 30 keV phosphorus ions distribution as they pass through a $0.1 \mu\text{m}$ of oxide grown onto the cutlines, obtained via SRIM simulation [104].

5.7.3 Basic electrical characterization: IV and CV measurements of 6DLG2-v1 detectors

The average IV and CV curves of 6DLG2-v1 devices, at 20°C , are shown in Figure 5.68. The measurements were carried out using the same equipment as described for the CMS 6LG2-v2 run, and over 10 devices randomly allocated across the wafer were measured. On one hand, the V_{gl} was found to differ significantly from the values predicted by TCAD Sentaurus simulation with its default 2018.06 version. At this point, it is worth remarking that the simulation using the CMS 6LG2-v2 calibrated diffusivity parameters resulted in minimal changes to the 6DLG2-v1 V_{gl} prediction shown in Figure 5.63. That is, **neither the default nor the CMS 6LG2-v2 tuned diffusivity parameters were able to predict the V_{gl} of 6DLG2-v1 devices.** This highlights the importance of addressing TCAD Sentaurus models separately for each LGAD technology. .

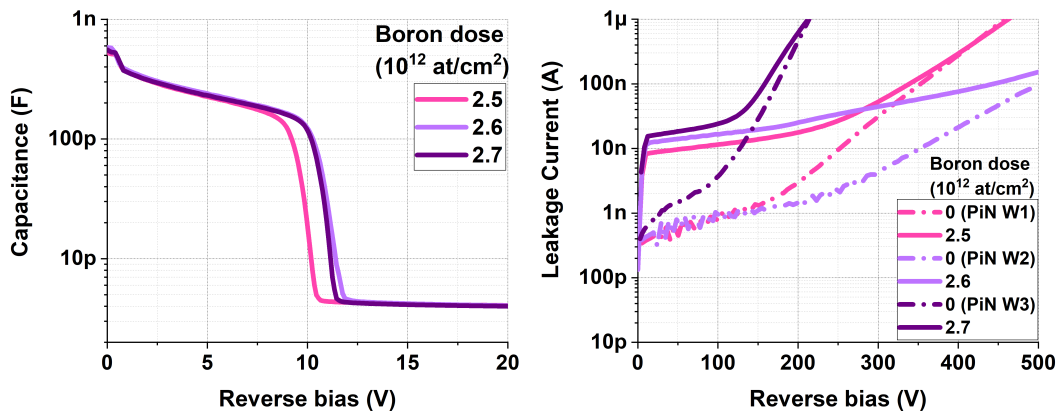


FIGURE 5.68: Average IV and CV measurements of 6DLG2-v1 dL-GAD and PiN devices.

On the other hand, the V_{BD} of the devices could not be determined for voltages under 500 V, as the guard ring was typically breaking down before the core did. Additionally, the leakage current was found to be very high and independent on the avalanche multiplication mechanism (i.e. the fabricated PiNs exhibited a similar behavior). This setback was identified with a new equipment used to deposit the passivation oxide. Specifically, this oxide was found to contain a significant number of defects, which introduced charges within the material. This phenomenon mirrors the radiation-induced effect described in section 3.2. In a nutshell, the presence of defects within the $Si - SiO_2$ interface allow for charge trapping, creating an effective conductive layer across the device surface, which can significantly increase leakage current. As Figure 5.68 shows, this effect was particularly pronounced in the devices fabricated on the third wafer. Lastly, it is important to emphasize that the addition of carbon and boron layers in dLGAD, compared to PiN diodes (which lack these layers), resulted in an increase in leakage current by more than an order of magnitude. This can be inferred by examining the IV curves at sufficiently low voltages, where the oxide defects still do not contribute to the increase in leakage current.

Figure 5.69 (A) shows the CV-extracted boron profiles in the multiplication layers for 6DLG2-v1 devices. In Figure 5.69 (B) these profiles are compared with TCAD Sentaurus simulations. Two elemental results can be deduced from this comparison. First, the CV-extracted boron peaks are lower than the simulated ones, whether using the default Sentaurus diffusivity parameters or the tuned 6LG2-v2 ones. Additionally, the shape of the CV-extracted profiles suggests that the multiplication layer had been partially neutralized by phosphorus, similar to what occurs in traditional IMB-CNM LGADs. This is inferred by comparing the CV-extracted and simulated boron profiles when the depth is scaled to the position of the doping concentration peaks (Figure 5.69 (B)). For the CV-extracted profiles, it appears that almost half of the Gaussian shape is lost, which can only be explained by the partial overlap of the N^{++} layer with the multiplication one.

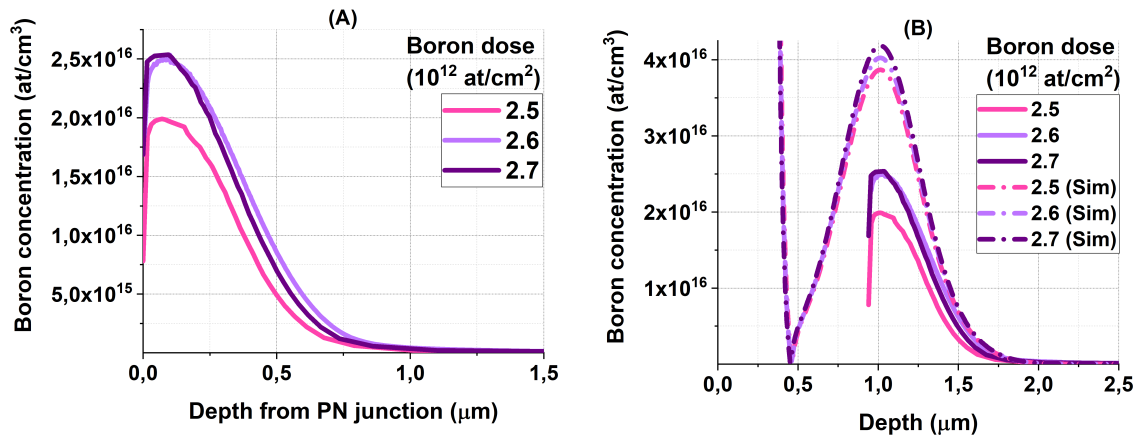


FIGURE 5.69: (A): CV-extracted boron profiles for 6DLG2-v1 dLGADs. (B): Comparison of the profiles in (A) with TCAD Sentaurus simulations.

Furthermore, the possibility of partial activation of boron in the multiplication layers needed to be ruled out. To address this, the three wafers were reprocessed, each undergoing an additional (RTA). The average CV curves and CV-extracted doping profiles after this process are shown in Figure 5.70. The results demonstrated

that the multiplication was completely activated with the original RTA described in Table 5.13, as the V_{gl} and boron peaks dropped after the extra RTA processes.

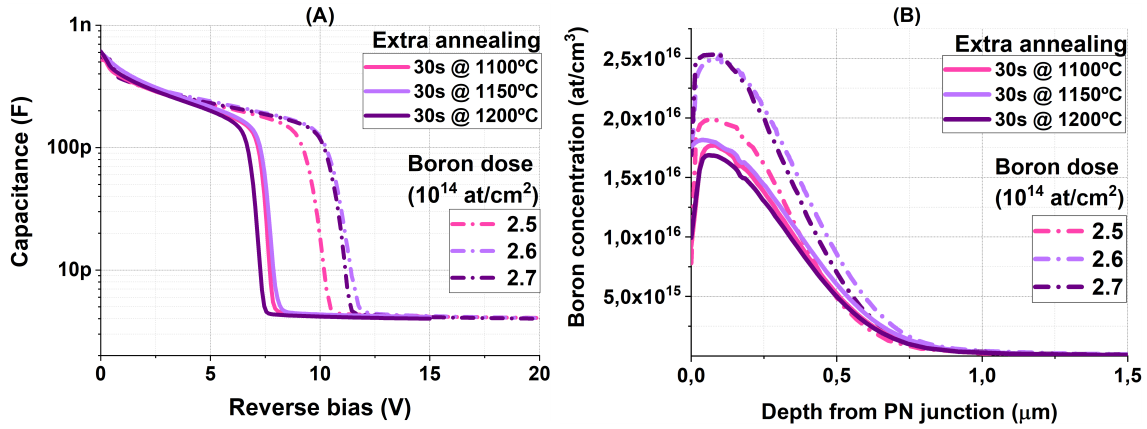


FIGURE 5.70: (A): CV-extracted boron profiles for 6DLG2-v1 devices. (B): Comparison of the profiles in (A) with TCAD Sentaurus simulations.

All these results led to the conclusion that an overlap occurred between the N^{++} and the multiplication layer due to the implantation and annealing scheme described in Table 5.13, which had in turn degraded the dLGAD inner gain originally expected. The neutralization of half of the Gaussian-shaped multiplication layer could not be predicted by TCAD Sentaurus simulations without assuming a boost of both boron and phosphorus diffusivity parameters compared to traditional IMB-CNM LGAD. Nevertheless, the lost information about the screen oxide prior implantation processes impeded a proper calibration of the diffusivity parameters. Specifically, the screen oxide prior to the N^{++} layer seemed to play a crucial role on the dLGAD performance, as predicted by TCAD Sentaurus. This is depicted in Figure 5.71. In such Figure, the boron implantation dose for the multiplication layer was fixed at $2.5 \cdot 10^{12} \text{ at/cm}^2$. When the screen oxide for the N^{++} (multiplication) layer was swept, the one of the multiplication (N^{++}) was held at 250 Å.

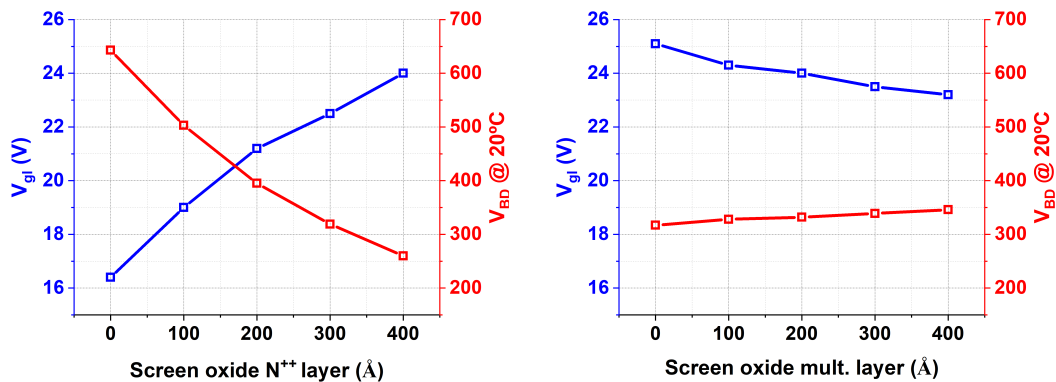


FIGURE 5.71: TCAD Sentaurus simulations of the V_{gl} and V_{BD} dependence on screen oxide grown prior to the N^{++} and multiplication layer implantations for 6DLG2-v1 dLGADs.

5.7.4 The choice of dopant for the N^{++}

To mitigate the effect of phosphorus partially neutralizing the multiplication layer, reducing the RTA time or temperature, as well as the phosphorus implantation dose and energy, could be an effective solution. Conversely, this approach introduces uncertainty regarding the functionality of the N electrode. The RTA and implantation strategy used for the 6DLG2-v1 run was previously proven effective to active phosphorus at a sufficient extent to serve as an ohmic contact, which was not granted if some of these fabrication parameters were adjusted. Nevertheless, thin N electrodes fabricated with the same RTA and implantation scheme had also shown effectiveness at the IMB-CNM when using arsenic instead of phosphorus ions. As arsenic atoms are more massive than phosphorus ones, their diffusivity in silicon is significantly lower for a given annealing process [54], [55]. In turn, this would reduce the potential neutralization of boron in the multiplication layer. With all that in mind, a new design of IMB-CNM dLGAD was implemented, using arsenic for the N^{++} layer.

Figure 5.72 shows the TCAD Sentaurus simulation of dLGAD doping profiles when using arsenic or phosphorus for the N^{++} construction. The simulation was carried out using the carbon and N^{++} layers implantation and RTA parameters given in Table 5.13, with boron implanted for the multiplication layer at 480 keV and a dose of $2.3 \cdot 10^{12} \text{ at/cm}^2$. Additionally, the screen oxide thickness was kept fixed at 200 Å for all implantations during the simulation.

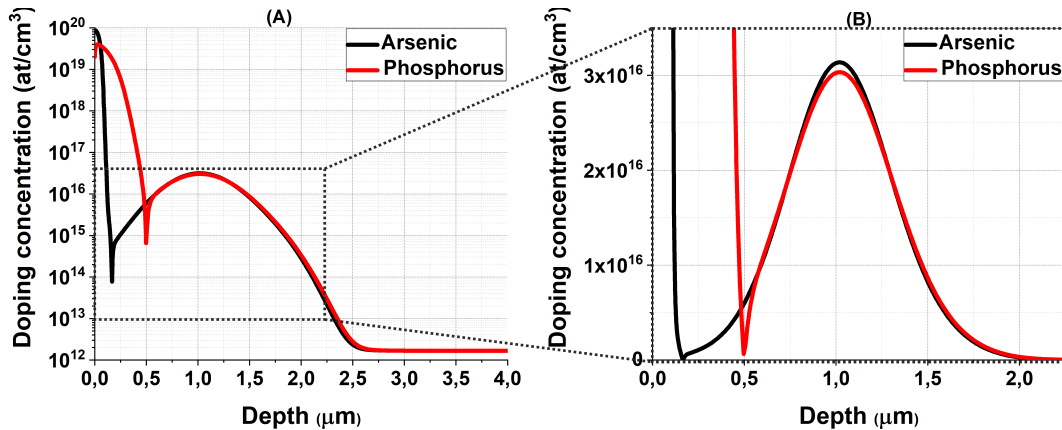


FIGURE 5.72: TCAD Sentaurus simulations of a dLGAD doping profile when using arsenic and phosphorus for the N^{++} layer fabrication. (A): logarithmic scale. (B): linear scale around the PN junction.

It is worth noting that the multiplication layer is slightly narrower and exhibits a higher boron peak when arsenic is used in the N^{++} layer. This effect was observable in TCAD Sentaurus simulations when sweeping the boron implantation dose, indicating that the phenomenon is related to a slight change in the diffusivity of boron when the dopant species of the N^{++} is changed. Nevertheless, the fundamental result inferred from Figure 5.72 is that **the N^{++} layer is significantly further from the multiplication one when arsenic is implanted instead of phosphorus under the same conditions**. This does not only translates into a minimal likelihood of neutralizing boron in the multiplication layer, but also suggests that dLGAD fabricated with arsenic in their N^{++} layer will tend to have a higher inner gain. As the N^{++} and multiplication layers are more widely separated for arsenic use, the electric field

extends deeper at a given bias (Figure 5.73). As a result, charge carriers generated by an incident particle will cause impact ionization over a longer distance as they drift toward the electrodes.

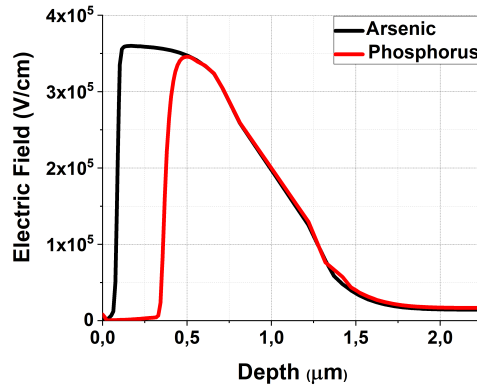


FIGURE 5.73: TCAD Sentaurus simulations of a dLGAD electric field at 20°C and 100 V for dLGAD devices constructed with the doping profiles shown in Figure 5.72.

The aforementioned effect was studied using TCAD Sentaurus by simulating the V_{gl} and breakdown voltage, at 20°C, of dLGAD sensors fabricated with arsenic and phosphorus in their N^{++} under the same fabrication scheme and for different screen oxide thicknesses. The results are shown in Figures 5.74 and 5.75, highlighting that the use of arsenic, for a given boron implantation dose and screen oxide thickness before either the N^{++} or multiplication layer, results in higher V_{gl} and lower V_{BD} values. Moreover, such results also suggest that fabricating dLGAD devices with arsenic in their N^{++} layer could improve the stabilization of LGAD technology at the IMB-CNM by means of fabrication reproducibility. This is inferred by studying how the V_{gl} and V_{BD} of LGAD and dLGAD detectors change as a function of the screen oxide thickness.

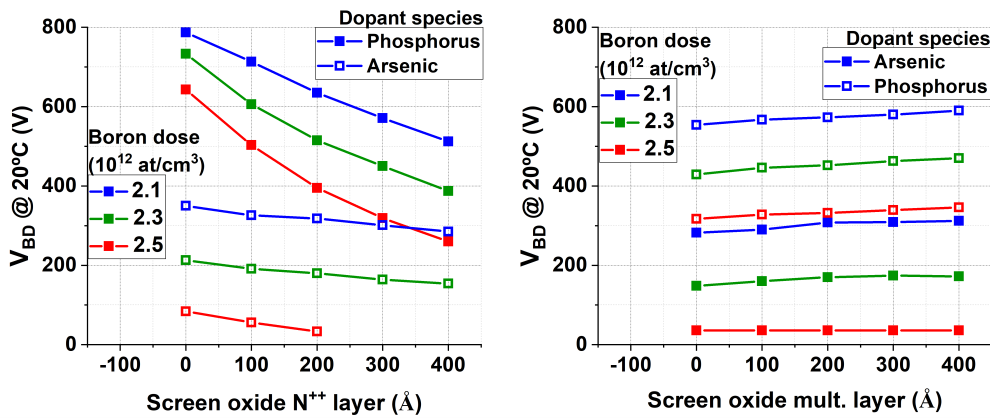


FIGURE 5.74: TCAD Sentaurus simulations of V_{BD} (at 20°C) of dLGAD devices as a function of the N^{++} dopant species, t_{ox} prior to the N^{++} and multiplication layer implantations, and boron implantation dose.

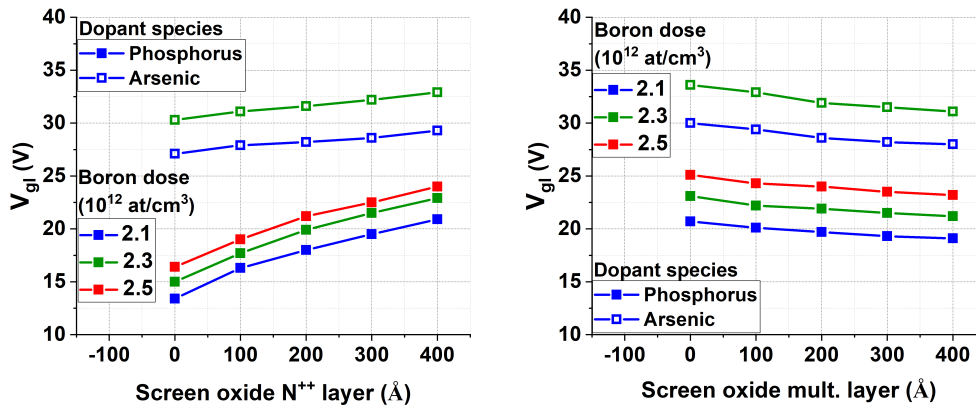


FIGURE 5.75: TCAD Sentaurus simulations of V_{gl} of dLGAD devices as a function of the N^{++} dopant species, t_{ox} prior to the N^{++} and multiplication layer implantations, and boron implantation dose.

Let t_{ox} denote the screen oxide thickness and evaluate the V_{BD} (at 20°C) and V_{gl} variation (ΔV_{BD} and ΔV_{gl}) with t_{ox} by linear fits of the graphs presented in Figures 5.74, 5.74, 4.10 and 4.11. The last referenced figures were analysed in Chapter 4, where V_{BD} (at 20°C) and V_{gl} vs t_{ox} was studied via TCAD Sentaurus for 6LG2-v2 LGADs. The results are listed in Table 5.14, showcasing that the performance of dLGAD devices manufactured by doping the N^{++} with arsenic may be less affected by variations in t_{ox} .

	t_{ox} for N^{++}			t_{ox} for multiplication layer		
	LGAD 6LG2-v2	dLGAD		LGAD 6LG2-v2	dLGAD	
N^{++} dopant	P		As	P		As
$\Delta V_{BD} / \Delta t_{ox}$ V/(100 Å)	55	83	15	26	8	7
$\Delta V_{gl} / \Delta t_{ox}$ V/(100 Å)	1.6	1.9	0.6	1.2	0.5	0.5

TABLE 5.14: V_{BD} (at 20°C) and V_{gl} average variation per 100 Å of screen oxide thickness (for the N^{++} and multiplication layer implantations) and its dependence on the N^{++} dopant species for LGAD and dLGAD devices.

5.7.5 CMS 6DLG2-v2 run

The second IMB-CNM dLGAD batch was manufactured on 150 mm high-resistivity p-type Si-Si wafers (6DLG2-v2 run) of 50 μm active thickness with the CNM1159 mask, just as the 6DLG2-v1 run was. Table 5.15 shows the fabrication parameters for the 6DLG2-v2 PN junction, which were chosen based on the results addressed in the last section. In a nutshell, the fabrication strategy was identical to that of the 6DLG2-v1 run, except phosphorus was replaced with arsenic in the N^{++} layer, and the boron implantation dose in the multiplication layer was lowered for one of the wafers.

	W1	W2	W3
Carbon implantation dose in multiplication layer (10^{13} at/cm^2)	5		
Carbon implantation energy in multiplication layer (keV)	480		
Boron implantation dose in multiplication layer (10^{12} at/cm^2)	2.1	2.3	2.5
Boron implantation energy in multiplication layer (keV)	480		
Arsenic implantation dose in N^{++} layer (10^{14} at/cm^2)	10		
Arsenic implantation energy in N^{++} layer (keV)	30		
Annealing of boron (phosphorus) in multiplication (N^{++}) layer	30 s at 1100°C + 30s at 1050°C		
Screen oxide prior to boron and carbon implantations (\AA)	~ 100		
Screen oxide prior to phosphorus implantation (\AA)	160		

TABLE 5.15: Fabrication features for 6DLG2-v2 LGAD run.

Nevertheless, 6DLG2-v2 devices were not functional, as the *spiking* phenomenon described in Chapter 3 (see section 3.3) caused a short-circuit in the devices. To recall, spiking refers to a failure during fabrication, where the metal layer used to form electrical contacts penetrates through the electrodes into the underlying silicon. This generally occurs when the electrodes are too thin, as is the case for N^{++} layers based on RTA activated arsenic. When this phenomenon arises, a short circuit is likely to be created between the metal contact and the high-resistivity layer, rendering the device non-functional. This short circuit occurs because the metal effectively bypasses the intended PN junction, creating a direct electrical connection where there should not be one. The spikes were directly observed using the IMB-CNM SEM microscope, on both the device core and guard ring opening contacts, as shown in Figure 5.76.

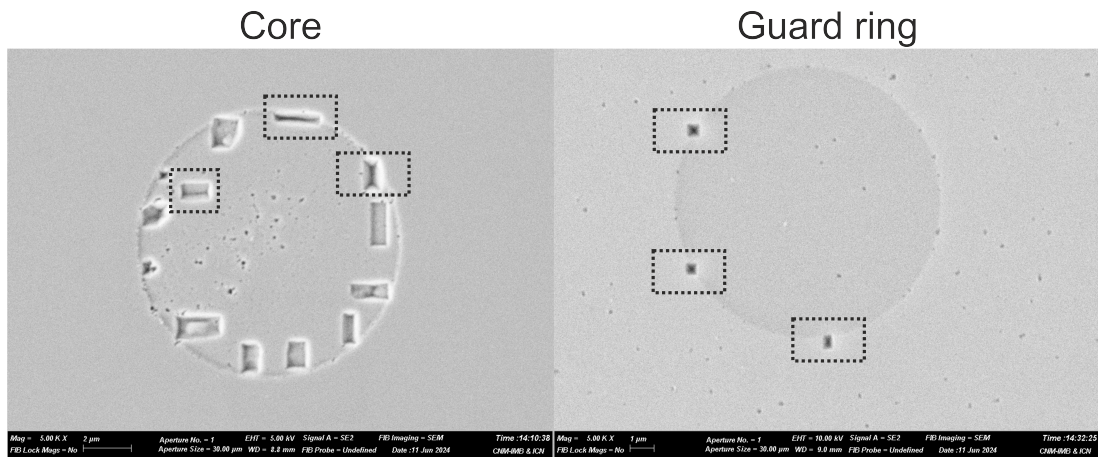


FIGURE 5.76: SEM pictures of the core and guard ring opening contacts of a PiN detector from 6DLG2-v2 run, where spikes can be spotted.

It is worth mentioning that the presence of spikes did not cause a failure of the guard ring, as its N electrode included the JTE profile, which extended into the silicon bulk at sufficient depth to prevent a short circuit between the metal and the high-resistivity layer. This can be inferred from Figure 5.77, where the average IV measurements of single-pad LGADs and PiNs from 6DLG2-v2 run are shown. The measurements were conducted at 20°C using the same equipment as in the previous IV measurements (Keithley 2410), and 10 dLGADs and PiNs per wafer were tested. Additionally, the increase in leakage current due to spiking-induced short circuits was found to be higher for a dLGAD than for a PiN, as the first includes charge injection from the multiplication layer.

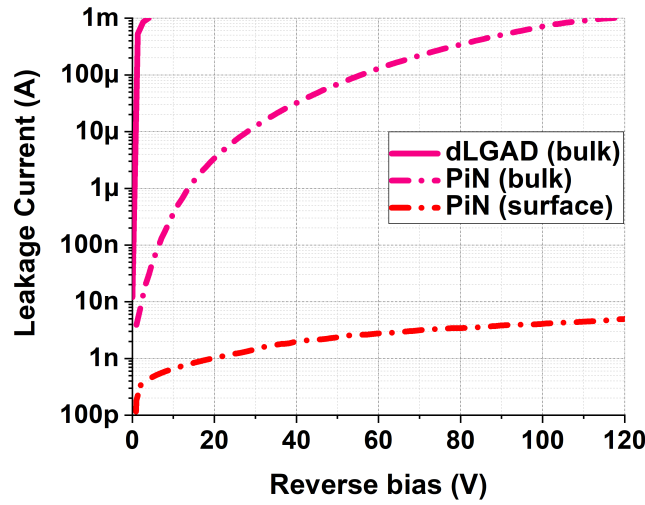


FIGURE 5.77: Average bulk and surface current measurements, at 20°C, of dLGAD and PiN detectors from 6DLG2-v2 run.

5.7.6 CMS 6DLG3-v1 run

The spiking phenomenon for thin electrodes construction has a known mitigation technique at the IMB-CNM, that will be used in an ongoing dLGAD manufacturing batch. Such technique consists in depositing a thin layer of titanium in between the high-resistivity silicon and the aluminum layer. By doing so, the titanium layer acts as a diffusion barrier between the silicon and aluminum, which prevents the former from reacting to form spikes [105]. Thin N electrodes were successfully manufactured with arsenic implantation and activation using the parameters in Table 5.14, without the presence of spikes, by adding a 300 Å layer of titanium between the silicon and aluminum during the metallization process. This approach was used in the design of the upcoming dLGAD batch, being fabricated on 150 mm high-resistivity epitaxial Si-Si wafers (6DLG3-v1 run) of 55 μm active thickness and with the CNM1159 mask. Its main manufacturing features are listed in Table 5.16.

The 6DLG3-v1 run will include a wafer (W5) that mirrors one of the 6DLG2-v1 wafers (W2 in Table 5.13), with the only difference being the use of arsenic instead of phosphorus for the N^{++} layer construction, as well as the previously addressed difference in metallization. The range of boron implantation doses in the multiplication layer has also been widened to ensure enough data is available to calibrate TCAD Sentaurus with experimental results.

	W1	W2	W3	W4	W5
Carbon implantation dose in multiplication layer (10^{13} at/cm ²)	5			-	
Carbon implantation energy in multiplication layer (keV)	480			-	
Boron implantation dose in multiplication layer (10^{12} at/cm ²)	2.0	2.25	2.5	2.0	2.5
Boron implantation energy in multiplication layer (keV)	480				
Arsenic implantation dose in N^{++} layer (10^{14} at/cm ²)	10				
Arsenic implantation energy in N^{++} layer (keV)	30				
Annealing of boron (phosphorus) in multiplication (N^{++}) layer	30 s at 1100°C + 30s at 1050°C				
Metallization layers	1.5 μ m of Al _{99.5%} Cu _{0.5%} on 300 Å of titanium				
Screen oxide prior to boron and carbon implantations (Å)	under fabrication				
Screen oxide prior to phosphorus implantation (Å)	under fabrication				

TABLE 5.16: Fabrication features for 6DLG3-v1 run.

5.8 Conclusions and future work

The results presented in this chapter lead to several conclusions and potential directions for future work. One key finding is that **IMB-CNM fabricated LGADs have shown improved radiation tolerance** across different manufacturing runs. However, further enhancement is needed to meet the harsh radiation conditions forecast in the ATLAS and CMS Phase-II experiment upgrades.

The results from the ATLAS 6LG2-v1 LGAD batch indicated that an optimal balance between gain and radiation hardness is achieved with LGADs fabricated with a carbon implantation dose around $3 \cdot 10^{14}$ at/cm². Further studies from the CMS 6LG2-v2 run showed that this optimal point is more linked to carbonation effects during LGAD fabrication than to device gain. Specifically, **a turning point for the carbon-enhanced suppressed diffusion** was observed at a carbon dose around $4 \cdot 10^{14}$ at/cm². However, the potential optimal point for radiation tolerance at this carbon dose still requires further investigation.

Another fundamental evidence extracted from the results is **the need to stabilize LGAD technology at the IMB-CNM**. Devices from the 6LG2-v1 and 6LG2-v2 runs exhibited significantly different electrical performances before irradiation, despite being fabricated, in principle, under similar conditions. Setting carbonation aside, Table 5.17 provides an overview of how the performance of IMB-CNM LGADs fabricated with 6LG technology has evolved over the years. The gain data has been inferred from the reports found in [25], [51], [78]. The listed results highlight the need for technology stabilization at the IMB-CNM. A rigorous control and understanding of all fabrication parameters during the manufacturing, such as the screen

oxide thickness before implantation, suggests a potential area for investigation to stabilize the technology.

6LG run	Year of competition	clean-room equipment	Gain at 180 V at -30°C for a mip	$V_{gl}(V)$	V_{BD} at 20°C (V)
6LG3-v1	2020	Old	≈ 4	≈ 30	≈ 450
6LG3-v2	2022	New	≈ 8	≈ 30	≈ 400
6LG2-v1	2023	New	≈ 30	≈ 31	≈ 200
6LG2-v2	2024	New	to measure	≈ 28	≈ 420

TABLE 5.17: Overview of the performance of 6LG detectors.

Regarding the aforementioned stabilization, IMB-CNM has used TCAD Sentaurus, a powerful simulation tool for designing and predicting LGAD behavior before fabrication. Additionally, the SRP technique was also introduced to analyse LGAD doping profiles. However, **TCAD Sentaurus and SRP correction models need further refinement** to better align with the various LGAD manufacturing scenarios and to **serve as reliable prediction and validation tools**, respectively.

Last but not least, **transitioning from LGAD to dLGAD** devices could be a promising direction for future work. On one hand, several studies have reported that dLGAD detectors exhibit better radiation resistance compared to traditional LGADs. Moreover, TCAD Sentaurus simulations indicate that dLGAD devices may be less affected by manufacturing variances (e.g., changes in screen oxide thickness before implantation), which provides an advantage in terms of technology stabilization.

Chapter 6

nLGAD for low-penetrating particles detection

6.1 Introduction

The stepping stones for what detectors with intrinsic amplification built up on n-type substrates are and their intended purpose were reviewed in Chapter 2. In this chapter we will dig deeper into the topic and present the characterization of the two nLGAD batches fabricated at the IMB-CNM to date.

6.2 LGAD limitations for low-penetrating particles detection

A good gain response of a p-type LGAD is limited to high-penetrating particles, that is, to highly energetic charged particles and photons within a certain energy range (e.g. IR light or x-rays with relatively high penetration depth). This limitation is due to the distinction between how electrons and holes trigger the avalanche multiplication mechanism, being the first much more effective to do so. As discussed in the previous chapter, LGAD devices built up on p-type substrates have demonstrated their outstanding timing resolution and SNR when detecting high-penetrating particles in silicon while avoiding the high noise levels associated to a traditional APD. The aim to construct a similar device for low-penetrating particles was the seed of the nLGAD conception. The first evidence of p-type LGAD detectors being limited for such particles was found at the IMB-CNM, being the methodology to do so here-under detailed.

An LGAD from the 6LG3-v1 run (section 5.4) was investigated for its gain response via Transient Current Technique (TCT) [106] with laser sources of 1064 nm (IR) and 404 nm (blue visible light) wavelength. Detectors from this fabrication batch have an active area of $3.3 \times 3.3 \text{ mm}^2$, a circular entrance window of 2.3 mm diameter and 50 μm of active thickness. The devices were biased with a Keithley 2410 voltage source. During the measurements, the laser beam was focused around the center of the active area of the LGAD, at normal incidence with respect to it and with a projected area of $\approx (\pi/4)60 \cdot 60 \mu\text{m}^2$ on the surface of the entrance window. Such center was found by scanning the signal response of the devices in X and Y using steps of 2 μm . The laser pulse intensity, frequency and width were kept constant for every wavelength and for both LGAD and reference PiN. Before processing, the laser-generated signals went through a Particulars AM-01A amplifier, with an analog bandwidth of 2 GHz, 53 dB gain and connected to a Particulars BT-01 Bias-Tee, to be further analysed using a DRS4 Evaluation Board Oscilloscope. For every device, wavelength and voltage point, 5000 waveforms were averaged to extract the

gain, that was inferred by dividing the integrated amplified output signal (Collected Charge or CC) of the LGAD by the reference PiN one.

The results are shown in Figure 6.1. As the studied LGAD has its entrance window by the N electrode (where electrons drift), the difference in gain response vs wavelength can be understood as it follows. A photon of 1064 nm, with a penetration depth of ~ 1 mm in silicon [17], will be absorbed at any depth of the 50 μm LGAD with the same probability. Thus, the IR pulse will generate a uniform distribution of electron-hole pairs within the active depth of the detector. Under these circumstances, there will be a greater number of electrons crossing the high electric field region, so they will be the main carrier contributing to the avalanche mechanism triggering. In contrast, a visible photon of 404 nm, with a penetration depth of ~ 0.1 μm in silicon [17], will be either absorbed within the N electrode (not causing any detectable signal) or close to the PN junction. In this latter situation, most of the electrons will quickly drift to the N electrode without traversing the high electric field region, hence the majority of charge carriers crossing such region will be holes. As electrons are more effective in triggering impact ionization than holes, a regular p-type LGAD will see its gain response degraded for the 404 nm visible light beam. Moreover, the results in Figure 6.1 highlight that LGAD sensors from the 6LG3-v1 batch have a response to 404 nm photons that differ little to that of the reference PiN, as the gain is nearly one for the studied voltage range.

With that in mind, one could argue that we may turn the tables by developing **LGAD devices**, alike to the 6LG3-v1 batch, but in where **electrons and holes exchange its drift direction**. This can indeed be achieved by swapping the conductivity type of all layers composing the device. **As the bulk comprising the raw wafer would be n-type in such case, an LGAD built up this way was called nLGAD.**

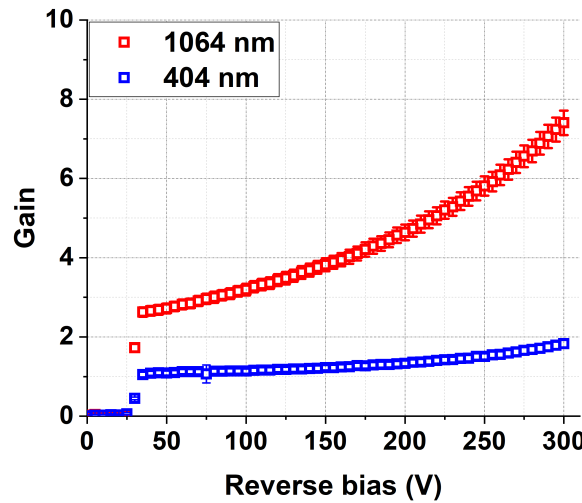


FIGURE 6.1: LGAD gain response, at 20°C, to 404 and 1064 nm wavelength photons inferred via TCT.

Before getting into the characterization of IMB-CNM fabricated nLGAD devices, it is worth itemizing some of the potential applications that such devices may have.

6.3 Potential nLGAD applications

6.3.1 Detection of low-penetrating photons

In the case of photon science applications, it is worth discussing them while evaluating the photoabsorption penetration depth in silicon for different photon species. This is depicted in Figure 6.2. It is important to define the term penetration depth, as it may be misunderstood as the very depth at which a photon beam is completely attenuated in silicon. In fact, it is a parameter that determines the depth at which a photon beam, incident normally to the surface of silicon, has its intensity reduced by a factor of $1/e$ by means of the photoelectric effect. Hence, **the probability of having photo-absorption in a silicon detector is still possible even though the penetration depth of the species is smaller than the dead layers of the entrance window** (e.g. passivation or electrodes). With all that set forth, we may propose that the potential of nLGAD in photon science can be narrowed to applications involving the detection of visible light in the higher energy spectrum ($\gtrsim 3$ eV), UV light and soft x-rays under 1 keV).

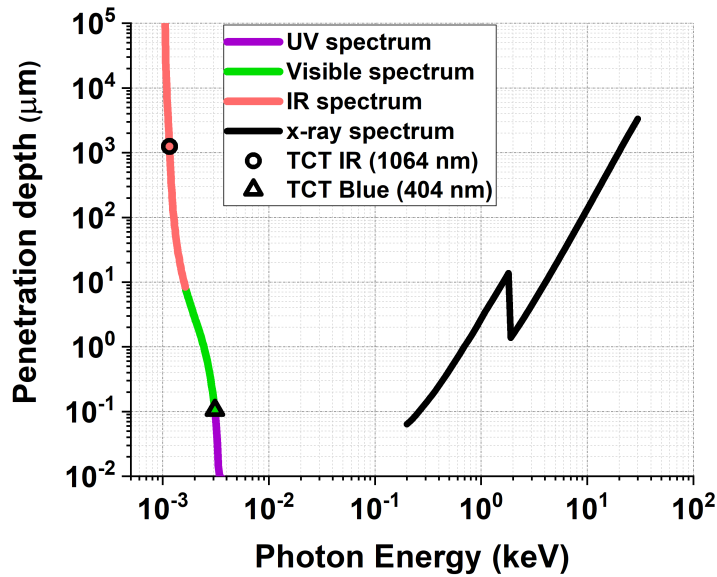


FIGURE 6.2: Penetration depth of different photon species that interact mainly via photo-effect with silicon [17], [22], [107].

Such photon species have a penetration depth in silicon under ≈ 1 μm . Thus, regardless of the specific application, their very detection has always been challenging due to their potential absorption within the non active regions of the sensor [108], [109]. This limitation led to the development of silicon-based detectors optimized to enhanced their sensitivity to these low-penetrating photons. Some typical examples are the reduction of the dead entrance window while broadening the active area of the sensors [110], or the replacement of the dead layer components with alternative materials transparent to the target photon [111]. Along with these strategies, the development of APDs entailed an upgrade, as their high inner gain enhanced the sensitivity to low intensity photon sources [109]. Nevertheless, APDs are not suitable for applications that require spatial resolution, as segmenting them in small pixels leads to non-uniformities in their performance. Moreover, the excess noise

factor inherent to APDs can be counterproductive if the photo-generated signal falls below the baseline noise level.

Traditional pixelated nPiN detectors or Charged Couple Devices (CCD) tailored for low-penetrating photons overcome this drawback, allowing high spatial resolution [108]. However, their time response and sensitivity is generally poor for applications that require time resolution and enhanced SNR. The interest of the nLGAD for photon science lies in their potential to detect low-penetrating particles with high temporal and spatial resolution while maintaining low noise levels.

Some specific applications of photon science that require the detection of UV light and soft x-rays are listed in [108]. An interesting application that involves the manufacturing of silicon detectors itself is the photolithography mask inspection using UV light [112]. In a nutshell, such technique consists in determining the presence of photolithography masks defects by studying how they diffract UV photons, which requires a proper particle detection system to do so. On the other hand, large synchrotron facilities such as the ESRF (European Synchrotron Radiation Facility in Grenoble) and ALBA (Barcelona, Spain) require particle monitoring during operation, where nLGAD devices could be implemented for soft x-rays detection.

6.3.2 Detection of low-penetrating charged particles

The aforementioned argument can also apply for low-penetrating charged particles detection like low-energy protons or alphas. The *range* for such particles in silicon is shown in Figure 6.3.

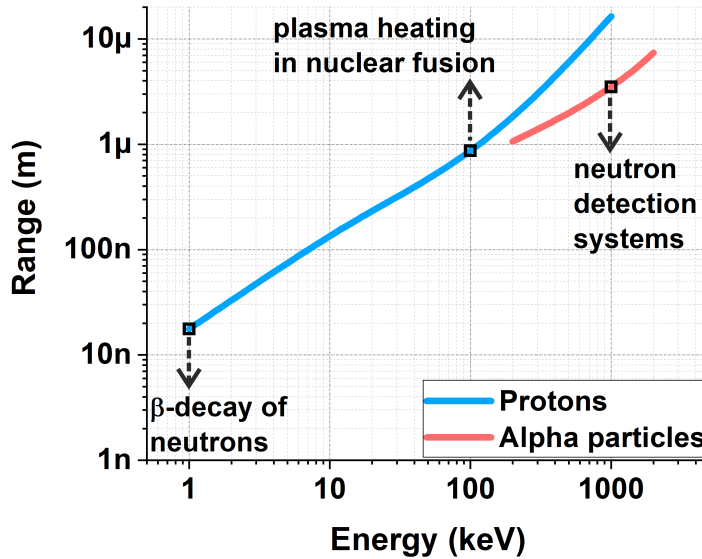


FIGURE 6.3: Range in silicon for protons and alpha particles of relative low energy [113].

It is important to make a distinction between the penetration depth for photons and the range for charged particles. Both concepts are used to describe how far these particles can travel through a material. However, they refer to different mechanisms of interaction with it. On one hand, photons interact with silicon in a probabilistic way (via photoelectric effect), so the penetration depth is defined statistically (e.g.

the distance at which the beam intensity falls to $1/e$). On the other hand, charged particles interact continuously with silicon (via Coulomb interaction), ionizing the material as they pass through, hence leading to a more predictable path and energy deposition pattern. Thus, **the range is defined deterministically as the average distance cover by the ion until it is completely stopped within silicon**. To put it another way, a photon with a penetration depth of $1\ \mu\text{m}$ has a high probability of being absorbed for depths $>1\ \mu\text{m}$, as only $\approx 37\%$ of the beam has been lost up to such depth. In contrast, the likelihood of the same happening for a charged particle with a range of $1\ \mu\text{m}$ is negligible.

Additionally, it is worth remarking that strategies to enhance the sensitivity of sensors to low-penetrating ions are more limited when compared to low-penetrating photons. As charged particles interact with any material composing the dead entrance window, there are no means of developing transparent coatings for ions, as is the case for photons. Thus, approaches to upgrade the sensitivity of detectors to low-penetrating charged particles are narrowed to the reduction of the dead entrance window or its construction with low-density materials that increase the ions range within them. In light of that, we may advance the **the potential of nLGAD sensors is bounded to ions which range falls by the PN junction of the detector**. Depending on the entrance window and the electrode construction, such range should be of the order of $\sim 1\ \mu\text{m}$ or less. A few examples of potential applications are depicted in Figure 6.3 and hereunder briefly discussed.

Neutrons are neutral particles, making them difficult to detect directly with silicon detectors. However, by coating the entrance window with specific materials, neutrons can be detected indirectly. Such materials include Li-6 or B-10, that are able to capture neutrons, a reaction that produces other charged particles, including alphas of $\approx 1\ \text{MeV}$ [31]. On the other hand, plasma heating for nuclear fusion experiments is often performed by injection of protons accelerated at $\approx 100\ \text{keV}$ [114]. A proper particle detection system for such protons is needed for plasma diagnosis during its heating. Perhaps the most ambitious experiments involving low-penetrating ions detection are those that study of the natural β -decay of neutrons [115], [116], as it aims to detect and analyse the properties of the remnant proton of such reaction, with an energy of $\approx 1\ \text{keV}$ (and a range in silicon of the order of the nm).

The aforementioned examples are just a few compared to the wide range of applications where nLGAD have the potential to enhance the performance of low-penetrating particles detection systems. While we have narrowed the discussion to protons or alpha particles, the argumentation may be extrapolated to any heavier charged particle whose range in silicon is small enough to trigger the avalanche mechanism for electrons in a specific nLGAD design. With all that set forth, let us delve into the characterization of the first nLGAD prototypes fabricated at the IMB-CNM.

6.4 IMB-CNM 4NLG1-v1 fabrication run

As stated in Chapter 2, the first nLGAD prototypes were designed, fabricated and tested at the IMB-CNM [6], [25], [117], [118]. They were manufactured on 4" (100 mm) n-type high resistivity Flat Zone Si-Si wafers, and its technology was coded as 4NLG1. The fabrication was done with a mask containing only single-pad like detectors with a $\approx 275\ \mu\text{m}$ active thickness, a $5.3 \times 5.3\ \text{mm}^2$ active area and an entrance

window of 5 mm in diameter, as Figure 6.4 shows. Such entrance window is composed of a layer of $0.7 \mu\text{m}$ of silicon nitride over a $0.4 \mu\text{m}$ layer of silicon dioxide. These first prototypes lacked of a channel stopper, which was introduced in the second nLGAD batch that will be addressed in the next section. For the multiplication layer, phosphorus was implanted with an energy and dose of 100 keV and $1.9 \cdot 10^{13} \text{ at/cm}^2$ and annealed at 1100°C for 180 minutes. For the P^{++} construction, boron was implanted with two energies and doses: 150 keV and $5 \cdot 10^{14} \text{ at/cm}^2$, and 70 keV and $1 \cdot 10^{15} \text{ at/cm}^2$ and annealed at 1000°C for 52 minutes. In Figure 6.4, the full thickness of the detector is $\approx 271 \mu\text{m}$, as about $3\text{--}4 \mu\text{m}$ were lost in oxidation processes.

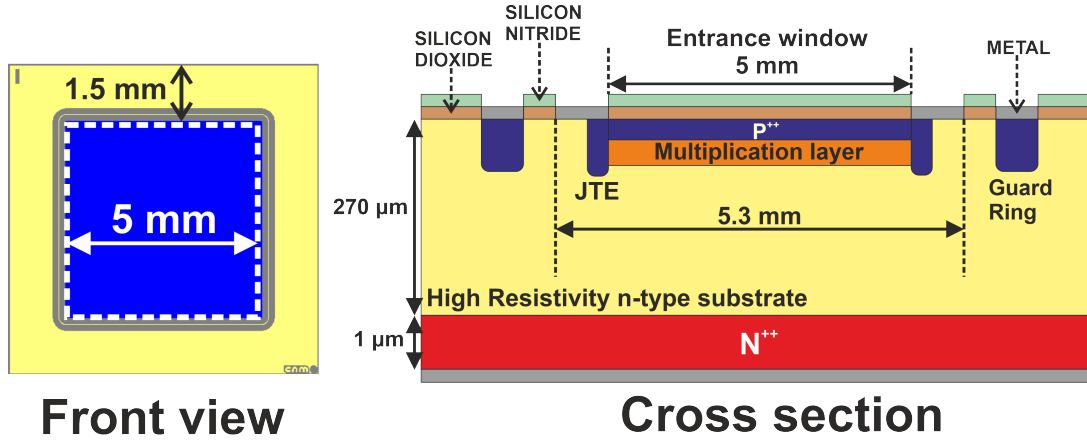


FIGURE 6.4: schematic of the front view and cross section of an nLGAD from the IMB-CNM 4NLG1-v1 fabrication run.

The detectors showed a V_{gl} of $\simeq 26 \text{ V}$, a full depletion voltage of $\simeq 30 \text{ V}$, an average breakdown voltage of $\simeq 150 \text{ V}$ (at 20°C) and a leakage current in their operational voltage region of the order of 100 nA. Their electrical characterization can be found in [25], [117]. The nLGAD detectors were first investigated at the IMB-CNM for its gain response via TCT with laser sources of 1064 nm (IR) and 404 nm (blue visible light) wavelength. The methodology to do so is similar to the one detailed for the LGAD gain response measurements presented in Figure 6.1, and its main results can be found in [25], [117]. It was found that the gain response to 404 nm wavelength photons was ≈ 10 times higher than for the 1064 nm wavelength ones. Such result represented the first evidence of the potential of nLGAD for low-penetrating particles detection.

As a contribution to the aforementioned work, this section presents the gain response measurements of 4NLG1-v1 detectors to TCT visible light of 660 nm and 15 keV x-rays from synchrotron radiation [6]. Additionally, the gain response as a function of every photon species investigated for nLGAD devices of this fabrication run (visible light of 404 and 660 nm wavelength, IR light of 1064 nm wavelength and 15 keV x-rays) will be reviewed.

6.4.1 nLGAD response to TCT visible light of 660 nm wavelength

An nLGAD detector from the 4NLG1-v1 run was investigated for its gain response while illuminated with 660 nm visible light. A photon of such wavelength has a penetration depth in silicon of $\approx 3 \mu\text{m}$ [17], so it is halfway between a low- and a high-penetrating particle in silicon. The measurements were carried out at room

temperature with a TCT setup [106] available at the School of Physics and Astronomy at the University of Glasgow. The devices were biased with a Keithley 2410 voltage source. During the measurements, the laser beam was focused around the center of the active area of the LGAD, at normal incidence with respect to it and with a projected area of $\approx (\pi/4)10 \cdot 10 \mu\text{m}^2$ on the surface of the entrance window (of $\approx (\pi/4)5000 \cdot 5000 \mu\text{m}^2$). Such center was found by scanning the signal response of the devices in X and Y using steps of $2 \mu\text{m}$. The laser pulse intensity, frequency and width were kept constant for both nLGAD and reference nPiN measurements. In the setup, the laser-generated signals go through a Particulars AM-01A amplifier, with an analog bandwidth of 2 GHz, 53 dB gain and connected to a Particulars BT-01 Bias-Tee, before being digitized using a Agilent MSO9404A Oscilloscope. For every device (nLGAD and reference nPiN) and voltage point, 5000 waveforms were averaged to extract the gain, that was inferred by dividing the integrated amplified output signal (Collected Charge or CC) of the nLGAD by the reference nPiN one. In short, the measurements presented in this subsection were carried out with the same setup produced by Particulars [119] that was used in the results shown in Figure 6.1 and those reported in [117]. The sole difference was the oscilloscope used to digitized the signals, that are shown in Figure 6.5. In such figure, the X and Y axis is adjusted for every device to better distinguished the differences between the nLGAD and the nPiN signals.

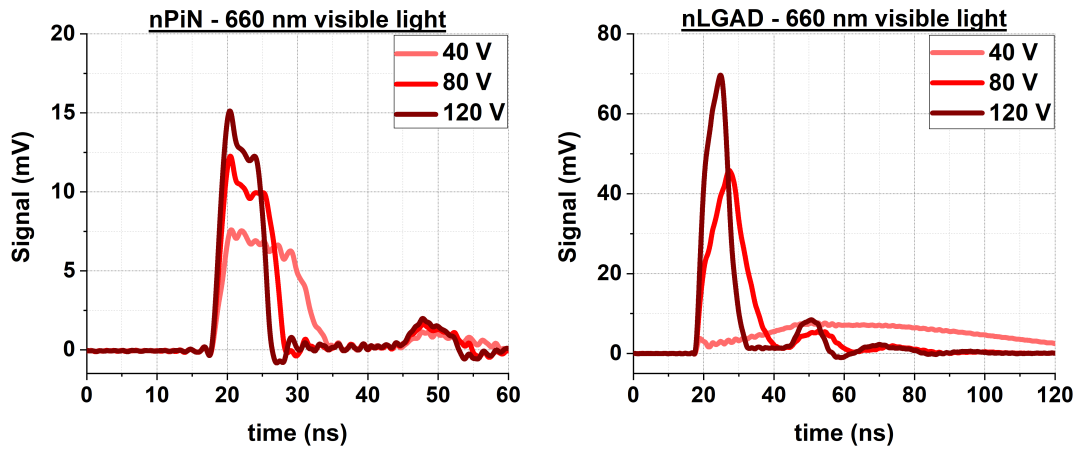


FIGURE 6.5: TCT output signal, at 20°C, for the studied nLGAD and reference nPiN under illumination with 660 nm visible light.

The results clearly indicate that the signal amplitude is higher for the nLGAD than for the nPiN, indicating a better SNR for the first. Additionally, we may notice that, regardless of the bias, the nPiN signals are shorter in time than the nLGAD ones. This is a clear indicator of impact ionization occurring within the nLGAD detector, as the avalanche-generated electrons are delayed with respect to the primary ones (generated via photo-absorption). This effect is particularly enhanced at bias values at which the charge carriers are not drifting at their maximum velocity in silicon (see Chapter). As a case in point, the nLGAD signal duration for biases under 45 V exceeded the bandwidth limitations of the oscilloscope. For the nPiN, such limitation was observed for biases under 10 V. This effect can be grasped by evaluating the end-tail of the nLGAD signal at 40 V in Figure 6.5.

Lastly, it is worth remarking that a source of noise, that often generated spurious signals in the range $\approx 40\text{-}60$ ns, was encountered during the measurements. nLGAD and nPiN signals were long enough to be affected by this noise source for biases under 75 and 30 V, respectively. The identification of this sort of noise sources is crucial when determining the response of the devices, as it affects the inferred CC for both nLGAD and reference nPiN. This is shown in Figure 6.6.

For the reference nPiN, we can distinguish the bias range (30-120) V as the one where the time width of the signals is high enough to both fit within the bandwidth of the oscilloscope and fall far from the (40-60) ns region where the spurious signals are. For the studied nLGAD, and discarding biases under V_{gl} (≈ 26 V), four CC vs voltage regions can be identified. For $V \in (30, 45)$ the signal duration exceeds the bandwidth limitations of the oscilloscope. While this underestimates the CC, the integration of the spurious signals along with the photo-generated ones overestimates it, impeding inferring the actual CC in this range. For $V \in (45, 60)$ V the CC is clearly overestimated, as the signals fit within the bandwidth but the noise is being integrated along with them. For 65 and 70 V, there is a decreased of CC, as the end-tail of the generated signals start to move out of the (40-60) ns range. For $V \geq 75$ V, the spurious signals are ultimately left aside from the photo-generated signals. Hence, given the oscilloscope bandwidth and noise limitation, **the actual nLGAD CC for TCT 660 nm wavelength light could only be determined for $V \geq 75$ V**. This result highlights the importance of understanding and controlling the limitations of any setup equipment both prior and during characterization measurements of any silicon detector device.

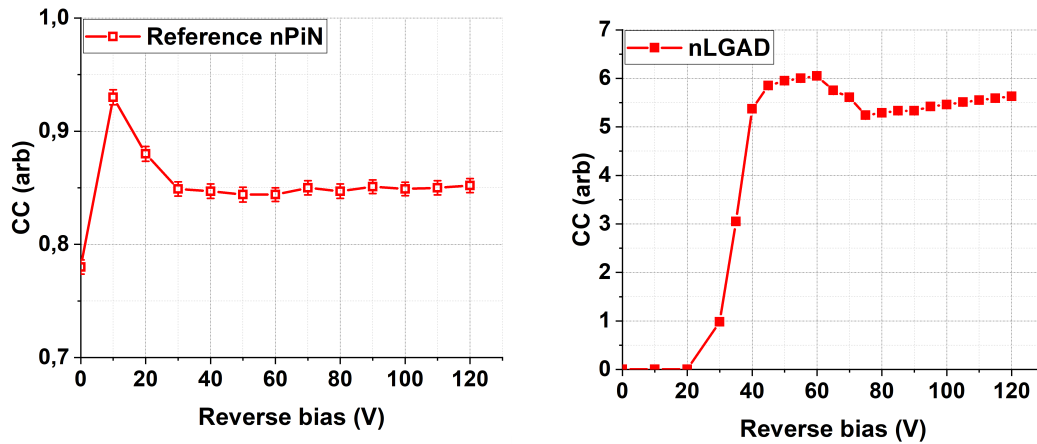


FIGURE 6.6: CC vs reverse bias, at 20°C, of an nLGAD and a reference nPiN from the 4NLG1-v1 run when illuminated with TCT 660 nm wavelength light.

6.4.2 nLGAD response to synchrotron 15 keV x-rays

The methodology to extract the gain response to 15 keV x-rays was different than to laser beam pulses with a TCT. Such measurements were conducted, at 20°C, at the B16 beamline available at Diamond Light Source [23]. By using a crystal monochromator, this beamline offers ultra-fast monochromatic x-ray beams, in the range of 4-45 keV and generated from synchrotron radiation. Additionally, a Compound Refractive Lens (CRL) was employed to achieve spot sizes of the beam of the order

of a μm . Specifically, the beam spot size was measured to be $2.6 \pm 0.1 \mu\text{m}$ FWHM (X direction) and $1.3 \pm 0.1 \mu\text{m}$ FWHM (Y direction). For every measurement, the beam was projected around the center of the detectors (perpendicular to the beam direction) with the aid of a visible red laser available within the experimental setup of the beamline. The beam intensity (of the order of 10^8 photons/s when micro-focused [23]) was monitored by an ionization chamber during the entire lifespan of the measurements. The energy of the x-rays in the beam was set at 15 keV for all measurements. X-rays of such energy have an absorption depth in silicon of the order of a millimeter [22], so the beam energy is partially deposited in the detector uniformly along its active thickness, just as IR photons of 1064 nm wavelength do. In other words, 15 keV x-rays are high-penetrating particles for the studied nLGAD.

For every measurement, the gain was extracted by dividing the photocurrent of the nLGAD by the one of a reference nPiN. The photocurrent is defined as the current generated in the detector while irradiated with the x-ray beam around its center (called *Beam On* current from now on), minus the leakage current. The current was measured with a Keithley 2410. Twenty measurements per device and voltage point were carried out, and all plots presented in this section have error bars indicating the standard deviation of such measurements, although such bar errors are so small that are indistinguishable within the graphs. It is worth remarking that, for every voltage point, the measurement time was always much longer than x-ray the beam pulses.

Figure 6.7 shows the leakage and Beam On current for the studied nLGAD and reference nPiN, and Figure 6.8 shows the inferred photocurrent for both devices.

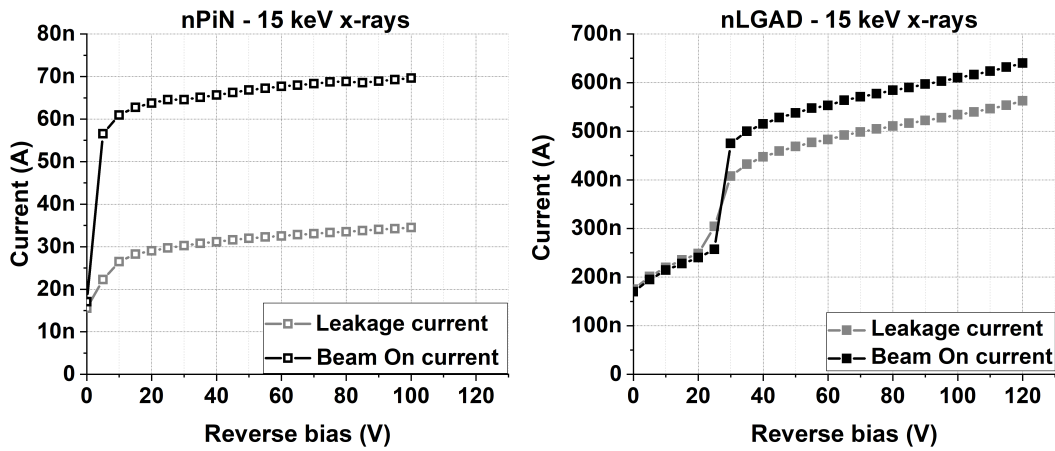


FIGURE 6.7: Leakage current and Beam On current for the studied nLGAD and reference nPiN diode, while illuminated with synchrotron 15 keV x-rays.

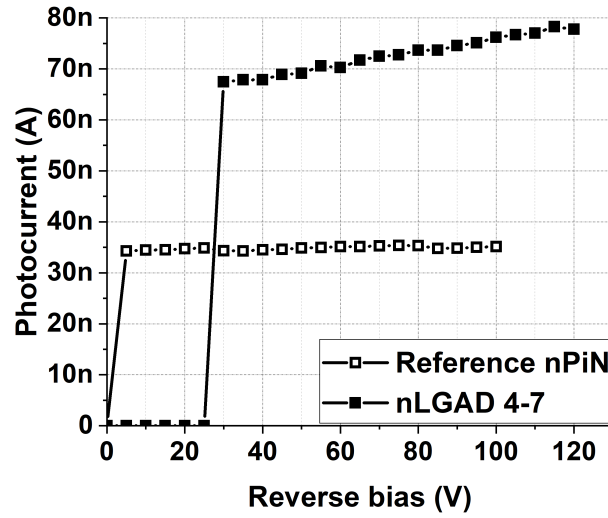


FIGURE 6.8: Photocurrent (difference between leakage and Beam On) for the studied nLGAD and reference nPiN diode, while illuminated with synchrotron 15 keV x-rays.

6.4.3 Review of the gain response measurements for 4NLG1-v1 detectors

Figure 6.9 shows the gain response results for visible light of 660 nm wavelength and 15 keV x-rays, using the two different techniques and methodologies aforementioned described.

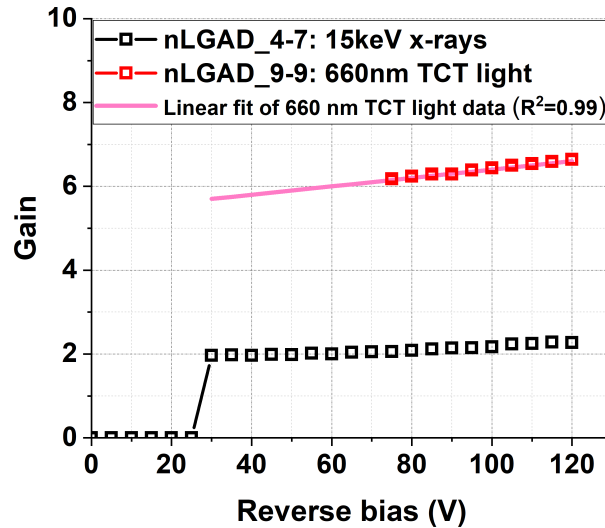


FIGURE 6.9: Gain response of 4NLG1-v1 detectors to 660 nm wavelength visible light and 15 keV x-rays, by using the techniques and methodologies described in sections 6.4.1 and 6.4.2.

As stated, the gain response to 660 nm wavelength photons could only be accurately determined for $V \geq 75$ V due to the presence of high noise levels at certain ranges of the oscilloscope time axis. Figure 6.9 shows a linear fit of such data, where

the gain response to 660 nm wavelength photons can be approximated for voltages $V < 75$ V down to the full depletion one (≈ 30 V). The studied nLGAD devices were different for every experiment and their labelling (9-9 for TCT and 4-7 for x-ray measurements) is also displayed in the graph legend.

Figure 6.10 shows the gain response, at 100 V (50 V below the average breakdown voltage), and 20°C, as a function of the penetration depth of all photon species studied with 4NLG1-v1 devices. The figure also shows gain response measurements to TCT 404 nm and 1064 nm wavelength for 6LG3-v1 detectors (Figure 6.1). For LGAD sensors, the gain is also shown at 50 V below the average breakdown voltage, which in this case corresponds to 400 V.

The interest of plotting the gain response for LGAD and nLGAD devices not at the same bias but at one that lays equally close to their V_{BD} has its significance. As Figure 6.10 shows, by doing so we observe that the gain responses to 404 and 1064 nm wavelength light for an nLGAD is practically a specular image of the LGAD one. This highlights the importance of the substrate conductivity type choice when developing sensors with low inner gain, with independence on how large the operational voltage range of the fabrication detector is. If the aim of such sensor is to detect low-penetrating particles, **the nLGAD is indeed the best candidate**. Conversely, **a traditional LGAD should be used if the experiment targets to detect high-penetrating particles**. Additionally, the results clearly evidence that the gain response of the nLGAD strongly depends on the penetration depth of the photon species.

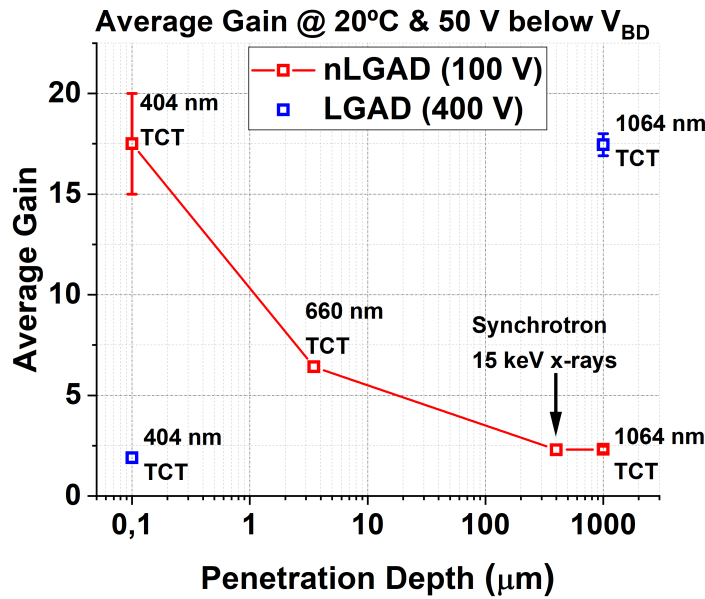


FIGURE 6.10: Gain response of 4NLG1-v1 and 6LG3-v1 detectors, at 50 V below their breakdown voltage value and 20°C, for different photon species.

The bar errors in Figure 6.10 correspond to the standard deviation when evaluating the gain response of different devices. Three nLGAD devices (labelled as LG2-7, LG4-7 and LG9-9) were investigated with 404 and 1064 nm wavelength photons,

and only one was investigated for 660 nm wavelength photons (LG9-9) and 15 keV x-rays (LG4-7). Regarding LGAD, three devices were investigated for 1064 nm wavelength photons and only one was tested for 404 nm wavelength photons. The standard deviation for nLGAD devices under visible light illumination is higher than for IR illumination (for either nLGAD or LGAD). An initial argument might be that such fact is due to non-uniformities of the multiplication layer along the nLGAD wafer. Nevertheless, this in turn would translate into having also large standard deviation bars in the gain response to 1064 nm wavelength photons, which is not observed. A more relatable argument is obtained if we bring up the *gain suppression* mechanism described in Chapter 5, a phenomenon that was not accounted for during the measurements. The gain response to 404 wavelength photons for the three studied nLGAD sensors was performed without having an exhaustive control of the laser pulse beam flux. Thus, the preliminary results presented in Figure 6.10, along with their large bar errors, may suppose an indicative of the **beam intensity to be a key factor to control, particularly to detect possible gain suppression effects**. As we will discuss in the next section, this was done when evaluating the gain response of nLGAD devices from the second IMB-CNM fabrication run.

6.5 IMB-CNM Fabrication run 4NLG1-v2

The second IMB-CNM nLGAD batch was also fabricated on 4" (100 mm) n-type high resistivity Flat Zone Si-Si wafers (4NLG1 technology). For the 4NLG1-v2 run, single-pad devices with an active area and thickness of $1.3 \times 1.3 \text{ mm}^2$ and $270 \text{ }\mu\text{m}$, respectively, were studied. As Figures 6.11 and 6.12 show, a channel stopper was included in the nLGAD periphery for this nLGAD batch. Figure 6.13 shows a photograph of a manufactured wafer from this run.

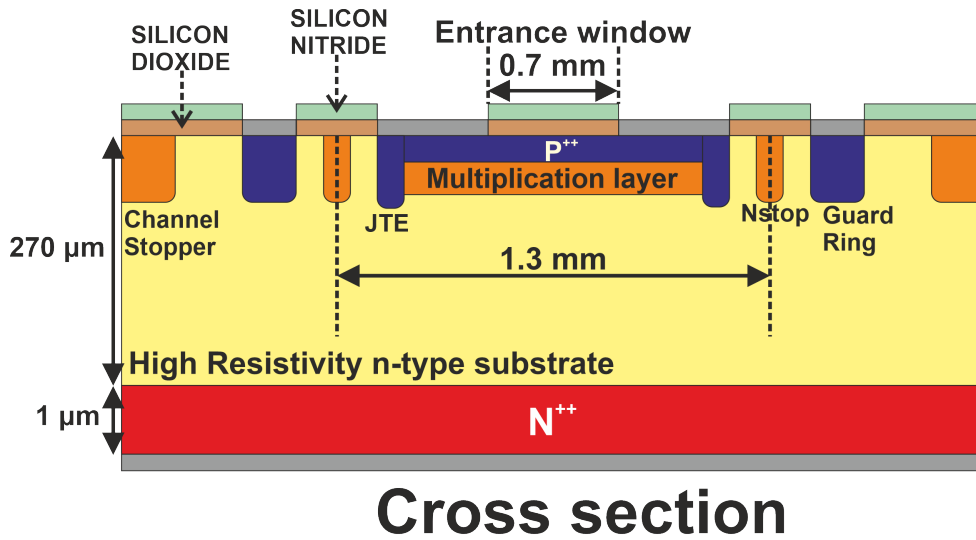


FIGURE 6.11: schematic of the cross section of an nLGAD from the 4NLG1-v2 run.

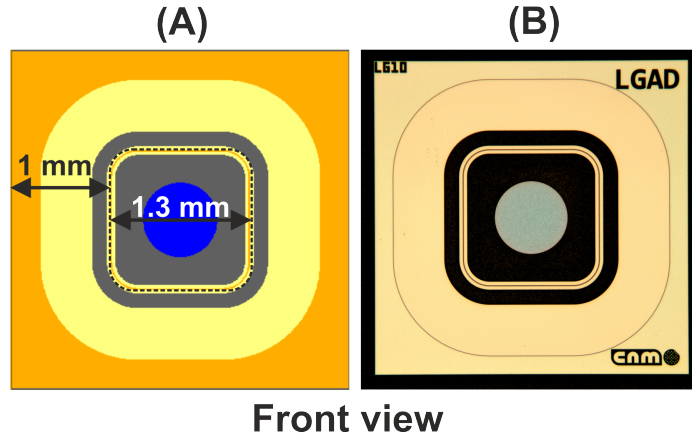


FIGURE 6.12: (A): schematic of the front view of nLGAD from the 4NLG1-v2 run. (B): Actual photograph of a single-pad nLGAD.

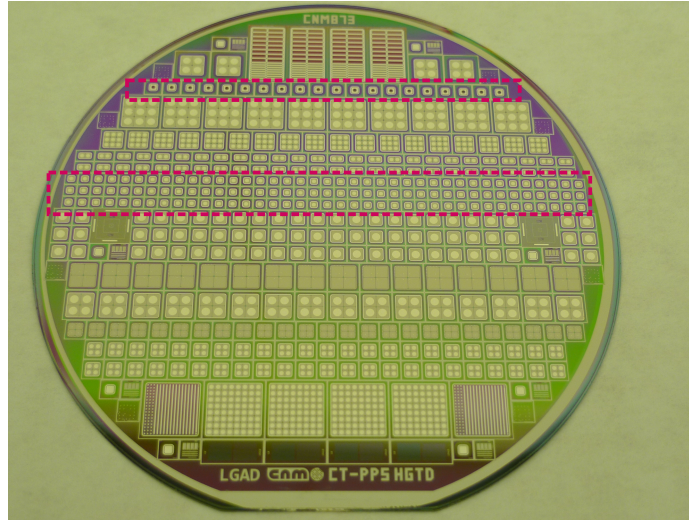


FIGURE 6.13: Photograph of a manufactured wafer from the 4NLG1-v2 run. The single-pad LGADs for testing are located within the red boxes.

As in the 4NLG1-v1 batch, phosphorus was implanted for the multiplication layer with an energy and dose of 100 keV and $1.9 \cdot 10^{13} \text{ at/cm}^2$ and annealed at 1100°C for 180 minutes. For the P^{++} construction, boron was implanted with two energies and doses: 150 keV and $5 \cdot 10^{14} \text{ at/cm}^2$, and 70 keV and $1 \cdot 10^{15} \text{ at/cm}^2$ and annealed at 1000°C for 52 minutes. Within the active area, the n-type multiplication region has an area of $1 \times 1 \text{ mm}^2$. During the fabrication, a circular entrance window of 0.7 mm diameter was etched on the metal surface covering the active area, to avoid light reflection during gain response measurements. Such entrance window is composed of a layer of $0.7 \mu\text{m}$ of silicon nitride over a $0.4 \mu\text{m}$ layer of silicon dioxide.

6.5.1 Evaluation of the entrance window thickness: SRP measurements

The doping concentration of the PN junction composing the nLGAD devices was investigated via SRP technique (see section 5.6.4). Such measurements helped us to estimate the thickness of the P^{++} layer ($\sim 1 \mu\text{m}$), which never gets depleted and hence composes, along with the passivation layers, the dead entrance window of the device. The results are shown in Figure 6.14. The profile was obtained by using the junction field correction model labelled as *model 1* in section 5.6.4).

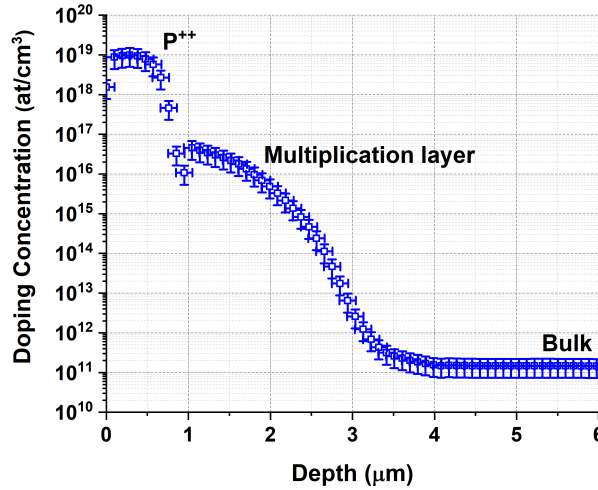


FIGURE 6.14: Doping concentration around the PN junction of the studied nLGAD samples, extracted via SRP technique [91]

The determination and optimization of the entrance window thickness is fundamental for detectors tailored to detect low-penetrating particles. A low-penetrating charged particle may, before reaching the active region of the detector, lose a significant portion of their energy as they pass through the dead entrance window. If such window is too thick, some low-energy ions may be completely absorbed within it or lose so much energy that the generated signal in the active volume falls below the threshold set by the noise of the detection system. The same applies for low-penetrating photons. If the penetration depth of the photon species is too small, or the intensity of the beam source is too low, we may be unable to detect the impinging particles.

As stated, in Chapters 4 and 5, the furnaces at the IMB-CNM were replaced with new equipment during the period 2020-2022 and the 4NLG1-v1 run was manufactured with the IMB-CNM old equipment. The 4NLG1-v2 was an engineering run aimed to replicate the results of the nLGAD first version with the aforementioned new equipment. Thus, the optimization of the dead entrance window layer was not covered for this nLGAD batch. Nevertheless, it is important to acknowledge that **future nLGAD productions at the IMB-CNM will require a deep-level study of how the dead entrance window can be optimized with dependence on the desired application (e.g. the desired target particles to detect).**

6.5.2 Basic electrical characterization: IV and CV measurements at 20°C

Capacitance vs bias voltage measurements were performed on more than 20 devices distributed across different places on the wafer. The CV curves were obtained with a Keysight Agilent 4284A LCR-meter in parallel mode, at 20°C, 10 kHz and 500 mV AC. Figure 6.15 displays the average CV curve of such measurements, showing a very uniform depletion voltage of the gain layer ($V_{gl} \simeq 28$ V) across the wafer. Alongside, leakage current vs bias voltage measurements were carried out for the same samples, at 20°C and with a Keithley 2410. The guard ring (Figures 6.11 and 6.12) was connected in every measurement to separate the surface current from the leakage current in the detector bulk. The average IV curve is also shown in Figure 6.15, highlighting a leakage current (in the operational voltage region) of the order of the nA, and a mean breakdown voltage of $V_{BD} \simeq 225$ V. In Figure 6.15, the bar errors in the IV curve are only displayed up to the mean breakdown voltage of $V_{BD} \simeq 225$ V, as the relative error in the current measurements grows exponentially after such bias point.

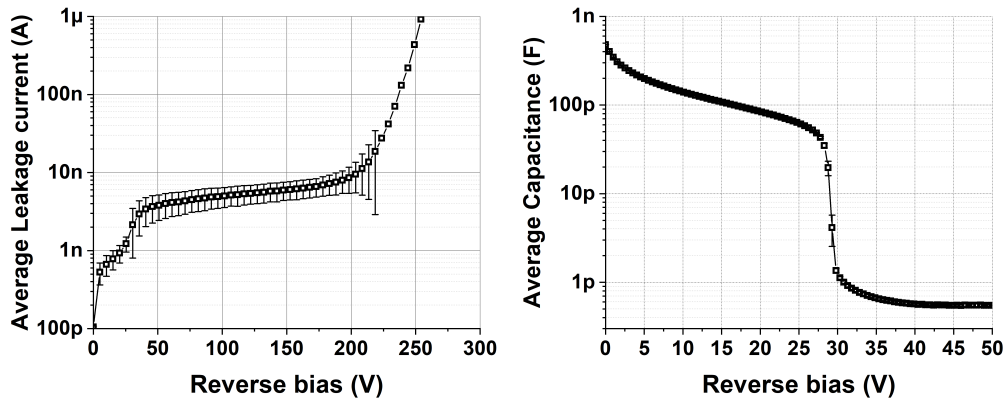


FIGURE 6.15: Average curves (with standard deviation errors) of the capacitance and leakage current measurements at 20°C.

There are a few differences in the CV and IV behavior with respect to the 4NLG1-v1 batch. Firstly, the V_{gl} was smaller for 4NLG1-v1 nLGAD sensors (≈ 26 V) in contrast to 4NLG1-v2 ones (≈ 28 V). This slight variation may be due a change in the furnace where the multiplication and P^{++} layers were annealed, since the diffusivity of dopants in silicon is highly dependent on the manufacturing conditions. As discussed in section 4.3, a larger V_{gl} value does not necessarily translate into a higher gain response for a gives bias. Thus, it is not reasonable to claim that the difference in V_{gl} has supposed a technological upgrade.

Nonetheless, the actual improvement in this second IMB-CNM nLGAD run is related to the leakage current. Devices from the 4NLG1-v1 run had a bigger active area than 4NLG1-v2 detectors, hence a lower leakage current was already expected. For devices of the same active thickness, as it is the case, a more precise comparison can be made by calculating the surface density current (that is, the total leakage current divided by the active area). For 4NLG1-v1 nLGAD devices, the average current density was ≈ 900 nA/cm² while for 4NLG1-v2 ones, such value went down to ≈ 300 nA/cm². As thoroughly discussed during this thesis, low leakage current values are always desirable in particle detection applications, as it reduces the overall noise. While this upgrade in leakage current may be multifactorial, it is worth

remarking that 4NLG1-v2 nLGAD detectors were manufactured in new furnaces, which are less likely to have particulate contamination from several years of previous processes.

6.5.3 Gain response to UV, visible and IR light

Three nLGAD detectors were investigated for their gain response when exposed to ultraviolet (UV) light of 369 nm, visible light of 404 nm and infrared (IR) light of 1064 nm. The measurements were carried out at room temperature with a Transient Current Technique (TCT) setup [106]. The laser beam was focused around the center of the active area (Figures 6.11 and 6.12), at normal incidence with respect to it and with a projected area of $\approx (\pi/4)60 \cdot 60 \mu\text{m}^2$ on the surface of the entrance window (of $\approx (\pi/4)700 \cdot 700 \mu\text{m}^2$). Such center was found by scanning the signal response of the devices in X and Y using steps of $2 \mu\text{m}$. The laser pulse frequency (1kHz) was kept constant for all wavelengths and both nLGAD and reference nPiN during the measurements. The pulse width was also fixed to the minimum value of the laser diodes, though it differed for each wavelength: ≈ 100 ps for 369 nm and ≈ 300 ps for 404 and 1064 nm.

The laser-generated signal is read from the device frontside (as shown in Figure 6.12), goes through a C2-HV Broadband Cividex amplifier, with an analog bandwidth of 2 GHz, 40 dB gain and an integrated Bias-Tee, before being analysed using a DRS4 Evaluation Board Oscilloscope. For every device, wavelength and voltage point, 10000 waveforms were averaged to extract the gain, that was inferred by dividing the integrated amplified output signal (CC) of the nLGAD by the nPiN one.

As the 369 nm UV light is the least penetrating in silicon of all the studied wavelengths [17], the laser intensity was first controlled to achieve an acceptable Signal to Noise Ratio (SNR) in both the reference nPiN and the nLGAD. It was found that a reasonable SNR for the reference PiN was only obtained with the laser diode power at its maximum value (5 mW), for which SNR ranged between 2 and 4 (Figure 6.16) within the studied voltage range. For lower values of the laser diode power, the UV signals in the nPiN were degraded ($\text{SNR} < 2$) or even lost ($\text{SNR} \leq 1$), which would have impeded a gain response analysis. This maximum laser diode power value was maintained when evaluating the nLGADs gain for light pulses of 404 and 1064 nm. For these wavelengths, the maximum power values were 50 mW and 100 mW, respectively.

Nevertheless, the number of photons being absorbed within the active volume of the detector was always smaller than those composing the actual laser pulse, regardless of the used wavelength. This can be understood by evaluating the reference PiN signal (Figure 6.16) and the penetration depth in silicon for every photon species. For IR light of 1064 nm, with a mean penetration depth of $\approx 1000 \mu\text{m}$ [17] ($> 270 \mu\text{m}$ of active thickness), most of the photons will cross the detector without interacting with it, and only a negligible number of them will be absorbed close to the PN junction, hence triggering the avalanche mechanism for electrons. For visible light of 404 nm, with a penetration depth of $\approx 0.1 \mu\text{m}$ [17] ($< 270 \mu\text{m}$), the largest part of the photons will be absorbed within the dead entrance window (passivation and P^{++} layers) without causing a detectable signal, and just a few of them will reach the surface of the depletion width to do so. The situation is even more drastic for UV light of 369 nm, with a penetration depth of $\approx 0.01 \mu\text{m}$ [17].

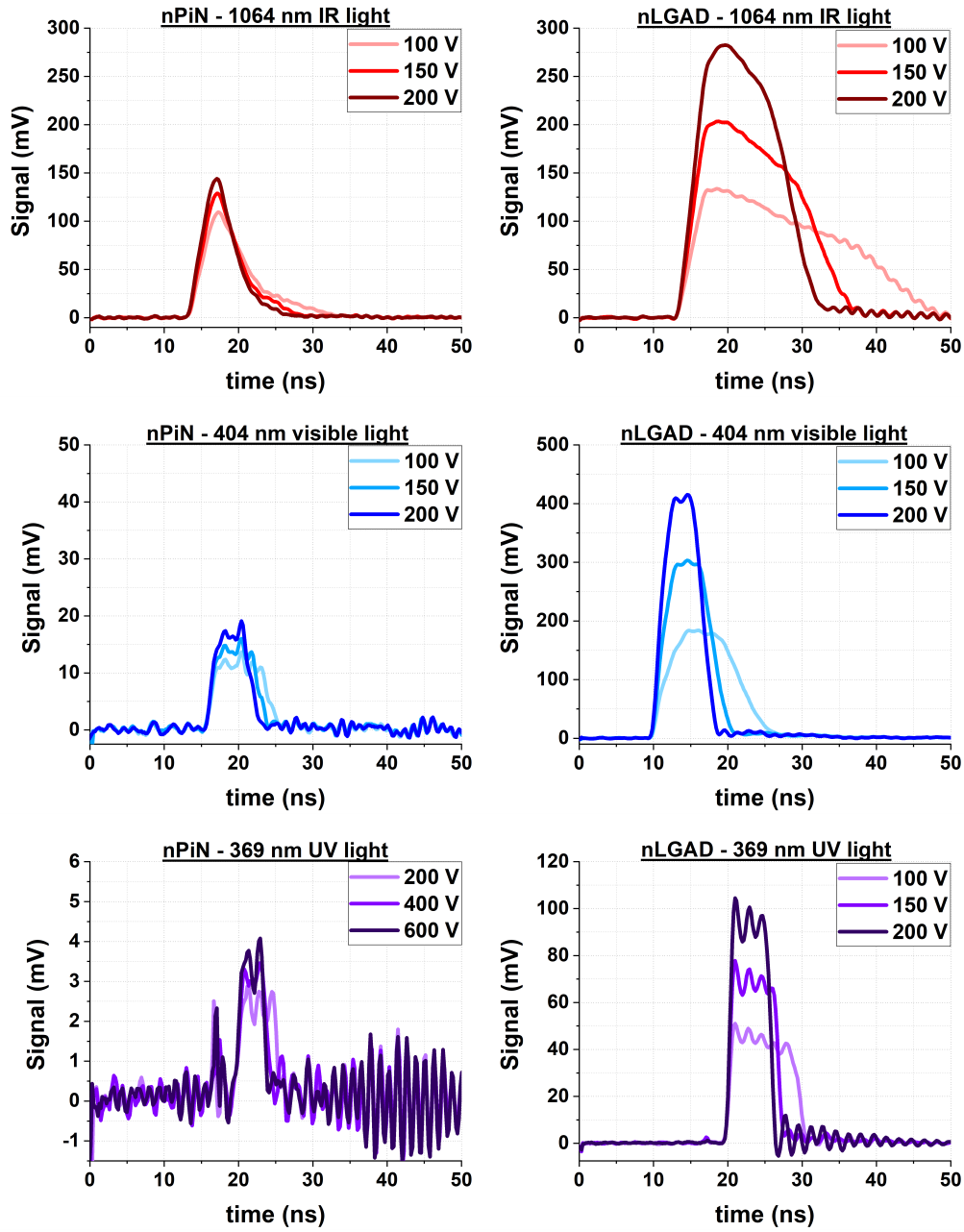


FIGURE 6.16: TCT output signals for illumination of an nLGAD and an nPiN with light of 369, 404 and 1064 nm wavelength. The Y axis is adjusted for every wavelength to better distinguished the differences between the nLGAD and the nPiN signals.

As a result, the actual intensity within the active volume of the detectors varied between wavelengths, despite the laser diodes being operated at their maximum power. By evaluating the nPiN signals in Figure 6.16, we may infer that the highest intensity within the active volume occurs for IR light, followed by visible and UV light.

It is worth noticing that the duration of the laser-generated signals is higher for IR than for visible or UV light. This is a direct consequence of the depth at which the charge carriers are generated. For the IR laser beam, the photons are absorbed with the same probability all along the active thickness of the nLGAD, so both electrons

and holes have to cover a larger distance to the electrodes. Moreover, these primary holes (with a smaller mobility than electrons) will trigger the avalanche mechanism as they cross the PN junction in their motion from the bulk to the P electrode. In turn, this generates an extra bunch of electrons that delays the fall of the signal even further as they traverse the $270\ \mu\text{m}$ thickness to the N electrode. In contrast, visible and UV laser pulses are absorbed very close to the PN junction. In this situation, holes are swiftly collected at the P electrode, leaving only the faster electrons to contribute to the signal duration as they drift to the N one.

The potential of the nLGAD is highlighted when we examine the gain response (Figure 6.17) and the signal amplitude (in contrast to the nPiN ones) for every one of the aforementioned photon wavelengths. **The inner multiplication mechanism of the nLGAD allows for a greater SNR for all the studied wavelengths. When compared to an nPiN, such improvement of the SNR is boosted for UV light, with the lowest penetration depth in silicon of all the photon species investigated via TCT.**

It is significant to mention that the error associated to the reference PiN signals when illuminated with UV light was quite large due to their low SNR (Figure 6.16). In turn, this caused an impact on how accurate the gain for such wavelength could be determined.

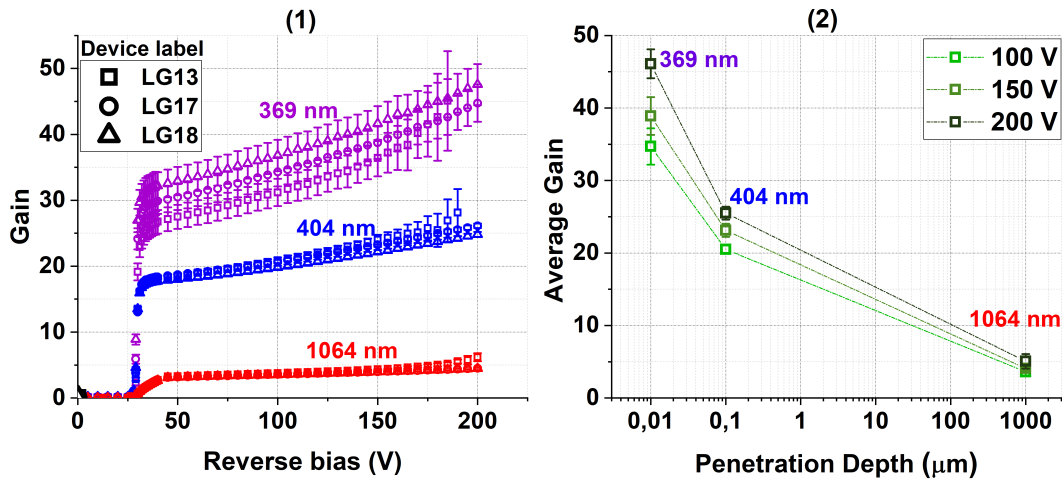


FIGURE 6.17: (1): Gain response to TCT light pulses of 369, 404 and 1064 nm wavelength for the three studied nLGAD detectors. (2): Average gain (with standard deviation error bars) at 100, 150 and 200 V of reverse bias as a function of the penetration depth [17] of the photon species.

Lastly, one nLGAD device (labelled as LG13 in Figure 6.17) was investigated for its gain response for voltages over 200 V. The results are shown in Figure 6.18, where the transition between Linear and Geiger mode can clearly be distinguished for the detector. Moreover, the standard deviation bars (for 10000 measurements per voltage point) boosts when the nLGAD is operated at Geiger mode, which is a direct consequence of the increase in shot noise (see section 2.3.1) for high gain values.

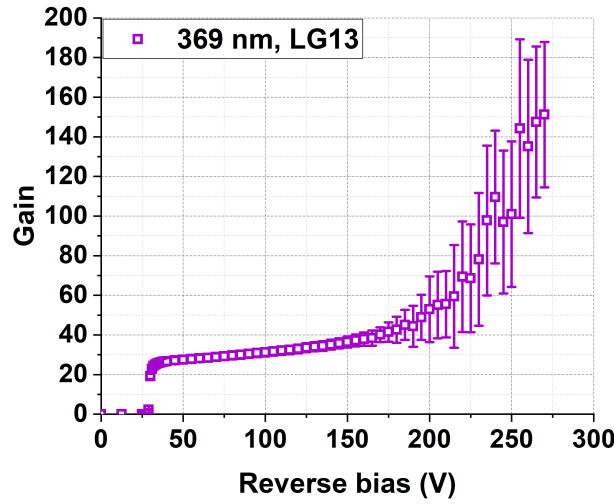


FIGURE 6.18: Gain response to TCT light pulses of 369 nm wavelength for the nLGAD labelled as LG13.

6.5.4 Gain response to 404 nm wavelength visible light as a function of the beam flux

The penetration depth of the target particle to be detected is not the only parameter that determines the gain response of an nLGAD. Evidence of gain reduction in p-type LGADs for high TCT beam fluxes was observed in [84] for IR photons of 1064 nm. Similar gain response measurements as a function of the beam flux of the 404 nm wavelength TCT laser were conducted on one nLGAD device (labelled as LG13 in Figure 6.17). By definition, the beam flux is expressed as

$$I = \frac{N_\gamma}{A} \quad (6.1)$$

where N_γ is the number of incident photons per unit time (that is, the intensity) and A is the projected area of the laser beam on the device surface.

With a TCT setup, N_γ can be tuned by adjusting a Digital to Analog Converter (DAC) threshold V_{th} , that controls the amount of power that is fed to the laser diode. The smaller the V_{th} value is, the greater the number of photons composing the output laser beam pulse [119]. The reference nPiN detector was first measured to find values of V_{th} where the integral of the laser-generated signal (e.g. the Collected Charge or CC) was linear. That is, to find a V_{th} range where we can assume that $CC(nPiN) \sim N_\gamma \propto -V_{th}$. The results are shown in Figure 6.19.

On the other hand, A can be adjusted by displacing the board where the nLGAD is mounted in the z position (the perpendicular to the beam direction). By moving the detector towards or opposite to the opening of the laser source, the projection of the beam on the center of the detector surface de-focuses, so A can grow larger or smaller. As in the previous section, A was estimated by assuming an elliptical projection of the beam on the detector surface, which axes length are inferred by scanning in X and Y in steps of $2 \mu\text{m}$. Larger values of A translate into having a bigger spatial spread of the incident photons onto the detector, hence reducing the beam flux. For a given V_{th} , it was observed that the reference nPiN signal did not change with A . In contrast, the nLGAD signal did, as Figure 6.20 depicts. This

result showed the first evidence of gain suppression in nLGADs, as both the signal height and its CC got reduced for smaller values of A (i.e. for larger values of the beam flux). Both the DAC threshold V_{th} and the projected area A were swept to investigate the nLGAD gain response dependence on the 404 nm wavelength beam flux, which was estimated to be proportional to $CC(nPiN, V_{th})/A$. Table 6.1 shows the DAC, CC(nPiN) and A values that were used during the measurements.

DAC (mV)	CC(nPiN) (arb)	X (μm)	Y (μm)	$A=(\pi/4)XY$ (μm^2)	Rel. flux (%)
1353	109.7	150	144	16953	3.7
1254	143.5	162	135	17143	4.8
1056	235.7	161	148	18706	7.2
1056	235.7	133	122	12801	10.5
825	318.9	144	138	15675	11.6
1056	235.7	108	97	8285	16.2
825	318.9	115	113	10203	17.8
1056	235.7	83	73	4775	28.2
825	318.9	91	90	6388	28.5
825	318.9	69	68	3686	49.4
1056	235.7	60	52	2415	55.7
825	318.9	48	48	1819	100

TABLE 6.1: DAC, CC(nPiN) at 20°C and 100 V, axes length in X and Y for the beam projection, estimated A and relative flux.

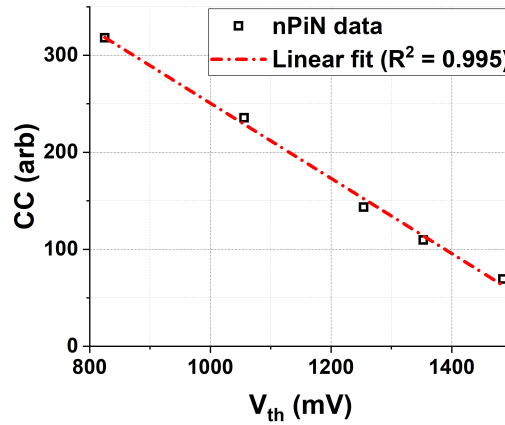


FIGURE 6.19: CC of the laser-generated nPiN signals (CC) dependence on V_{th} within a linear range, at 100 V and 20°C. The projected area $A \approx (\pi/4)155 \cdot 136 \mu\text{m}^2$ was unchanged during the measurements.

The measurements were carried out at 100 V and 20°C. V_{th} was swept within the linear range presented in Figure 6.19, while A was always kept smaller than half the area of the entrance window ($\approx (\pi/4)700 \cdot 700 \mu\text{m}^2$) to ensure that there was no reflection of the incident photons with the metal. The beam was always pointed at the center of the entrance window and at normal incidence. For every flux point, the gain was inferred by dividing the integrated output signal of the nLGAD by the

nPiN one. The results are shown in Figure 6.21, where a clear gain reduction with increasing beam flux is observed. In this figure, the flux was scaled to its maximum value, which corresponds to the minimum value of both V_{th} and A . This result highlights that the gain response of an nLGAD for low-penetrating photons is subjected to both the penetration depth of the species and the beam flux of the source.

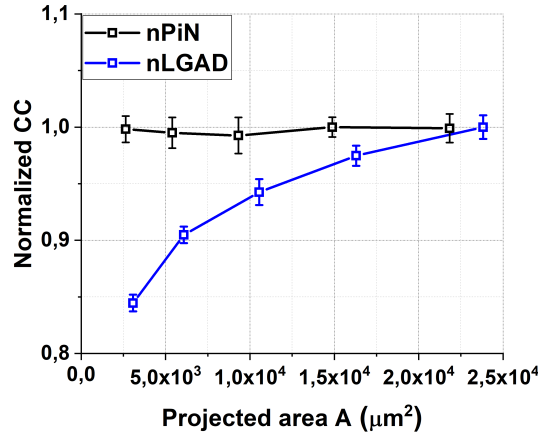


FIGURE 6.20: CC of the laser-generated nLGAD and nPiN signals dependence on the projected area A , at 100 V and 20°C. The DAC threshold $V_{th} = 1056mV$ was unchanged during the measurements. The CC is normalized, for every device, with respect to its maximum value across A , in order to better distinguish the trend for the nLGAD and the reference nPiN.

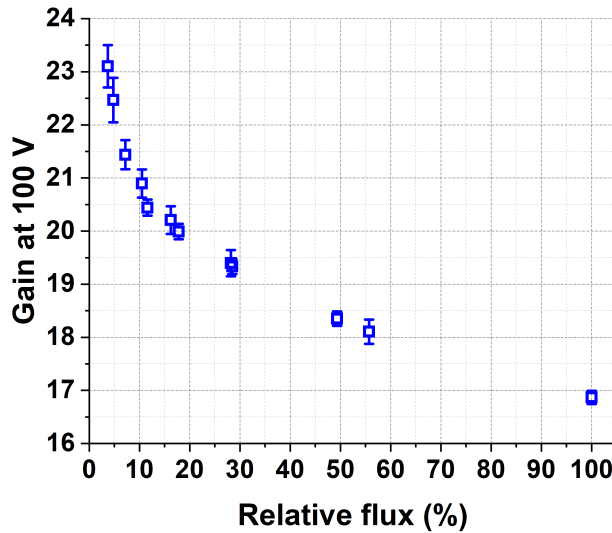


FIGURE 6.21: nLGAD gain response, at 100 V and 20°C, as a function of the 404 nm wavelength laser beam flux (as defined in Equation 6.1). The intensity is scaled to its maximum value, which corresponds to the the minimum value of V_{th} and A in Table 6.1.

6.5.5 Gain response to low-energy protons

Gain response to low-energy protons measurements were performed using the nuclear microprobe beamline at the Centro Nacional de Aceleradores (CNA, Seville) using a 600 keV proton beam. Protons with such energy are low-penetrating in silicon, as their range is $\approx 10 \mu\text{m}$ [113]. The microprobe is connected to a 3 MV tandem accelerator that provides different species and ion energies [120]. It showcases a set of micrometer slits designed to avoid radiation damage during Ion Beam Induced Current (IBIC) characterization and to prevent the ion beam halo, which decreases the spatial resolution. The quadrupole lens system allows for focusing the ion beam to micrometer dimensions. This setup is further complemented by a 2D scanning system synchronized with the acquisition one, allowing spatial information by enabling mapping with excellent spatial resolution for areas of up to a few millimeters. A more detailed description of the nuclear microprobe beamline is provided in [121].

To investigate the gain response in nLGAD devices as a function of depth, we employed the same methodology developed in a previous work, where the effect of the ionization charge density in the gain response of p-type LGAD devices was studied [85]. For that,

IBIC measurements can be conducted with the ion beam incident at different angles with respect to the normal of the detector. This is enabled by a special sample holder capable of rotating under vacuum with an accuracy of 1 degree. Furthermore, the signal acquisition and subsequent processing were carried out using a conventional electronic chain, comprising an HV source (model NHR 22 20X), a CANBERRA pre-amplifier (Model 2003BT), a Tennelec TC 245 amplifier, and connected to the OMDAQ acquisition software. One nLGAD and one reference nPiN detector were tested via IBIC. The nLGAD under test was previously measured via TCT, and corresponds to the one labelled as LG13 in Figure 6.17. The reference nPiN was also the same as the one used during the TCT measurements reported in the previous section.

Figure 6.22 shows a typical energy spectrum obtained when conducting an IBIC 2D scan on the nLGAD under test.

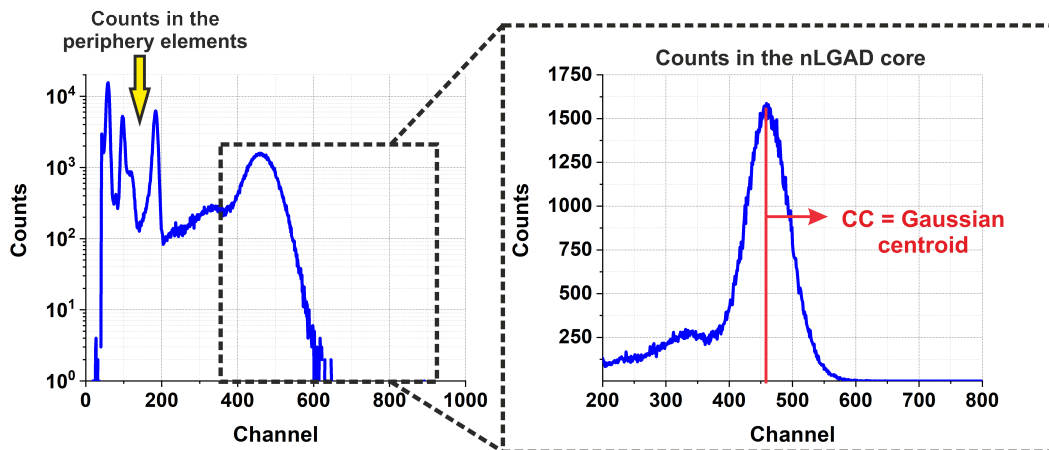


FIGURE 6.22: Energy spectrum, at normal incidence, 50 V and room temperature, for 600 keV impinging on the nLGAD under test. The left picture shows the spectrum in logarithmic scale, where counts in the nLGAD periphery elements can be grasped. The right picture shows, in linear scale, only the channel range around the multiplication area, along with its Gaussian centroid.

The energy deposited by a 600 keV proton in the nLGAD sample generates an electrical signal, that is processed by the aforementioned electronics chain. The energy spectrum can further be imaged as a 2D mapping, which allows to evaluate the channel range where the counts correspond to protons crossing the multiplication layer (Figure 6.22). Once such channel range is identified, the collected charge (CC) in the device can be defined as its centroid (Figure 6.22), obtained via Gaussian fit.

The same procedure is then done with the reference nPiN, which allows us to estimate the gain by dividing the CC of the nLGAD by the nPiN one. The CC experimental error is statistically inferred by dividing the Full Width at Half Maximum (FWHM) of the Gaussian fit by the square root of number of counts within its channel range. In Figure 6.22, the spectra of the nPiN and nLGAD were obtained at normal incidence, 50 V and room temperature. The 2D sweep in the nPiN case was done around the active area (discarding periphery elements), reason why only a peak is observed in the energy spectrum. Also, in such figure the channel number has been scaled to the CC of the reference nPiN, so a gain spectrum and map are obtained.

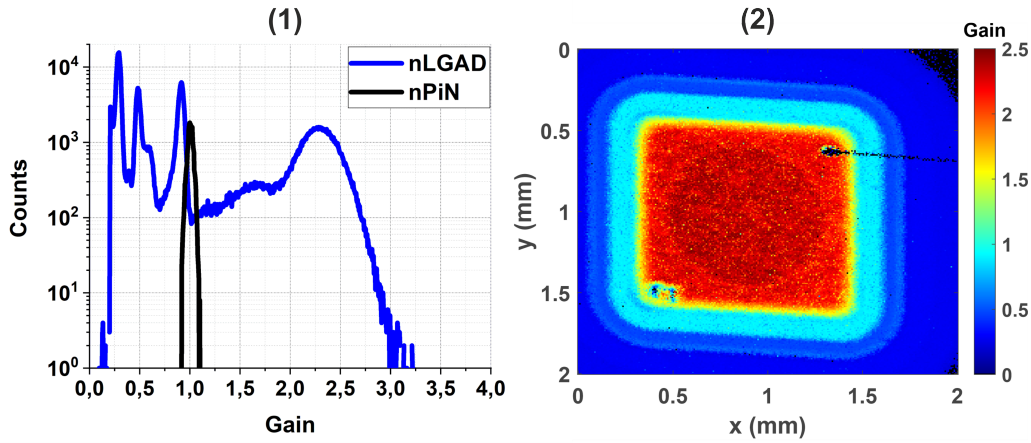


FIGURE 6.23: (1): Spectra of the nPiN and nLGAD, at normal incidence, 50 V and room temperature. (2): Image reconstruction of the nLGAD spectrum in (1), where both the active area and the periphery elements (Figures 6.11 and 6.12) can be distinguished. The channel number has been scaled, in both pictures, to the CC of the reference nPiN, so a gain spectrum and map are obtained.

It is worth noticing that the energy peak around the nLGAD active area is way broader than that of the nPiN. This is due to statistical fluctuations in the number of avalanche-generated charge carriers. The energy resolution at 50 V, estimated as $FWHM/CC$, was found to be 0.5% for the nPiN and 17.7% for the nLGAD.

With the aforementioned methodology, gain response measurements were conducted on the devices under test. The first set of measurements were carried out at room temperature, normal incidence and sweeping the bias voltage. The gain response was evaluated both by impinging the 600 keV proton beam through the frontside (P^{++} in Figure 6.11) and the backside (N^{++} in Figure 6.11) of the devices. Taking into account the thickness of the passivation, P^{++} and multiplication layers (Figures 6.11 and 6.14), a 600 keV proton has its Bragg peak within the high-resistivity substrate when the beam is incident through the nLGAD frontside. In particular, the position of such peak occurs at a depth of $\approx 6.5 \mu\text{m}$, setting the zero depth at the PN junction, as displayed in Figure 6.14. Given this scenario, holes

will be the main contributor to trigger the avalanche mechanism as they are drifted to the P^{++} , leaving just a few electrons to do so on the opposite direction. On the other hand, impinging the proton beam through the backside leave us with holes as the sole contributor to trigger the avalanche mechanism. The results are shown in Figure 6.24, along with the gain response to 1064 nm IR TCT beam pulses already presented in Figure 6.17.

As in the case of having the 600 keV beam incident to the device frontside, most of the avalanche-generated charge is caused to the drift of holes for TCT IR photons under the same incident conditions. In turn, this would result in a similar gain response for both particle species, as confirmed by the results in Figure 6.24. It is worth noting that gain suppression effects still need to be investigated both for TCT IR photons and 600 keV protons.

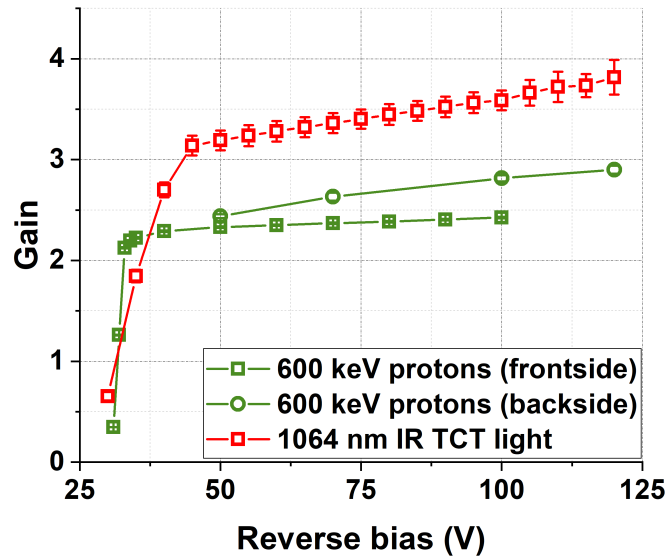


FIGURE 6.24: nLGAD gain response to 600 keV protons (with the beam incident to the device front and backside) and 1064 nm IR TCT beam pulses.

The interest in rotating the nLGAD during the measurements is to modify the depth of the Bragg peak of the incident protons within the detector. In other words, the more we rotate the nLGAD holder, the closer to the detector surface the ions deposit the majority of their energy. This occurs due to the longer track within the dead entrance window layers that protons need to traverse as the rotation angle increases. Taking into account the thicknesses of the dead entrance window layers that cover the nLGAD multiplication layer (Figures 6.11 and 6.14), the Bragg peak depth dependence on rotation angle for 600 keV protons can be estimated via SRIM simulation [104], as shown in Figure 6.25 (1). The gain response results obtained by varying the incidence angle (i.e. the Bragg peak depth) at room temperature are shown in Figure ?? (2). The reverse bias was fixed at 50 V because, at higher voltages and incidence angles (corresponding to high inner gain values), the noise in the pre-amplifier increased significantly.

The analysis of the results reveals that there are three gain response regions based on the protons Bragg peak depth within the device. When the Bragg peak is located within the bulk, the gain is nearly constant, and holes are the major contributor to

cause impact ionization. When the Bragg peak is located within the multiplication layer, more electrons start to be involved in the avalanche mechanism, so the gain increases steadily from ≈ 2 to ≈ 4 . Lastly, once the Bragg peak is located within the P^{++} layer, the gain response is boosted from ≈ 4 to ≈ 15 . On one hand, this is due to the larger number of electrons triggering avalanche multiplication. On the other hand, the ionization charge density within the PN junction drastically drops once the Bragg peak is located within the P^{++} , as the generated charge is quickly recombined in this layer. In turn, this may reduce potential gain suppression effects.

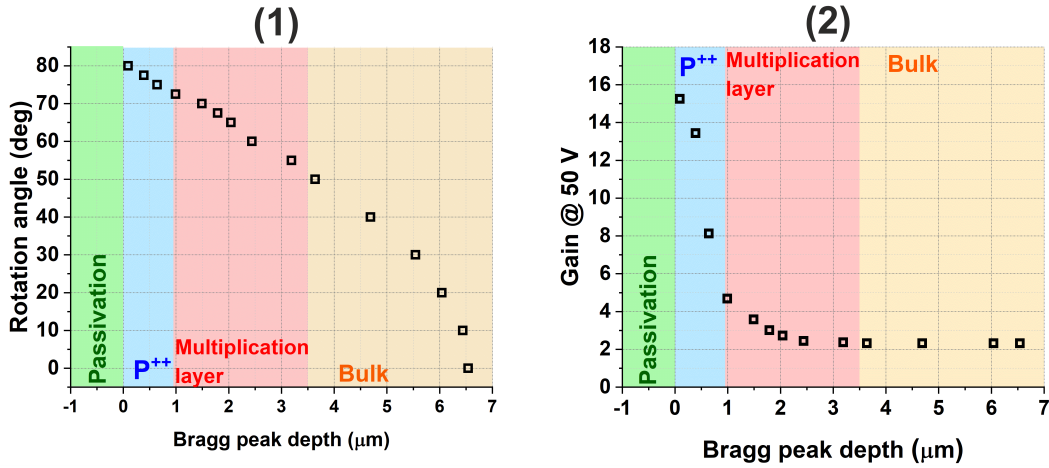


FIGURE 6.25: (1): Bragg peak depth dependence on rotation angle, inferred via SRIM simulations, for 600 keV protons impinging on the studied nLGAD. (2): nLGAD gain response, at 50 V and room temperature, to 600 keV protons as a function of the Bragg peak depth.

The behavior of nLGAD sensors in terms of electron impact ionization contribution can be better understood by evaluating the CC dependence on the rotation angle, as shown in Figure 6.26. As the Bragg peak begins to move from the bulk toward the PN junction, the CC of the nLGAD and nPiN drops due to the increase of energy loss in the dead layers. However, there is a turning point in between $60\text{-}70^\circ$, where the Bragg peak starts entering the very PN junction. At this stage, the contribution of electron impact ionization begins to counterbalance the scenario, leading to enhanced CC and gain for the nLGAD. For the last rotation angle values, the CC drops again, as most of the proton energy starts being lost within the dead layers. However, the gain is maximum for such rotation angle values, as electron impact ionization contribution is at its highest. Additionally, the charge ionization density around the high-electric field region is at its minimum, so a reduction of potential gain suppression effects cannot be discarded to explain the boost in gain.

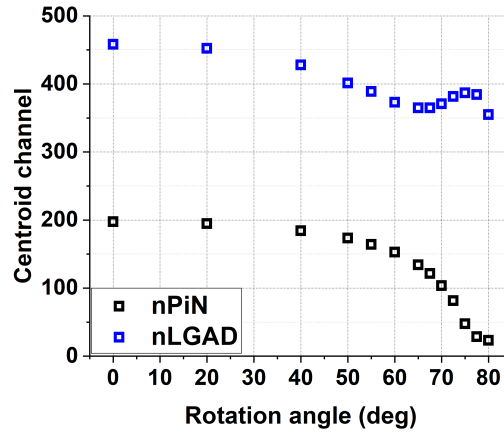


FIGURE 6.26: CC vs rotation angle for the studied nLGAD and nPiN irradiated with 600 keV protons.

Despite the aforementioned arguments, a clear conclusion inferred from Figure 6.26 is that **the CC for a nLGAD is improved with respect to a standard nPiN detector when detecting low-energy 600 keV protons.**

6.6 Conclusions and future work

Overall, the results presented in this chapter demonstrate that **the nLGAD gain response is enhanced for low-penetrating photons detection.** Moreover, they also highlight that the flux of the beam source is a key parameter to consider when evaluating the performance of such devices, as **higher fluxes lead to lower gain values.** This is a direct consequence of having a higher ionization charge density around the PN junction (i.e. where the electric field is at its maximum value), an effect already observed in [84], [85] for traditional p-type LGAD devices.

Additionally, IBIC measurements to 600 keV protons indicate that relatively **moderate levels of gain (5-20) are obtained for low energy charged particles only when electrons are the major contributor to trigger the avalanche mechanism.** In particular, this was observed once the Bragg peak of the protons located within the dead entrance window. Taking that into account, we cannot discard that the gain enhancement may also be due to **low levels of ionization charge density around the high-electric field region, that might reduce gain suppression effects.**

The gain response results presented in this chapter are tied to the way the nLGAD sensors have been manufactured. Different strategies for the implantation and annealing of phosphorus and boron for the multiplication and P electrode layers, respectively, can change the nLGAD gain dependence on particle species. On one hand, the peak and width of the multiplication layer dependence on implantation and annealing can modify the electrical performance of the nLGAD in a great extent. Moreover, the thickness of the P^{++} is also highly dependent on implantation and annealing. **As the P electrode is part of the dead entrance window, its tailoring is crucial to assure that the fabricated nLGAD will be sensitive to the target low-penetrating particle** [117], [118]. The same argument applies when designing the passivation layers.

Furthermore, the 4NLG1-v2 run is the first manufactured at the IMB-CNM with its new furnace equipment. As in the case of traditional LGAD, **the nLGAD technology is in need of stabilization** by means of replicating controlled manufacturing runs.

As stated previously in this chapter, the first nLGAD detectors fabricated at the IMB-CNM were not customized to fulfill the requirements of any particular application, but rather to serve as a proof of concept. Upon succeeding on that, the doors are open to further study the nLGAD performance, such as their time or space resolution when pixelated, their entrance window tailoring for specific applications or their radiation hardness. Additionally, different nLGAD technological configurations may be considered, as fabricating them with the DLG technology (see [section 5.7](#)).

Chapter 7

Trench iLGADs for fill factor optimization

7.1 Introduction

In Chapter 5, the importance of optimizing the fill factor in segmented LGADs was briefly addressed. In this last chapter, we will delve deeper into the topic and introduce a potential technological solution to approach the matter. For LGAD, the *fill factor* (FF) is defined as the ratio of the active detection area, where the avalanche mechanism occurs, to the total active area of the detector. In another words, **it represents the percentage of the detector's active area that counts with a multiplication layer actively contributing to impact ionization**. As an example, we may evaluate the FF for the ATLAS and CMS devices studied in Chapter 4: 15x15 pixels of 1.3x1.3 mm² and 47 μm IP, and 16x16 pixels of 1.3x1.3 mm² and 80 μm IP, respectively. For them, the detector's area where the passage of an incident particle will not trigger avalanche multiplication is enclosed by the IP region between pixels. Thus, the FF can be evaluated as $FF(IP) \approx (1300 - IP(\mu m))^2 / 1300^2$, obtaining $FF(47 \mu m) \approx 92\%$ and $FF(80 \mu m) \approx 88\%$. Either case, a rough $\approx 10\%$ of the active area is deprived from causing avalanche multiplication. Moreover, let us recall that a reduction of the IP from 80 to 47 μm resulted in an increase in pop-corn noise [51]. While strategies are being investigated to reduce the likelihood of such noise appearing as the IP decreases [52], achieving a fill factor of 100 % is impossible as long as the multiplication layer is pixelated.

Enhancing the FF is fundamental for many reasons. First, the good time resolution inherent to LGADs will be degraded for particles that hit the no-gain regions. By improving the FF, LGAD devices can more precisely determine where the interaction occurs, which is critical for reconstructing particle trajectories. Additionally, detection efficiency improves with higher FF values, which is particularly important in high-luminosity environments like the HL-LHC, where detectors must handle a large number of particle interactions while minimizing data loss.

An LGAD tailored to achieve 100 % FF, the *Trench iLGAD* (TiLGAD for short), is presented in this chapter. It was first fabricated at the IMB-CNM, and its design simplifies the engineering process of LGADs targeted for timing applications.

7.2 LGAD designs for fill factor optimization

The FF optimization may be first investigated by substituting the p-stop (or p-spray) and JTE structure between pixels with *trenches*, leading to a new LGAD variant called *Trench-Isolated* LGAD (TI-LGAD) [122], [123]. The cross-sectional schematic of this TI-LGAD is illustrated in Figure 7.1. A trench is a structure that replaces

both the JTE and p-stop/p-spray, where the high-resistivity silicon between pixels is patterned and etched deep into the wafer ($\sim 10\ \mu\text{m}$). This is generally achieved using a technique called Deep Reactive Ion Etching (DRIE), which is a subtechnique of plasma etching, discussed in section 3 (see section 3.2). In short, the process involves placing the wafer, after photolithography to define the trench pattern and width, into a vacuum chamber containing specific plasma species that etch silicon. The desired depth of the trenches depends on the duration the wafer remains in the chamber, which is calibrated beforehand using a test wafer. Once the trenches are created, they are filled with a dielectric material, typically SiO_2 [122], [123]. This process provides effective pixel isolation and a smooth electric field at the pixel edge by physically separating them with insulating material.

While trench isolation of pixels does not provide 100% FF, functional TI-LGAD devices with a nominal IP distance as small as $\approx 3\ \mu\text{m}$ have been achieved [123]. For comparison, the ATLAS and CMS IMB-CNM detectors mentioned earlier in this chapter had IP distances of 47 and $80\ \mu\text{m}$, respectively.

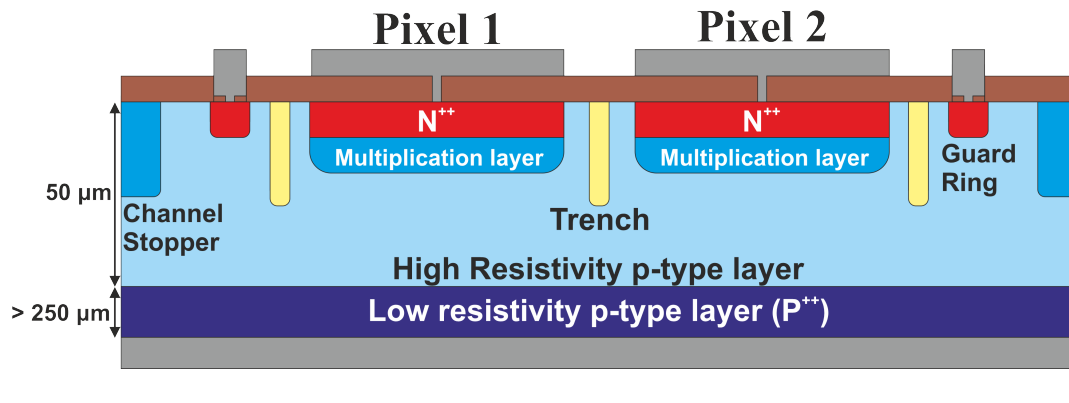


FIGURE 7.1: Cross-section schematic of a pixelated TI-LGAD with a matrix of 2×2 pixels.

Another technological approach to enhance the FF of LGADs is the *Capacitively – Coupled* LGAD (AC-LGAD) [124]. The main difference compared to a traditional LGAD is the construction of the N electrodes, which are AC-coupled (hence their name). This means they are not directly connected to a metal layer but are capacitively coupled to it through an insulating layer, typically SiO_2 [124] or Si_3N_4 [125]. A brief description of the AC-LGAD functioning will be hereunder provided. For a more extensive overview, the reader may refer to [108], [124]–[126].

In AC-LGAD sensors, the avalanche-generated charges do not pass directly through a highly-doped N^{++} layer to the metal pixels, as is the case for a traditional LGAD. Instead, such charges spread laterally along a moderately doped N^+ resistive layer toward the grounded N^{++} contact located at the edge of the core (Figure 7.2). As the charges move through the resistive layer, they create a time-varying electric field that influences the metal pads. Even though no actual charge is flowing through the insulating layer, the changing electric field effectively induces a current in the metal pad, which is what we detect with the read-out electronics. Since the N^+ layer is designed to have a certain resistivity further from ohmic contact values, the signals appear on the metal pads with a delay and attenuation that depend on the distance from the particle interaction point. In other words, the avalanche-generated charge carriers are partially lost in the resistive layer as they move further from the region

where they were originally created. This allows for precise spatial resolution, as the signal amplitudes will be larger in pixels near the particle's impinging point.

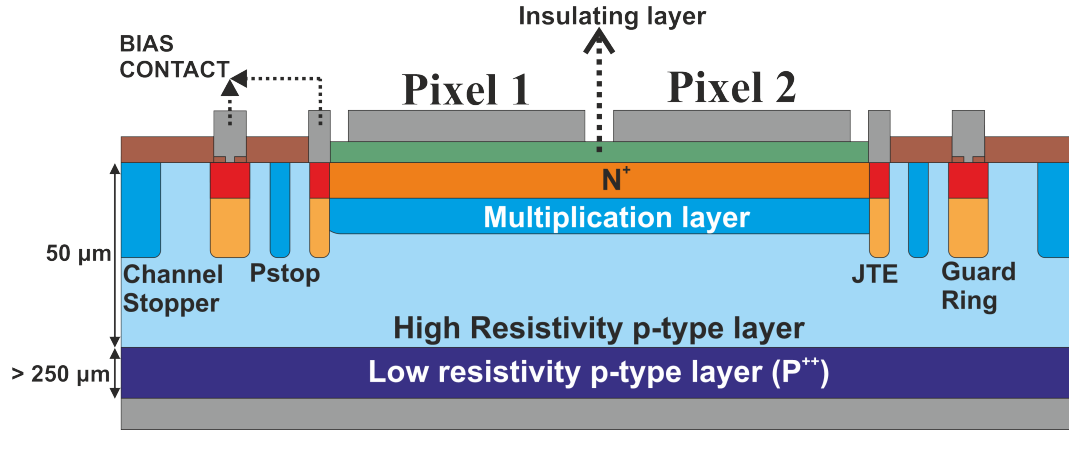


FIGURE 7.2: Cross-section schematic of a pixelated AC-LGAD with a matrix of 2×2 pixels.

It is worth noting that the aforementioned N^+ layer also plays a key role in generating the high electric field responsible for triggering avalanche multiplication. Therefore, its construction must be carefully designed to fulfill both the requirement of moderate inner gain and its role as a resistive layer for the AC-LGAD functionality. On the other hand, signal inductance on the metal pads is enhanced for thinner insulator layers. Nevertheless, such thickness must be maintained at a sufficient high value to avoid *dielectric rupture* of the insulator, a phenomenon that physically damages such layer if the electric field generated by the AC-LGAD PN junction is high enough. Moreover, high values of the dielectric capacitance $C \propto A/d$ (e.g. low values of the insulator thickness d or high values of the metal pad area A) reduce the time response of the device, which may cause the complete loss of the signal below the amplitude threshold set by the noise. Thus, **a delicate trade-off must be made between the metal pixel size and the features of the N^+ , multiplication and insulator layers in order to obtain a functional AC-LGAD.** Despite that, it is clear from Figure 7.2 that **a well designed AC-LGAD has a 100% FF.** Lastly, it is important to remark that the delay caused by the lateral spread of the signal through the resistive layer poses a challenge for AC-LGAD devices, making them less optimal than a traditional LGAD for high-luminosity environments. Additionally, their radiation tolerance under high fluence conditions remains an active investigation topic.

Another alternative technological solution to achieve 100% FF is the *i*LGAD (short for *inverted* LGAD), schematically depicted in Figure 7.3. In an *i*LGAD, it is not the multiplication layer that is segmented to create pixels. Instead, such pixels are created by segmenting the P electrodes on the backside of the device. This approach was investigated at the IMB-CNM, and two *i*LGAD batches were manufactured, showing promising results [25], [124], [127].

Nevertheless, the *i*LGAD fabrication presents a few drawbacks. As it is a double-sided process, photolithography steps are necessary on both sides of the wafer. On one hand, this increases the risk of wafer degradation during manufacturing (e.g., surface scratches or breakage due to handling). Additionally, more engineering steps are needed for double-sided processes, which in turn raises the cost and extends the manufacturing time.

On the other hand, double-sided processing of Si-Si or epitaxial wafers imposes an upper limit on the active thickness of the devices, as pixelating the P electrode would not be feasible for thick low-resistivity handle wafers. Let us recall that fabrication processes at the IMB-CNM clean-room on wafers with a total thickness under $\approx 300\ \mu\text{m}$ are never desirable, as the protection against mechanical crack during wafer handling would be compromised (see section 3.2). That is the reason why the first IMB-CNM iLGAD batch was fabricated on high-resistivity FZ wafers of 100 mm diameter and $\approx 300\ \mu\text{m}$ thickness (4ILG1 technology), which is not optimal for timing applications. An overview of the design, fabrication and characterization of 4ILG1-v1 detectors can be found in [124], and its cross section is schematically depicted in Figure 7.3.

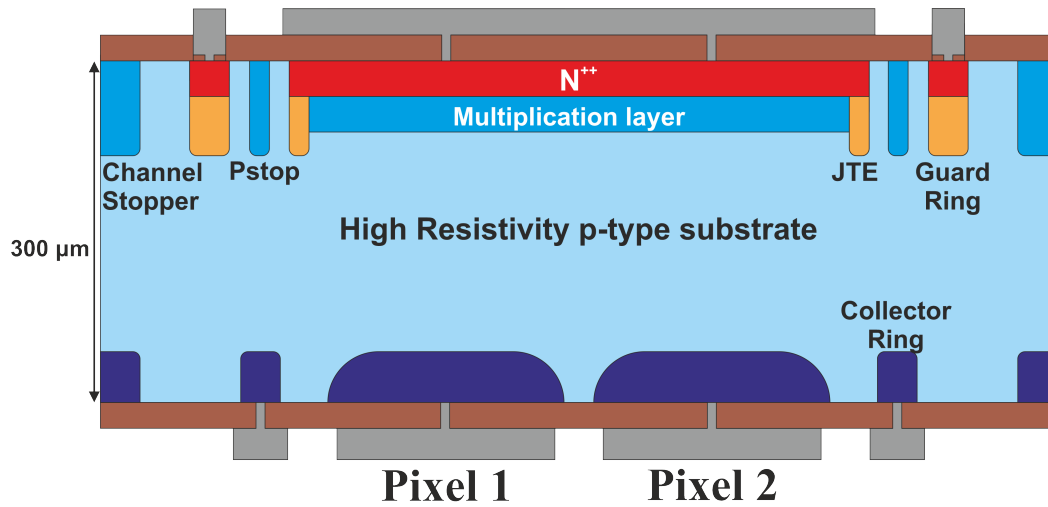


FIGURE 7.3: Cross-section schematic of a pixelated 4ILG1-v1 detector with a matrix of 2×2 pixels.

Furthermore, the periphery of both sides of an iLGAD detector needs to include additional elements in order to be functional for certain applications. Specifically for synchrotron x-rays detection, it was found that 4ILG1-v1 devices fabricated as depicted in Figure 7.3 would not be feasible, as radiation-induced trapped charges at the $\text{SiO}_2\text{-Si}$ interface increased the leakage current to the extent that the devices became non-functional [25], [127].

This setback was resolved in the second iLGAD generation fabricated at the IMB-CNM (4ILG1-v2 run). A cross-sectional illustration of 4ILG1-v2 detectors is shown in Figure 7.4. By adding float guard rings on the PN junction side and p-stop structures on the pixelated P electrodes side, the electric field generated by these trapped charges was smoothed at the device periphery [25], [127]. However, this solution also led to increased manufacturing complexity.

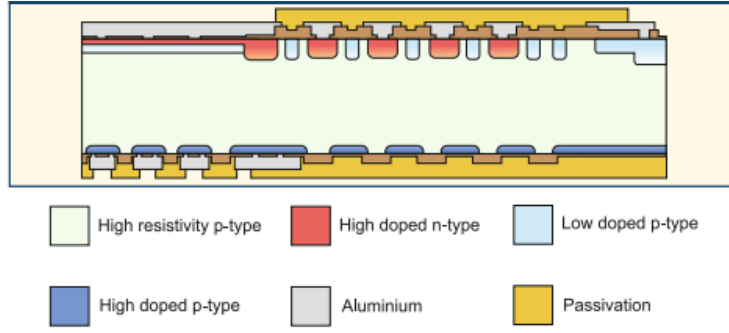


FIGURE 7.4: Cross-section schematic of a 4ILG1-v2 single-pad detector.

Let us sum up the three alternative solutions presented for optimizing FF in LGAD. On one hand, AC-LGAD devices achieve a 100% FF, but their design requires careful balancing of several fabrication parameters, including the metal pixel size and the N^{++} , multiplication, and insulator layers. On the other hand, iLGAD sensors also achieve a 100% FF with fewer design constraints. However, their fabrication involves double-sided processes, which complicate the engineering processes and limit the active thickness of the devices to values over $\approx 300 \mu\text{m}$, which is not ideal for timing applications. Finally, TI-LGADs offer significant pixel isolation with a nominal IP distance as small as $\approx 3 \mu\text{m}$, but do not achieve a 100% FF as AC-LGAD and iLGAD detectors do.

A new LGAD variation, the **Trench iLGAD (TiLGAD)**, was designed and fabricated at the IMB-CNM with the aim to overcome the aforementioned drawbacks. In a TiLGAD, the multiplication layer is fabricated over a thick ($> 250 \mu\text{m}$) high-resistivity n-type handle wafer. Unlike the iLGAD, the JTE is replaced by a deep trench etched from the opposite side of the wafer, enabling single-sided photolithography processes and the reduction of the device active thickness for timing applications while maintaining a 100% fill factor. Its schematic is shown in Figure 7.5.

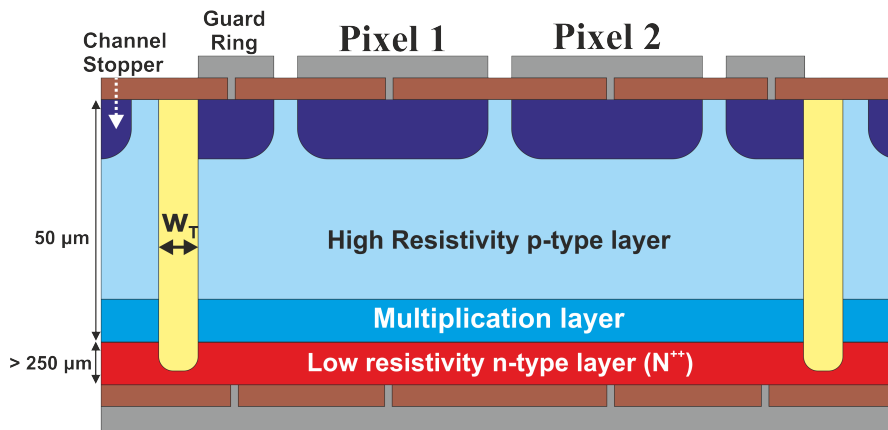


FIGURE 7.5: Cross-section schematic of a pixelated TiLGAD with a matrix of 2×2 pixels.

7.3 Design and fabrication of TiLGAD devices at the IMB-CNM

TiLGAD sensors were first manufactured at the IMB-CNM on 100 mm and 50 μm active thickness Si-Si and epitaxial wafers (4TiLG2 and 4TiLG3 technologies, respectively), as part of the RD50 project [2]. This project aimed, among other goals, to develop pixelated detectors for tracking and timing applications with small pixel pitches ($<55 \mu\text{m}$). In particular, this first TiLGAD batch focused on TimePix3 detectors, with a pitch of 55 μm with an IP of 10 μm [2]. Apart from the TimePix3 structures, the mask used to fabricate the 4TiLG2-v1 and 4TiLG3-v1 runs (CNM1086) also included test structures, both single-pad and pixelated, to validate the TiLGAD proof of concept. A photograph of a TiLGAD wafer manufactured with such mask is shown in Figure 7.6, where the test structures are enclosed within red squares. The TiLGAD periphery elements were optimized using TCAD simulation before the beginning of this thesis. The main results can be found in [25] and are hereunder summarized.

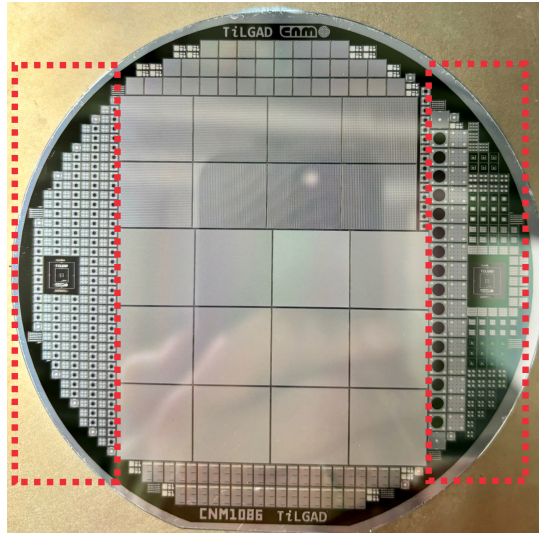


FIGURE 7.6: Photograph of the first TiLGAD wafer fabricated with the CNM1086 mask.

On one hand, it was found that the trench width (w_t in Figure 7.5) played a key role in the periphery's stability. **The wider the trench, the higher the breakdown voltage of the device, which is a direct consequence of having a larger amount of dielectric material smoothing the electric field at the core edge.** Nevertheless, wider trenches present a drawback from a technological standpoint, as they are more difficult to fully fill with deposited SiO_2 and poly-silicon. Additionally, they complicate subsequent photolithography processes, as the photoresist would slide into the partially filled trenches. Thus, the CNM1086 mask was designed with a trench width of 8 μm , which would theoretically ensure a breakdown voltage over 300 V, enough for operating the device, while maintaining a sufficiently narrow trench to try to avoid the aforementioned technological issue. On the other hand, it was found that the trench would necessarily need to be in direct contact with the P^{++} layer. Otherwise, edge electric field effects would cause an earlier breakdown at the gap between it and the trench. The TiLGAD core optimization was partially designed in [25] and further refined as part of this thesis. As previously mentioned, **two types of wafers**

(Si-Si and epitaxial) were used to manufacture the first TiLGAD prototypes, each requiring a different design approach. Let us talk through it.

Si-Si wafers for the TiLGAD batch were obtained by metallurgically bonding two 300 μm FZ wafers: an n-type low-resistivity wafer (phosphorus-doped) that serves as the handle wafer, and a p-type high-resistivity wafer (boron-doped). The latter was implanted with boron prior to the bonding process to create a deep multiplication layer, as schematically represented in Figure 7.5. The boron implantation parameters are detailed in Table 7.1. Notably, the boron implantation dose ($\sim 10^{14} \text{ at/cm}^2$) was one order of magnitude higher than the typical value used for IMB-CNM LGADs ($\sim 10^{13} \text{ at/cm}^2$). This is because the bonding process was known to be conducted at 1200°C for 60 minutes, which causes a greater diffusion of the multiplication layer compared to the typical annealing process at 1100°C for 180 minutes. Thus, implantation doses on the order of $\sim 10^{13} \text{ at/cm}^2$ would have been insufficient to construct devices with inner gain. In other words, the 1200°C bonding process would have diffused a multiplication layer implanted at $\sim 10^{13} \text{ at/cm}^2$ to such an extent that the devices would have ended up being PiN detectors. Once the two wafers were bonded, the high-resistivity one was thinned from 300 μm to 50 μm , an optimal thickness for timing applications. The resulting wafer is schematically represented in Figure 7.7.

The manufacturing process for epitaxial wafers differs significantly from that for Si-Si wafers. In this process, two epitaxial layers are tailored onto a low-resistivity n-type substrate. First, the multiplication layer is created via epitaxial growth (see section 3.2) onto the 450 μm thick n-type low-resistivity substrate (arsenic-doped). Subsequently, a high-resistivity epitaxial p-type layer is grown onto the multiplication layer. The result is a wafer like the one depicted in Figure 7.7, and the different epitaxial layer features are listed in Table 7.1.

It is worth remarking that both the Si-Si and epitaxial processes described above were carried out by external vendors (i.e., not conducted at the IMB-CNM). Therefore, an additional advantage of TiLGAD manufacturing at the IMB-CNM is that the raw wafers already include the multiplication layer, which further reduces the number of photolithography steps.

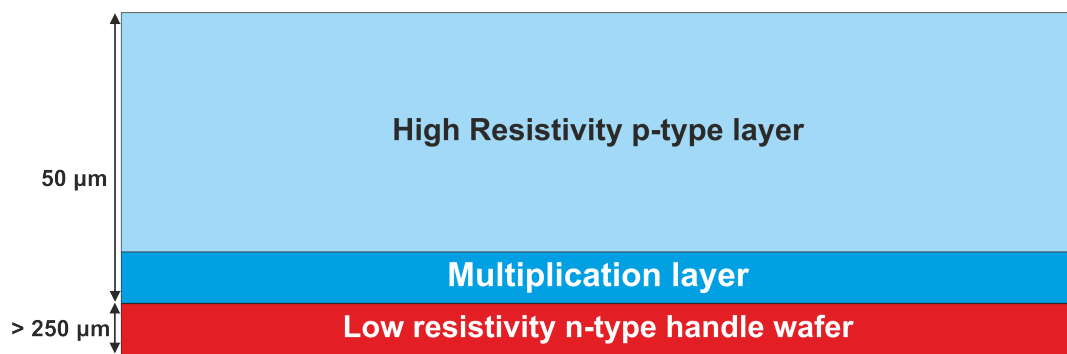


FIGURE 7.7: schematic of a Si-Si or epitaxial wafer used for 4TiLG2 and 4TiLG3 fabrication runs.

4TILG2-v1 (Si-Si wafers)			
	W1	W2	W3
Handle wafer thickness (μm)	300		
Handle wafer dopant concentration (at/cm^3) and type	$\approx 10^{19}$ (Phosphorus)		
Active thickness (μm)	50		
Bulk doping concentration (at/cm^3)	$< 10^{13}$		
Boron implantation dose in multiplication layer ($10^{14} \text{ at}/\text{cm}^2$)	3.7	3.9	4.1
Boron implantation energy in multiplication layer (keV)	150		
4TILG3-v1 (epitaxial wafers)			
	W4	W5	W6
Handle wafer thickness (μm)	\approx 450		
Handle wafer dopant concentration (at/cm^3) and type	$\approx 4 \cdot 10^{19}$ (Arsenic)		
Active thickness (μm)	45-55		
Bulk doping concentration (at/cm^3)	$< 10^{13}$		
Boron doping concentration in multiplication layer ($10^{16} \text{ at}/\text{cm}^3$)	3.0-4.5		
Multiplication layer thickness (μm)	2.7-3.3		

TABLE 7.1: Fabrication features of the 4TILG2-v1 and 4TILG3-v2 runs.

7.3.1 TiLGAD core optimization via TCAD Sentaurus simulation

As discussed in Chapter 3, the first process in any detector fabrication workflow is the growth of a field oxide through oxidation (see section 3.3). In the case of TiLGAD sensors, this oxidation step also serves as a thermal conditioning process for the multiplication layer. To determine the optimal annealing recipe for growing a sufficiently thick field oxide while maintaining a multiplication layer suitable for impact ionization, TCAD Sentaurus simulations were implemented. The outcome was that the typical IMB-CNM annealing recipe for the multiplication layer (180 minutes at 1100°C) was suitable, including temperature ramps and stabilization times, provided that the temperature was increased from 1100°C to 1175°C . Such annealing grows $\approx 8000 \text{ \AA}$ of oxide, which is the standard thickness for field oxide layers at the IMB-CNM. Additionally, TCAD Sentaurus simulations indicated that the operational voltage of the devices would be reasonable if an initial thermal step of 180 minutes at 1175°C is conducted. It is worth noting that in the simulation not only such annealing was taken into account, but the entire thermal load of the fabrication process (e.g. P^{++} annealing or screen oxide processes), which will be addressed in the next subsection. The simulation results of the expected V_{gl} and V_{BD} values are shown in Figure 7.8.

The simulation for TiLGAD devices on epitaxial wafers (Figure 7.8 B) was conducted considering three scenarios based on the multiplication layer thickness and doping concentration ranges listed in Table 7.1. **The minimum (maximum) gain scenario corresponds to the lowest (largest) initial thickness and doping concentration values, while the average gain scenario corresponds to the average initial thickness and doping concentration.**

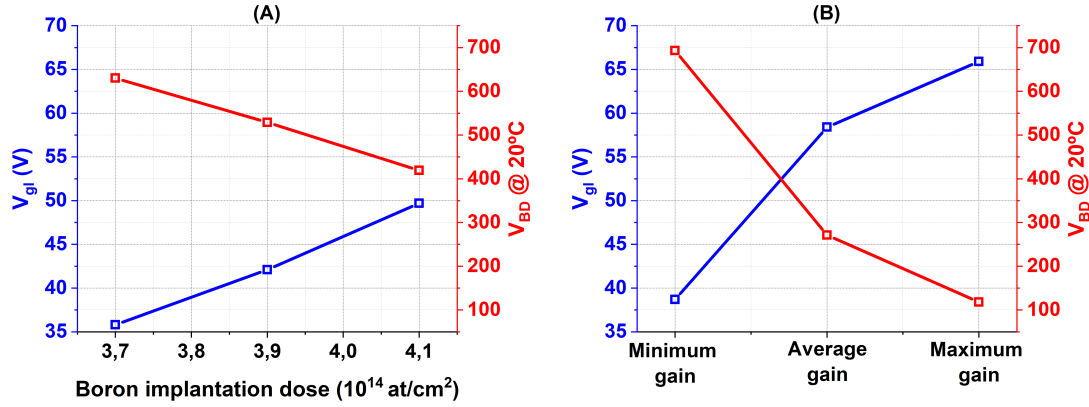


FIGURE 7.8: TCAD Sentaurus predicted V_{gi} and V_{BD} for TiLG2-v1 (A) and TiLG3-v1 (B) devices.

It is important to note that the simulation was performed using a set of boron and phosphorus diffusivity values that were initially tuned to predict the electrical behavior of a traditional LGAD (see Section 5.5.1). However, it was later discovered that this tuning was based on inaccurate fabrication parameters, specifically the screen oxide thickness prior to implantation processes. As a result, the quantitative accuracy of the TiLGAD core optimization conducted via TCAD Sentaurus with these diffusivity values was likely detrimental. Despite this limitation, a few fundamental qualitative insights were still derived from the simulation.

On one hand, Figure 7.8 suggests that **the TiLGAD performance is more difficult to predict if the multiplication layer is epitaxially grown rather than implanted**. This is due to the large relative error of the epitaxial layer parameter values provided by the wafer manufacturer, with the layer thickness and doping concentration varying by up to 20% and 40%, respectively, of their average values. In contrast, **a multiplication layer constructed by ion implantation is a more controlled process**, where parameters like the dose and energy have a relative error generally under 5%. Potential non-uniformities in the doping concentration of thin silicon layers was a setback that was known beforehand, as the epitaxial growth technique was not optimized for the resistivity values required to construct a multiplication layer.

On the other hand, **TiLGAD detectors are expected to have a lower active thickness when using Si-Si wafers**, despite the fact that its high-resistivity layer has the same initial thickness (50 μm) as the epitaxial wafers. This is a direct consequence of the difference in diffusivity for every N^{++} handle wafer dopant species. In the epitaxial case, the dopant is arsenic, which has a very low diffusivity in silicon. Conversely, the handle wafer in the Si-Si case is doped with phosphorus, which has a much higher diffusivity in silicon compared to arsenic [54]. As a result, the N^{++} layer will diffuse more deeply into the silicon bulk, leading to a reduction in the TiLGAD active thickness when the device is fabricated on Si-Si wafers. This is illustrated in Figure 7.9.

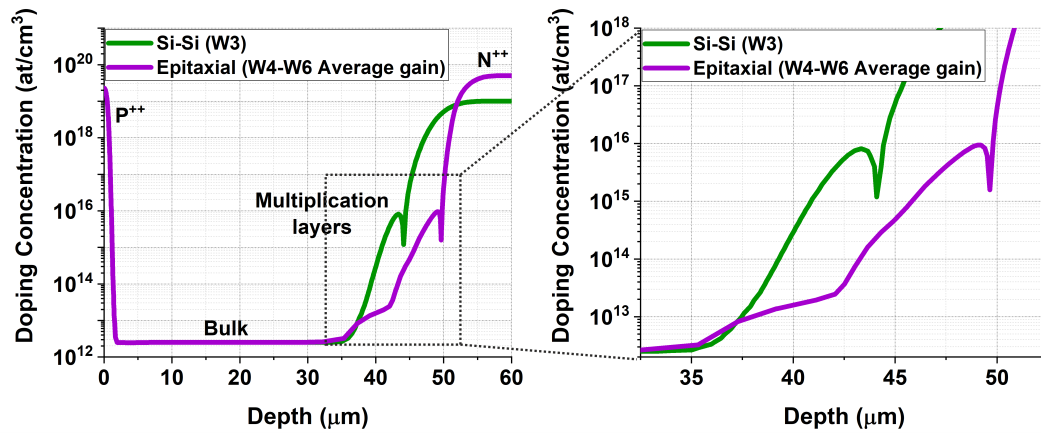


FIGURE 7.9: TCAD Sentaurus simulation of the doping profiles for TiLGAD fabricated on Si-Si (W3 in Table 7.1) and epitaxial wafers.

Last but not least, an theoretical result from TCAD Sentaurus simulations is that **TiLGAD devices might be suitable for applications that imply the detection of both low- and high-penetration particles in silicon with a moderate gain.** Let us recall that traditional IMB-CNM LGAD devices are well-suited for high-penetrating particle detection experiments, but its performance is degraded if the particle is stopped or absorbed close to the entrance window surface. This led to the development of nLGAD sensors (see section 6.3), which are able to detect low-penetrating particles with a high SNR, but are also limited to a penetration depth (photons) or range (charged ions) in silicon below $\sim 1 \mu\text{m}$. As Figure 7.10 shows, TiLGAD have the potential to overcome such limitations of traditional LGAD and nLGAD devices by providing a good gain response for both low-penetrating (e.g. 404 nm wavelength photons of $\approx 0.1 \mu\text{m}$ penetration depth in silicon [17]) and high-penetrating (e.g. 1064 nm wavelength photons of $\approx 1000 \mu\text{m}$ penetration depth in silicon [17]) particles.

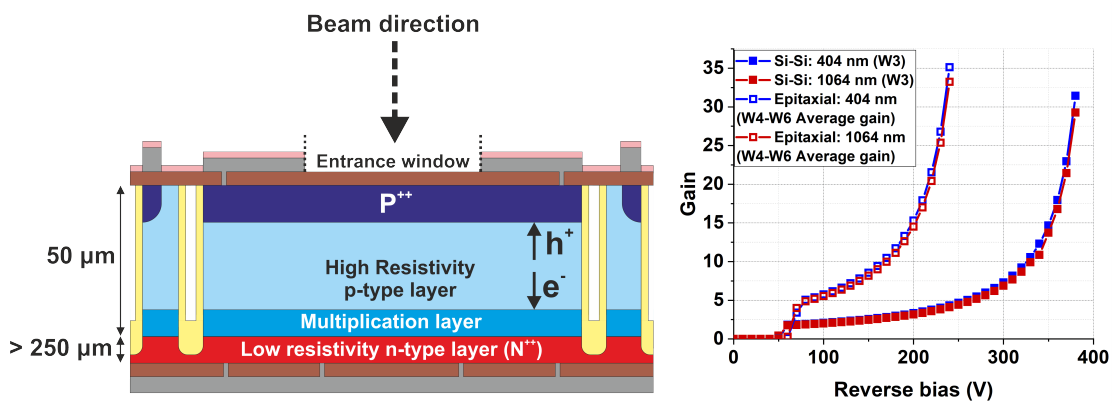


FIGURE 7.10: TCAD Sentaurus simulation of a single-pad TiLGAD gain response, at 20°C, to 404 nm (blue light) and 1064 (IR light) wavelength.

It is worth mentioning that a TiLGAD built on a n-type high-resistivity layer would not, theoretically, provide the same values of inner gain for both high- and

low-penetrating particles. This was simulated using TCAD Sentaurus, and the results are shown in Figure 7.11. In the simulation, all layers of the n-type and p-type TiLGAD devices are identical in terms of doping concentration, with only the conductivity type exchanged. Photon-beam illumination was conducted under the same conditions and through the same entrance window (opposite the thick handle wafer). To keep the illustration clear, the figure only presents the simulation results for TiLGAD sensors (n- or p-type) on epitaxial wafers.

The simulated results suggest a gain drop for both wavelengths when an n-type TiLGAD is used. This is attributed to the nature and number of charge carriers responsible for impact ionization in each scenario. In a p-type TiLGAD, and regardless of the photon species, electrons are the primary contributors to triggering avalanche multiplication as they drift towards the N electrode. Conversely, in a n-type TiLGAD, the major contributors are holes, which are less efficient at causing impact ionization (see Section 2.3.4). However, it is important to point out that the results in Figures 7.10 and 7.11 are based on TCAD Sentaurus simulations, and they may not hold true until validated by scientific evidence.

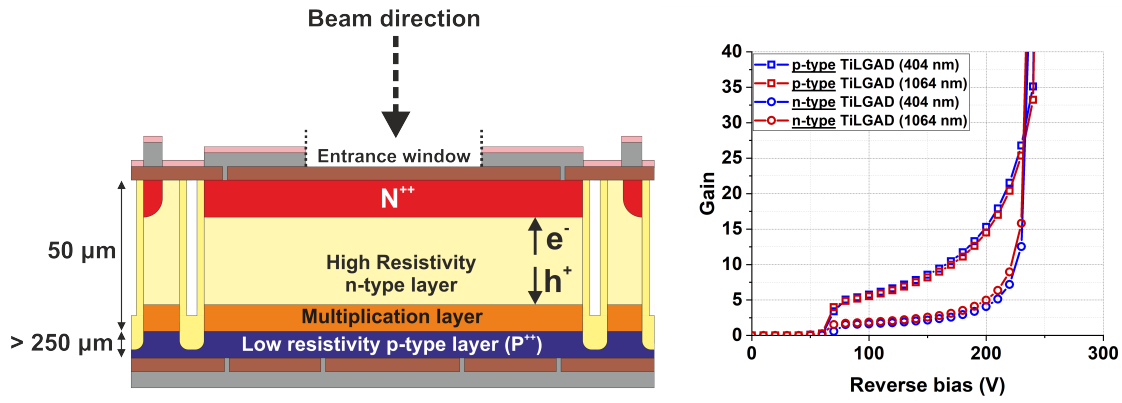


FIGURE 7.11: TCAD Sentaurus simulation of a single-pad n-type and p-type TiLGAD gain responses, at 20°C, to 404 nm (blue light) and 1064 (IR light) wavelength.

7.3.2 TiLGAD fabrication process at the IMB-CNM

As previously mentioned, the first TiLGAD fabrication step is an annealing to both grow $\approx 8000 \text{ \AA}$ of field oxide and thermally pre-condition the multiplication layer. Following this, a photolithography process is performed to implant and diffuse boron for the P^{++} , guard ring and channel stopper wells, as shown in Figure 7.12. Boron is implanted at 50 keV with a dose of 10^{15} at/cm^2 , to be further annealed at 1000°C for 30 minutes. It is worth remarking that, while a traditional LGAD (or nL-GAD) requires three separate photolithography processes to construct each of these layers, the **TiLGAD achieves this with a single photolithography step.**

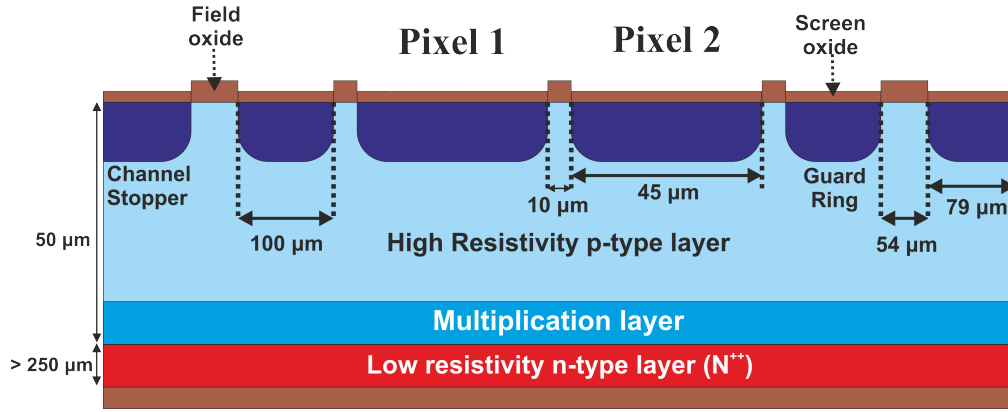


FIGURE 7.12: Cross section of a detector of 2 × 2 TiLGAD pixels after the P^{++} , guard ring and Channel stopper fabrication.

Next, the fabrication of the trenches begins, consisting of several sub-processes. First, a $0.5\ \mu\text{m}$ thick layer of aluminum is deposited uniformly across the surface of the silicon wafer. This layer acts as a protective mask during the trench etching process. After a photolithography step, the exposed aluminum is etched away via wet etching, leaving behind an aluminum mask that protects the silicon underneath it where the creation of trenches is not desired. The wafer is then subjected to the aforementioned DRIE process. The status of the wafer after such processes is depicted in Figure 7.13.

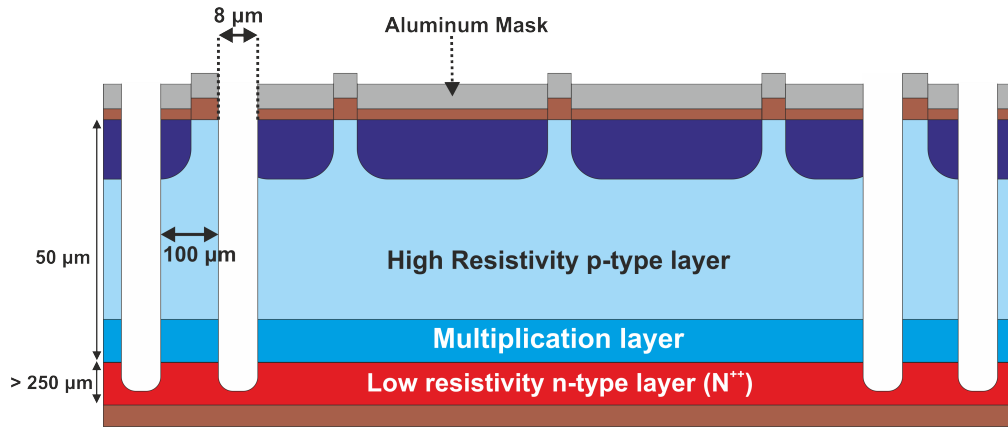


FIGURE 7.13: Cross section of a detector of 2 × 2 TiLGAD pixels after the DRIE process to create the trenches.

After that, the aluminum mask is removed from the wafer surface via wet etching and the process of *trench filling* starts. First, an oxidation is conducted to grow $0.1\ \mu\text{m}$ of oxide on both the wafer and trench inner surfaces. This thermal process consists of two steps. Initially, a dry oxidation is conducted, which grows an oxide layer of $\approx 100\ \text{\AA}$. This thin oxide layer forms the interface with the PN junction and the guard ring, providing the necessary isolation and insulation for these structures. That is the reason why it is grown using dry oxidation, as such process produces a higher-quality oxide compared to wet oxidation or deposition (see section 3.3). The second step involves wet oxidation, which grows the remaining $\approx 900\ \text{\AA}$.

Next, the trenches are capped with a $2.5\ \mu$ layer of poly-silicon. On one hand, this seals the trenches cap more effectively than oxide to recover surface planarization. On the other hand, it also provides mechanical strength to the structure. This step is particularly important in TiLGAD manufacturing, as the wafer will undergo further planar fabrication steps that subjects it to mechanical stress. The poly-silicon layer is uniformly deposited across the wafer surface and then selectively removed through plasma etching. This process ensures that the poly-silicon outside the trenches is completely removed, while the material inside the trenches remains largely intact. Following that, an extra oxide layer of $1\ \mu$ m is deposited to further cap the trenches. This is schematically depicted in Figure 7.14.

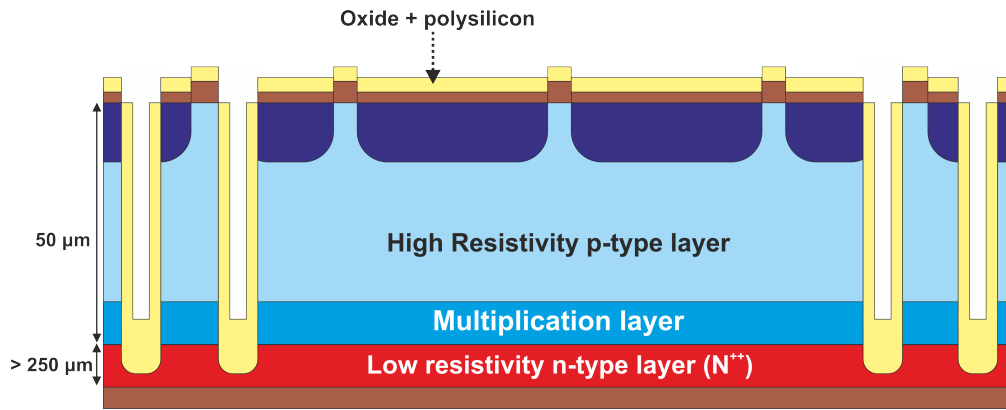


FIGURE 7.14: Cross section of a detector of 2×2 TiLGAD pixels after trench filling process.

The status of the trench after filling was investigated using Scanning Electron Microscopy (SEM). It was found that the trenches had not been completely capped by the aforementioned processes. This is shown in Figure 7.15, where the poly-silicon (granulated bands of $\approx 2.5\ \mu$ m on both sides of the trench) can be spotted. Additionally, the trench width was slightly larger than expected, as the photolithography was designed to pattern $8\ \mu$ m trenches. However, this partial cap was sufficient to ensure both isolation and enhanced mechanical strength, further filling processes were discarded to avoid additional mechanical stress on the wafers.

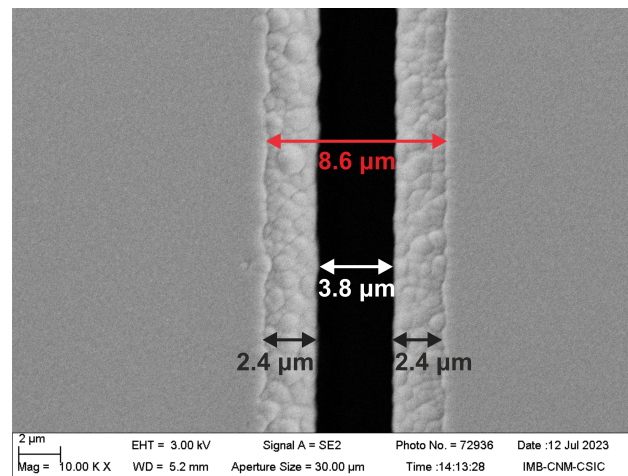


FIGURE 7.15: Top view of a filled trench, obtained via SEM.

Nevertheless, this introduced a setback already mentioned earlier. Due to the partial capping of the trenches, photoresist seeped into them during subsequent photolithography steps, as shown in Figure 7.16. An attempt was made to resolve this issue by depositing thicker photoresist layers during the photolithography process, increasing the typical thickness from $1.2\ \mu\text{m}$ to $3\ \mu\text{m}$. This method partially mitigated the problem, as only a few localized regions on the wafers were observed where the photoresist had seeped through the trenches. These localized defects were corrected by manually applying photoresist.

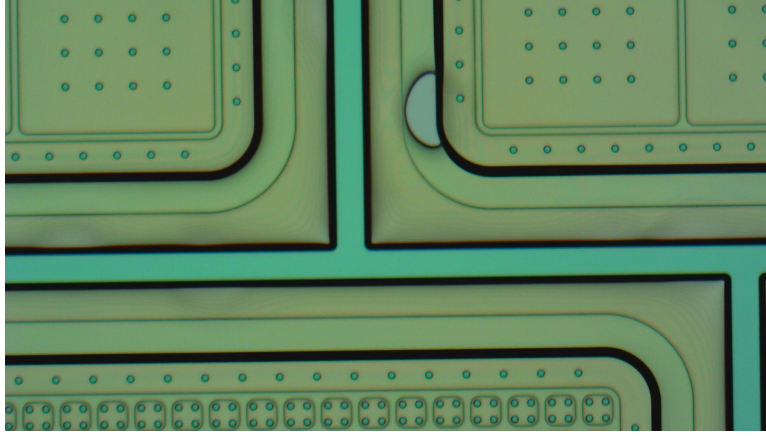


FIGURE 7.16: Optical view of the TiLGAD wafer around the trenches after the oxide and poly-silicon filling process.

After the trench filling process, the wafers underwent the photolithography for opening contacts, metallization and passivation, fabrication steps that were discussed in detail in Chapter 3 (see section 3.3). The final manufactured devices are schematically represented in Figure 7.17, regardless the wafer type (Si-Si or epitaxial). The only difference during these processes was the dielectric material used for the passivation layers. For Si-Si wafers, the standard passivation layers were used: $0.7\ \mu\text{m}$ of silicon nitride over $0.4\ \mu\text{m}$ of oxide. For the epitaxial wafers, hafnium oxide was used. This dielectric material had been previously employed at the IMB-CNM for constructing passivation layers, yielding good results. The main advantage of hafnium oxide lies in its high density and excellent dielectric properties, which allow it to function effectively as a passivation layer with a reduced thickness down to $0.03\ \mu\text{m}$. Its use was implemented in this TiLGAD run with the aim of studying the potential enhancement of the device's sensitivity to low-penetrating particles. A thinner passivation layer (reduced from the standard $1.1\ \mu\text{m}$ to $0.03\ \mu\text{m}$) over the entrance window of the TiLGAD could potentially improve the detection of particles with very low penetration depth (photons) or range (charged ions) in silicon.

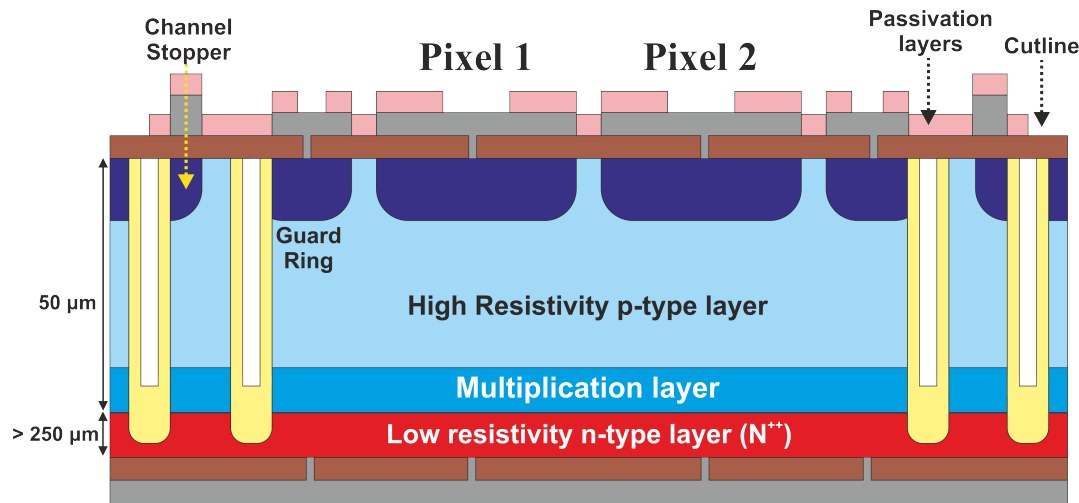


FIGURE 7.17: Cross section of a detector of 2 x 2 TiLGAD pixels after metallization and passivation processes.

It is worth remarking that a **second trench is also manufactured at the periphery to define the cut lines**. The separation between this outer trenches between adjacent devices was designed to be 50 μm, which matches the average thickness of the diamond saw used for wafer dicing. Consequently, the dicing process was expected to remove roughly half of this trench, leaving an outer periphery in the devices as schematically represented in Figure 7.18. This procedure helps to avoid having a floating PN junction at the TiLGAD periphery, which could potentially lead to high leakage current issues. Additionally, the remaining inner fill of the trench serves as a passivation layer that encloses the entire volume of the detectors, enhancing protection against contamination and preventing potential surface leakage current paths from edge defects.

As in the case of previous LGAD runs, the electrical characterization of TiLGAD devices was carried out on single-pad devices, depicted in Figure 7.18.

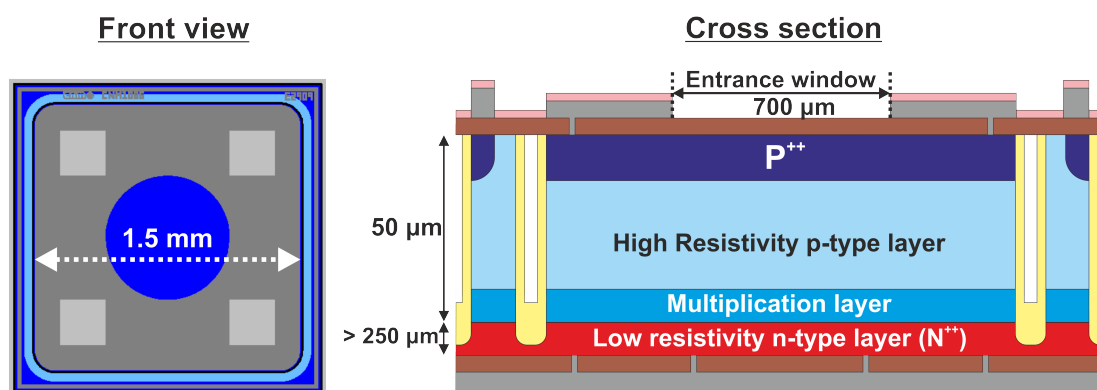


FIGURE 7.18: Front view and cross section schematic of a single-pad TiLGAD.

7.4 4TILG3-v1 run: TiLGAD on epitaxial wafers

7.4.1 IV and CV measurements of single-pad TiLGAD sensors

Single-pad TiLGAD devices on epitaxial wafers (as the ones depicted in Figure 7.18) were tested for their IV and CV behavior at 20°C. IV measurements were performed on 10 devices distributed across different regions of the wafers and using a Keithley 2410. CV measurements were carried out for the same samples using a Keysight Agilent 4284A LCR-meter in parallel mode, at 10 kHz and 500 mV AC. Initially, the IV measurements were conducted by reverse biasing the P^{++} ($V < 0$) and grounding the N^{++} , finding an average V_{BD} of ≈ 20 V at 20°C, significantly different from the expected value. At a later stage, the same IV measurements were conducting by reverse biasing the N^{++} ($V > 0$) and grounding the P^{++} . While the average V_{BD} remained the same, a difference in the leakage current value during linear mode was observed. **Specifically, a low level of leakage current was observed when reverse biasing the P^{++} , as Figure 7.19 shows.**

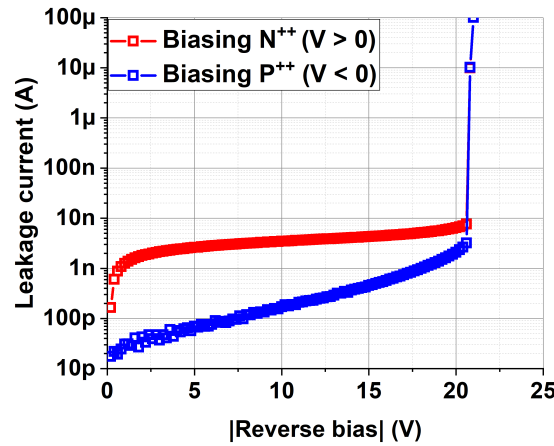


FIGURE 7.19: Average leakage current, at 20°C, of 4TILG3-v1 devices.

Figure 7.20 displays the average CV curve (A) and CV-extracted boron profile (B), obtained when biasing the P^{++} and grounding the N^{++} . **The results indicate that the TiLGAD sensors do not fully deplete before breakdown occurs.** This could also explain the low levels in leakage current when biasing the P^{++} , as the charge may be partially recombining on its drift through a non-depleted active thickness of 50 μm . Additionally, the boron concentration values from the CV-extracted profiles suggest that the multiplication layer is significantly more doped than expected. Let us recall that the maximum doping concentration expected at it, before any thermal annealing, was $4.5 \cdot 10^{16} \text{ at/cm}^2$ (Table 7.1).

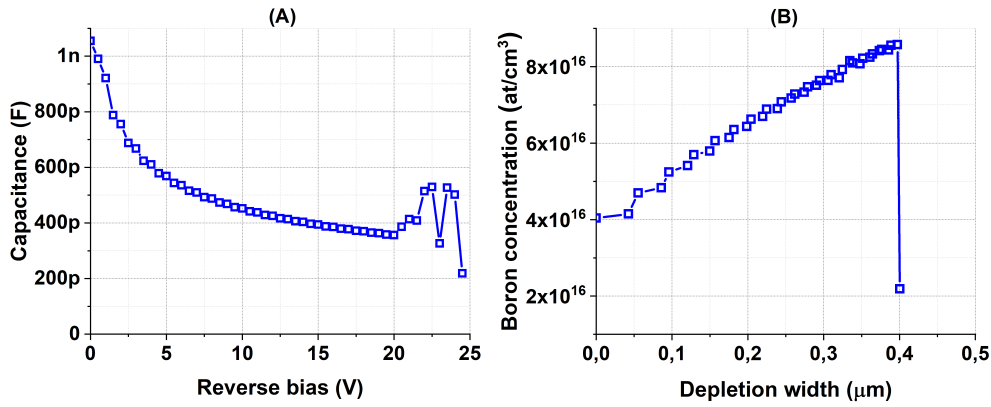


FIGURE 7.20: Average CV curve (A) and CV-extracted boron profile (B) of 4TiLG3-v1 devices.

In order to discard that the devices were experiencing *Zener* rather than avalanche breakdown, the leakage current dependence on temperature was studied for one TiLGAD device. In a nutshell, Zener breakdown occurs in a silicon diode when a reverse bias creates an electric field intense enough to cause electron tunneling across a narrow depletion region [128]. This results in a sudden increase in leakage current at a specific Zener breakdown voltage, which **decreases with increasing temperature** due to the increased energy of the charge carriers. Conversely, the avalanche breakdown voltage **increases with increasing temperature** because, at higher temperatures, charge carriers have a shorter mean free path [129], making it less likely for them to gain sufficient energy between collisions to cause impact ionization.

The results of this temperature dependence study, shown in Figure 7.21, indicated that the TiLGAD devices were experiencing avalanche, not Zener breakdown. This, in turn, suggested that the early V_{BD} was being caused by impact ionization rather than due to any other technological malfunction. However, this could not yet be fully determined, as TCAD Sentaurus simulation also pointed out that a TPiN (that is, without a multiplication layer) would also experience avalanche breakdown at the trenches.

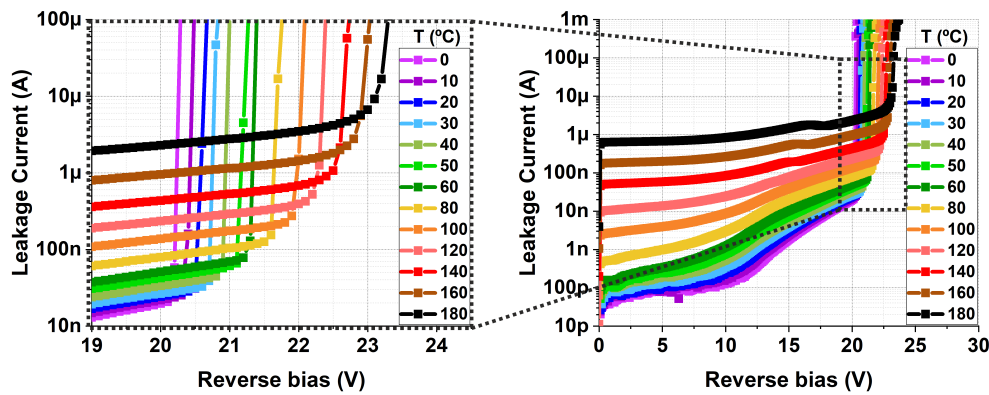


FIGURE 7.21: Leakage current dependence on temperature for a TiLG3-v1 device.

This simulation was carried out with the structure depicted in Figure 7.22, that aimed to qualitatively replicate the studied TiLGAD devices layout. Figure 7.23 shows the simulated IV curves for different temperatures, highlighting an increasing dependence on the breakdown voltage with temperature. Therefore, a potential malfunction of the trenches leading to early breakdown of the device could not be ruled out, and further measurements needed to be planned and conducted in order to fully assure that the low V_{BD} was linked to an excessively high boron concentration in the multiplication layer.

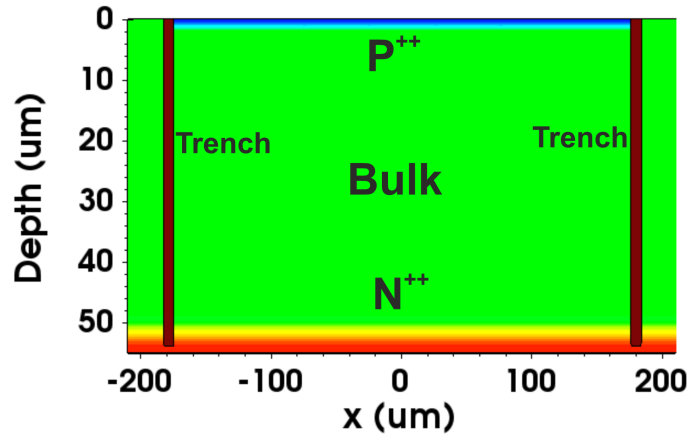


FIGURE 7.22: Structure used to simulate the breakdown voltage nature of TPiNs.

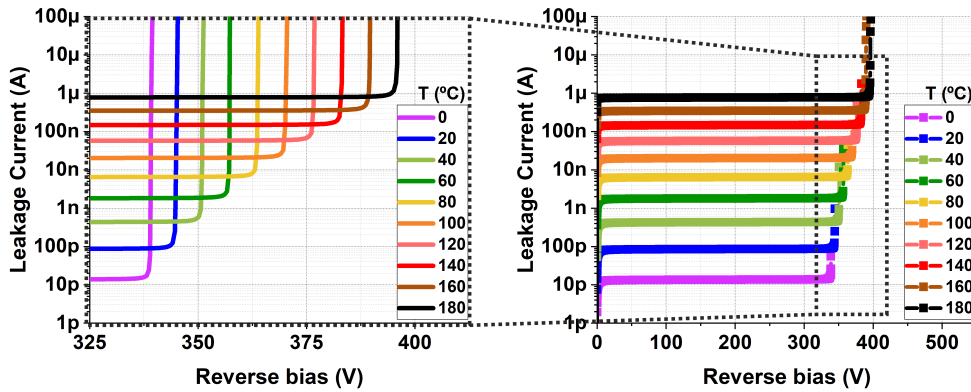


FIGURE 7.23: TCAD Sentaurus simulation of the leakage current dependence on temperature for a TPiN.

7.4.2 Reverse engineering measurements: SRP and cross-section

The doping concentration of the PN junction composing the TiLGAD samples was investigated via SRP technique. Two samples per wafer (six in total), taken out from the distant left and right parts of the wafers, were analysed using this method, and its averaged results are shown in Figure 7.24. Let us recall that the SRP technique requires correction models around the multiplication layer to account for junction

field effects (see section 5.6.4). Since the appropriate correction model for IMB-CNM LGADs has not yet been determined, the SRP method cannot provide a quantitative understanding of the shape of PN junctions.

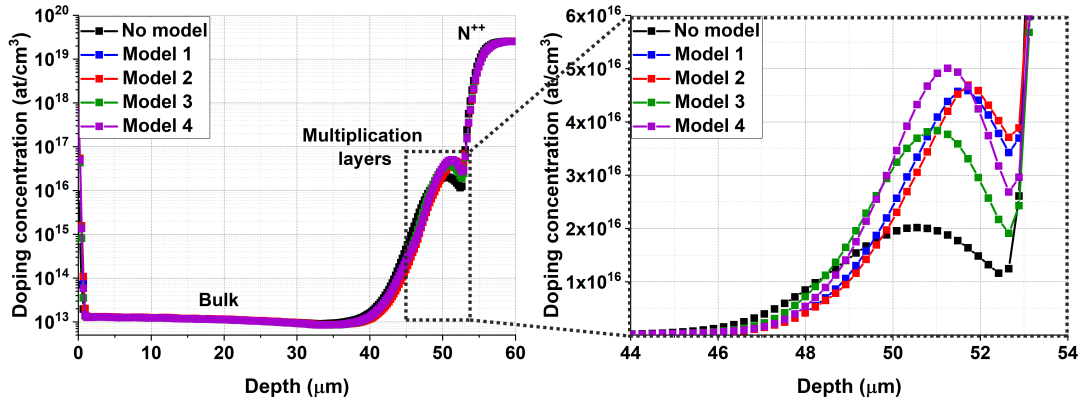


FIGURE 7.24: Averaged SRP doping profiles of TILG3-v1 devices dependence on the junction field correction model.

Despite the aforementioned limitation, **implementing TCAD Sentaurus simulations with the averaged SRP profiles provided some qualitative insights.** These simulations were conducted using the structure shown in Figure 7.22 and the Van Overstraeten-De Man avalanche model (set by default in Sentaurus). The simulations predicted that the breakdown voltage of the devices would be under 50 V, as shown in Figure 7.25. More importantly, regardless of the junction field correction model used, an early breakdown occurring before the multiplication layer reached its depletion voltage was also predicted. **These results qualitatively match the ones extracted via IV and CV measurements** (Figures 7.19 and 7.20).

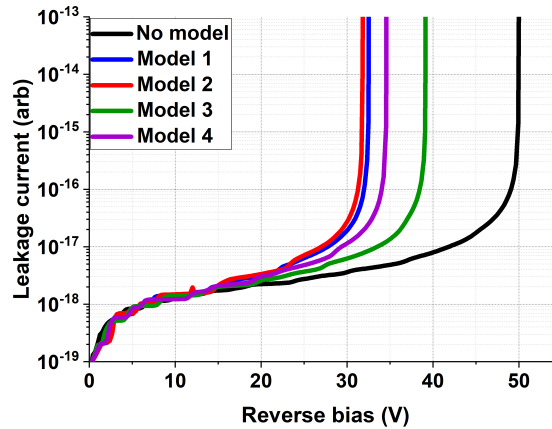


FIGURE 7.25: TCAD Sentaurus simulation of TILG3-v1 devices using the averaged SRP PN junction profiles.

Additionally, a raw epitaxial wafer was partially diced to study the original multiplication layer shape (e.g. before fabrication). The results are shown in Figure 7.26, highlighting that, with independence of the junction field correction model,

the boron concentration in the multiplication layer is always higher than the maximum value provided by the manufacturer ($4.5 \cdot 10^{16} \text{ at/cm}^3$). Only the SRP profile without any correction model fits within the manufacturing specifications. However, it is well established in several studies that applying no junction field correction to the inferred SRP profiles tends to underestimate their doping concentration [93]–[96], [130]. Therefore, the likelihood that the original shape of the multiplication layer matches the one obtained without a correction model is small.

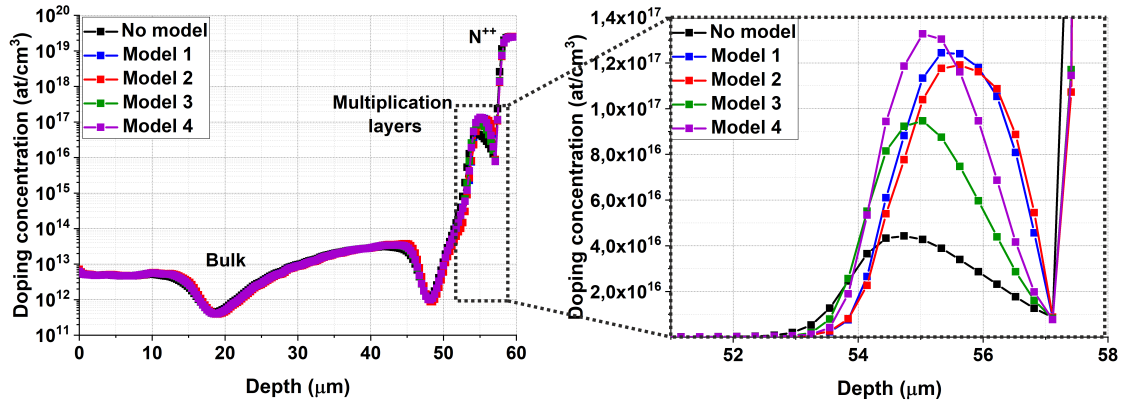


FIGURE 7.26: SRP doping profiles of raw epitaxial wafers (before fabrication) dependence on the junction field correction model.

It is worth remarking that the results shown in Figure 7.26 correspond to a single SRP measurement conducted on a sample from the far corner of the wafer. On one hand, this could explain the non-uniform behavior of the SRP-inferred bulk doping concentration, as edge defects are more likely at the wafer's outer periphery. On the other hand, a single SRP measurement from such a localized area does not provide insight into the uniformity of the multiplication layer across the wafer. Therefore, **further SRP measurements from different regions of the wafer are necessary to fully investigate the original multiplication layer profile.**

As stated at the beginning of this chapter, the development of TiLGAD devices aimed to overcome the technological drawbacks associated with other LGAD proposals featuring a 100% fill factor. However, based on the results presented in this section, it is clear that the use of epitaxial wafers for TiLGAD fabrication introduces a significant setback that cannot be overlooked. As previously mentioned, the epitaxial growth technique is not standardized for the doping concentrations required in the multiplication layer of an LGAD device. **Consequently, 4TiLG2 technology is dependent on the quality of a non-standardized process,** which can only be evaluated once the wafers have been tailored.

Additionally to SRP, a diced TiLGAD was inspected via optical microscopy to evaluate both the trench depth and the thickness of silicon layers with different resistivity. For the latter, the sample underwent a chemical development to expose the transition between layers of different doping concentration. The results are shown in Figures 7.27 and 7.28.

Before the chemical development (Figure 7.27) the geometrical parameters of the trench can be inferred. The trench is wider ($\approx 9.2 \mu\text{m}$) than originally designed ($8 \mu\text{m}$), as already spotted in the SEM picture shown in Figure 7.15. Also, the oxide

and poly-silicon layers are observed to fill the trench more effectively at its base than at its cap.

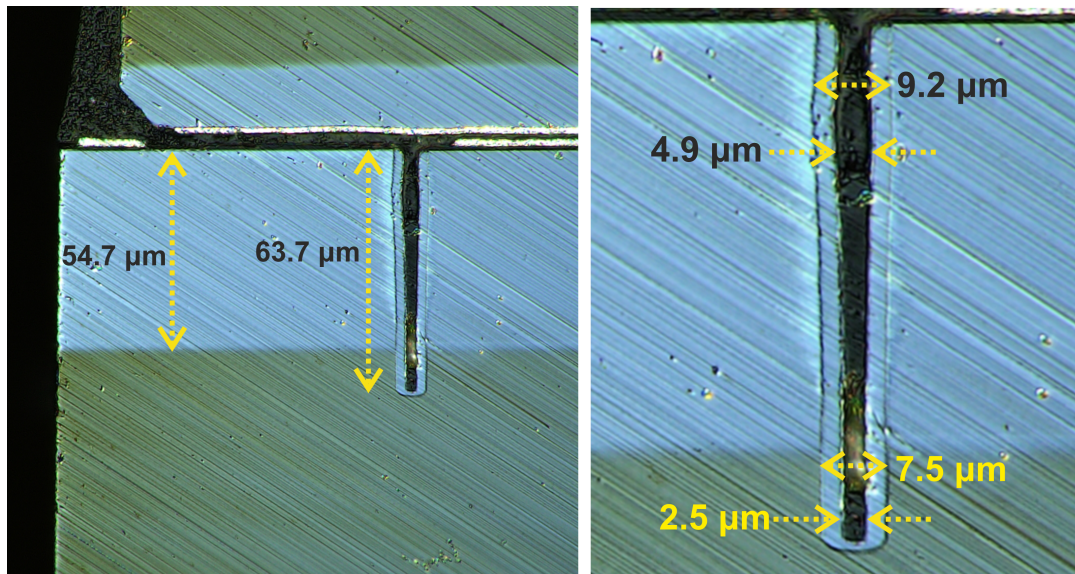


FIGURE 7.27: Optical view of the cross-section of a TiLGAD sample around a trench, before chemical development.

After chemical development, the transition regions between layers of different doping concentration can be clearly observed, as shown in Figure 7.28. Additionally, the second trench at the device periphery was observed to have been completely removed during the dicing process.

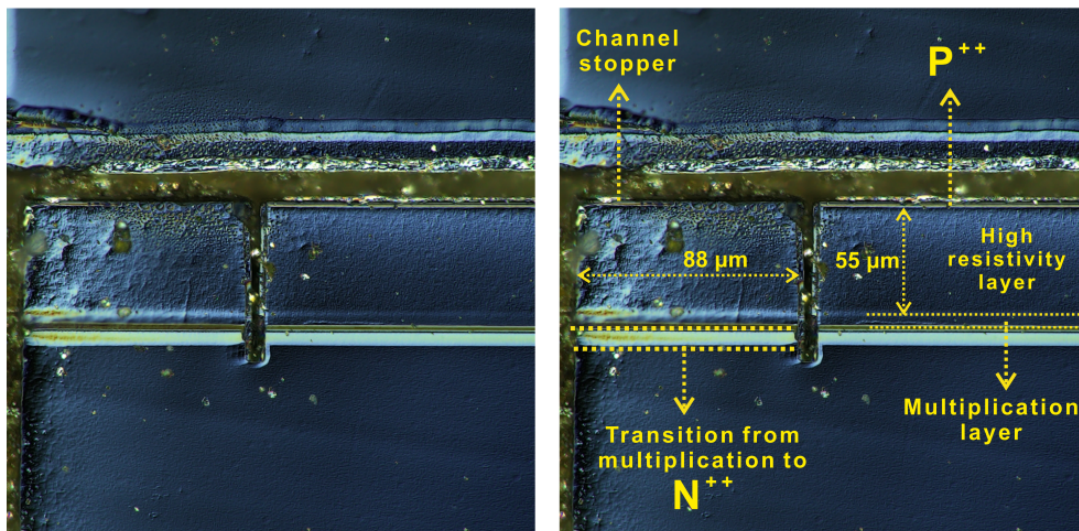


FIGURE 7.28: Optical view of the cross-section of a TiLGAD sample around a trench, after chemical development.

7.4.3 TCT Gain response to 1064 nm wavelength photons

One TiLGAD detector from the TiLG3-v1 run was investigated for its gain response when exposed to IR light of 1064 nm. The measurements were carried out at room temperature with a TCT setup [106]. The laser beam was focused around the center of the active area, at normal incidence with respect to it and with a projected area of $\approx (\pi/4)60 \cdot 60 \mu\text{m}^2$ on the surface of the entrance window (of $\approx (\pi/4)700 \cdot 700 \mu\text{m}^2$). Such center was found by scanning the signal response of the devices in X and Y using steps of $2 \mu\text{m}$. The laser pulse intensity, frequency and width were kept constant for both TiLGAD and reference PiN during the measurements. Such reference PiN belongs to the 6LG3-v1 run (see section 5.4), fabricated on high-resistivity p-type epitaxial wafers and with an active area and thickness of $3.3 \times 3.3 \text{ mm}^2$ and $55 \mu\text{m}$, respectively. For it, the laser beam was also focused around the center of the active area, at normal incidence with respect to it and with a projected area of $\approx (\pi/4)60 \cdot 60 \mu\text{m}^2$ on the surface of the entrance window (of $\approx (\pi/4)2300 \cdot 2300 \mu\text{m}^2$). Within the setup, the laser-generated signal goes through a C2-HV Broadband Cividec amplifier, with an analog bandwidth of 2 GHz, 40 dB gain and an integrated Bias-Tee, before being analysed using a DRS4 Evaluation Board Oscilloscope. For every device and voltage point, 10000 waveforms were averaged to extract the gain, that was inferred by dividing the integrated amplified output signal (CC) of the TiLGAD by the reference PiN one.

The measurements were conducted within a voltage range of 20 to 22 V, corresponding to the transition from linear to Geiger mode as inferred from the IV curves. Figure 7.29 (A) shows the signal response of both the TiLGAD and the reference PiN at reverse biases of 20, 21, and 22 V. Figure 7.29 (B) presents the gain response of the TiLGAD over the aforementioned voltage range. **The results indicate a clear Geiger behavior of the studied TiLGAD, as the gain response is boosted from 0 to 50 in less a volt.** It is also worth remarking that we are comparing the CC of a TiLGAD with a depletion width under $1 \mu\text{m}$ (Figure 7.20), to a fully depleted $55 \mu\text{m}$ PiN.

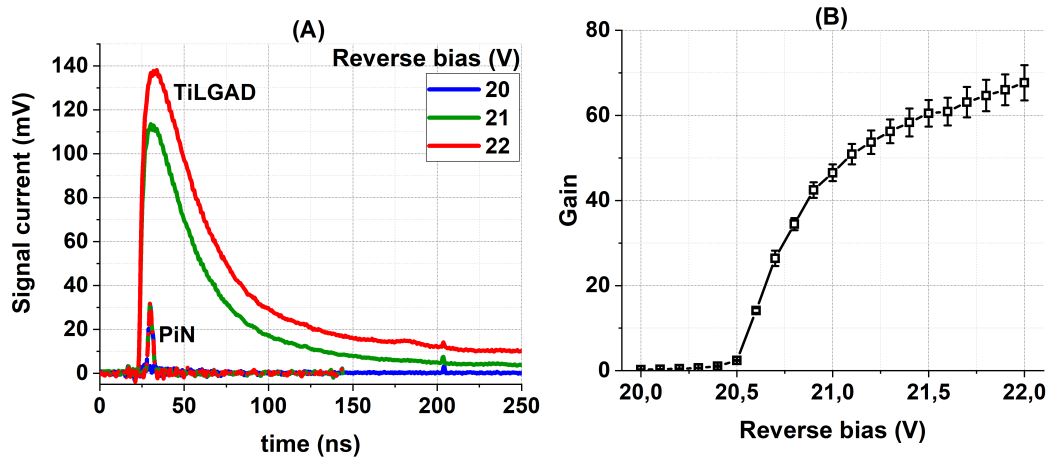


FIGURE 7.29: Signal (A) and gain (B) responses to TCT IR light of 1064 nm wavelength for a TiLG3-v1 device and a reference PiN.

Figure 7.30 shows a 2D map of the average TCT signal amplitude for the TiLGAD at reverse biases of 20.5 V and 22 V. At 20.5 V, the average gain for IR light is ≈ 2.5 , indicating that the device is operating in linear (LGAD) mode. The 2D scan

demonstrates that, while in linear mode, the trenches effectively serve their isolating purpose, as no signal is detected at the device periphery. In contrast, at 22 V, the average gain exceeds 50, and the device operates in Geiger mode. At this voltage, charge injection is observable from all areas of the device, even when the laser beam is projected on the reflecting metal layer. Moreover, the 2D map clearly shows that breakdown occurs at the trenches, where the amplitude of the signals is even higher than the photo-generated signals at the core.

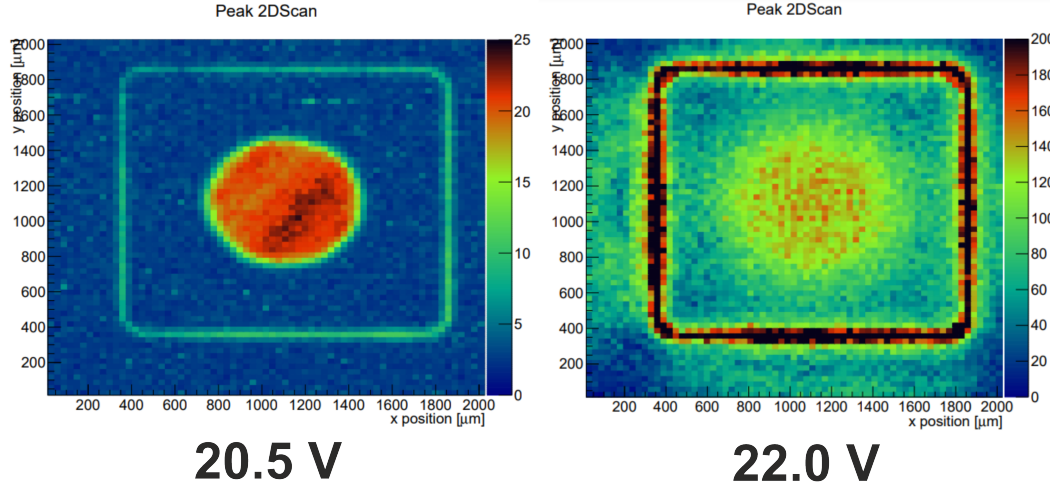


FIGURE 7.30: 2D map of the average TCT signal amplitude for the TiLGAD at 20.5 and 22 V.

7.5 4TiLG2-v1: TiLGAD on Si-Si wafers

In the case of Si-Si wafers, single-pad TiLGAD sensors were IV tested before the fabrication was completed, specifically between the metallization and passivation steps. These IV measurements were performed in the IMB-CNM clean-room at 20°C, using a probe station and a Keithley 6482 picoammeter with a maximum operating voltage of 200 V. **The setup had long been available at the IMB-CNM and was introduced as a best practice for this LGAD run and any future ones.**

This is particularly important for engineering fabrication runs, as in this case. As previously discussed, there was uncertainty regarding the temperature ramps to reach 1200°C during the Si-Si bonding process, so the total thermal load applied to the multiplication layer was not fully known. Moreover, this bonding process also removed, in most of the purchased wafers, the identification mark indicating the boron dose at which the multiplication layer was implanted. Only five wafers could be identified for their boron doses. Three were used for this 4TiLG2-v1 batch, while the other two were kept for the 4TiLG2-v2 run, which will be discussed later in this chapter.

By measuring the leakage current just after metallization, insight into how the thermal conditioning of the multiplication layer (180 minutes at 1175°C) affected the inner gain of the devices could be inferred. Additionally, if Geiger behavior had been observed, the aluminum layers could have been easily removed via wet etching, allowing for an additional thermal load to be applied to the wafers. Conversely, removing both the passivation and aluminum layers to do so is significantly more

complicated from a technological standpoint. Moreover, once the wafers are tested outside the clean-room, they are considered to be no longer in a clean state, meaning they have been exposed to environments or processes that do not meet the stringent cleanliness standards of the clean-room. Thus, any reprocessing (e.g. applying an additional thermal load) would need to be carried out using equipment that also does not meet these cleanliness standards, in order to avoid contaminating the clean furnaces. These are called *MNC equipment*, which stands for "Metales Nobles o Contaminante" in Spanish and translates to "Noble Metals or Contaminant". In a nutshell, **using such equipment increases the risk of further contamination of the TiLGAD wafers.**

Two devices per Si-Si wafer (see Table 7.1) were tested at the clean-room probe station. The results are shown in Figure 7.31, highlighting that the thermal conditioning of the multiplication layer was enough to avoid early breakdown due to Geiger behavior. Specifically, W1 and W2 (implanted with boron at $3.7 \cdot 10^{14}$ and $3.9 \cdot 10^{14}$ at/cm^2) exhibited PiN behavior, while W3 (implanted at $4.1 \cdot 10^{14}$ at/cm^2) exhibited LGAD behavior with a $V_{gl} \approx 25$ V. For all wafers, no breakdown voltage was observed below 200 V of reverse bias. However, the devices turned out to be non-functional once the passivation layers had been deposited and the fabrication was completed. This is also shown in Figure 7.31.

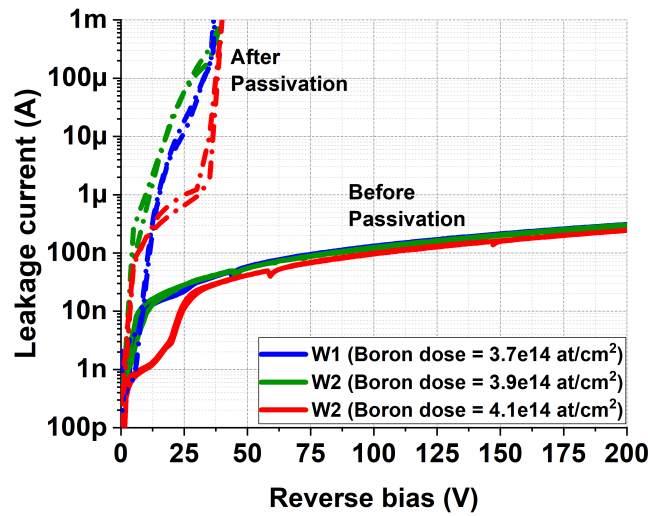


FIGURE 7.31: Leakage current, before (solid lines) and after (dashed lines) the passivation process, of 4TiLG2-v1 devices at 20°C.

The origin of this setback was afterwards identified with the SiO_2 passivation layer, as similarly discussed in Chapter 5 (see section 5.7). To recall, the SiO_2 deposited onto the devices surface contained a relatively large number of defects, which can cause local variations in the electric field at the interface with silicon, in turn boosting the surface current. The wafers were reprocessed to remove the passivation layers. However, the original IV behavior before passivation could not be recovered. As aforementioned, wafer reprocessing in MNC equipment is never desirable, as further contamination issues can degrade the devices performance. TiLGAD sensors on epitaxial wafers were fabricated with hafnium oxide as the dielectric material for the passivation layer. Thus, the aforementioned leakage current drawback could be sorted for them.

Nevertheless, it is worth pointing out that **the IV measurements conducted on single-pad TiLGAD detectors before passivation did demonstrate the proof of concept**, as devices showed to be functional either when exhibiting PiN or LGAD behavior. Furthermore, the devices behavior, PiN for W1 and W3 and LGAD with $V_{gl} \approx 25$ V, could still be inferred from the IV curves after passivation.

7.6 4TILG2-v2 and 4TILG3-v2 runs

The results presented in the previous sections have served to design a new TiLGAD run on both Si-Si (4TILG2-v2 run) and epitaxial wafers (4TILG3-v2 run). This batch was fabricated as part of the Advancement and Innovation for Detectors at Accelerators (AIDAInnova) WP6 project [131] which, among other goals, aims to develop TimePix4 sensors for tracking and timing applications with a pitch of 55 μm with an IP of 10 μm [131].

These fabrication runs served as a second engineering run aimed to understand and stabilize the 4TILG2 and 4TILG3 technologies at the IMB-CNM. Their main features are described in Table 7.2

4TILG2-v2 (Si-Si wafers)			
	W1	W2	
Handle wafer thickness (μm)	300		
Handle wafer dopant concentration (at/cm^3) and type	$\approx 10^{19}$ (Phosphorus)		
Active thickness (μm)	50		
Bulk doping concentration (at/cm^3)	$< 10^{13}$		
Boron implantation dose in multiplication layer ($10^{14} \text{ at}/\text{cm}^2$)	3.7	3.9	
Boron implantation energy in multiplication layer (keV)	150		
Pre-conditioning annealing	30 minutes at 1000°C		
4TILG3-v2 (epitaxial wafers)			
	W3	W4	W5
Handle wafer thickness (μm)	≈ 450		
Handle wafer dopant concentration (at/cm^3) and type	$\approx 4 \cdot 10^{19}$ (Arsenic)		
Active thickness (μm)	45-55		
Bulk doping concentration (at/cm^3)	$< 10^{13}$		
Boron doping concentration in multiplication layer ($10^{16} \text{ at}/\text{cm}^3$)	3.0-4.5		
Multiplication layer thickness (μm)	2.7-3.3		
Pre-conditioning annealing	180 minutes at 1250°C		

TABLE 7.2: Fabrication features of the 4TILG2-v2 and 4TILG3-v2 runs.

For the 4TILG2-v2 and 4TILG3-v2 run, a new mask was used (CNM1202) which is comprised mainly by TimePix4 and TimePix3 detectors. Additionally, single-pad and pixelated structures are included in the mask, which serve for IV, CV and TCT testing. A fabricated TiLG-v2 wafer is shown in Figure 7.32, where the single-pad detectors can be seen within blue squares.

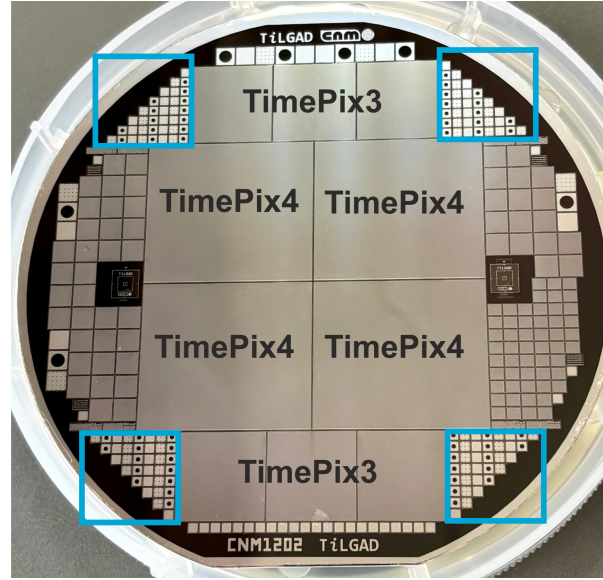


FIGURE 7.32: TILG-v2 wafer, fabricated with the mask CNM1202.

As listed in Table 7.2, the pre-conditioning annealing of the multiplication layer is different for every wafer type. The annealing features in each case were design based on the first TiLGAD run.

As mentioned earlier, only two Si-Si wafers with identified boron doses (3.7 and $3.9 \cdot 10^{14} \text{ at/cm}^2$) were available for this run. The preliminary IV curves of 4TiLG2-v1 devices, whose multiplication layers were implanted with such doses (W1 and W2 in Figure 7.31, respectively) suggested PiN behavior. Specifically, no V_{gl} could be inferred from their IV curves, in contrast to 4TiLG2-v1 devices implanted at $4.1 \cdot 10^{14} \text{ at/cm}^2$, which showed a $V_{gl} \approx 25 \text{ V}$.

This suggests that a thermal conditioning process of 180 minutes at 1175°C may have been excessive for Si-Si wafers (implanted at 3.7 and $3.9 \cdot 10^{14} \text{ at/cm}^2$) in the aim to balance between PiN and Geiger behavior. Consequently, 4TiLG2-v2 wafers were pre-annealed at a lower temperature and for a shorter time: **30 minutes at 1000°C** . As aforementioned, estimating the performance of TiLGAD devices under this annealing process is uncertain due to the lack of information regarding the thermal processes involved in Si-Si bonding. However, the introduction of IV testing in the clean-room between the metallization and passivation steps stands out as a valuable asset for quality control over the annealing process. Specifically, **if a pre-annealing of 30 minutes at 1000°C is not enough to achieve the desired LGAD behavior in the devices, the metal layer can be easily removed via wet etching, allowing for additional thermal process in clean furnaces.**

In the case of 4TiLG3-v1 detectors, the outcome was the opposite of 4TiLG2-v1 ones, as APDs were obtained instead of LGADs. Thus, the pre-annealing process of 180 minutes at 1175°C was insufficient to properly adjust the multiplication layer for LGAD behavior. For 4TiLG3-v1 samples, qualitative information about the raw wafers was inferred using the SRP technique (see section 7.4.2). **For each junction field correction model, TCAD simulations were performed to explore potential annealing processes that could resolve this issue.** The results indicate that a **pre-annealing time of 180 minutes at 1225°C** could produce LGAD devices. This is shown in Figure 7.33, where the simulated IV and CV curves point out to LGAD behavior for two out of the four junction field correction models (Model 3 and Model

4 in the figure). Once again, IV measurements in the clean-room enable thermal reprocessing if the pre-annealing is insufficient to achieve LGAD behavior in the devices.

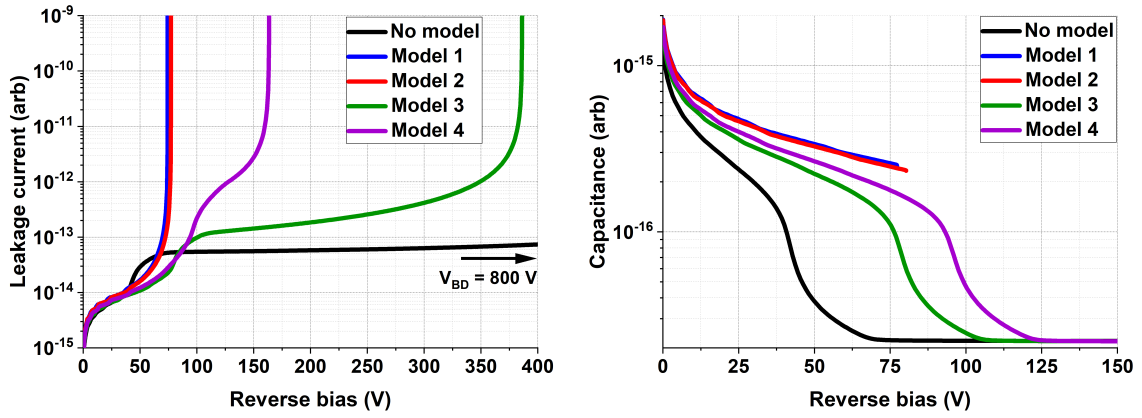


FIGURE 7.33: TCAD Sentaurus prediction of the IV and CV curves of 4TILG3 devices when annealed for 180 minutes at 1250°C, based on the raw wafer SRP profiles for every junction field correction model.

7.6.1 Preliminary IV measurements

Although the completion of the TILG2-v2 and TILG3-v2 fabrications occurred almost at the same time as the completion of this thesis, it is important to highlight the preliminary results of the IV measurements of single-pad devices, that are shown in Figure 7.34. The IV curves correspond to single-pad detectors from the fabrications TILG2-v1, TILG2-v2, TILG3-v1 and TILG3-v2, which main characteristics can be found in Tables 7.1 and 7.2.

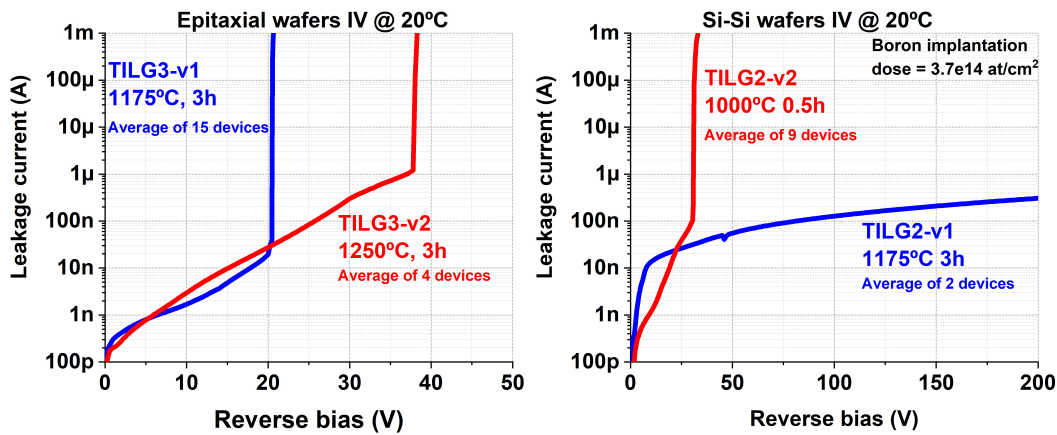


FIGURE 7.34: IV measurements, at 20°C, for TiLGAD on Epitaxial and Si-Si wafers (implanted with a boron dose of $3.7 \cdot 10^{14} \text{ at/cm}^2$).

The results suggest that for TiLGAD, both in epitaxial and Si-Si wafers, the devices show APD behavior. However, a more comprehensive set of measurements, including CV ones, should be conducted to continue understanding and optimizing

this structure. Moreover, the fact that the breakdown voltage is so similar for both types of wafers suggests the possibility that this breakdown is caused by a peripheral issue rather than a problem at the core of the device. This was investigated in a very preliminary way via TCAD Sentaurus, and its main results are described below.

7.6.2 Preliminary TCAD Simulation of the TiLGAD periphery

The structure shown in Figure 7.35 (left) was simulated to investigate potential electric field effects at the periphery termination of the TiLGAD devices. The termination structure for the IMB-CNM 4TiLG fabrications is shown in Figure 7.18. The TCAD Sentaurus version used was v2023.12, instead of v2018.06 used throughout this thesis, as the simulator had been updated at IMB-CNM by the time this simulation was performed. For the sake of simplicity, the core of the device was assumed to be a PiN detector (i.e., without a multiplication layer), so that only breakdown effects due to the periphery termination design could be observed. Figure 7.35 (right) shows the simulated IV curve at 20°C for the aforementioned structure, evidencing that, under ideal conditions, the device would break down at $\simeq 350$ V.

The electric field at this breakdown voltage point was also simulated around the structure. The results are shown in Figure 7.36, indicating that **the device breaks down at the silicon-trench interface by the P^{++} layer**. That is, the breakdown does not occur at the PN junction core, as intended by design, but rather at the periphery termination. Moreover, it is important to note that the trench structure was simulated under ideal conditions: no defects at the silicon-trench interface, no trapped charges within the oxide, and a fully capped structure. Therefore, the breakdown voltage of 350 V at 20°C represents an upper limit, which is expected to decrease when more realistic trenches, such as the one depicted in Figure 7.27, are considered.

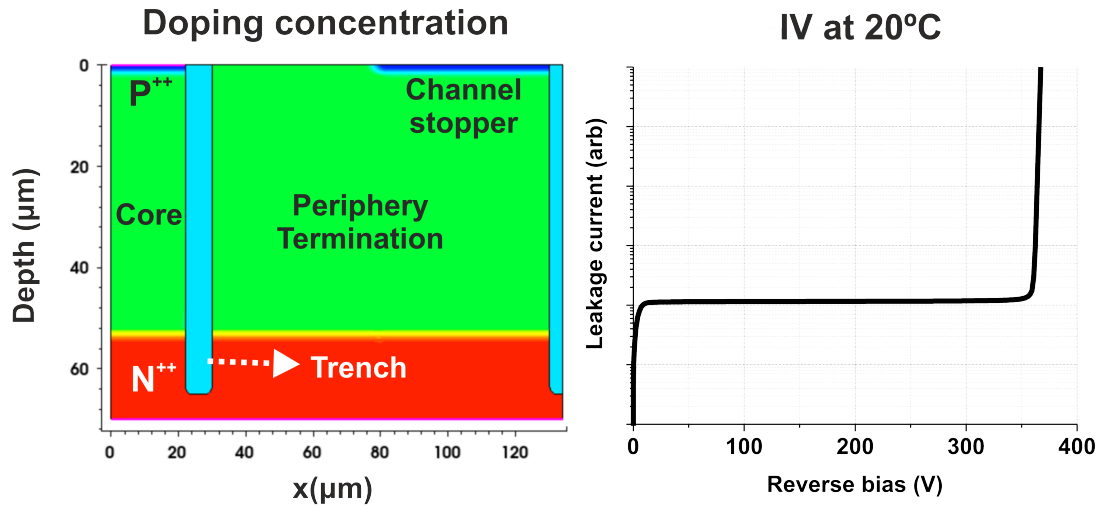


FIGURE 7.35: TCAD Sentaurus simulation of the TiLGAD periphery termination (left) and its IV curve, at 20°C, for a core composed of a PiN detector (right).

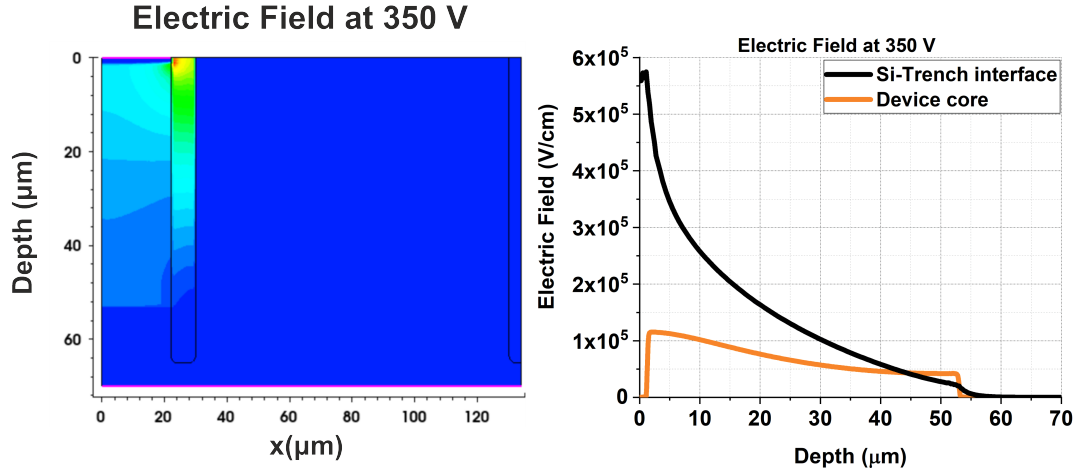


FIGURE 7.36: TCAD Sentaurus simulation of the electric field, at 350 V and 20°C, of a TiLGAD termination with a core composed of a PiN detector (left) and cutlines of such electric field at the Si-Trench interface and core (right).

The same simulations as those in Figures 7.35 and 7.36 were performed on a structure without the termination, where the device edge is defined by the inner trench in contact with the PN junction. The results, shown in Figures 7.37 and 7.38, suggest that the termination design may contribute to the early breakdown voltage observed in TiLGADs, regardless of their inner gain.

On one hand, removing the termination in the simulation structure increases the predicted breakdown voltage at 20°C from 350 V to $\simeq 910$ V. On the other hand, the peak electric field is observed not only at the silicon-trench interface near the P^{++} layer but also at the PN junction core (Figure 7.38), just as intended by design. Nevertheless, it is important to recall that these simulations were conducted under ideal conditions and with a PiN detector at the device core. Future simulations with more realistic structures are necessary to confirm or rule out potential effects of the periphery termination on the breakdown voltage.

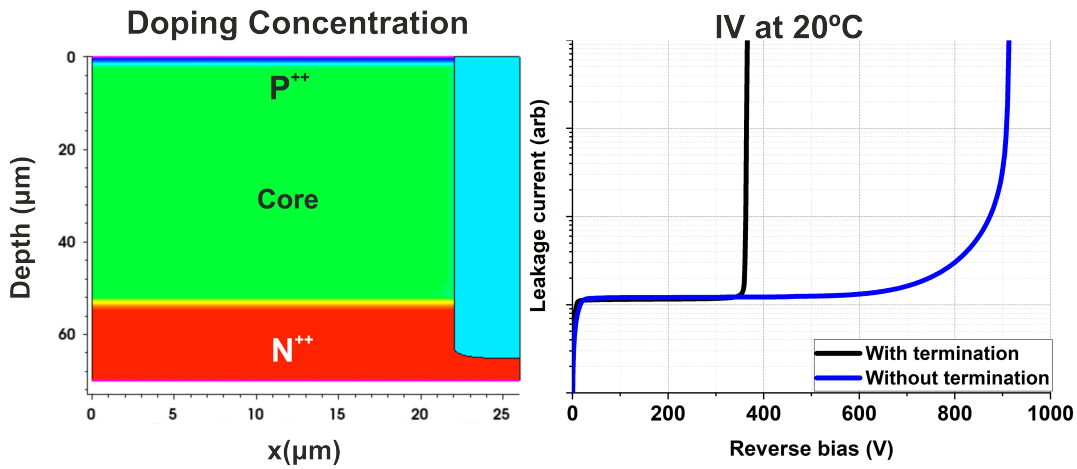


FIGURE 7.37: TCAD Sentaurus simulation of the TiLGAD periphery with the termination removed (left) and its IV curve, at 20°C, for a core composed of a PiN detector (right).

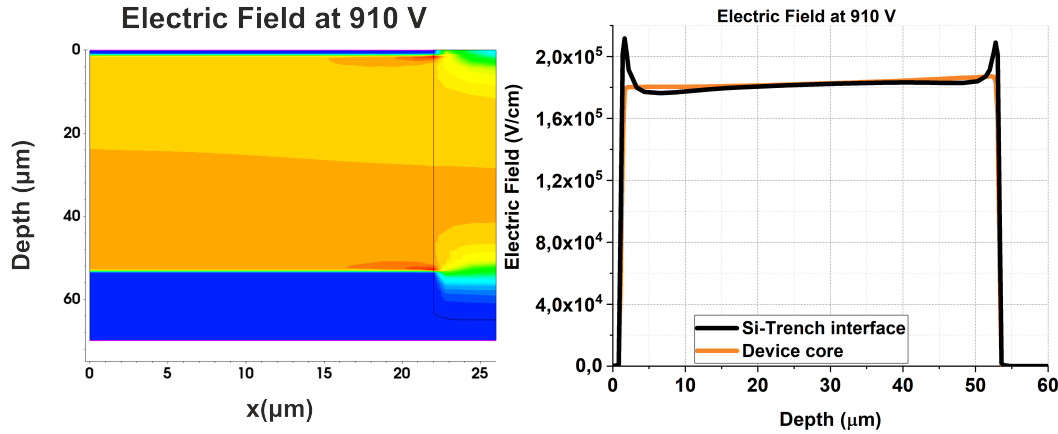


FIGURE 7.38: TCAD Sentaurus simulation of the electric field, at 350 V and 20°C, of a TiLGAD, with a core composed of a PiN detector, with its termination removed (left) and cutlines of such electric field at the Si-Trench interface and core (right).

7.7 Conclusions and future work

Despite the issues encountered during TiLGAD fabrication at the IMB-CNM, **the main outcome is that the proof of concept was successfully demonstrated**. However, several manufacturing challenges that require proper attention arose during this work.

For TiLGAD sensors fabricated on epitaxial wafers (4TiLG3-v1 run), it was demonstrated that **the technology heavily depends on the quality of a non-standardized epitaxial growth technique**. This poses a challenge for fabrication, as **the raw wafer must be thoroughly characterized before starting the manufacturing process**, as confirmed by SRP measurements. 4TiLG3-v1 detectors exhibited a clear APD behavior, with the gain response to IR light transitioning from linear to Geiger values in under one volt.

For TiLGAD devices fabricated on Si-Si wafers (4TiLG2-v1 run), implantation techniques offer a more controlled process. However, the Si-Si bonding process, performed outside of the IMB-CNM clean-room, results in limited knowledge of the full thermal load applied to the multiplication layer. This likely led to the production of PiN detectors instead of LGADs in this batch. Nevertheless, **the introduction of IV testing in the clean-room between the metallization and passivation steps proved to be a valuable tool for quality control over the annealing process in engineering runs**. Additionally, the importance of controlling the quality of the deposited oxide was highlighted, as the leakage current of the devices significantly increased after the deposition of a poor-quality passivation layer.

The 4TiLG2-v2 and TiLG3-v2 manufacturing batches were targeted to overcome the aforementioned drawbacks. While the preliminary IV measurements suggest APD behavior in both cases, a more comprehensive study needs to be carried out to confirm such hypothesis. Moreover, **TCAD Sentaurus simulations suggest that the periphery termination may contribute to the observed early breakdown**, indicating that a redesign of the termination could be necessary.

Additionally, their goal goes beyond merely reconfirming the proof of concept, as it also seeks for **studying and stabilizing the technology for TiLGAD fabrication at the IMB-CNM**, as well as investigating the hypothesis, TCAD Sentaurus

simulation based, that **TiLGAD detectors might be suitable for both high- and low-penetrating particles in silicon.**

Conclusions and future lines of work

This thesis has covered the development of Low Gain Avalanche Detectors (LGAD) at the IMB-CNM. Specifically, the work has been focused on the design, simulation, optimization and fabrication of LGAD sensors across various technological configurations. The primary conclusions are hereunder detailed, along with potential lines of future work.

LGAD devices for HEP experiments

- IMB-CNM fabricated LGAD sensors have shown improved radiation tolerance across different manufacturing runs. Nevertheless, additional improvements are required to withstand the extreme radiation conditions forecast for the ATLAS HGTD and CMS ETL Phase-II experiment upgrades.
- The study of this radiation tolerance dependence on carbonation has been thoroughly investigated. The results from the ATLAS 6LG2-v1 LGAD batch suggested that an optimal balance between gain and radiation hardness is achieved for LGAD sensors fabricated using a carbon implantation dose of $\approx 3 \cdot 10^{14} \text{ at/cm}^2$. Subsequent studies from the CMS 6LG2-v2 run suggested that this optimal point is more influenced by carbonation effects during LGAD fabrication than by the very inner gain. Specifically, a critical point for carbon-enhanced diffusion suppression was observed at a carbon dose around $4 \cdot 10^{14} \text{ at/cm}^2$. However, further investigation is needed to determine whether this dose represents the optimal point for radiation tolerance.
- Despite the need for improved radiation tolerance, it is important to remark that detectors from the ATLAS 6LG2-v1 run, carbonated at $9 \cdot 10^{14} \text{ at/cm}^2$, were shown to meet the CMS ETL specifications both before and after irradiation. However, after irradiation, these specifications were only met at the upper voltage limit defined by the same standards.
- Apart from carbonation, transitioning from LGAD to dLGAD devices represents a promising direction for future research, as several studies have reported that dLGAD detectors offer improved radiation resistance compared to traditional LGAD devices. An upcoming dLGAD manufacturing batch is currently being developed at the IMB-CNM, which aims to serve as the baseline for investigating the 6DLG technology.

nLGAD devices for low-penetrating particles in silicon

- The characterization of 4NLG1-v1 and 4NLG1-v2 detectors showed that their gain response is improved for low-penetrating photons detection. Additionally, the importance of considering the photon beam flux when assessing the performance of these devices was highlighted, as higher flux levels result in lower gain values. The nature of this gain suppression effect lies on the increased ionization charge density near the PN junction, that locally drops the high electric field responsible of triggering the avalanche multiplication mechanism.
- IBIC measurements with 600 keV protons on 4NLG1-v2 sensors indicated that moderate gain levels in the range of 5-20 are achieved for low-energy charged particles only when electrons predominantly trigger the avalanche mechanism. Such inner gain levels were observed when the protons Bragg peak was positioned within the dead entrance window. Considering this, we cannot rule out that the gain enhancement may also be attributed to a low ionization charge density around the high-electric field region, which could mitigate gain suppression effects.
- The aforementioned results also indicate that the dead entrance window plays a crucial role on nLGAD gain response to low-penetrating particle detection. Thus, the design of the P^{++} and passivation layers represents a potential future line of work, as their optimization during manufacturing would assure that the fabricated nLGAD will enhance its sensitivity to the target low-penetrating particle.
- The 4NLG1-v1 and 4NLG1-v2 runs were not tailored to meet the requirements of any specific application, but rather to serve as a proof of concept. Following their success, opportunities now arise to further investigate the nLGAD performance, including their timing and spatial resolution when pixelated, as well as their radiation hardness. Additionally, different nLGAD technological configurations may be considered, as fabricating them with the DLG technology.

TiLGAD devices for fill factor optimization

- The first TiLGAD batches for fill factor optimization to 100% were fabricated at the IMB-CNM on Si-Si (4TiLG2-v1 run) and epitaxial (4TiLG3-v1 run) wafers. Despite the setbacks encountered during the fabrication, the TiLGAD proof of concept was successfully demonstrated. 4TiLG2-v1 detectors shown, in their preliminary IV testing, both LGAD and PiN behavior. Conversely, 4TiLG3-v1 sensors clearly showed APD behavior during their characterization. Nevertheless, both technologies proved to work to manufacture silicon detectors.
- The study of TiLGAD sensors on epitaxial wafers highlighted that the 4TiLG3 technology is heavily dependent on the quality of a non-standardized epitaxial growth technique, conducted outside the IMB-CNM clean-room, for the multiplication layer. This represents a fabrication challenge, as the raw wafer must undergo characterization before the manufacturing process can begin.
- The TiLG2 technology does not face the aforementioned challenge, as the multiplication layer is created through ion implantation, a well-understood and

controlled process at the IMB-CNM. However, the Si-Si wafer bonding, conducted outside the IMB-CNM facilities, leads to limited insight into the full thermal load applied to the multiplication layer during the process.

- Overcoming these challenges in TiLG2 and TiLG3 technologies represents the future direction of TiLGAD fabrication at the IMB-CNM. A key focus is determining the optimal thermal load for the multiplication layers to ensure the fabricated devices exhibit LGAD behavior, rather than PiN or APD. The introduction of IV testing in the clean-room between the metallization and passivation steps has proven to be a valuable quality control measure, as it allows for additional thermal adjustments before completing the manufacturing process.
- The 4TiLG2-v2 and TiLG3-v2 manufacturing batches aimed to address the aforementioned challenges. The 4TiLG2-v2 and TiLG3-v2 manufacturing batches were targeted to overcome the aforementioned drawbacks. While the preliminary IV measurements suggest APD behavior in both cases, a more comprehensive study needs to be carried out to confirm such hypothesis. Moreover, TCAD Sentaurus simulations suggest that the periphery termination may contribute to the observed early breakdown, indicating that a redesign of the termination could be necessary. Furthermore, their objectives extend beyond simply reconfirming the proof of concept. They also focus on studying and stabilizing the TiLGAD fabrication technology at the IMB-CNM, as well as exploring the hypothesis, suggested by TCAD Sentaurus simulations, that TiLGAD devices are suitable for detecting both high- and low-penetrating particles in silicon.

Stabilization of LGAD technology at the IMB-CNM

- Regardless of the LGAD technological configuration (traditional, dLGAD, nLGAD or TiLGAD), the work presented in this thesis also highlighted the importance of stabilizing the fabrication at the IMB-CNM. LGAD devices from the ATLAS-CMS engineering 6LG3-v2, ATLAS 6LG2-v1 and CSM 6LG2-v2 runs exhibited significantly different electrical performance, despite being fabricated, in principle, under similar conditions. Therefore, a thorough control and understanding of all fabrication parameters during manufacturing, such as the screen oxide thickness before implantation steps, represent a promising area for investigation to stabilize the technology.
- For this purpose, TCAD Sentaurus simulations are a powerful tool for designing and testing the LGAD behavior before and after fabrication. However, TCAD Sentaurus by default is unable to predict IMB-CNM LGAD performance accurately. The calibration of TCAD Sentaurus models to predict carbonated LGAD performance was investigated in this thesis. In particular, the diffusivity of boron and phosphorus through interstitials was tuned during the simulation calibration, as studies have reported that these diffusion paths are altered in silicon in the presence of carbon. These adjusted diffusivity parameters accurately predicted (before irradiation) all V_{gl} , V_{BD} at 20°C and CV-extracted boron profiles of CMS 6LG2-v2 detectors carbonated at a dose of $4 \cdot 10^{14} \text{ at/cm}^2$. However, the same parameters did not accurately predict the performance of 6LG2-v2 devices with different carbon doses. This result suggested that the diffusivity of boron and phosphorus does not only depend on

the presence of carbon itself, but on its actual concentration around the PN junction. This opens the door to further investigation, by means of TCAD Sentaurus, the effects of carbonation on dopant diffusion in LGAD detectors.

- Additionally, the Spreading Resistance Profiling (SRP) technique was also introduced to analyse LGAD doping profiles (for all LGAD, nLGAD and TiLGAD devices). However, correction models are always needed around a device PN junction to avoid underestimating the inferred doping concentration using the SRP technique. These correction models need further refinement to better align with the various LGAD manufacturing scenarios and to serve as a reliable validation tool.
- TCAD Sentaurus and the SRP technique are crucial for stabilizing LGAD technology at the IMB-CNM, but the tuning of their models relies on precise fabrication parameters. LGAD devices from the CMS 6LG2-v2 batch are the first for which all fabrication parameters were documented, making them the baseline for optimizing TCAD and SRP models and hence stabilizing the technology. To date, no manufacturing run for dLGAD, nLGAD, or TiLGAD devices has been completed where all fabrication parameters are fully known. To stabilize the technologies for these LGAD variations, comprehensive control of future fabrication runs at the IMB-CNM is essential.

Scientific Contributions

Scientific publications

Publications as co-author

- W. Khaleed, M. Valentan, A. Doblas, D. Flores, S. Hidalgo, G. Konrad, J. Marton, N. Moffat, D. Moser, S. Onder, G. Pellegrini and **J. Villegas**. "First results for the pLGAD sensor for low-penetrating particles". *Nuclear Instruments and Methods in Physics Research Section A: Accelerators, Spectrometers, Detectors and Associated Equipment*, Volume 1040, 167220, 2022. <https://doi.org/10.1016/j.nima.2022.167220>
- C. Grieco, L. Castillo, A. Doblas, E.L. Gkougkousis, S. Grinstein, S. Hidalgo, N. Moffat, G. Pellegrini, **J. Villegas**. "Overview of CNM LGAD results: boron Si-on-Si and epitaxial wafers". *JINST*, 17, C09021, 2022. <https://doi.org/10.1088/1748-0221/17/09/C09021>
- A. Doblas, D. Flores, S. Hidalgo, N. Moffat, G. Pellegrini, D. Quirion, **J. Villegas**, D. Maneuski, M. Ruat, P. Fajardo. "Inverse LGAD (iLGAD) Periphery Optimization for Surface Damage Irradiation". *Sensors*, 23(7), 3450. ISSN: 1424-8220, 2023. <https://doi.org/10.3390/s23073450>

Publications as corresponding author

- J. Villegas et al. "Gain measurements on NLGAD detectors". *Nuclear Instruments and Methods in Physics Research Section A: Accelerators, Spectrometers, Detectors and Associated Equipment*, Volume 1055, 168377, 2023. <https://doi.org/10.1016/j.nima.2023.168377>
- J. Villegas et al. "The effects in fabrication and performance of carbon doping on IMB-CNM manufactured LGADs". *Nuclear Instruments and Methods in Physics Research Section A: Accelerators, Spectrometers, Detectors and Associated Equipment*, Volume 1064, 169424, 2024. <https://doi.org/10.1016/j.nima.2024.169424>
- J. Villegas et al. "nLGAD gain response to low-penetrating particles". *Nuclear Instruments and Methods in Physics Research Section A: Accelerators, Spectrometers, Detectors and Associated Equipment*, 170208, 2025. <https://doi.org/10.1016/j.nima.2025.170208>

Scientific conferences and workshops

Talks in conferences as first author

- J. Villegas et al. "LOW GAIN AVALANCHE DETECTOR (LGAD) FOR ATLAS AND CMS EXPERIMENTS". *6th Summer School on Intelligent signal processing*

for frontier research and industry (Madrid, Spain), 2021. <https://indico.cern.ch/event/850479/contributions/4505191/>

- J. Villegas et al. "Timing measurements on neutron-irradiated LGADs in epitaxial wafers". *The 38th RD50 Workshop (online)*, 2021. <https://indico.cern.ch/event/1029124/contributions/4411245/>
- J. Villegas et al. "Timing measurements on neutron-irradiated LGADs in epitaxial wafers". *The 39th RD50 Workshop (Valencia, Spain)*, 2021. <https://indico.cern.ch/event/1074989/contributions/4614672/>
- J. Villegas et al. "Measurements on last IMB-CNM LGADs production". *The 40th RD50 Workshop (CERN, Geneva, Switzerland)*, 2022. <https://indico.cern.ch/event/1157463/contributions/4922755/>
- J. Villegas et al. "Measurements on NLGAD detectors". *The 41st RD50 Workshop (Seville, Spain)*, 2022. <https://indico.cern.ch/event/1132520/contributions/5140054/>
- J. Villegas et al. "Measurements on last IMB-CNM LGADs production". *The 43rd RD50 Workshop (CERN, Geneva, Switzerland)*, 2023. <https://indico.cern.ch/event/1334364/contributions/5672080/>
- J. Villegas et al. "nLGAD Detectors for Low Penetrating Particles: Concept and First Results". *14th Spanish Conference on Electron Devices (Valencia, Spain)*, 2023. <https://doi.org/10.1109/CDE58627.2023.10339519>
- J. Villegas. "Calibration of TCAD Sentaurus simulation models with LGAD measurements". *The 5th School of Silicon Detectors Simulation (Paris, France)*, 2023. <https://indico.in2p3.fr/event/30704/sessions/19552/#20231124>
- J. Villegas et al. "Gain measurements of the latest IMB-CNM fabricated nLGAD detectors". *The 19th TREDI Workshop on Advanced Silicon Radiation Detectors (Torino, Italy)*, 2024. <https://agenda.infn.it/event/39042/contributions/222898/>

Talks in conferences as co-author

- N. Moffat, G. Rius, **J. Villegas** and G. Pellegrini. "Graphene-Enabled Silicon-Integrated Photodiode for DUV Imaging". *The 22nd International Conference on Nanotechnology (Mallorca, Spain)*, 2022. <https://doi.org/10.1109/NANO54668.2022.9928637>

International Collaborations

- Collaboration with the *School of Physics and Astronomy, University of Glasgow, Scotland, UK* to characterize iLGAD medipix devices for tracking and timing applications. May 2022 - August 2022.

Appendix A: Acronyms for IMB-CNM Runs

Acronyms for IMB-CNM Runs			
Acronym	Project(s)	Year	Description
4NLG1-v1	AIDAINNOVA	2022	First version of nLGAD on FZ(1) wafers of 4 inches (100 mm) diameter and 300 μm thickness.
4NLG1-v2	AIDAINNOVA	2024	Second version of nLGAD on FZ(1) wafers of 4 inches (100 mm) diameter and 300 μm thickness.
4TiLG2-v1	AIDAINNOVA	2023	First version Trench inverse LGAD on Si-Si(2) wafers of 4 inches (100 mm) diameter and 50 μm active thickness.
4TiLG2-v2	AIDAINNOVA	2024	Second version of Trench inverse LGAD on Si-Si(2) wafers of 4 inches (100 mm) diameter and 50 μm active thickness.
4TiLG3-v1	AIDAINNOVA	2023	First version of Trench inverse LGAD on Epitaxial(3) wafers of 4 inches (100 mm) diameter.
4TiLG3-v2	AIDAINNOVA	2024	Second version of Trench inverse LGAD on Epitaxial(3) wafers of 4 inches (100 mm) diameter.
6DLG2-v1	CMS experiment phase-II upgrade	2023	First version of Deep profile carbonated LGAD on Si-Si(2) wafers of 6 inches (150 mm) diameter and 50 μm active thickness.
6DLG2-v2	CMS experiment phase-II upgrade	2024	Second version of Deep profile carbonated LGAD on Si-Si(2) wafers of 6 inches (150 mm) diameter and 50 μm active thickness.
6DLG3-v1	CMS experiment phase-II upgrade	Exp. 2025	First version of Deep profile carbonated LGAD on Epitaxial(3) wafers of 6 inches (150 mm) diameter and 50 μm active thickness.
6LG2-v1	ATLAS experiment phase-II upgrade	2023	First version of carbonated LGAD on Si-Si(2) wafers of 6 inches (150 mm) diameter and 50 μm active thickness.
6LG2-v2	CMS experiment phase-II upgrade	2023	Second version of carbonated LGAD on Si-Si(2) wafers of 6 inches (150 mm) diameter and 50 μm active thickness.
6LG3-v1	ATLAS and CMS experiments phase-II upgrade	2021	First version of carbonated LGAD on Epitaxial(3) wafers of 6 inches (150 mm) diameter and 50 μm active thickness.
6LG3-v2	ATLAS and CMS experiments phase-II upgrade	2022	Second version of carbonated LGAD on Epitaxial(3) wafers of 6 inches (150 mm) diameter and 50 μm active thickness.

Bibliography

- [1] CERN official website, <https://home.cern/>.
- [2] RD50 (Radiation hard semiconductor devices for very high luminosity colliders) official website, <https://rd50.web.cern.ch/>.
- [3] T. Affolder, "ATLAS Phase II Upgrade," *30th International Symposium on Lepton Photon Interactions at High Energies*, 2022. [Online]. Available: <https://cds.cern.ch/record/2799535/>.
- [4] G. Pásztor, "The Phase-2 Upgrade of the CMS Detector," *The 10th Annual Conference on Large Hadron Collider Physics (LHCP2022)*, 2022. DOI: [10.22323/1.422.0045](https://doi.org/10.22323/1.422.0045).
- [5] G. Pellegrini *et al.*, "Technology developments and first measurements of Low Gain Avalanche Detectors (LGAD) for high energy physics applications," *Nuclear Instruments and Methods in Physics Research Section A: Accelerators, Spectrometers, Detectors and Associated Equipment*, vol. 765, pp. 12–16, 2014. DOI: [/10.1016/j.nima.2014.06.008](https://doi.org/10.1016/j.nima.2014.06.008).
- [6] J. Villegas *et al.*, "Gain measurements on NLGAD detectors," *Nuclear Instruments and Methods in Physics Research Section A: Accelerators, Spectrometers, Detectors and Associated Equipment*, vol. 1055, no. 168377, 2023. DOI: [/10.1016/j.nima.2023.168377](https://doi.org/10.1016/j.nima.2023.168377).
- [7] D. McGregor and J. K. Shultis, *Radiation Detection: Concepts, Methods, and Devices*. CRC Press. Florida, 2020.
- [8] G. F. Knoll, *Radiation Detection and Measurement*. John Wiley and Sons. New York, 2000.
- [9] G. Lutz, *Semiconductor radiation detectors*. Springer. Berlin, 1999.
- [10] R. F. Pierret, *Semiconductor fundamentals*. Addison-Wesley. Massachusetts, 1988.
- [11] U. K. Mishra and J. Singh, *Semiconductor device physics and design*. Springer. Dordrecht, 2008.
- [12] E. Cavallaro, "Novel silicon detector technologies for the HLC-LHC ATLAS upgrade," *Doctoral Thesis. Universitat Autònoma de Barcelona*, 2019. [Online]. Available: <https://ddd.uab.cat/record/207901?ln=en>.
- [13] P. Fernandez, "Diseño, fabricación y optimización de detectores con multiplicación (LGAD) para experimentos de Física de altas energías," *Doctoral Thesis. Universitat Autònoma de Barcelona*, 2014. [Online]. Available: <https://ddd.uab.cat/record/127485?ln=es>.
- [14] M. S. Sze and M. K. Lee, *Semiconductor devices: physics and technology*. John Wiley and Sons. New York, 2010.
- [15] S. Otero, "Characterisation and optimization of radiation-tolerant silicon sensor with intrinsic gain," *Doctoral Thesis. Universidade de Santiago de Compostela*, 2018. [Online]. Available: <https://cds.cern.ch/record/2649130?ln=en>.

- [16] E. Schibli and A. G. Milnes, "Deep impurities in silicon," *Materials Science and Engineering*, vol. 2, no. 4, pp. 173–180, 1967. DOI: [/10.1016/0025-5416\(67\)90056-0](https://doi.org/10.1016/0025-5416(67)90056-0).
- [17] M. A. Green, "Self-consistent optical parameters of intrinsic silicon at 300 K including temperature coefficients," *Solar Energy Materials and Solar Cells*, vol. 92, no. 4, pp. 1305–1310, 2008. DOI: [/10.1016/j.solmat.2008.06.009](https://doi.org/10.1016/j.solmat.2008.06.009).
- [18] N. Cartiglia *et al.*, "Topics in LGAD design," *The 10th "Trento" Workshop on Advanced Silicon Radiation Detectors*, 2015. [Online]. Available: <https://indico.cern.ch/event/351695/>.
- [19] X. Yang *et al.*, "Layout and performance of HPK prototype LGAD sensors for the High-Granularity Timing Detector," *Nuclear Instruments and Methods in Physics Research Section A: Accelerators, Spectrometers, Detectors and Associated Equipment*, vol. 980, no. 164379, 2020. DOI: [/10.1016/j.nima.2020.164379](https://doi.org/10.1016/j.nima.2020.164379).
- [20] M. Ferrero *et al.*, *An Introduction to Ultra-Fast Silicon Detectors*. CRC Press. New York, 2021.
- [21] G. Giacomini, "Noise characterization of silicon strip detectors," *Doctoral Thesis. Università degli studi di Trieste*, 2007. [Online]. Available: <https://cds.cern.ch/record/2093586/>.
- [22] J. Hubbell and S. Seltzer, "Tables of X-Ray Mass Attenuation Coefficients and Mass Energy-Absorption Coefficients from 1keV to 20MeV for Elements Z = 1 to 92 and 48 Additional Substances of Dosimetric Interest," *NISTIR*, no. 5632, 1995. DOI: [/10.18434/T4D01F](https://doi.org/10.18434/T4D01F).
- [23] Diamond Light Source. B16 Beamline. Official website, <https://www.diamond.ac.uk/Science/Research/Optics/B16.html>.
- [24] N. Cartiglia *et al.*, "Tracking in 4 dimensions," *Nuclear Instruments and Methods in Physics Research Section A: Accelerators, Spectrometers, Detectors and Associated Equipment*, vol. 845, pp. 47–51, 2017. DOI: [/10.1016/j.nima.2016.05.078](https://doi.org/10.1016/j.nima.2016.05.078).
- [25] A. Doblas, "Low Gain Avalanche Detectors (LGADs and iLGADs) for High-Energy Physics and Synchrotron Applications," *Doctoral Thesis. Universitat Autònoma de Barcelona*, 2022. [Online]. Available: https://ddd.uab.cat/pub/tesis/2024/hdl_10803_689771/adm1de1.pdf.
- [26] R. V. Overstraeten and H. de Man, "Measurement of the ionization rates in diffused p-n junctions," *Solid-State Electronics*, vol. 13, no. 5, pp. 538–608, 1970. DOI: [/10.1016/0038-1101\(70\)90139-5](https://doi.org/10.1016/0038-1101(70)90139-5).
- [27] LHC official website, <https://home.cern/science/accelerators/large-hadron-collider>.
- [28] J. Frost, "Dark Matter Searches at the LHC," *The ATLAS collaboration. Report number: ATL-PHYS-SLIDE-2022-630*, 2022. [Online]. Available: <https://cds.cern.ch/record/2843045/>.
- [29] G. Aad *et al.*, "Observation of a new particle in the search for the Standard Model Higgs boson with the ATLAS detector at the LHC," *Physics Letters B*, vol. 765, no. 1, pp. 1–29, 2012. DOI: [/10.1016/j.physletb.2012.08.020](https://doi.org/10.1016/j.physletb.2012.08.020).
- [30] A. Lopes, *Recreating Big Bang matter on Earth*, 2020. [Online]. Available: <https://home.cern/news/series/lhc-physics-ten/recreating-big-bang-matter-earth>.

- [31] B. F. Philips *et al.*, "Neutron detection using large area silicon detectors," *Nuclear Instruments and Methods in Physics Research Section A: Accelerators, Spectrometers, Detectors and Associated Equipment*, vol. 579, no. 1, pp. 173–176, 2007. DOI: [/10.1016/j.nima.2007.04.033](https://doi.org/10.1016/j.nima.2007.04.033).
- [32] A. Darafsheh, *Radiation therapy dosimetry: a practical handbook*. CRC Press. Florida, 2021.
- [33] G. May and S. Sze, *Fundamentals of Semiconductor Fabrication*. John Wiley and Sons. New York, 2010.
- [34] IMB-CNM official website, <https://www.imb-cnm.csic.es/>.
- [35] W. Jian *et al.*, "Study of electron mobility on silicon with different crystalline orientations," *IEEE 11th International Conference on Solid-State and Integrated Circuit Technology*, pp. 1–3, 2012. DOI: [/10.1109/ICSICT.2012.6467830](https://doi.org/10.1109/ICSICT.2012.6467830).
- [36] F. Hartmann, *Evolution of Silicon Sensor Technology in Particle Physics*. Springer. Gewerbestrasse, 2009.
- [37] G. S. May and C. J. Spanos, *Fundamentals of semiconductor manufacturing and process control*. John Wiley and Sons. New Jersey, 2006.
- [38] D. K. Sadana *et al.*, "The effect of recoiled oxygen on damage regrowth and electrical properties of through-oxide implanted Si," *Nuclear Instruments and Methods in Physics Research*, vol. 209-210, no. 2, pp. 743–750, 1983. DOI: [/10.1016/0167-5087\(83\)90877-3](https://doi.org/10.1016/0167-5087(83)90877-3).
- [39] E. W. Haas *et al.*, "Activation analytical investigation of contamination and cross-contamination," *Journal of Electronics Materials*, vol. 7, pp. 525–533, 1978. DOI: [/10.1007/BF02655416](https://doi.org/10.1007/BF02655416).
- [40] S. Sze and J. Irvin, "Resistivity, mobility and impurity levels in GaAs, Ge, and Si at 300°K," *Solid-State Electronics*, vol. 11, no. 6, pp. 599–602, 1968. DOI: [/10.1016/0038-1101\(68\)90012-9](https://doi.org/10.1016/0038-1101(68)90012-9).
- [41] K. Cho *et al.*, "Channeling effect for low energy ion implantation in Si," *Nuclear Instruments and Methods in Physics Research Section B: Beam Interactions with Materials and Atoms*, vol. 7-8, no. 1, pp. 265–272, 1985. DOI: [/10.1016/0168-583X\(85\)90564-6](https://doi.org/10.1016/0168-583X(85)90564-6).
- [42] T. Hirao *et al.*, "The concentration profiles of phosphorus, arsenic and recoiled oxygen atoms in Si by ion implantation into SiO₂-Si," *Japanese Journal of Applied Physics*, vol. 18, no. 3, p. 647, 1979. DOI: [10.1143/JJAP.18.647](https://doi.org/10.1143/JJAP.18.647).
- [43] S. Franssila, *Introduction to Microfabrication*. Wiley. West Sussex, 2010.
- [44] E. H. Snow *et al.*, "Effects of ionizing radiation on oxidized silicon surfaces and planar devices," *Proceedings of the IEEE*, vol. 55, no. 7, pp. 1168–1185, 1967. DOI: [10.1109/PROC.1967.5776](https://doi.org/10.1109/PROC.1967.5776).
- [45] I. W. Anokhin *et al.*, "Evolution of radiation induced defects and the type inversion in high resistivity silicon under neutron irradiation," *Radiation Protection Dosimetry*, vol. 101, no. 1-4, pp. 107–110, 2002. DOI: [/10.1093/oxfordjournals.rpd.a005947](https://doi.org/10.1093/oxfordjournals.rpd.a005947).
- [46] F. Lemeilleur *et al.*, "Electrical properties and charge collection efficiency for neutron-irradiated p-type and n-type silicon detectors," *Nuclear Physics B*, vol. 32, pp. 415–424, 1993. DOI: [/10.1016/0920-5632\(93\)90054-A](https://doi.org/10.1016/0920-5632(93)90054-A).
- [47] M. G. Buehler, "Design Curves for Predicting Fast-Neutron-Induced Resistivity Changes in Silicon," *Proceedings of the IEEE*, vol. 56, no. 10, pp. 1741–1743, 1968. DOI: [/10.1109/PROC.1968.6728](https://doi.org/10.1109/PROC.1968.6728).

- [48] P. Fernandez *et al.*, “Design and fabrication of an optimum peripheral region for low gain avalanche detectors,” *Nuclear Instruments and Methods in Physics Research Section A: Accelerators, Spectrometers, Detectors and Associated Equipment*, vol. 821, pp. 93–100, 2016. DOI: [/10.1016/j.nima.2016.03.049](https://doi.org/10.1016/j.nima.2016.03.049).
- [49] R. Heller *et al.*, “Combined analysis of HPK 3.1 LGADs using a proton beam, beta source, and probe station towards establishing high volume quality control,” *Nuclear Instruments and Methods in Physics Research Section A: Accelerators, Spectrometers, Detectors and Associated Equipment*, vol. 1018, no. 165828, 2021. DOI: [/10.1016/j.nima.2021.165828](https://doi.org/10.1016/j.nima.2021.165828).
- [50] V. Sola *et al.*, “Characterisation of 50 μm thick LGAD manufactured by FBK and HPK,” *CERN technical report*, 2019. [Online]. Available: <https://cds.cern.ch/record/2667026>.
- [51] E. Navarrete *et al.*, “Radiation Tolerance Study of IMB-CNM Run15973,” *The 43rd RD50 workshop on Radiation Hard Semiconductors Devices for High Luminosity Colliders*, 2023. [Online]. Available: <https://indico.cern.ch/event/1334364/contributions/5674846/>.
- [52] F. Siviero *et al.*, “Design optimization of the UFSD inter-pad region,” *Nuclear Instruments and Methods in Physics Research Section A: Accelerators, Spectrometers, Detectors and Associated Equipment*, vol. 1061, no. 169153, 2024. DOI: [/10.1016/j.nima.2024.169153](https://doi.org/10.1016/j.nima.2024.169153).
- [53] B. J. Baliga, *Fundamentals of Power Semiconductor Devices*. Wiley. West Sussex, 2008.
- [54] P. M. Fahey, “Point defects and dopant diffusion in silicon,” *Reviews of Modern Physics*, vol. 61, no. 2, pp. 289–384, 1989. DOI: [/10.1103/RevModPhys.61.289](https://doi.org/10.1103/RevModPhys.61.289).
- [55] P. Pichler, *Intrinsic Point Defects, Impurities, and Their Diffusion in Silicon*. Springer. Vienna, 2004.
- [56] Synopsis. Advanced Calibration for Process Simulation User Guide. Version O-2018.06, June 2018.
- [57] M. D. et al, “Comparing Spreading Resistance Profiling and CV characterisation to identify defects in silicon sensors,” *Journal of Instrumentation*, vol. 8, no. C02018, 2013. DOI: [10.1088/1748-0221/8/02/C02018](https://doi.org/10.1088/1748-0221/8/02/C02018).
- [58] E. Curras and M. Moll, “Study of impact ionization coefficients in silicon with Low Gain Avalanche Diodes,” *IEEE Transactions on Electron Devices*, vol. 70, no. 6, pp. 2919–2926, 2023. DOI: [/10.1109/TED.2023.3267058](https://doi.org/10.1109/TED.2023.3267058).
- [59] K. Iniewski, *Radiation Effects in Semiconductors*. CRC Press. Boca Raton, 2011.
- [60] M. Moll, “Radiation Damage in Silicon Particle Detectors,” *Doctoral Thesis. Universitat Hamburg*, 1999. [Online]. Available: <https://bib-pubdb1.desy.de/record/300958>.
- [61] V. Zerkin, “The experimental nuclear reaction data (EXFOR): Extended computer database and Web retrieval system,” *Nuclear Instruments and Methods in Physics Research Section A: Accelerators, Spectrometers, Detectors and Associated Equipment*, vol. 888, pp. 31–43, 2018. DOI: [/10.1016/j.nima.2018.01.045](https://doi.org/10.1016/j.nima.2018.01.045).
- [62] J. R. Srouf, “Review of displacement damage effects in silicon devices,” *IEEE Transactions on Nuclear Science*, vol. 50, no. 3, pp. 653–670, 2003. DOI: [/10.1109/TNS.2003.813197](https://doi.org/10.1109/TNS.2003.813197).

- [63] F. Lemeilleur *et al.*, “Neutron-induced radiation damage in silicon detectors,” *IEEE Transactions on Nuclear Science*, vol. 39, no. 4, pp. 551–557, 1992. DOI: [10.1109/23.159664](https://doi.org/10.1109/23.159664).
- [64] J. Villegas *et al.*, “Measurements on last IMB-CNM LGADs production,” *The 43rd RD50 workshop on Radiation Hard Semiconductors Devices for High Luminosity Colliders*, 2023. [Online]. Available: <https://indico.cern.ch/event/1334364/contributions/5672080/>.
- [65] M. Moll, “Acceptor removal - Displacement damage effects involving the shallow acceptor doping of p-type silicon devices,” *The 28th International Workshop on Vertex Detectors*, 2020. DOI: [/10.22323/1.373.0027](https://doi.org/10.22323/1.373.0027).
- [66] Y. Feng *et al.*, “Study of the Acceptor Removal Effect of LGAD,” *IEEE Transactions on Nuclear Science*, vol. 69, no. 12, pp. 2324–2329, 2022. DOI: [/10.1109/TNS.2022.3221482](https://doi.org/10.1109/TNS.2022.3221482).
- [67] J. Villegas *et al.*, “The effects in fabrication and performance of carbon doping on IMB-CNM manufactured LGADs,” *Nuclear Instruments and Methods in Physics Research Section A: Accelerators, Spectrometers, Detectors and Associated Equipment*, vol. 1064, no. 169424, 2024. DOI: [/10.1016/j.nima.2024.169424](https://doi.org/10.1016/j.nima.2024.169424).
- [68] B. J. Pawlak *et al.*, “Effect of amorphization and carbon co-doping on activation and diffusion of boron in silicon,” *Applied Physics Letters*, vol. 89, no. 062110, 2006. DOI: [/10.1063/1.2227863](https://doi.org/10.1063/1.2227863).
- [69] H. Rucker *et al.*, “Suppressed diffusion of boron and carbon in carbon-rich silicon,” *Applied Physics Letters*, vol. 73, pp. 1682–1684, 1998. DOI: [/10.1063/1.122244](https://doi.org/10.1063/1.122244).
- [70] B. J. Pawlak *et al.*, “Suppression of phosphorus diffusion by carbon co-implantation,” *Applied Physics Letters*, vol. 89, no. 062102, 1998. DOI: [/10.1063/1.2234315](https://doi.org/10.1063/1.2234315).
- [71] A. Hayrapetyan *et al.*, “Combination of Measurements of the Top Quark Mass from Data Collected by the ATLAS and CMS Experiments at $\sqrt{s}=7$ and 8 TeV,” *Physical Review Letters*, vol. 132, no. 261902, 2024. DOI: [/10.1103/PhysRevLett.132.261902](https://doi.org/10.1103/PhysRevLett.132.261902).
- [72] M. P. Casado, “A High-Granularity Timing Detector for the ATLAS Phase-II upgrade,” *Nuclear Instruments and Methods in Physics Research Section A: Accelerators, Spectrometers, Detectors and Associated Equipment*, vol. 1032, no. 166628, 2022. DOI: [/10.1016/j.nima.2022.166628](https://doi.org/10.1016/j.nima.2022.166628).
- [73] F. Siviero, “The Endcap Timing Layer of the CMS experiment: detector development and impact on physics analyses,” *Doctoral Thesis. Università Degli Studi di Torino*, 2022. [Online]. Available: <https://cds.cern.ch/record/2839829>.
- [74] G. Laštovička-Medin, “Studies of LGAD performance limitations, Single Event Burnout and Gain Suppression, with Femtosecond-Laser and Ion Beams,” *Nuclear Instruments and Methods in Physics Research Section A: Accelerators, Spectrometers, Detectors and Associated Equipment*, vol. 1041, no. 167388, 2022. DOI: [/10.1016/j.nima.2022.167388](https://doi.org/10.1016/j.nima.2022.167388).
- [75] E. Navarrete *et al.*, “Radiation Tolerance Study of CNM-IMB Run15246,” *The 42nd RD50 workshop on Radiation Hard Semiconductors Devices for High Luminosity Colliders*, 2022. [Online]. Available: <https://indico.cern.ch/event/1132520/contributions/5140038/>.

- [76] C. Grieco *et al.*, “Overview of CNM LGAD results: Boron Si-on-Si and epitaxial wafers,” *Journal of Instrumentation*, vol. 17, no. C09021, 2022. DOI: [10.1088/1748-0221/17/09/C09021](https://doi.org/10.1088/1748-0221/17/09/C09021).
- [77] C. Grieco, “Low Gain Avalanche Detector for the ATLAS High Granularity Timing Detector,” *Doctoral Thesis. Universitat Autònoma de Barcelona*, 2022. [Online]. Available: https://ddd.uab.cat/pub/tesis/2022/hdl_10803_675616/chgr1de1.pdf.
- [78] V. Gautam, “New Silicon Devices with Charge Multiplication for the ATLAS Upgrade and Medical Applications,” *Doctoral Thesis. Universitat Autònoma de Barcelona*, 2024. [Online]. Available: https://ddd.uab.cat/pub/tesis/2024/hdl_10803_689771/adm1de1.pdf.
- [79] M. Ferrero *et al.*, “Radiation resistant LGAD design,” *Nuclear Instruments and Methods in Physics Research Section A: Accelerators, Spectrometers, Detectors and Associated Equipment*, vol. 919, pp. 16–26, 2019. DOI: [/10.1016/j.nima.2018.11.121](https://doi.org/10.1016/j.nima.2018.11.121).
- [80] M. Moll, “Acceptor removal - Displacement damage effects involving the shallow acceptor doping of p-type silicon devices,” *The 28th International Workshop on Vertex Detectors*, [Online]. Available: [10.22323/1.373.0027](https://doi.org/10.22323/1.373.0027).
- [81] B. E. Deal and M. Sklar, “Thermal Oxidation of Heavily Doped Silicon,” *Journal of Applied Physics*, vol. 116, no. 193503, 1965. DOI: [/10.1149/1.2423562](https://doi.org/10.1149/1.2423562).
- [82] J. D. Murphy *et al.*, “Enhanced oxygen diffusion in highly doped -type Czochralski silicon,” *Journal of Applied Physics*, vol. 100, no. 103531, 2006. DOI: [/10.1063/1.2369536](https://doi.org/10.1063/1.2369536).
- [83] K. Torigoe *et al.*, “Enhanced diffusion of oxygen depending on Fermi level position in heavily boron-doped silicon,” *Journal of Applied Physics*, vol. 116, no. 193503, 2014. DOI: [/10.1063/1.4901987](https://doi.org/10.1063/1.4901987).
- [84] E. Curras *et al.*, “Gain suppression mechanism observed in Low Gain Avalanche Detectors,” *Nuclear Instruments and Methods in Physics Research Section A: Accelerators, Spectrometers, Detectors and Associated Equipment*, vol. 1031, no. 166530, 2022. DOI: [/10.1016/j.nima.2022.166530](https://doi.org/10.1016/j.nima.2022.166530).
- [85] M. C. Jimenez *et al.*, “Study of Ionization Charge Density-Induced Gain Suppression in LGADs,” *Sensors*, vol. 22(3), no. 1080, 2022. DOI: [/10.3390/s22031080](https://doi.org/10.3390/s22031080).
- [86] A. Howard *et al.*, “First measurements of irradiated CNM LGADs with carbon enriched gain layer,” *The 42nd RD50 workshop on Radiation Hard Semiconductors Devices for High Luminosity Colliders*, 2023. [Online]. Available: <https://indico.cern.ch/event/1270076/contributions/5450203/>.
- [87] C. Yu *et al.*, “Update for the LGAD sensor test,” *CMS ETL meeting September 9th 2024*, 2024. [Online]. Available: <https://indico.cern.ch/event/1411350/>.
- [88] S. T. Lee and D. Nichols, “Outdiffusion and diffusion mechanism of oxygen in silicon,” *Applied Physics Letters*, vol. 47, pp. 1001–1003, 1985. DOI: [/10.1063/1.95969](https://doi.org/10.1063/1.95969).
- [89] F. Shimura *et al.*, “Outdiffusion of oxygen and carbon in Czochralski silicon,” *Applied Physics Letters*, vol. 53, pp. 69–71, 1988. DOI: [/10.1063/1.100126](https://doi.org/10.1063/1.100126).
- [90] W. Wijaranakula, “Oxygen diffusion in carbon-doped silicon,” *Applied Physics Letters*, vol. 68, pp. 6538–6540, 1990. DOI: [/10.1063/1.346833](https://doi.org/10.1063/1.346833).

- [91] R. G. Mazur and D. H. Dickey, "A Spreading Resistance Technique for Resistivity Measurements on Silicon," *Journal of The Electrochemical Society*, vol. 113, no. 255, 1966. DOI: [10.1149/1.2423927](https://doi.org/10.1149/1.2423927).
- [92] Semilab SRP-2100 Spreading Resistance Profiler. official website, <https://semilab.com/category/products/spreading-resistance-profiling>.
- [93] S. Choo *et al.*, "Spreading resistance calculations by the variational method," *Solid-State Electronics*, vol. 24, no. 6, pp. 557–562, 1981. DOI: [/10.1016/0038-1101\(81\)90076-9](https://doi.org/10.1016/0038-1101(81)90076-9).
- [94] S. Choo *et al.*, "An efficient numerical scheme for spreading resistance calculations based on the variational method," *Solid-State Electronics*, vol. 26, no. 8, pp. 723–730, 1983. DOI: [/10.1016/0038-1101\(83\)90032-1](https://doi.org/10.1016/0038-1101(83)90032-1).
- [95] R. G. Mazur and D. H. Dickie, "A Spreading Resistance Technique for Resistivity Measurements on Silicon," *Journal of The Electrochemical Society*, vol. 113, no. 255, 1966. DOI: [10.1149/1.2423927](https://doi.org/10.1149/1.2423927).
- [96] S. Choo *et al.*, "Spreading resistance calculations by the use of Gauss-Laguerre quadrature," *Solid-State Electronics*, vol. 21, no. 5, pp. 769–774, 1978. DOI: [/10.1016/0038-1101\(78\)90010-2](https://doi.org/10.1016/0038-1101(78)90010-2).
- [97] Y. Feng, "Study of the Acceptor Removal Effect of LGAD," *IEEE Transactions on Nuclear Science*, vol. 69, no. 12, pp. 2324–2329, 2022. DOI: [/10.1109/TNS.2022.3221482](https://doi.org/10.1109/TNS.2022.3221482).
- [98] M. Li *et al.*, "Effects of Shallow Carbon and Deep N++ Layer on the Radiation Hardness of IHEP-IME LGAD Sensors," *IEEE Transactions on Nuclear Science*, vol. 69, no. 5, pp. 1098–1103, 2022. DOI: [/10.1109/TNS.2022.3161048](https://doi.org/10.1109/TNS.2022.3161048).
- [99] K. Wu *et al.*, "Design and testing of LGAD sensor with shallow carbon implantation," *Nuclear Instruments and Methods in Physics Research Section A: Accelerators, Spectrometers, Detectors and Associated Equipment*, vol. 1064, no. 167697, 2023. DOI: [/10.1016/j.nima.2022.167697](https://doi.org/10.1016/j.nima.2022.167697).
- [100] M. Zhao *et al.*, "Low Gain Avalanche Detectors with good time resolution developed by IHEP and IME for ATLAS HGTD project," *Nuclear Instruments and Methods in Physics Research Section A: Accelerators, Spectrometers, Detectors and Associated Equipment*, vol. 1033, no. 166604, 2022. DOI: [/10.1016/j.nima.2022.166604](https://doi.org/10.1016/j.nima.2022.166604).
- [101] T. E. Seidel and A. U. M. Rae, "The isothermal annealing of boron implanted silicon," *Radiation Effects*, vol. 7, no. 1-2, pp. 1–6, 1971. DOI: [/10.1080/00337577108232558](https://doi.org/10.1080/00337577108232558).
- [102] E. Landi *et al.*, "Electrical activation of boron-implanted silicon during rapid thermal annealing," *Applied Physics Letters A*, vol. 47, pp. 359–366, 1988. DOI: [/10.1007/BF00615499](https://doi.org/10.1007/BF00615499).
- [103] J. J. Grob *et al.*, "Activation and diffusion during rapid thermal annealing of arsenic and boron implanted silicon," *Nuclear Instruments and Methods in Physics Research Section B: Beam Interactions with Materials and Atoms*, vol. 19-20, no. 2, pp. 501–506, 1987. DOI: [/10.1016/S0168-583X\(87\)80100-3](https://doi.org/10.1016/S0168-583X(87)80100-3).
- [104] J. F. Ziegler *et al.*, "SRIM – The stopping and range of ions in matter," *Nuclear Instruments and Methods in Physics Research Section B: Beam Interactions with Materials and Atoms*, vol. 268, no. 11-12, pp. 1818–1823, 2010. DOI: [/10.1016/j.nimb.2010.02.091](https://doi.org/10.1016/j.nimb.2010.02.091).

- [105] M. M. Farahani *et al.*, "Evaluation of Titanium as a Diffusion Barrier Between Aluminum and Silicon for 1.2 μm CMOS Integrated Circuits," *Journal of The Electrochemical Society*, vol. 134, no. 11, p. 2835, 1987. DOI: [10.1149/1.2100298](https://doi.org/10.1149/1.2100298).
- [106] G. Kramberger, "Advanced Transient Current Technique Systems," *The 23rd International Workshop on Vertex Detectors*, 2015. DOI: [/10.22323/1.227.0032](https://doi.org/10.22323/1.227.0032).
- [107] B. L. Henke *et al.*, "X-ray interactions: photoabsorption, scattering, transmission, and reflection at $E=50\text{--}30000\text{ eV}$, $Z=1\text{--}92$," *CXRO Atomic Data and Nuclear Data Tables*, vol. 54, no. 2, pp. 182–342, 1993. DOI: [/10.1006/adnd.1993.1013](https://doi.org/10.1006/adnd.1993.1013).
- [108] M. Centis and G. Paternoster, "Low gain avalanche diodes for photon science applications," *Frontiers in Physics*, vol. 12, no. 1359179, 2024. DOI: [/10.3389/fphy.2024.1359179](https://doi.org/10.3389/fphy.2024.1359179).
- [109] D. Renker and E. Lorenz, "Advances in solid state photon detectors," *Journal of Instrumentation*, vol. 4, no. P04004, 2009. DOI: [10.1088/1748-0221/4/04/P04004](https://doi.org/10.1088/1748-0221/4/04/P04004).
- [110] L. Shi and S. Nihtianov, "Comparative Study of Silicon-Based Ultraviolet Photodetectors," *IEEE Sensors Journal*, vol. 12, no. 2453—2459, 2012. DOI: [10.1109/JSEN.2012.2192103](https://doi.org/10.1109/JSEN.2012.2192103).
- [111] W. A. R. Franks *et al.*, "UV-responsive CCD image sensors with enhanced inorganic phosphor coatings," *IEEE Transactions on Electron Devices*, vol. 50, no. 352–358, 2003. DOI: [/10.1109/TED.2003.809029](https://doi.org/10.1109/TED.2003.809029).
- [112] R. Rajendran *et al.*, "Towards a stand-alone high-throughput EUV actinic photomask inspection tool: RESCAN," *Proceedings of the SPIE: Metrology, Inspection, and Process Control for Microlithography XXXI*, vol. 10145, no. 101450N, 2017. DOI: [/10.1117/12.2258379](https://doi.org/10.1117/12.2258379).
- [113] M. Berger *et al.*, "Stopping-Power and Range Tables for Electrons, Protons, and Helium Ions," *NISTIR*, no. 4999, 2017. DOI: [/10.18434/T4NC7P](https://doi.org/10.18434/T4NC7P).
- [114] H. Han *et al.*, "A sustained high-temperature fusion plasma regime facilitated by fast ions," *Nature*, vol. 609, pp. 269–275, 2022. DOI: [/10.1038/s41586-022-05008-1](https://doi.org/10.1038/s41586-022-05008-1).
- [115] L. J. Broussard *et al.*, "Using Nab to determine correlations in unpolarized neutron decay," *Hyperfine Interact*, vol. 240, no. 1, 2019. DOI: [/10.1007/s10751-018-1538-7](https://doi.org/10.1007/s10751-018-1538-7).
- [116] D. Moser *et al.*, "NoMoS: An $R\times B$ drift momentum spectrometer for beta decay studies," *International Workshop on Particle Physics at Neutron Sources (PPNS 2018)*, no. 04003, 2018. DOI: [/10.1051/epjconf/201921904003](https://doi.org/10.1051/epjconf/201921904003).
- [117] W. Khaled *et al.*, "First Results for the pLGAD Sensor for Low-Penetrating Particles," *Nuclear Instruments and Methods in Physics Research Section A: Accelerators, Spectrometers, Detectors and Associated Equipment*, vol. 1040, no. 167220, 2022. DOI: [/10.1016/j.nima.2022.167220](https://doi.org/10.1016/j.nima.2022.167220).
- [118] G. Pellegrini, S. Hidalgo, D. Flores, W. Khalid and M. Valenta. "Low-penetrating particles low-gain avalanche detector (PATENT)", 2022. <https://patentscope.wipo.int/search/es/detail.jsf?docId=W02022063852>.
- [119] Particulars official website, <https://www.particulars.si/products.php>.
- [120] J. Gomez-Camacho *et al.*, "Research facilities and highlights at the Centro Nacional de Aceleradores (CNA)," *European Physical Journal Plus*, vol. 136, no. 273, 2021. DOI: [/10.1140/epjp/s13360-021-01253-x](https://doi.org/10.1140/epjp/s13360-021-01253-x).

- [121] M. A. Ontalba *et al.*, “External microbeam set-up at the CNA (Sevilla) and its application to the study of Tartessian jewellery,” *Nuclear Instruments and Methods in Physics Research Section B: Beam Interactions with Materials and Atoms*, vol. 181, pp. 664–669, 2001. DOI: [/10.1016/S0168-583X\(01\)00355-X](https://doi.org/10.1016/S0168-583X(01)00355-X).
- [122] G. Paternoster *et al.*, “Trench-Isolated Low Gain Avalanche Diodes (TI-LGADs),” *IEEE Electron Device Letters*, vol. 41, no. 6, pp. 884–887, 2020. DOI: [10.1109/LED.2020.2991351](https://doi.org/10.1109/LED.2020.2991351).
- [123] A. Bisht *et al.*, “Characterization of novel trench-isolated LGADs for 4D tracking,” *Nuclear Instruments and Methods in Physics Research Section A: Accelerators, Spectrometers, Detectors and Associated Equipment*, vol. 1048, no. 167929, 2023. DOI: [/10.1016/j.nima.2022.167929](https://doi.org/10.1016/j.nima.2022.167929).
- [124] M. Carulla, “Thin LGAD timing detectors for the ATLAS experiment,” *Doctoral Thesis. Universitat Autònoma de Barcelona*, 2019. [Online]. Available: https://ddd.uab.cat/pub/tesis/2019/hdl_10803_667283/mdmca1de1.pdf.
- [125] N. Cartiglia *et al.*, “LGAD designs for Future Particle Trackers,” *Nuclear Instruments and Methods in Physics Research Section B: Beam Interactions with Materials and Atoms*, vol. 979, no. 164383, 2020. DOI: [/10.1016/j.nima.2020.164383](https://doi.org/10.1016/j.nima.2020.164383).
- [126] G. Giacomini *et al.*, “Fabrication and performance of AC-coupled LGADs,” *Journal of Instrumentation*, vol. 14, no. P09004, 2019. DOI: [10.1088/1748-0221/14/09/P09004](https://doi.org/10.1088/1748-0221/14/09/P09004).
- [127] A. Doblas *et al.*, “Inverse LGAD (iLGAD) Periphery Optimization for Surface Damage Irradiation,” *Sensors*, vol. 23(7), no. 3450, 2023. DOI: [/10.3390/s23073450](https://doi.org/10.3390/s23073450).
- [128] M. S. Tyagi *et al.*, “Zener and avalanche breakdown in silicon alloyed p-n junctions—II: Effect of temperature on the reverse characteristics and criteria for distinguishing between the two breakdown mechanisms,” *Solid-State Electronics*, vol. 11, no. 1, pp. 117–128, 1968. DOI: [10.1016/0038-1101\(68\)90142-1](https://doi.org/10.1016/0038-1101(68)90142-1).
- [129] C. R. Crowell and S. M. Sze, “Temperature dependence of avalanche multiplication in semiconductors,” *Applied Physics Letters*, vol. 9, no. 1, 242–244, 1966. DOI: [/10.1063/1.1754731](https://doi.org/10.1063/1.1754731).
- [130] H. L. Berkowitz and R. A. Lux, “An Efficient Integration Technique for Use in the Multilayer Analysis of Spreading Resistance Profiles,” *Journal of The Electrochemical Society*, vol. 128, no. 1137, 1981. DOI: [10.1149/1.2127565](https://doi.org/10.1149/1.2127565).
- [131] AIDAInnova 2nd Annual Meeting (2023), <https://indico.cern.ch/event/1191719/>.